Atmospheric Fate of Sulfur Species Emitted to the Pristine Marine Environment

By

Christopher M. Jernigan

A dissertation submitted in partial fulfillment of the requirements for the degree of

Doctor of Philosophy

(Chemistry)

at the

UNIVERSITY OF WISCONSIN-MADISON

2022

Date of final oral examination: August 5th, 2022

The dissertation is approved by the following members of the Final Oral Committee:

Timothy H. Bertram, Professor, Chemistry

Gilbert M. Nathanson, Professor, Chemistry

Susanna L. Widicus-Weaver, Professor, Chemistry

Christy K. Remucal, Associate Professor, Civil and Environmental Engineering

Thesis Abstract

Sulfur is an essential component of Earth's biogeochemical system with particular importance in atmospheric chemistry, air quality, and climate. A significant source of sulfur enters the atmosphere from the ocean primarily in the form of dimethyl sulfide (DMS). The oxidation products of DMS contribute to the production and growth of aerosol particles and to global climate regulation by scattering incoming solar radiation directly or indirectly by increasing cloud condensation nuclei (CCN). Recent work demonstrates DMS is oxidized by OH radicals to form the stable intermediate hydroperoxymethyl thioformate (HPMTF), which is both globally ubiquitous and efficiently lost to multiphase processes in the marine atmosphere. Here, I present a system of laboratory experiments aimed at identifying the mechanisms that dictate the gas-phase, multiphase, and aqueous fate of HPMTF under conditions representative of the marine environment. Utilizing the environmental chamber design and zero-dimensional box model developed for DMS oxidation, the oxidation of other marine emitted sulfur species (e.g. methanethiol, dimethyl disulfide, carbon disulfide) were investigated. A particular focus is made on the process that ties the oxidative mechanisms of marine environments to the production of long-lived climate relevant species, sulfur dioxide and carbonyl sulfide.

This thesis aims to reexamine the oxidation of marine sulfur species under pristine marine conditions with a mechanistic lens with the goal of applying the laboratory and computational findings to global climate models. In chapter 1, we present a detailed description of the design, operation, and modeling of a continuous flow environmental chamber aimed to simulate oxidative conditions indicative of the remote marine environment. In chapters 2, 4, and 5, we examine fate of HPMTF within the marine environment including the formation, OH-oxidation, uptake to marine aerosols, and aqueous processing to determine its connection to the formation of sulfur

dioxide, sulfate, and carbonyl sulfide. In chapter 3, we apply the knowledge learned from DMS oxidation to other sulfur species to determine the product yields and chemical mechanisms that dictate the production of SO_2 and OCS under conditions indicative of the marine environment.

Dedication

This work was supported by the NSF Center for Aerosol Impacts on Chemistry of the Environment under Grant CHE 1801971.

I would like to thank all the friends and family that have supported, encouraged, and worked with me over my years pursuing my PhD and before. I would like to start with every member in the Bertram group both past and present. I would like to thank Sean, Gordon and Michael who served as senior graduate students and good friends during my years in graduate school. I appreciate all the time and effort you spent to make me a great researcher and an even better Magic the Gathering player. Additional thanks to Rachel, Delaney, Tom, Stephanie, Corey, Martina, David, Subi, Shannon, and Kevin who have all acted as amazing friends and incredible colleagues. I have enjoyed all the lunches, group outings and slack gossip over the past years and I hope to stay in touch throughout the years. To Steve and Joe, y'all are amazing resources not only for your science knowledge, but also for advice on future careers and 70's rock bands. Lastly, I have been fortunate to work with an undergraduate researcher, Matt, and though our time working together was short, I appreciate working with you over the past year. Outside of the group, I would like to thank all the members of the CAICE team. CAICE has not only provided a consistent funding source, but also venue to present my work to colleges, to learn and discuss science from across multiple fields, and to form ongoing collaborations both as friends and future colleagues.

Thank you to Tim Bertram and George Dubay for being incredible supportive mentors, principal investigators, and friends throughout my research career. I am particularly grateful for the research guidance, independence, and the opportunities you gave me.

My parents, Dan and Stephanie, my brother, Tim, and my dog, Tucker, have been a critical to my success in both my personal and scientific career. Your love and support for me throughout my life has allowed me to get where I am today. I am also incredibly thankful to the various friends I have made over the years. The Spooner Estate, Brunchie Bunch, Shredder and the Goose, the Portofellos, and the Pick-up Volleyball squad are all made up of incredible friends that have made my life more enjoyable.

Thank you.

Co-Authors and Contributions

Chapter 1 is a reprint of the material as it appears in the supplemental information of Jernigan et al. (2022) within Geophysical Research Letters. Jernigan, C. M., Fite, C. H., Vereecken, L., Berkelhammer, M. B., Rollins, A. W., Rickly, P. S., et al. (2022). Efficient production of carbonyl sulfide in the low-NOx oxidation of dimethyl sulfide. Geophysical Research Letters, 49, e2021GL096838. https://doi.org/10.1029/2021GL096838 The dissertation author was the primary investigator and author of this paper.

Chapter 2 is a reprint of the material as it appears in Geophysical Research Letters. Jernigan, C. M., Fite, C. H., Vereecken, L., Berkelhammer, M. B., Rollins, A. W., Rickly, P. S., et al. (2022). Efficient production of carbonyl sulfide in the low-NOx oxidation of dimethyl sulfide. Geophysical Research Letters, 49, e2021GL096838. https://doi.org/10.1029/2021GL096838 The dissertation author was the primary investigator and author of this paper.

Chapter 3, Contributing Authors: Christopher M. Jernigan, Max B. Berkelhammer, and Timothy H. Bertram. An additional thanks to Delaney B. Kilgour and Michael P. Vermeuel for their help and support running gas chromatography on the chamber experiments.

Chapter 4, in full, is a reprint of the material as it appears in Journal of Physical Chemistry A. Jernigan, C. M., Cappa, C. D., & Bertram, T. H. (2022). Reactive Uptake of Hydroperoxymethyl Thioformate to Sodium Chloride and Sodium Iodide Aerosol Particles. *The Journal of Physical Chemistry A.* https://doi.org/10.1021/acs.jpca.2c03222. The dissertation author was the primary investigator and author of this paper.

Chapter 5, Contributing Authors: Christopher M. Jernigan, Matt J. Rivard, Max B. Berkelhammer and Timothy H. Bertram. An additional thanks to James Lazarcik and the Water Science and Engineering Laboratory for their help and support in running Ion Chromatography.

Table of Contents

Thesis Introduction

I.1 Emission of Sulfur

Sulfur is an essential component of Earth's biochemical system with particular importance in atmospheric chemistry, air quality, and climate. Depending on the source, sulfur can enter Earth's atmosphere in a variety of reduced and oxidized forms. A key species within the atmospheric sulfur cycle is sulfur dioxide (SO_2). SO_2 plays an important role in air quality as it contributes to acid rain and haze events known to be detrimental to aquatic systems, forests and human health(T.-M. Chen et al., 2007). SO_2 and its oxidation to sulfate aerosol contributes to global climate regulation by scattering incoming solar radiation directly or indirectly by increasing cloud condensation nuclei (CCN). SO_2 can be emitted directly to the atmosphere through anthropogenic (e.g. coal combustion, ship emissions) or natural (e.g. volcanic eruptions, biomass burning) processes and it can be produced through the oxidation of reduced and oxidized sulfur compounds (Barnes et al., 2006; Bates et al., 1992; Faloona, 2009; Rodhe, 1999; Wine et al., 1981). Global anthropogenic emissions of SO_2 have been dropping over the past decades as regional emission standards have taken hold (Shukla et al., 2019). The global burden of SO_2 is primarily driven by the combustion of sulfur containing fuels, mineral ore processing and global shipping with an estimated emission of c.a. 70 TgS yr^{-1} (Faloona, 2009; Liu et al., 2000; Rodhe, 1999). Additional direct SO_2 emissions can come through the passive and explosive emission of SO_2 from volcanoes, an efficient source of direct emissions to the stratosphere, and through biomass burning thought to supply c.a. 9 and 1 TgS yr^{-1} to the atmosphere, respectively (Bates et al., 1992; Langner & Rodhe, 1991a; Pinto et al., 1989). Lastly, SO_2 can be added to the atmosphere through the oxidation of emitted reduced sulfur species either from terrestrial (e.g. forests, marshes, and fresh water) or marine origins (Bates et al., 1992).

Carbonyl sulfide (OCS) is the most abundant sulfur-containing gas ([OCS] = 500 pptv) in Earth's atmosphere with an estimated lifetime of greater than 2 years (Brühl et al., 2012; Chin & Davis, 1993a; Montzka et al., 2007). The relatively long lifetime of OCS allows for the continuous entrainment of OCS into the lower stratosphere from the troposphere. In the stratosphere, OCS is oxidized through photochemical means to sulfate aerosol which plays a critical role in Earth's climate regulation. Stratospheric sulfate can directly scatter incoming solar radiation, cooling the planet, as well as serve to catalyze heterogeneous reactions with importance to stratospheric ozone depletion (Crutzen, 1976; Solomon et al., 1986). In the troposphere, OCS is readily consumed by the terrestrial biosphere via similar mechanisms as carbon dioxide uptake and has proven to be an effective tool for estimating gross primary production (GPP) (Asaf et al., 2013). Despite the importance of OCS, the spatial distribution and production of OCS sources remain poorly constrained (Kremser et al., 2016; Ma et al., 2021). It has been shown that OCS is directly emitted to the atmosphere from oceans(Von Hobe et al., 2001), wetlands(Watts, 2000), and anoxic soils(Devai & DeLaune, 1995), is formed chemically in the atmosphere through the oxidation of dimethyl sulfide (DMS)(Barnes et al., 1994b; Jernigan et al., 2022) and carbon disulfide (CS_2) (Chin & Davis, 1993b), and is released through a wide variety of anthropogenic activities (Zumkehr et al., 2018).

A significant source of reduced sulfur to the atmosphere is the ocean, with origins primarily driven by biological activity. The primary sulfur molecule emitted is dimethyl sulfide, DMS, but along with its emission is a collection of other reduced sulfur molecules. The majority of atmospheric DMS comes from the degradation of dimethylsulfoniopropionate (DMSP) by marine bacteria (Lana et al., 2011). DMS predominantly stays within the oceans with only a small fraction emitted to the atmosphere (Yoch, 2002). The magnitude of DMS flux from the ocean to the

atmosphere is dependent on physical variables, such as sea surface DMS concentration, wind speed, sea surface temperature and salinity (Kloster et al., 2006). While ocean dynamics play an important role in the transport from the ocean to the atmosphere, the flux to the atmosphere is predominately dictated by the sea surface concentration of DMS due to its low dimensionless gas over liquid Henry's law constant ($K_H = 0.07$) (Wong & Wang, 1997). Depending on the weight of the different flux parameters, average global DMS ocean-atmosphere flux has been calculated to be from 15-36 TgS/yr (Faloona, 2009; Kloster et al., 2006; Lana et al., 2011; Watts, 2000).

Dimethyl sulfide is the primary source of reduced sulfur to the marine atmosphere, but it is not the only emission source that contributes to secondary SO_2 and OCS production. Methanethiol (MeSH) and dimethyl disulfide (DMDS) are reduced sulfur species emitted from the ocean, with similar biological origins as dimethyl sulfide (Kiene, 1996; Lee & Brimblecombe, 2016; Tanzer & Heumann, 1992). MeSH is produced in higher yields than DMS in sea water and is consumed more rapidly either by marine microorganisms, reactions with organic matter or by oxidation (Kiene, 1996; Kiene & Linn, 2000). Only a few studies have observed marine DMDS and MeSH, with most concluding that MeSH tracks DMS emissions and DMDS is significant in coastal regions when compared to that of open ocean(Kettle et al., 2001). Like DMDS, carbon disulfide (CS_2) is a reduced sulfur compound with marine sources driven by biological and photochemical processes and is present in higher concentrations in coastal and regions than the open ocean (Chin & Davis, 1993a; Lee & Brimblecombe, 2016; Lennartz et al., 2021; T Lennartz et al., 2020). All of the reduced sulfur emissions are known to oxidize to sulfur dioxide, but up until the work performed in chapter 3 only DMS and CS_2 are currently known to contribute to indirect OCS production through OH-oxidation.

I.2 Gas-phase oxidation within the marine environment

A significant source of SO_2 and OCS production arises in the marine sources, stemming in part from an incomplete understanding of the oxidation of marine sulfur gases. SO_2 is a significant oxidation product that arises from the oxidation of reduced sulfur species (Wine et al., 1981). The median fraction of the SO_2 source from marine environment is thought to be 20%, primarily driven by the oxidation of DMS, but recent work says the oxidation of methanethiol (MeSH), a marine co-emitter with DMS, can also significantly contribute (Faloona, 2009; G. A. Novak et al., 2022). It is not yet clear what fraction of marine-derived OCS is directly emitted from the ocean compared with that formed in the oxidation of biogenic dimethyl sulfide (DMS) and carbon disulfide (CS_2). In response to recent suggestions that the production of OCS from the OH-initiated oxidation of other marine sulfur species may be a significant source of uncertainty in the OCS budget, we have revisited the chemical mechanism for OCS and SO_2 production in the oxidation of known sulfur compounds emitted to the marine atmosphere (DMS, DMDS, MeSH and CS_2). A particular focus is made on the oxidation mechanism of DMS as it is the dominant source of marine reduced sulfur to the atmosphere. Once emitted from the ocean, DMS is primarily oxidized by the hydroxy radical (OH), halogen radicals (BrO and Cl), and the nitrate radical (NO_3) to a variety of oxidized species. While halogen radical oxidation can be a source of significant loss for DMS, the primary loss pathway over the open ocean is OH-initiated oxidation. OH loss initializes via one of two initial steps: (R1) OH addition or (R2) hydrogen abstraction, as seen in **Figure I.1**.(Barnes et al., 2006; Barone et al., 1996; Yin et al., 1990a) The branching between the two reactions is highly temperature dependent with the hydrogen abstraction rate being roughly twice that of the addition rate at 298K and nearly equal at 288K. The driver of this difference is the weakly bound S-OH adduct that is formed in the OH addition (Hynes et al., 1995). This adduct formation is a reversible

reaction that, at higher temperatures, starts to favor dissociation of the OH adduct. In both cases, reaction with OH generates a new radical species that promptly reacts with ambient oxygen (O_2). An oxygen adduct radical is formed, known as a peroxy radical species (RO_2), that can react with a variety of environment-dependent species. The current understanding is that the RO_2 formed by the OH addition pathway and BrO will primarily transform into highly soluble species (e.g**.** dimethyl sulfoxide and methanesolfonic acid) which contribute to aerosol growth(Hoffmann et al., 2016a; Kreidenweis & Seinfeld, 1988) while the RO_2 generated by the OH and Cl hydrogen abstraction pathway (methylthiomethyl peroxy radical, MTMP) can react with various radical species including nitric oxide (NO), the hydroperoxyl radical (HO_2), or other RO_2 species to predominately form SO_2 (**R3 in Figure I.1**)(Barnes et al., 2006). The stable intermediates formed from bimolecular reactions are methyl thioformate (MTF) and methylthiomethyl hydroperoxide (MTMHP), driven by reactions with ambient RO_2 and HO_2, respectively. The majority of MTMP produced is thought to eventually form the thioradical ($CH_3S•$), which will efficiently convert to SO_2. $CH_3S•$ is a critical radical species found within the oxidation mechanism of a majority of the reduced sulfur species co-emitted with DMS (methane thiol and dimethyl disulfide).

Previous laboratory DMS oxidation studies were conducted under high DMS and oxidant concentrations to facilitate faster rates and detectable signal for kinetic analysis.(T. Chen & Jang, 2012a; Patroescu et al., 1998; Turnipseed et al., 1996; Wellington et al., 1993) The high concentrations of NO_x (NO_x = NO + NO_2) and HO_x (HO_x = OH + HO_2) used in these early laboratory studies emulate mixing ratios found in urban environments, while the majority of DMS is emitted over the pristine remote ocean far removed from polluted areas.(Atkinson et al., 1984; Berndt & Richters, 2012; Librando et al., 2004) The remote ocean is characterized as an environment with very low concentrations of NO_x, HO_x, and RO_2 (<10 ppt), resulting in long RO_2

lifetimes for species such as MTMP.(Brune et al., 2019; Creasey et al., 2003; Vaughan et al., 2012) In addition, the elevated initial DMS concentration in previous laboratory studies facilitates substantial production of DMS derived RO_2 (predominantly MTMP), which can facilitate RO_2 recombination reactions (Barnes et al., 1994a). Without competitive bimolecular reactions, slower unimolecular recombination and autoxidation mechanisms become more significant, which is expected to be the case over the remote ocean.

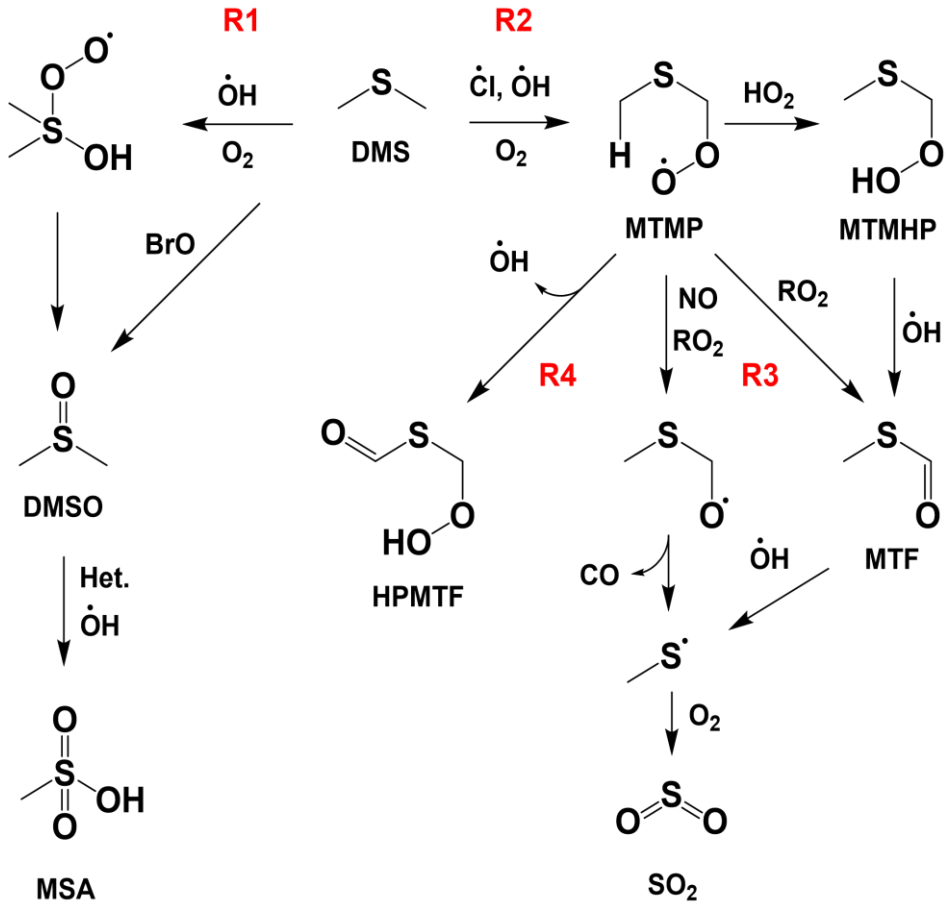

Figure I.1: Simplified DMS oxidation scheme

Isomerization reactions refer to the intramolecular recombination of a molecule, typically through a 1,5 or 1,6 cyclization. In recent years, isomerization reactions have been identified and

quantified within hydrocarbons (Curran et al., 1998; Jalan et al., 2013; Peeters et al., 2009), amines (Møller et al., 2020) and sulfides (Berndt et al., 2020; Veres et al., 2020). In all classes of compounds, RO_2 isomerization dominates either through increased temperatures, sustained in a combustion engine, or due to an extended lifetime, driven by the low concentration of bimolecular reactants. The mechanism of these isomerization reactions is driven by an initial hydrogen shift mechanism, where the oxygen radical within the RO_2 species abstracts an internal hydrogen forming a new internal radical. The newly formed radical species can either decompose into lower energy products or react with ambient oxygen to regenerate an RO_2 species. The process of this internal isomerization can lead to a higher oxygen-to-carbon ratio (O/C), a lower volatility, increased functionalization (carbonyl, hydroperoxyl and hydroxyl), and a greater propensity condense onto existing aerosols (Crounse et al., 2013). Recently, a novel species within the DMS oxidation product containing an aldehyde (keto-), hydroperoxyl (-OOH) and sulfide group, known as hydroperoxymethyl thioformate (HPMTF) has been discovered. HPMTF is only formed from the DMS hydrogen abstraction RO_2 followed by a OH regenerating two-step hydrogen shift (H-shift) mechanism, initially proposed by Wu et al (**R4 in Figure I.1 and Figure I.2**)(Wu et al., 2015).

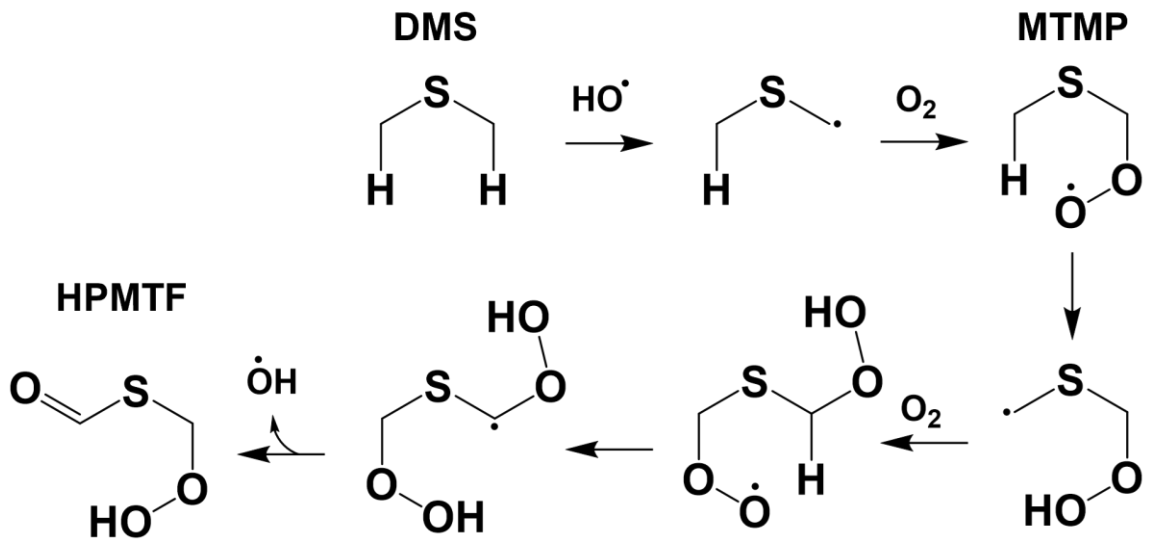

Figure I.2: Formation of hydroperoxymethyl thioformate (HPMTF) initialized by the OH oxidation of DMS. HPMTF forms via a 2-step hydrogen shift mechanism of the primary peroxy radical of the hydrogen abstraction channel, methylthiomethyl peroxy radical (MTMP).

While it is now clear that HPMTF is a key intermediate in the OH-oxidation of DMS, it is not yet known what fraction of HPMTF is converted to SO_2 and sulfate aerosol (Jernigan et al., 2022; Khan et al., 2021; G. A. Novak et al., 2021; Veres et al., 2020; Vermeuel et al., 2020). In chapters 2 through 5 of the thesis, we examine fate of HPMTF within the marine environment including the formation, OH-oxidation, uptake to marine aerosols and connection to the formation of sulfate and OCS.

I.3 Multiphase and heterogeneous chemistry within the marine environment

The role of heterogeneous and multiphase reactions play an important role in the atmosphere as they can catalyze reactions that are energetically or kinetically unfavorable in the gas-phase. Of particular importance is the ability for trace gases to be irreversibly lost through multiphase and heterogeneous pathways, with reactions on marine aerosol particles and low-level

cloud droplets being two of the dominant mediums. Sea spray aerosol (SSA) is a major component of marine aerosols and is one of the most abundant forms of atmospheric aerosol, where SSA number density and organic carbon mass fraction play controlling roles in cloud condensation nuclei (CCN) and ice nuclei (IN) concentrations.(Farmer et al., 2015; Wang et al., 2017) Most SSA particles arise from bursting bubbles produced by the breaking of whitecaps (Wang et al., 2017). Two mechanisms dominate the number and size distribution of SSA produced: (1) a film drop resulting from the bubble film popping, and (2) a jet drop resulting from the fragmentation of a water jet formed during the collapse of the burst bubble.(Matthias-Maser et al., 1999; Wang et al., 2017) Film droplets transport hydrophobic (i.e. aliphatic) species from the sea surface and jet drops transport more hydrophilic species from the bulk ocean. The majority of SSA is composed of sea salt ions (e.g. Na^+, Cl^-, and SO_4^{2-})(O'Dowd & de Leeuw, 2007; Xiao et al., 2018) and organic molecules.(Aller et al., 2005; Michaud et al., 2018) The second class of aerosol particles that can exist in the marine atmosphere is mineral dust particles originating from arid regions.(Prospero, 1999) Mineral dust is composed primarily of metal oxides can act as effective surfaces for the loss of key trace gases (e.g. N_2O_5, SO_2, HO_2, and O_3) (Usher et al., 2003).

Beyond marine aerosol, cloud droplets play an important role in the regulation of trace gases in the marine boundary layer. The lifetime of a soluble and/or reactive molecule (e.g. HNO_3, HPMTF, N_2O_5) is driven by the rate of mixing into the cloud layer. As an example, for typical marine stratocumulus cloud properties (number concentration of 75 cm^{-3} and average diameter of 15 μm), and mixing timescales (mean in-cloud residence time of 40 min) cloud loss can dominate the removal of soluble gases. The loss of trace gases to cloud processing can be with particular importance over the Southern Ocean with increased biological activity and constant cloud cover (Shon et al., 2001; Vallina et al., 2006).

One metric used by atmospheric chemists to determine the propensity of a molecule to be lost to atmospheric surface area is the unitless reactive uptake coefficient (γ)(Ravishankara, 1997). The uptake coefficient is the fraction of collisions of gas molecules with the surface which result in an irreversible reaction. The uptake coefficient of a molecule can be dependent on the composition, phase and acidity of the particle. To experimentally determine γ an observed first-order rate coefficient for reactant gas loss to particles can be derived as a function of the particle surface area and dependent on the reactive uptake of the gas to a surface (**EI.1**):

$$\mathrm{k}_{het}(\mathrm{S}_a) = \frac{\omega \cdot \gamma}{4} \times S_a \qquad \text{(EI.1)}$$

where S_a is the total surface area concentration per unit volume (units of cm^{-1}), ω is the mean molecular speed of the trace gas (units of cm s^{-1}) and γ is the measured uptake coefficient (unitless) and a linear regression of k_{het} against aerosol surface area yields a slope of ($\frac{\omega \cdot \gamma}{4}$).

Once a gas molecule collides with a cloud droplet or aerosol particle it can undergo a variety of chemical transformations (e.g. oxidation, hydrolysis, photolysis) on or within the particle. DMS and the intermediates associated with the OH-addition channel (MSA, MSIA, DMSO) can be driven to the aqueous phase through scavenging. Once sequestered, these species can be further oxidized by dissolved OH and ozone leading to the formation of sulfate. The highly soluble nature of the condensed and oxidized products maintains their consistency within the droplet and the subsequent increase in the hygroscopicity of the particle. The interplay of new particle formation and growth onto existing particles can have major effects on cloud microphysics and climate and as such recent publications have highlighted the importance of multiphase chemistry on the sulfur budget (Fung et al., 2021; Hoffmann et al., 2016b, 2021; G. A. Novak et al., 2021; Vermeuel et al., 2020). Within the complete DMS oxidation mechanism, the majority of

DMS-derived sulfur is thought to end up as methane sulfonic acid (MSA) or as sulfate (Barnes et al., 2006; Q. Chen et al., 2018a; Fung et al., 2021; Hoffmann et al., 2021). Understanding the origin of the MSA and the MSA to sulfate ratio has been used as an indicator for pre-industrial temperature and sulfur emissions, relying on the assumption that observed MSA concentration is derived primarily from DMS oxidation and dictated by the temperature dependent initial OH reaction (Gondwe et al., 2004; Hansson & Saltzman, 1993; Legrand & Mayewski, 1997). SO_2 is a relatively insoluble species with an unitless henry's law coefficient of 1.23 at 298K. The current understanding of the SO_2 multiphase processes includes the condensation of SO_2 onto atmospheric surfaces, the dissolution and hydration of SO_2 into S(IV) (= $SO_2{\cdot}H_2O + HSO_3^- + SO_3^{2-}$) (Beilke & Gravenhorst, 1978), and the oxidation of S(IV) by dissolved or generated oxidants (e.g. OH, NO_2, O_3, and ROOH) (Dovrou et al., 2019; Huang et al., 2015; Martin et al., 1981; Yao et al., 2019) and minerals (e.g. TiO_2, Mn (II)) to sulfate (Y. Chen et al., 2021; Möller, 1980). In chapter 4 and 5 of the thesis, we examine the reactive uptake to HPMTF to marine aerosols, as well as the potential mechanisms and yields of sulfate and OCS from condensed HPMTF.

I.4 Impact of Sulfur on the Climate

In the atmosphere, DMS is primarily oxidized to either sulfur dioxide (SO_2), sulfate (SO_4^{-2}), and/or a stable oxidized intermediate (e.g., methane sulfonic acid, MSA). As DMS oxidizes, the resulting low volatility sulfur species is more available to accumulate into new sulfate aerosol particles or be incorporated into existing aerosols (Karl et al., 2007a). Aerosols particles play an important role in the global climate and energy budget through an overall net cooling via direct and indirect radiative effects (Shukla et al., 2019). The radiative budget or forcing of the planet refers to the amount of solar radiation that gets trapped or reflected by the earth. The net cooling effect provided by aerosol occurs through the direct scattering of incoming solar radiation off a

particle itself, or through the indirect scattering of light off a cloud droplet formed on an aerosol particle. A particle that acts as a nuclei for cloud condensation is referred to as a cloud condensation nuclei (CCN). The composition and size of the atmospheric particle indicates the ability for the nuclei to act as a CCN. The products of DMS oxidation, in particular sulfate through OCS and SO_2 oxidation, can act as strong CCN and promote the formation of cloud droplets. The interplay of DMS emissions and oxidation, cloud formation, and solar surface exposure has been the basis of the negative climate feedback loop, known as the CLAW hypothesis (Charlson et al., 1987). The localization of DMS derived sulfate that forms reflective white clouds over the absorptive dark blue of the ocean provides a strong contrast in global albedo and radiative forcing. In the stratosphere, the oxidation of carbonyl sulfide (OCS) is the primary, continuous source of stratospheric sulfate aerosol particles, which scatter shortwave radiation and catalyze heterogeneous reactions central to stratospheric ozone chemistry (Crutzen, 1976; Solomon et al., 1986). In the troposphere, OCS is readily consumed by the terrestrial biosphere, and has proven to be an effective tool for estimating gross primary production (GPP) (Asaf et al., 2013). Despite the importance of OCS to stratospheric chemistry and its utility for estimating GPP, the magnitude and spatial distribution of OCS sources remain poorly constrained (Kremser et al., 2016; Ma et al., 2021).

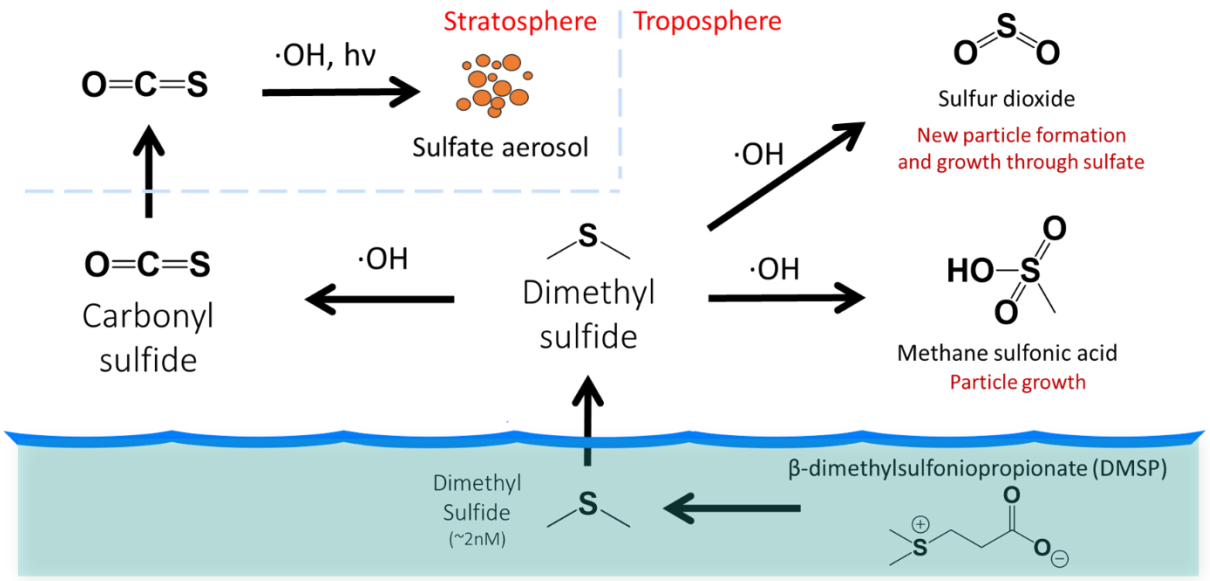

Figure I.3: Schematic of DMS origin and atmospheric oxidation with corresponding impact on climate relevant species

Comprehensive studies on aerosols and climate-related molecules are essential constraints for predictions on the planet's temperature change, solar radiation budget and annual precipitation. Computation time can become limiting in global climate models as number of terms explicitly treated increases, requiring simplifying parameterizations. The oxidation of DMS to SO_2 is consistently maintained in global climate models, yet the intricacy of the oxidation pathway is typically replaced with a few reactions or a single number that defines relative amount of emitted DMS that contributes to new particles (Capaldo & Pandis, 1997; Q. Chen et al., 2018b; Faloona, 2009; Karl et al., 2007b). The relative amount of DMS emitted is well constrained using remote sensing algorithms or field measurements of sea surface DMS concentrations to approximate spatial distributions of DMS flux. The aerosol and phytoplankton measurements acquired by NASA remote sensing satellites, like Terra and Aqua, and NASA's North Atlantic Aerosols and Marine Ecosystems Study (NAAMES) provide crucial data and observations for climate

predictions, but inferred relationships between DMS flux and CCN activity will not hold without a complete and accurate DMS oxidation mechanism.(Behrenfeld et al., 2019; Galí et al., 2018) The uncertainty in DMS oxidation is highlighted by the DMS to SO_2 and SO_4^{2-} conversion ratio varying from 31% to near 100% over the past 20 years of climate model publications (Q. Chen et al., 2018b; Faloona, 2009; Langner & Rodhe, 1991b). The uncertainty in the biogenic emissions and CCN generation has a major impact on assessing the relative weight of anthropogenic and natural CCN radiative forcing (Carslaw et al., 2013). Without measurements and complete understanding of processes over the pristine environment (e.g. open ocean) the pre-industrial global radiative forcing background will not be fully constrained. The lack of convergence on a major biogenic climate forcer points towards more comprehensive and explorative research quantifying the possible gas and multiphase fates of DMS and its oxidation products. For this reason, more comprehensive and explorative research should be done on quantifying all the possible fates of DMS and its downstream oxidized species. In chapter 2 and 3, we examine the product yields and chemical mechanisms that dictate the production of SO_2 and OCS from the oxidation of sulfur under conditions indicative of the marine environment. The rate constants and product yields taken from the chamber experimentations are translated using a global climate model to determine the atmospheric burden of OCS under a new chemical mechanism.

I.5 Environmental chambers for atmospheric analysis

Environmental chambers and flow reactors are an important tool for atmospheric chemists in isolating and investigating components of the atmosphere. Earth's atmosphere is a complex mixture of various organic and inorganic compounds that are constantly being produced, lost and transformed. Field measurements are conducted to study the interplay of these species in their natural environment. While field work is critical to understanding the atmosphere, the countless

meteorological and chemical process happening during sampling can complicate the analysis. To isolate individual aspects of the atmosphere, atmospheric chemists can rely on environmental chambers to focus on a narrow window of the global processing. An important application of chambers and flow reactors is the quantification of kinetic rate constants(Borduas et al., 2013; Crounse et al., 2011; Yin et al., 1990b), product and secondary organic aerosol yields (T. Chen & Jang, 2012b; D'Ambro et al., 2019), reactive uptake coefficients (Kroll et al., 2005; Liggio et al., 2005) and surface reactions (Y. Chen et al., 2021; Kuang & Shang, 2020; Zhang et al., 2020). The isolation and quantification of various atmospheric reactions can be used and applied to various box, regional, and global models.

In chapter 1, we present a detailed description of the design, operation and modeling of a chemical chamber for the observation of chemical oxidation under oxidative conditions indicative of the remote marine environment. The methodology presented in chapter 1 was used to complete the work performed in chapters 2-5 and is capable of being adapted to studying the oxidation of other trace gases.

I.6 Chemical Ionization Mass Spectrometry

Chemical Ionization Mass Spectrometery (CIMS) is a technique uses a generated reagent ion, to selectively ionize a class of analytes within a complex mixture (Crounse et al., 2006; Huey, 2007; Huey et al., 1995). The reagent ion is generated by passing a neutral molecule, such as methyl iodide, benzene or water, through an ionization apparatus, such as an α-particle emitter or an arc discharge. The reagent ion subsequently directed into an Ion-Molecule Reaction chamber (IMR) where it is mixed with a sample flow. The reagent ion ($[X]^+$), upon collision with the analyte ([M]), will continue down one of several potential ion-molecule reactions potentially forming a detectable ion, seen as a cluster ($[M \cdot H]^+$) or charged species ($[M]^+$). The likelihood an analyte will

ionize is dependent on its chemical properties and those of the reagent ion, as seen in Table 1. For instance, iodine CIMS (I-CIMS) uses iodine (I^-) as the reagent ion and it selectively ionizes nitrates, hydroperoxides and acids via ion-molecule cluster (Huey, 2007; Huey et al., 1995). To predict the selectivity of the reagent ion, computational chemistry is used to simulate an analyte's CIMS sensitivity. A study by Iyer et al., has shown a linear trend between the measured sensitivity (counts/parts per trillion) of a given acid molecule and its computed binding energy with iodine (2016). Once the generated ions are continuously directed through the CIMS instrument through a system of ion optics and ion guiding quadrupoles to a mass analyzer. The voltage gradient established throughout the ion guide can selective control decluster and mass transmission of the generate ions. By scanning the electric field at the entrance to one of the focusing quadrupoles thus changing the collisional energy imparted on a cluster in the CIMS, one can selectively determine a relative binding energy of the cluster (Brophy & Farmer, 2016; Lopez-Hilfiker et al., 2016). This technique can be used to determine the instrument sensitivity, chemical composition and potential ion molecule reactions.

Reagent Ion	Compound Class Selectivity	Detectable Ion	Thesis Chapters
Iodine (I^-, $[I\cdot(H_2O)_n]^-$)	Hydroperoxides, Nitrates, Organic Acids	$[I\cdot M]^-$, $[I\cdot M\cdot(H_2O)_n]^-$	2,3,4,5
Oxygen (O_2^-, $[O_2\cdot(H_2O)_n]^-$)	Sulfur dioxide, Ozone, Organic Acids	$[M]^-$, $[O_2\cdot M]^-$, $[M\text{-}H]^-$	3,5
Proton Transfer Reaction (H_3O^+)	Reduced VOC and VOSC, Partially oxidized VOC	$[H\cdot M]^+$, $[M]^+$, $[M\text{-}H_2O]^+$	2,3,4

Table I.1: Chemical ionization modes used throughout thesis. Selectivity and main detection mode within CIMS is presented

Two chemical ionization mass spectrometers were used throughout this thesis: a Compact Time of Flight Chemical Ionization Mass spectrometer (C-ToF) (Bertram et al., 2011) and Aerodyne/TOFWERK Vocus - Proton Transfer Reaction Time of Flight Mass Spectrometer

(Vocus-PTR-MS) (Krechmer et al., 2018). The C-ToF was used with two different reagent ions: iodide and oxygen anions. Iodine CIMS has been used extensively for the analysis of organic acids and hydroperoxide species in the atmosphere, while oxygen anion CIMS (Oxy-CIMS) is sensitive to measurements of sulfur dioxide (SO_2) and ozone(G. Novak et al., 2019; Veres et al., 2020). The Vocus-PTR-MS will be used to quantify the mixing ratios of various reduced and oxidized VOCs. The Vocus-PTR-MS uses a focusing ion-molecule region (FIMR) composed of four quadrupole rods under a fixed RF voltage. The FMIR works as an ion guide to enhance the ion transmission and detection efficiencies. The high resolving power allows for high resolution (HR) peak fitting of the mass spectrum. The higher resolution and HR peak fitting of the Vocus allows for compositional information to be acquired from the mass spectrum.

Thesis Overview

Sulfur plays a critical role in global climate regulation through its tie to atmospheric particle and their cooling via direct and indirect radiative effects. Dimethyl sulfide is the primary source of reduced sulfur to the marine atmosphere with a complicated environment dependent oxidation pathway. The tie between DMS oxidation and climate has been studied for the past 30 years, but consistent uncertainty in climate models associated with DMS oxidation lends to the need to reexamine DMS oxidation.

This thesis attempts to describe the fate of dimethyl sulfide in the remote marine environment with a focus on the chemical mechanisms driving the connection between sulfur and climate. Recent field work has found that HPMTF is a key intermediate in the OH-oxidation of DMS, but it is not yet known what the complete atmospheric fate of HPMTF. More than 30% of oxidized sulfur is thought to oxidize through HPMTF, upending the textbook definition of DMS oxidation leading to primarily SO_2 and MSA. A primary goal of this thesis is to determine how

HPMTF and its fate in the atmosphere plays into our current understanding of the role of DMS on climate. This work includes the description and operation of an environmental chamber used to examine sulfur oxidation under oxidative conditions representative of the marine environment (Chapter 1), the application of the chamber to determine the rates and product yields of SO_2 and OCS from OH-oxidation of sulfur emitted from the ocean (Chapter 2,3), a calculated reactive uptake of HPMTF to marine aerosols and its effect on global OCS production (Chapter 2,4), and the connection, mechanisms, and rates driving the connection between condensed HPMTF, sulfate, and OCS (Chapter 4,5). A list of abbreviations and acronyms can be found in **Table I.2** to help guide one through the thesis.

Table I.2: List of common abbreviations and acronyms used throughout thesis

Abbreviation	Definition
·OH	Hydroxyl radicals
Alk-OOH	Primary ROOH from Alkene oxidation
CCN	Cloud condensation nuclei
CIMS	Chemical Ionization Mass Spectrometers
CS_2	Carbon disulfide
C-ToF	Compact Time of Flight CIMS
DMDS	Dimethyl disulfide
DMS	Dimethyl sulfide
DMSO	Dimethyl sulfoxide
DORC	Dimethyl sulfide Oxidation Reaction Chamber
E_{DMS}	DMS ocean emissions
F0AM	Framework for 0-D Atmospheric Modeling
γ	reactive uptake coefficient
GPP	Gross primary production
H_2CS	Thioformaldehyde
H_2SO_4	Sulfuric acid
HPMDTF	Hydroperoxymethyl dithioformate, HOOCH2SSCH=O
HPMTF	Hydroperoxymethyl thioformate, HOOCH2SCH=O
IC	Ion chromatography
k_{Het}	Rate constant for pseudo first order heterogeneous loss

$k_{HPMTF+OH}$	Rate constant for HPMTF+OH
k_{isom}	Rate constant for MTMP isomerization
k_{MTF+OH}	Rate constant for MTF+OH
L_{DMS}	The loss rate of DMS to reaction with OH
LGR	Los Gatos Research Enhanced Performance OCS analyzer
LIF	Laser-induced fluorescence
LOD	Limits of detection
MCM	Master Chemical Mechanism
MeSH	Methane thiol
mil	0.001 of an inch
MSIA	Methanesulfinic acid
MTF	Methyl thioformate
MTMP	Methylthiomethylperoxy radical,CH3SCH2O2·
ncps	Normalized counts per second
NO_3	Nitrate radical
NO_x	NOx = NO + NO_2
OCS	Carbonyl sulfide
PFA	Perfluoroalkoxy alkane
P_{OCS}	OCS production
ϕ_{OCS}	OCS branching fraction from HPMTF+ ·OH
ppbv	Parts per billion per volume
pptv	Parts per trillion per volume
RH	Relative humidity
RO_2·	Peroxy radical species
ROOH	Hydroperoxide species
S_a	Surface Area concentration
SEMS	Scanning Electrical Mobility Sizer
SO_2	Sulfur dioxide
TARP	Total Atinic Radiation Protection
TFA	Thioformic anhydride, CHOSCHO
TgS yr^{-1}	Teragrams sulfur per year
TME	Tetramethyl ethene
TPA	Thioperformic acid, HC(=S)OOH
Vocus	Aerodyne/TOFWERK Vocus - Proton Transfer Reaction Time of Flight Mass Spectrometer
Y_{OCS}	Yield of OCS from total DMS oxidation
Y_{OH}	Yield of ·OH from TME ozonolysis

References

Aller, J. Y., Kuznetsova, M. R., Jahns, C. J., & Kemp, P. F. (2005). The sea surface microlayer as a source of viral and bacterial enrichment in marine aerosols. *Journal of Aerosol Science*, *36*(5–6), 801–812. https://doi.org/10.1016/j.jaerosci.2004.10.012

Asaf, D., Rotenberg, E., Tatarinov, F., Dicken, U., Montzka, S. A., & Yakir, D. (2013). Ecosystem photosynthesis inferred from measurements of carbonyl sulphide flux. *Nature Geoscience*, *6*(3), 186–190. https://doi.org/10.1038/ngeo1730

Atkinson, R., Pitts, J. N., & Aschmann, S. M. (1984). Tropospheric reactions of dimethyl sulfide with nitrogen oxide (NO3) and hydroxyl radicals. *The Journal of Physical Chemistry*, *88*(8), 1584–1587. https://doi.org/10.1021/j150652a029

Barnes, I., Becker, K. H., & Patroescu, I. (1994a). The tropospheric oxidation of dimethys ulfide: A new source of carbonyl sulfide. *Geophysical Research Letters*, *21*(22), 2389–2392.

Barnes, I., Becker, K. H., & Patroescu, I. (1994b). The tropospheric oxidation of dimethyl sulfide: A new source of carbonyl sulfide. *Geophysical Research Letters*, *21*(22), 2389–2392. https://doi.org/https://doi.org/10.1029/94GL02499

Barnes, I., Hjorth, J., & Mihalapoulos, N. (2006). Dimethyl sulfide and dimethyl sulfoxide and their oxidation in the atmosphere. *Chemical Reviews*, *106*(3), 940–975. https://doi.org/10.1021/cr020529+

Barone, S. B., Turnipseed, A. A., & Ravishankara, A. R. (1996). Reaction of OH with dimethyl sulfide (DMS). 1. Equilibrium constant for OH + DMS reaction and the kinetics of the OH·DMS + O2reaction. *Journal of Physical Chemistry*, *100*(35), 14694–14702. https://doi.org/10.1021/jp960866k

Bates, T. S., Lamb, B. K., Guenther, A., Dignon, J., & Stoiber, R. E. (1992). Sulfur emissions to the atmosphere from natural sourees. *Journal of Atmospheric Chemistry*, *14*(1), 315–337. https://doi.org/10.1007/BF00115242

Behrenfeld, M. J., Moore, R. H., Hostetler, C. A., Graff, J., Gaube, P., Russell, L. M., Chen, G., Doney, S. C., Giovannoni, S., Liu, H., Proctor, C., Bolaños, L. M., Baetge, N., Davie-Martin, C., Westberry, T. K., Bates, T. S., Bell, T. G., Bidle, K. D., Boss, E. S., … Ziemba, L. (2019). The North Atlantic Aerosol and Marine Ecosystem Study (NAAMES): Science motive and mission overview. *Frontiers in Marine Science*, *6*(MAR), 1–25. https://doi.org/10.3389/fmars.2019.00122

Beilke, S., & Gravenhorst, G. (1978). Heterogeneous SO2-oxidation in the droplet phase. In *Sulfur in the Atmosphere* (pp. 231–239). Elsevier.

Berndt, T., Chen, J., Møller, K. H., Hyttinen, N., Prisle, N. L., Tilgner, A., Hoffmann, E. H., Herrmann, H., & Kjaergaard, H. G. (2020). SO2 formation and peroxy radical isomerization in the atmospheric reaction of OH radicals with dimethyl disulfide. *Chemical Communications*, *56*(88), 13634–13637. https://doi.org/10.1039/D0CC05783E

Berndt, T., & Richters, S. (2012). Products of the reaction of OH radicals with dimethyl sulphide in the absence of NO x: Experiment and simulation. *Atmospheric Environment*, *47*(x), 316–322. https://doi.org/10.1016/j.atmosenv.2011.10.060

Bertram, T. H., Kimmel, J. R., Crisp, T. A., Ryder, O. S., Yatavelli, R. L. N., Thornton, J. A., Cubison, M. J., Gonin, M., & Worsnop, D. R. (2011). A field-deployable, chemical ionization time-of-flight mass spectrometer. *Atmospheric Measurement Techniques*, *4*(7), 1471–1479. https://doi.org/10.5194/amt-4-1471-2011

Borduas, N., Abbatt, J. P. D., & Murphy, J. G. (2013). Gas phase oxidation of monoethanolamine (MEA) with oh radical and ozone: Kinetics, products, and particles. *Environmental Science and Technology*, *47*(12), 6377–6383. https://doi.org/10.1021/es401282j

Brophy, P., & Farmer, D. K. (2016). Clustering, methodology, and mechanistic insights into acetate chemical ionization using high-resolution time-of-flight mass spectrometry. *Atmospheric Measurement Techniques*, *9*(8), 3969–3986. https://doi.org/10.5194/amt-9-3969-2016

Brühl, C., Lelieveld, J., Crutzen, P. J., & Tost, H. (2012). The role of carbonyl sulphide as a source of stratospheric sulphate aerosol and its impact on climate. *Atmospheric Chemistry and Physics*, *12*(3), 1239–1253. https://doi.org/10.5194/acp-12-1239-2012

Brune, W. H., Miller, D. O., Thames, A. B., Allen, H. M., Apel, E. C., Blake, D. R., & Bui, T. P. (2019). *Exploring Oxidation in the Remote Free Troposphere : Insights From Atmospheric Tomography (ATom) Journal of Geophysical Research : Atmospheres*. 1–17. https://doi.org/10.1029/2019JD031685

Capaldo, K. P., & Pandis, N. (1997). Evaluation and sensitivity analysis of available mechanisms i + Ai (C j , fcloud). *October*, *102*.

Carslaw, K. S., Lee, L. A., Reddington, C. L., Pringle, K. J., Rap, A., Forster, P. M., Mann, G. W., Spracklen, D. V., Woodhouse, M. T., Regayre, L. A., & Pierce, J. R. (2013). Large contribution of natural aerosols to uncertainty in indirect forcing. *Nature*, *503*(7474), 67–71. https://doi.org/10.1038/nature12674

Charlson, R. J., Lovelock, J. E., Andreae, M. O., & Warren, S. G. (1987). Oceanic phytoplankton, atmospheric sulphur, cloud albedo and climate. *Nature*, *326*(6114), 655–661.

Chen, Q., Sherwen, T., Evans, M., & Alexander, B. (2018a). DMS oxidation and sulfur aerosol formation in the marine troposphere: A focus on reactive halogen and multiphase chemistry. *Atmospheric Chemistry and Physics*, *18*(18), 13617–13637. https://doi.org/10.5194/acp-18-13617-2018

Chen, Q., Sherwen, T., Evans, M., & Alexander, B. (2018b). DMS oxidation and sulfur aerosol formation in the marine troposphere: A focus on reactive halogen and multiphase chemistry. *Atmospheric Chemistry and Physics*, *18*(18), 13617–13637. https://doi.org/10.5194/acp-18-13617-2018

Chen, T., & Jang, M. (2012a). Chamber simulation of photooxidation of dimethyl sulfide and isoprene in the presence of NO x. *Atmospheric Chemistry and Physics*, *12*(21), 10257–10269. https://doi.org/10.5194/acp-12-10257-2012

Chen, T., & Jang, M. (2012b). Chamber simulation of photooxidation of dimethyl sulfide and isoprene in the presence of NO x. *Atmospheric Chemistry and Physics*, *12*(21), 10257–10269.

Chen, T.-M., Kuschner, W. G., Gokhale, J., & Shofer, S. (2007). Outdoor air pollution: nitrogen dioxide, sulfur dioxide, and carbon monoxide health effects. *The American Journal of the Medical Sciences*, *333*(4), 249–256.

Chen, Y., Tong, S., Li, W., Liu, Y., Tan, F., Ge, M., Xie, X., & Sun, J. (2021). Photocatalytic Oxidation of SO2 by TiO2: Aerosol Formation and the Key Role of Gaseous Reactive Oxygen Species. *Environmental Science & Technology*, *55*(14), 9784–9793. https://doi.org/10.1021/acs.est.1c01608

Chin, M., & Davis, D. D. (1993a). Global sources and sinks of OCS and CS2 and their distributions. *Global Biogeochemical Cycles*, *7*(2), 321–337. https://doi.org/10.1029/93GB00568

Chin, M., & Davis, D. D. (1993b). Global sources and sinks of OCS and CS2 and their distributions. *Global Biogeochemical Cycles*, *7*(2), 321–337. https://doi.org/10.1029/93GB00568

Creasey, D. J., Evans, G. E., Heard, D. E., & Lee, J. D. (2003). Measurements of OH and HO2 concentrations in the Southern Ocean marine boundary layer. *Journal of Geophysical Research D: Atmospheres*, *108*(15), 1–12. https://doi.org/10.1029/2002jd003206

Crounse, J. D., McKinney, K. A., Kwan, A. J., & Wennberg, P. O. (2006). Measurement of gas-phase hydroperoxides by chemical ionization mass spectrometry. *Analytical Chemistry*, *78*(19), 6726–6732. https://doi.org/10.1021/ac0604235

Crounse, J. D., Nielsen, L. B., Jørgensen, S., Kjaergaard, H. G., & Wennberg, P. O. (2013). Autoxidation of organic compounds in the atmosphere. *Journal of Physical Chemistry Letters*, *4*(20), 3513–3520. https://doi.org/10.1021/jz4019207

Crounse, J. D., Paulot, F., Kjaergaard, H. G., & Wennberg, P. O. (2011). Peroxy radical isomerization in the oxidation of isoprene. *Physical Chemistry Chemical Physics*, *13*(30), 13607–13613. https://doi.org/10.1039/c1cp21330j

Crutzen, P. J. (1976). The possible importance of CSO for the sulfate layer of the stratosphere. *Geophysical Research Letters*, *3*(2), 73–76. https://doi.org/https://doi.org/10.1029/GL003i002p00073

Curran, H. J., Pitz, W. J., Westbrook, C. K., Dagaut, P., Boettner, J. C., & Cathonnet, M. (1998). A wide range modeling study of dimethyl ether oxidation. *International Journal of Chemical Kinetics*, *30*(3), 229–241. https://doi.org/10.1002/(SICI)1097-4601(1998)30:3<229::AID-KIN9>3.0.CO;2-U

D'Ambro, E. L., Schobesberger, S., Gaston, C. J., Lopez-Hilfiker, F. D., Lee, B. H., Liu, J., Zelenyuk, A., Bell, D., Cappa, C. D., & Helgestad, T. (2019). Chamber-based insights into the factors controlling epoxydiol (IEPOX) secondary organic aerosol (SOA) yield, composition, and volatility. *Atmospheric Chemistry and Physics*, *19*(17), 11253–11265.

Devai, I., & DeLaune, R. D. (1995). Formation of volatile sulfur compounds in salt marsh sediment as influenced by soil redox condition. *Organic Geochemistry*, *23*(4), 283–287. https://doi.org/10.1016/0146-6380(95)00024-9

Dovrou, E., Rivera-Rios, J. C., Bates, K. H., & Keutsch, F. N. (2019). Sulfate Formation via Cloud Processing from Isoprene Hydroxyl Hydroperoxides (ISOPOOH). *Environmental Science & Technology*, *53*(21), 12476–12484. https://doi.org/10.1021/acs.est.9b04645

Faloona, I. (2009). Sulfur processing in the marine atmospheric boundary layer: A review and critical assessment of modeling uncertainties. *Atmospheric Environment*, *43*(18), 2841–2854. https://doi.org/10.1016/j.atmosenv.2009.02.043

Farmer, D. K., Cappa, C. D., & Kreidenweis, S. M. (2015). Atmospheric Processes and Their Controlling Influence on Cloud Condensation Nuclei Activity. *Chemical Reviews*, *115*(10), 4199–4217. https://doi.org/10.1021/cr5006292

Fung, K. M., Heald, C., Kroll, J., Wang, S., Jo, D., Gettelman, A., Lu, Z., Liu, X., Zaveri, R., Apel, E., Blake, D., Jimenez, J.-L., Campuzano-Jost, P., Veres, P., Bates, T., Shilling, J., & Zawadowicz, M. (2021). Exploring DMS oxidation and implications for global aerosol radiative forcing. *Atmospheric Chemistry and Physics*, *2021*, 1–58. https://doi.org/10.5194/acp-2021-782

Galí, M., Levasseur, M., Devred, E., Simó, R., & Babin, M. (2018). Sea-surface dimethylsulfide (DMS) concentration from satellite data at global and regional scales. *Biogeosciences*, *15*(11), 3497–3519. https://doi.org/10.5194/bg-15-3497-2018

Gondwe, M., Krol, M., Klaassen, W., Gieskes, W., & de Baar, H. (2004). Comparison of modeled versus measured MSA:nss SO4= ratios: A global analysis. *Global Biogeochemical Cycles*, *18*(2). https://doi.org/https://doi.org/10.1029/2003GB002144

Hansson, M. E., & Saltzman, E. S. (1993). The first Greenland ice core record of methanesulfonate and sulfate over a full glacial cycle. *Geophysical Research Letters*, *20*(12), 1163–1166.

Hoffmann, E. H., Heinold, B., Kubin, A., Tegen, I., & Herrmann, H. (2021). The Importance of the Representation of DMS Oxidation in Global Chemistry-Climate Simulations. *Geophysical Research Letters*, *48*(13), e2021GL094068. https://doi.org/https://doi.org/10.1029/2021GL094068

Hoffmann, E. H., Tilgner, A., Schrödner, R., Bräuer, P., Wolke, R., & Herrmann, H. (2016a). An advanced modeling study on the impacts and atmospheric implications of multiphase dimethyl sulfide chemistry. *Proceedings of the National Academy of Sciences of the United States of America*, *113*(42), 11776–11781. https://doi.org/10.1073/pnas.1606320113

Hoffmann, E. H., Tilgner, A., Schrödner, R., Bräuer, P., Wolke, R., & Herrmann, H. (2016b). An advanced modeling study on the impacts and atmospheric implications of multiphase dimethyl sulfide chemistry. *Proceedings of the National Academy of Sciences of the United States of America*, *113*(42), 11776–11781. https://doi.org/10.1073/pnas.1606320113

Huang, L., Zhao, Y., Li, H., & Chen, Z. (2015). Kinetics of Heterogeneous Reaction of Sulfur Dioxide on Authentic Mineral Dust: Effects of Relative Humidity and Hydrogen Peroxide. *Environmental Science & Technology*, *49*(18), 10797–10805. https://doi.org/10.1021/acs.est.5b03930

Huey, L. G. (2007). Measurement of trace atmospheric species by chemical ionization mass spectrometry: Speciation of reactive nitrogen and future directions. *Mass Spectrometry Reviews*, *26*(2), 166–184.

Huey, L. G., Hanson, D. R., & Howard, C. J. (1995). Reactions of SF6-and I-with atmospheric trace gases. *The Journal of Physical Chemistry*, *99*(14), 5001–5008.

Hynes, A. J., Stoker, R. B., Pounds, A. J., McKay, T., Bradshaw, J. D., Nicovich, J. M., & Wine, P. H. (1995). A mechanistic study of the reaction of OH with dimethyl-d6 sulfide. Direct observation of adduct formation and the kinetics of the adduct reaction with O2. *Journal of Physical Chemistry*, *99*(46), 16967–16975. https://doi.org/10.1021/j100046a024

Iyer, S., Lopez-Hilfiker, F., Lee, B. H., Thornton, J. A., & Kurtén, T. (2016). Modeling the Detection of Organic and Inorganic Compounds Using Iodide-Based Chemical Ionization. *Journal of Physical Chemistry A*, *120*(4), 576–587. https://doi.org/10.1021/acs.jpca.5b09837

Jalan, A., Alecu, I. M., Meana-Pañeda, R., Aguilera-Iparraguirre, J., Yang, K. R., Merchant, S. S., Truhlar, D. G., & Green, W. H. (2013). New pathways for formation of acids and carbonyl products in low-temperature oxidation: The Korcek decomposition of γ- ketohydroperoxides. *Journal of the American Chemical Society*, *135*(30), 11100–11114. https://doi.org/10.1021/ja4034439

Jernigan, C. M., Fite, C. H., Vereecken, L., Berkelhammer, M. B., Rollins, A. W., Rickly, P. S., Novelli, A., Taraborrelli, D., Holmes, C. D., & Bertram, T. H. (2022). Efficient Production of Carbonyl Sulfide in the Low-NO x Oxidation of Dimethyl Sulfide . *Geophysical Research Letters*, *49*(3), e2021GL096838. https://doi.org/10.1029/2021gl096838

Karl, M., Gross, A., Leck, C., & Pirjola, L. (2007a). Intercomparison of dimethylsulfide oxidation mechanisms for the marine boundary layer: Gaseous and particulate sulfur constituents. *Journal of Geophysical Research Atmospheres*, *112*(15), 1–20. https://doi.org/10.1029/2006JD007914

Karl, M., Gross, A., Leck, C., & Pirjola, L. (2007b). Intercomparison of dimethylsulfide oxidation mechanisms for the marine boundary layer: Gaseous and particulate sulfur constituents. *Journal of Geophysical Research Atmospheres*, *112*(15), 1–20. https://doi.org/10.1029/2006JD007914

Kettle, A. J., Rhee, T. S., von Hobe, M., Poulton, A., Aiken, J., & Andreae, M. O. (2001). Assessing the flux of different volatile sulfur gases from the ocean to the atmosphere. *Journal of Geophysical*

Research: Atmospheres, *106*(D11), 12193–12209. https://doi.org/https://doi.org/10.1029/2000JD900630

Khan, M. A. H., Bannan, T. J., Holland, R., Shallcross, D. E., Archibald, A. T., Matthews, E., Back, A., Allan, J., Coe, H., Artaxo, P., & Percival, C. J. (2021). Impacts of Hydroperoxymethyl Thioformate on the Global Marine Sulfur Budget. *ACS Earth and Space Chemistry*, *5*(10), 2577–2586. https://doi.org/10.1021/acsearthspacechem.1c00218

Kiene, R. P. (1996). Production of methanethiol from dimethylsulfoniopropionate in marine surface waters. *Marine Chemistry*, *54*(1–2), 69–83.

Kiene, R. P., & Linn, L. J. (2000). The fate of dissolved dimethylsulfoniopropionate (DMSP) in seawater: tracer studies using 35S-DMSP. *Geochimica et Cosmochimica Acta*, *64*(16), 2797–2810.

Kloster, S., Feichter, J., Maier-Reimer, E., Six, K. D., Stier, P., & Wetzel, P. (2006). DMS cycle in the marine ocean-atmosphere system - A global model study. *Biogeosciences*, *3*(1), 29–51. https://doi.org/10.5194/bg-3-29-2006

Krechmer, J., Lopez-Hilfiker, F., Koss, A., Hutterli, M., Stoermer, C., Deming, B., Kimmel, J., Warneke, C., Holzinger, R., Jayne, J., Worsnop, D., Fuhrer, K., Gonin, M., & de Gouw, J. (2018). Evaluation of a New Reagent-Ion Source and Focusing Ion-Molecule Reactor for Use in Proton-Transfer-Reaction Mass Spectrometry. *Analytical Chemistry*, *90*(20), 12011–12018. https://doi.org/10.1021/acs.analchem.8b02641

Kreidenweis, S. M., & Seinfeld, J. H. (1988). Nucleation of sulfuric acid-water and methanesulfonic acid-water solution particles: Implications for the atmospheric chemistry of organosulfur species. *Atmospheric Environment (1967)*, *22*(2), 283–296. https://doi.org/10.1016/0004-6981(88)90034-0

Kremser, S., Thomason, L. W., von Hobe, M., Hermann, M., Deshler, T., Timmreck, C., Toohey, M., Stenke, A., Schwarz, J. P., Weigel, R., Fueglistaler, S., Prata, F. J., Vernier, J.-P., Schlager, H., Barnes, J. E., Antuña-Marrero, J.-C., Fairlie, D., Palm, M., Mahieu, E., … Meland, B. (2016). Stratospheric aerosol—Observations, processes, and impact on climate. *Reviews of Geophysics*, *54*(2), 278–335. https://doi.org/https://doi.org/10.1002/2015RG000511

Kroll, J. H., Ng, N. L., Murphy, S. M., Varutbangkul, V., Flagan, R. C., & Seinfeld, J. H. (2005). Chamber studies of secondary organic aerosol growth by reactive uptake of simple carbonyl compounds. *Journal of Geophysical Research Atmospheres*, *110*(23), 1–10. https://doi.org/10.1029/2005JD006004

Kuang, Y., & Shang, J. (2020). Changes in light absorption by brown carbon in soot particles due to heterogeneous ozone aging in a smog chamber. *Environmental Pollution*, *266*, 115273. https://doi.org/https://doi.org/10.1016/j.envpol.2020.115273

Lana, A., Bell, T. G., Simó, R., Vallina, S. M., Ballabrera-Poy, J., Kettle, A. J., Dachs, J., Bopp, L., Saltzman, E. S., Stefels, J., Johnson, J. E., & Liss, P. S. (2011). An updated climatology of surface dimethlysulfide concentrations and emission fluxes in the global ocean. *Global Biogeochemical Cycles*, *25*(1), 1–17. https://doi.org/10.1029/2010GB003850

Langner, J., & Rodhe, H. (1991a). A global three-dimensional model of the tropospheric sulfur cycle. *Journal of Atmospheric Chemistry*, *13*(3), 225–263. https://doi.org/10.1007/BF00058134

Langner, J., & Rodhe, H. (1991b). A global three-dimensional model of the tropospheric sulfur cycle. *Journal of Atmospheric Chemistry*, *13*(3), 225–263. https://doi.org/10.1007/BF00058134

Lee, C.-L., & Brimblecombe, P. (2016). Anthropogenic contributions to global carbonyl sulfide, carbon disulfide and organosulfides fluxes. *Earth-Science Reviews*, *160*, 1–18.

Legrand, M., & Mayewski, P. (1997). Glaciochemistry of polar ice cores: A review. *Reviews of Geophysics*, *35*(3), 219–243. https://doi.org/https://doi.org/10.1029/96RG03527

Lennartz, S. T., Gauss, M., von Hobe, M., & Marandino, C. A. (2021). Monthly resolved modelled oceanic emissions of carbonyl sulphide and carbon disulphide for the period 2000–2019. *Earth Syst. Sci. Data*, *13*(5), 2095–2110. https://doi.org/10.5194/essd-13-2095-2021

Librando, V., Tringali, G., Hjorth, J., & Coluccia, S. (2004). OH-initiated oxidation of DMS/DMSO: Reaction products at high NO x levels. *Environmental Pollution*, *127*(3), 403–410. https://doi.org/10.1016/j.envpol.2003.08.003

Liggio, J., Li, S. M., & McLaren, R. (2005). Reactive uptake of glyoxal by particulate matter. *Journal of Geophysical Research D: Atmospheres*, *110*(10), 1–13. https://doi.org/10.1029/2004JD005113

Liu, Q., Kogan, Y. L., Lilly, D. K., Johnson, D. W., Innis, G. E., Durkee, P. A., & Nielsen, K. E. (2000). Modeling of ship effluent transport and its sensitivity to boundary layer structure. *Journal of the Atmospheric Sciences*, *57*(16), 2779–2791.

Lopez-Hilfiker, F. D., Iyer, S., Mohr, C., Lee, B. H., D'Ambro, E. L., Kurtén, T., & Thornton, J. A. (2016). Constraining the sensitivity of iodide adduct chemical ionization mass spectrometry to multifunctional organic molecules using the collision limit and thermodynamic stability of iodide ion adducts. *Atmospheric Measurement Techniques*, *9*(4), 1505–1512.

Ma, J., Kooijmans, L. M. J., Cho, A., Montzka, S. A., Glatthor, N., Worden, J. R., Kuai, L., Atlas, E. L., & Krol, M. C. (2021). Inverse modelling of carbonyl sulfide: Implementation, evaluation and implications for the global budget. *Atmospheric Chemistry and Physics*, *21*(5), 3507–3529. https://doi.org/10.5194/acp-21-3507-2021

Martin, L. R., Damschen, D. E., & Judeikis, H. S. (1981). The reactions of nitrogen oxides with SO2 in aqueous aerosols. *Atmospheric Environment (1967)*, *15*(2), 191–195.

Matthias-Maser, S., Brinkmann, J., & Schneider, W. (1999). The size distribution of marine atmospheric aerosol with regard to primary biological aerosol particles over the South Atlantic Ocean. *Atmospheric Environment*, *33*(21), 3569–3575. https://doi.org/10.1016/S1352-2310(98)00121-6

Michaud, J. M., Thompson, L. R., Kaul, D., Espinoza, J. L., Richter, R. A., Xu, Z. Z., Lee, C., Pham, K. M., Beall, C. M., Malfatti, F., Azam, F., Knight, R., Burkart, M. D., Dupont, C. L., & Prather, K. A. (2018). Taxon-specific aerosolization of bacteria and viruses in an experimental ocean-atmosphere mesocosm. *Nature Communications*, *9*(1). https://doi.org/10.1038/s41467-018-04409-z

Möller, D. (1980). Kinetic model of atmospheric SO2 oxidation based on published data. *Atmospheric Environment (1967)*, *14*(9), 1067–1076. https://doi.org/https://doi.org/10.1016/0004-6981(80)90037-2

Møller, K. H., Berndt, T., & Kjaergaard, H. G. (2020). Atmospheric Autoxidation of Amines. *Environmental Science & Technology*, *54*(18), 11087–11099. https://doi.org/10.1021/acs.est.0c03937

Montzka, S. A., Calvert, P., Hall, B. D., Elkins, J. W., Conway, T. J., Tans, P. P., & Sweeney, C. S. (2007). On the global distribution, seasonality, and budget of atmospheric carbonyl sulfide (COS) and some similarities to CO<inf>2</inf>. *Journal of Geophysical Research Atmospheres*, *112*(9), 1–15. https://doi.org/10.1029/2006JD007665

Novak, G. A., Fite, C. H., Holmes, C. D., Veres, P. R., Neuman, J. A., Faloona, I., Thornton, J. A., Wolfe, G. M., Vermeuel, M. P., Jernigan, C. M., Peischl, J., Ryerson, T. B., Thompson, C. R., Bourgeois, I., Warneke, C., Gkatzelis, G. I., Coggon, M. M., Sekimoto, K., Bui, T. P., … Bertram, T. H. (2021). Rapid cloud removal of dimethyl sulfide oxidation products limits SO 2 and cloud condensation nuclei production in the marine atmosphere. *Proceedings of the National Academy of Sciences*, *118*(42), e2110472118. https://doi.org/10.1073/pnas.2110472118

Novak, G. A., Kilgour, D. B., Jernigan, C. M., Vermeuel, M. P., & Bertram, T. H. (2022). Oceanic emissions of dimethyl sulfide and methanethiol and their contribution to sulfur dioxide production in the marine atmosphere. *Atmospheric Chemistry and Physics*, *22*(9), 6309–6325.

Novak, G., Vermeuel, M., & Bertram, T. (2019). Simultaneous Detection of Ozone and Nitrogen Dioxide by Oxygen Anion Chemical Ionization Mass Spectrometry: A Fast Time Response Sensor Suitable for Eddy Covariance Measurements. *Atmospheric Measurement Techniques Discussions*, *1*, 1–41. https://doi.org/10.5194/amt-2019-445

O'Dowd, C. D., & de Leeuw, G. (2007). Marine aerosol production: a review of the current knowledge. *Philosophical Transactions of the Royal Society A: Mathematical, Physical and Engineering Sciences*, *365*(1856), 1753–1774. https://doi.org/10.1098/rsta.2007.2043

Patroescu, I. V., Barnes, I., Becker, K. H., & Mihalopoulos, N. (1998). FT-IR product study of the OH-initiated oxidation of DMS in the presence of NO(x). *Atmospheric Environment*, *33*(1), 25–35. https://doi.org/10.1016/S1352-2310(98)00120-4

Peeters, J., Nguyen, T. L., & Vereecken, L. (2009). HOx radical regeneration in the oxidation of isoprene. *Physical Chemistry Chemical Physics*, *11*(28), 5935–5939. https://doi.org/10.1039/B908511D

Pinto, J. P., Turco, R. P., & Toon, O. B. (1989). Self-limiting physical and chemical effects in volcanic eruption clouds. *Journal of Geophysical Research: Atmospheres*, *94*(D8), 11165–11174. https://doi.org/https://doi.org/10.1029/JD094iD08p11165

Prospero, J. M. (1999). Long-range transport of mineral dust in the global atmosphere: Impact of African dust on the environment of the southeastern United States. *Proceedings of the National Academy of Sciences*, *96*(7), 3396–3403.

Ravishankara, A. R. (1997). Heterogeneous and Multiphase Chemistry in the Troposphere. *Science*, *276*(5315), 1058–1065. https://doi.org/10.1126/science.276.5315.1058

Rodhe, H. (1999). Human impact on the atmospheric sulfur balance. *Tellus B*, *51*(1), 110–122.

Shon, Z. H., Davis, D., Chen, G., Grodzinsky, G., Bandy, A., Thornton, D., Sandholm, S., Bradshaw, J., Stickel, R., Chameides, W., Kok, G., Russell, L., Mauldin, L., Tanner, D., & Eisele, F. (2001). Evaluation of the DMS flux and its conversion to SO2 over the southern ocean. *Atmospheric Environment*, *35*(1), 159–172. https://doi.org/10.1016/S1352-2310(00)00166-7

Shukla, P. R., Skeg, J., Buendia, E. C., Masson-Delmotte, V., Pörtner, H.-O., Roberts, D. C., Zhai, P., Slade, R., Connors, S., & van Diemen, S. (2019). *Climate Change and Land: an IPCC special report on climate change, desertification, land degradation, sustainable land management, food security, and greenhouse gas fluxes in terrestrial ecosystems*.

Solomon, S., Garcia, R. R., Rowland, F. S., & Wuebbles, D. J. (1986). On the depletion of Antarctic ozone. *Nature*, *321*(6072), 755–758. https://doi.org/10.1038/321755a0

T Lennartz, S., A Marandino, C., von Hobe, M., O Andreae, M., Aranami, K., Atlas, E., Berkelhammer, M., Bingemer, H., Booge, D., Cutter, G., Cortes, P., Kremser, S., S Law, C., Marriner, A., Simó, R., Quack, B., Xie, H., & Xu, X. (2020). Marine carbonyl sulfide (OCS) and carbon disulfide (CS2): A compilation of measurements in seawater and the marine boundary layer. *Earth System Science Data*, *12*(1), 591–609. https://doi.org/10.5194/essd-12-591-2020

Tanzer, D., & Heumann, K. G. (1992). Gas chromatographic trace-level determination of volatile organic sulfides and selenides and of methyl iodide in Atlantic surface water. *International Journal of Environmental Analytical Chemistry*, *48*(1), 17–31.

Turnipseed, A. A., Barone, S. B., & Ravishankara, A. R. (1996). Reaction of OH with dimethyl Sulfide. 2. Products and mechanisms. *Journal of Physical Chemistry*, *100*(35), 14703–14713. https://doi.org/10.1021/jp960867c

Usher, C. R., Michel, A. E., & Grassian, V. H. (2003). Reactions on Mineral Dust. *Chemical Reviews*, *103*(12), 4883–4940. https://doi.org/10.1021/cr020657y

Vallina, S. M., Simó, R., & Gassó, S. (2006). What controls CCN seasonality in the Southern Ocean? A statistical analysis based on satellite-derived chlorophyll and CCN and model-estimated OH radical and rainfall. *Global Biogeochemical Cycles*, *20*(1), 1–13. https://doi.org/10.1029/2005GB002597

Vaughan, S., Ingham, T., Whalley, L. K., Stone, D., Evans, M. J., Read, K. A., Lee, J. D., Moller, S. J., Carpenter, L. J., Lewis, A. C., Fleming, Z. L., & Heard, D. E. (2012). Seasonal observations of OH and HO2in the remote tropical marine boundary layer. *Atmospheric Chemistry and Physics*, *12*(4), 2149–2172. https://doi.org/10.5194/acp-12-2149-2012

Veres, P. R., Andrew Neuman, J., Bertram, T. H., Assaf, E., Wolfe, G. M., Williamson, C. J., Weinzierl, B., Tilmes, S., Thompson, C. R., Thames, A. B., Schroder, J. C., Saiz-Lopez, A., Rollins, A. W., Roberts, J. M., Price, D., Peischl, J., Nault, B. A., Møller, K. H., Miller, D. O., … Ryerson, T. B. (2020). Global airborne sampling reveals a previously unobserved dimethyl sulfide oxidation mechanism in the marine atmosphere. *Proceedings of the National Academy of Sciences of the United States of America*, *117*(9), 4505–4510. https://doi.org/10.1073/pnas.1919344117

Vermeuel, M. P., Novak, G. A., Jernigan, C. M., & Bertram, T. H. (2020). Diel Profile of Hydroperoxymethyl Thioformate: Evidence for Surface Deposition and Multiphase Chemistry. *Environmental Science and Technology*, *54*(19), 12521–12529. https://doi.org/10.1021/acs.est.0c04323

Von Hobe, M., Cutter, G. A., Kettle, A. J., & Andreae, M. O. (2001). Dark production: A significant source of oceanic COS. *Journal of Geophysical Research: Oceans*, *106*(C12), 31217–31226. https://doi.org/10.1029/2000jc000567

Wang, X., Deane, G. B., Moore, K. A., Ryder, O. S., Stokes, M. D., Beall, C. M., Collins, D. B., Santander, M. V., Burrows, S. M., Sultana, C. M., & Prather, K. A. (2017). The role of jet and film drops in controlling the mixing state of submicron sea spray aerosol particles. *Proceedings of the National Academy of Sciences of the United States of America*, *114*(27), 6978–6983. https://doi.org/10.1073/pnas.1702420114

Watts, S. F. (2000). The mass budgets of carbonyl sulfide, dimethyl sulfide, carbon disulfide and hydrogen sulfide. *Atmospheric Environment*, *34*(5), 761–779. https://doi.org/10.1016/S1352-2310(99)00342-8

Wellington, T. J., Ellermann, T., & Nielsen, O. J. (1993). Atmospheric chemistry of dimethyl sulfide: UV spectra and self-reaction kinetics of CH3SCH2 and CH3SCH2O2 radicals and kinetics of the reactions CH3SCH2 + O2 ??? CH3SCH2O2 and CH3SCH2O2 + NO ??? ... *Journal of Physical Chemistry*, *97*(32), 8442–8449. https://doi.org/10.1021/j100134a013

Wine, P. H., Kreutter, N. M., Gump, C. A., & Ravishankara, A. R. (1981). Kinetics of OH reactions with the atmospheric sulfur compounds H2S, CH3SH, CH3SCH3, and CH3SSCH3. *Journal of Physical Chemistry*, *85*(18), 2660–2665. https://doi.org/10.1021/j150618a019

Wong, P. K., & Wang, Y. H. (1997). Determination of the Henry's law constant for dimethyl sulfide in seawater. *Chemosphere*, *35*(3), 535–544.

Wu, R., Wang, S., & Wang, L. (2015). New mechanism for the atmospheric oxidation of dimethyl sulfide. The importance of intramolecular hydrogen shift in a CH3SCH2OO radical. *Journal of Physical Chemistry A*, *119*(1), 112–117. https://doi.org/10.1021/jp511616j

Xiao, H.-W., Xiao, H.-Y., Shen, C.-Y., Zhang, Z.-Y., & Long, A.-M. (2018). Chemical Composition and Sources of Marine Aerosol over the Western North Pacific Ocean in Winter. In *Atmosphere* (Vol. 9, Issue 8). https://doi.org/10.3390/atmos9080298

Yao, M., Zhao, Y., Hu, M., Huang, D., Wang, Y., Yu, J. Z., & Yan, N. (2019). Multiphase reactions between secondary organic aerosol and sulfur dioxide: kinetics and contributions to sulfate formation and aerosol aging. *Environmental Science & Technology Letters*, *6*(12), 768–774.

Yin, F., Grosjean, D., Flagan, R. C., & Seinfeld, J. H. (1990a). Photooxidation of dimethyl sulfide and dimethyl disulfide. II: Mechanism evaluation. *Journal of Atmospheric Chemistry*, *11*(4), 365–399. https://doi.org/10.1007/BF00053781

Yin, F., Grosjean, D., Flagan, R. C., & Seinfeld, J. H. (1990b). Photooxidation of dimethyl sulfide and dimethyl disulfide. II: Mechanism evaluation. *Journal of Atmospheric Chemistry*, *11*(4), 365–399. https://doi.org/10.1007/BF00053781

Zhang, F., Wang, Y., Peng, J., Chen, L., Sun, Y., Duan, L., Ge, X., Li, Y., Zhao, J., & Liu, C. (2020). An unexpected catalyst dominates formation and radiative forcing of regional haze. *Proceedings of the National Academy of Sciences*, *117*(8), 3960–3966.

Zumkehr, A., Hilton, T. W., Whelan, M., Smith, S., Kuai, L., Worden, J., & Campbell, J. E. (2018). Global gridded anthropogenic emissions inventory of carbonyl sulfide. *Atmospheric Environment*, *183*(March), 11–19. https://doi.org/10.1016/j.atmosenv.2018.03.063

Chapter 1: Development and parameterization of an environmental chamber and model for observations of sulfur oxidation

Abstract

Environmental chambers and flow reactors are an important tool for atmospheric chemists in isolating and investigating components of the atmosphere. The Earth's atmosphere is a complex mixture of various organic and inorganic compounds that are constantly being produced, lost and transformed. Of particular importance is the oxidative environment in which climate relevant molecules are oxidize. We present a method for the development, implementation and modeling of an environmental chamber for the observation of dimethyl sulfide oxidation under oxidative conditions indicative of the marine environment. A primary focus is made on validating and maintaining concentrations of oxidants and reactants consistent with that of the environment in which the studied molecule is emitted. The methodology present here can be expanded to various oxidants (OH and NO_3) and VOCs of various climate relevance to determine rate constants and product yields.

1.1. Environmental Chamber

1.1.1 Components and overview of environmental chamber

Chamber experiments were run in a rectangular 0.6 m^3, 5 mil (mil, 0.001 of an inch) PFA environmental chamber under ambient temperature (~298K), dark, dry (<0.5% RH), and typically under "NO_x free" conditions. The chamber was originally designed for the observation of dimethyl sulfide oxidation and as such referred to as the Dimethyl sulfide Oxidation Reaction Chamber (DORC). The chamber operated under ambient temperatures with an Omega iSeries thermocouple used to record the temperature throughout the chamber experiments. The chamber was covered

with an opaque Total Actinic Radiation Protection (TARP) tarp to remove any ambient light from initializing photolytic reactions within the chamber. The chamber was also run under a slight positive pressure to mitigate any potential inward diffusion of trace gases from outside the chamber. The absolute concentration of water vapor, observed by the LGR OCS analyzer, was measured throughout the experiments and used to determine the relative humidity within the chamber. The chamber was run under a continuous flow regime, set by flowing *ca.* 4 or 2 standard liters per minute (SLPM) of zero air with varying concentrations mixture of reactants (e.g. reduced sulfur compounds, ozone and nitrogen dioxide). The corresponding pull from the chamber was set by the multiple instruments used for monitoring the trace gases along with a supplemental diaphragm pump, utilized to make up additional pull not provided by the instruments. A condensation particle counter (TSI condensation particle counter, model 3787) was attached to the chamber at the start and end of several experiments to determine the concentration, and subsequent reactive surface area, of aerosol particles within the chamber.

1.1.1 Operation of environmental chamber

The chamber was run in two operational modes: 1) constraining mass and 2) isolating reactant products. In the constraining mass case, the chamber was run in in 2 distinct stages: 1) filling the chamber with a volatile organic sulfur compound (VOSC) and tetramethyl ethene (TME) (for "Dark OH" oxidation) or nitrogen dioxide (NO_2) (for nitrate radical "NO_3" oxidation), and 2) adding ozone to initialize oxidation. Dark OH refers to the generation of the hydroxyl radical (OH) via a unimolecular decomposition of the zwitterionic carbonyl oxide, generated by the bimolecular reaction of ozone and an alkene species. Though OH can be generated via the ozonolysis of a variety of different alkene species, TME and its zwitterionic carbonyl oxide ($(CH_3)_2COO$) was used due to its symmetric nature and high OH yield (0.8) (Alam et al., 2013).

The symmetric nature of TME facilitates fewer unique products to form throughout its OH and O_3 oxidation, while the high yield facilitates an increased oxidative capacity. The nitrate radical (NO_3•) is generated via the reaction of NO_2 with ozone. The chamber is run in excess of ozone over NO_2, promoting the formation of NO_3 ($O_3 + NO_2 \rightarrow NO_3$) rather than that of N_2O_5 ($NO_3 + NO_2 \rightarrow N_2O_5$). Additionally, the sustained ozone concentration allows for the efficient consumption and conversion of nitrogen monoxide (NO) to NO_2 within the camber ($NO + O_3 \rightarrow NO_2 + O_2$). In addition to excess ozone, the chamber was held under dark conditions which will shut off any photolytic production of NO from NO_2 ($NO_2 + h\nu \rightarrow NO + O(3P)$). Sustaining a low concentration of NO is important within the chamber experiments as it rapidly reacts with organic peroxy radicals (RO_2·), arresting potential isomerization reactions. Isomerization reactions become significant when NO concentrations are low, so the chamber was designed to explore these oxidative spaces.

At the start of every experiment, the chamber was flushed with dry nitrogen to remove all volatile organic compounds (VOC) and oxidants within the chamber between each experiment. The filling stage was run over 20 hours and was performed by flowing a VOSC and TME or NO_2 in zero air, generated by mixing 80% evaporated liquid nitrogen with 20% ultra-high purity oxygen (UHP O_2, Air Gas OX UHP300), into the chamber at a flow of ca. 4 or 2 SLPM. Depending on the availability of a gas cylinder, a mass flow controller backed by a gas cylinder was used to supply VOCs to the chamber. For the sulfur experiments, a gas cylinder containing a 5.08 ppm mixture of DMS, 1.40 ppm mixture of d3-DMS, 6.11 ppm mixture of methane thiol (MeSH), or 1.188 ppm of NO_2 in nitrogen was used, respectively. Any species required for experimentation that was not present in a gas cylinder was supplied to the environmental chamber by passing nitrogen over an in-house built permeation tube containing the pure compound sheltered in a

temperature-controlled heat block. TME (98% 2,3-Dimethyl-2-butene, Sigma Aldrich), dimethyl disulfide (DMDS, ≥99% Dimethyl disulfide, Sigma Aldrich), and carbon disulfide (CS2, ≥99% Carbon disulfide, Sigma Aldrich) were supplied to the chamber utilizing the permeation tube. The permeation tube for each of the compounds was made along the procedure outlined in Vermeuel et al (2019), and briefly described here. Permeation tubes were made by transferring the desired compound to a 3 mm ID PTFE tubing with both ends plugged with a piece of 1/8" diameter solid PTFE rod. The ends were further secured by crimping approximately 1 cm of 5-gauge stainless steel tubing (0.219" 141 OD, 0.205" ID, 0.007" wall). The length of tubing, the temperature applied to the permeation tubing within the custom housing, and the flow rate of N_2 over the tube dictated the concentration of the molecule supplied to the chamber. The first filling phase of the chamber was allowed typically 20 and 30 hours for a 4 and 2 SLPM experiment to reach steady state, respectively. Once at steady state, ozone was added to the zero-air flow entering the chamber and allowed to reach steady state for about >20 hours. Ozone, used for initializing the formation of OH through the ozonolysis of TME or NO_3 through the oxidation of NO_2, was supplied to the chamber by a custom-built ozone generator with the output ozone concentrations verified by a Thermo Scientific™ Model 49i Ozone Analyzer. Ozone was generated by passing a known low flow (0-20 sccm) of UHP O_2 over a low-pressure mercury Pen lamp (Jelight low pressure double bore lamps, model 95-2100-2). The low-pressure mercury Pen lamp emits 254 nm light, which is capable of photolyzing O_2 into O(3P) which can recombine with O_2 to form ozone (O_2 + O(3P) → O_3). The output concentration of ozone could be systematically increased by increasing the flow of UHP O_2 over the pen lamp. Ozone was produced in line of the zero-air flow to the chamber, leading to no change in flow to the chamber as a function of the addition of ozone. To avoid the potential for an unstable concentration of ozone at the start of the experiment driven by the pen

lamp warming up and approaching a stabilized photon flux, the O_2 flow bypassed the pen lamp while the lamp warmed up and was then redirected over the lamp after it stabilized (20-30 min.) to allow for a prompt constant production of ozone.

The environmental chamber in both cases was run under a continuous flow regime as compared to a conventional batch mode. The primary difference in the two methods is driven by the continuous addition of reactants in the continuous flow regime, while batch mode does not(J. E. Krechmer et al., 2020). A continuous flow designed was utilized in order to maintain a continuous and constant oxidative capacity within the chamber. This design allows intermediates and products formed as first-generation products to experience the same approximate oxidative capacity as that of multi-generation products. A consistent and low oxidative capacity is of particular importance in studying reactions with organic peroxy radical species ($RO_2\cdot$) and isomerization reactions. The oxidation precursor is not constantly added in batch mode, leading to a decrease in oxidation precursor and the oxidant production rate. Chambers that use photolysis as the oxidation initiator can avoid this problem by recycling the oxidant through photolysis, but photolysis was not used here to avoid the complications associated with separating photolytic and non-photolytic reactions (T. Chen & Jang, 2012; Rosati et al., 2021; Ye et al., 2021). Any multi-generational product that requires the buildup or further oxidation of another multi-generational precursor may not grow to concentrations detectable by the instrumentation. The continuous flow regime allows for the constant input of reactants and oxidants to promote oxidation until a steady state of all the species is reached. One of the primary directives of the chamber experimentation is to oxidize marine molecules under conditions typical of the remote marine environment ($[HO_x] \equiv [HO_2\cdot]+[\cdot OH]$ and $[NO_x] \equiv [NO]+[NO_2] <10$ pptv, and $[RO_2\cdot] < 150$ ppt) (Creasey et al., 2003; Lee et al., 2009; Vaughan et al., 2012). In the continuous flow mode, a constant concentration of

$[RO_2\cdot]$ < 150 ppt was maintained allowing the various marine sulfur species to be constantly oxidized under oxidative conditions of the marine environment. The process for verifying the oxidative conditions will be addressed later in the chapter (section 1.5). The steady state of the intermediates is primarily driven by its production term (e.g. flow into the chamber, or production through oxidation) and its loss term primarily driven by dilution, oxidation or wall loss. Dilution is the primarily loss pathway for most of the stable species. The constant influx of air containing the precursor molecules (VOSC + TME/NO_2) and outflow driven by the instrumentation flow, intermediates generated within the chamber are constantly flushed out. To constrain this important process within the chamber, the experimental dilution term for the chamber is measured for each experiment. The dilution rate of the chamber was mathematically calculated to be 1.1×10^{-4} s^{-1}, with a chamber volume of ~600 L and flow rate of 4 SLPM. The dilution rate was experimentally determined to be $k_{fill} = 9.7 \times 10^{-5}$ s^{-1} by fitting the decay of CO, detected by the LGR instrument, within the bag during the purging and filling of the chamber (**Figure 1.1a**). A trace concentration of CO exists within the evaporated liquid nitrogen flow used to purge the chamber of VOCs. The nitrogen background within the chamber containing CO is removed at the dilution limit as the chamber is filled with zero-air. The 12% deviation in the mathematical and experimental dilution rate is attributed to the chamber being slightly larger than 600 L calculated from the dimensions of the chamber. The experimental dilution rate is used for all model simulations. The chamber is also assumed to be well-mixed due to the increased turbulence of constant injection and removal of new air as a result of the continuous flow regime and the small size of the chamber (J. E. Krechmer et al., 2020).

The second operational mode is designed to isolate reactants and products within the instrumentational signal. To isolate sulfur-related oxidation products from TME/NO_3 oxidation

products within the Vocus-PTR and CIMS instrument, an “add sulfur” or a “remove sulfur” experiment was run in the chamber. The chamber was run in the same continuous flow format, but in two different stages from the typical add ozone experiment explained in this section. The first stage was run by adding ozone and TME or NO_2 to the chamber without a VOSC present (an example with DMS is seen in **Figure 1.2a**). After the chamber reached steady state, the compound of interest was added to the chamber and allowed to reach steady state (**Figure 1.2a**). Masses and species that arose in the first stage, TME/NO_2 + O_3, were associated with alkene or nitrogen dioxide oxidation. This is more important for the dark OH experimentation, where OH and O_3 oxidation of TME can generate a variety of VOC intermediates (e.g. Acetone, pinacol, formic acid) that can complicate the spectra. During these experiments, the primary focus is to isolate the background concentrations and signal that would arise at the masses associated with sulfur species. For TME, none of the species associated with TME oxidation fragmented or overlapped in significant fractions with sulfur related peaks. For NO_3, the primary focus was to determine the contribution of nitrogen pentoxide (N_2O_5) at the 235 m/z mass associated with HPMTF detection. As seen in **Figure 1.2b**, DMS is added to the chamber after the oxidation of TME has reached steady state. The masses and species that arose after DMS was added to the system were associated with sulfur oxidation products. These products included major DMS oxidants like hydroperoxymethyl thioformate (HPMTF) and methane sulfinic acid (MSIA) in the Iodine CIMS spectra and methyl thioformate (MTF) and dimethyl sulfoxide (DMSO) in Vocus-PTR spectra. In a similar fashion, sulfur was removed from the chamber while TME/NO_2 + O_3 was held constant. In this case, all species that showed a significant decay were attributed to sulfur oxidation products.

1.2. Measurements of Reduced and Oxidized Sulfur Species within Environmental chamber

The detection and quantification of a wide array of sulfur containing trace gases was conducted with two Chemical Ionization Mass Spectrometers (CIMS); a Compact Time of Flight CIMS (C-ToF) utilizing iodine anion or oxygen anion chemistry (Bertram et al., 2011; Novak et al., 2019; Vermeuel et al., 2020) and an Aerodyne/TOFWERK Vocus - Proton Transfer Reaction Time of Flight Mass Spectrometer (Vocus)(J. Krechmer et al., 2018). Hydroperoxymethyl thioformate (HPMTF), thioperformic acid (TPA), sulfur dioxide (SO_2), methane sulfenic acid (CH_3SOH), hydroperoxymethyl dithioformate (HPMDTF) and methanesulfinic acid (MSIA) measurements were made by the iodide CIMS instrument at masses of 235, 205, 191, 191, 267, and 207 m/Q, respectively. Sulfur dioxide (SO_2) measurements, during the methane thiol (MeSH), dimethyl disulfide (DMDS) and carbon disulfide (CS_2) experiment, were made by the oxygen anion CIMS instrument at a mass of 64, 96, 112 m/Q corresponding to $[SO_2]^-$, $[SO_4]^-$ and $[SO_5]^-$, respectively. Dimethyl sulfide (DMS), MeSH, dimethyl sulfoxide (DMSO), tetramethyl ethene (TME), methyl thioformate (MTF), an unknown MeSH oxidation product (CH_2SO), and pinacol were made by the Vocus-PTR instrument at masses of 63.026, 49.011, 79.021, 85.101, 77.006, 62.990, and 101.096 m/Q, respectively. A custom-built laser-induced fluorescence (LIF) spectrometer (Rollins et al., 2016) and a Los Gatos Research Enhanced Performance (LGR) OCS analyzer were used to detect SO_2 (for the DMS oxidation experiments) and carbonyl sulfide (OCS) (Berkelhammer et al., 2016), respectively. A humified dilution flow was added to the inlet of the C-ToF to increase the $[I{\cdot}H_2O]^-$:$[I]^-$ ratio in the C-ToF ion molecule reaction region and enhance sensitivity for the DMS experiments. The humified flow was generated by bubbling 500 sccm of evaporated liquid nitrogen through milli-Q water. The subsequent dilution was accounted for in the calculation of the absolute concentration of the gas phase species detected by the CIMS. The

sensitivities and signal intensity for all species recorded by the iodine and oxygen anion CIMS C-ToF instrument are presented as normalized counts per second (ncps), where the intensity is normalized to one million (10^6) counts per second, calculated as the sum of -m/*Q* 127 ($[I]^-$) and 145 ($[I\cdot H_2O]^-$) and of -m/*Q* 32 ($[O_2]^-$) and 50 ($[O_2\cdot H_2O]^-$), respectively. CIMS sensitivity to HPMTF was determined to be 5 ncps/pptv following the experimental method previously described in the SI of Vermeuel et al (2020). Even though the instruments are the same, the sensitivity in this experiment is significantly higher than that reported in Vermeuel et al (2020) as the $[I\cdot H_2O]^-$:$[I]^-$ ratio (25%) and the internal ion voltages were set to optimize the signal intensity of HPMTF. The HPMTF sensitivity was further constrained by mass balance of all the sulfur species within the chamber (**Figure 1.3**). The sensitivity of 5 ncps/ppt closes the sulfur to 11% matching the model results and product distribution. The iodine CIMS sensitivity to MSIA, TPA and other hydroperoxide species (ROOH) within the environmental chamber was calculated by comparing the computationally derived binding enthalpies of the given species to that of the experimentally derived HPMTF sensitivity. The binding enthalpies were calculated using the method described by Iyer et al (2016) using a M06/ 6-311+G(2d,p) level of theory to calculate the zero point energies for the individual molecules and corresponding iodide clusters. In summary, the zero-point energy of Iodide ($[I]^-$) and the analyte of interest ([A]) were summed to determine the combined energy of the two species ($[I]^-$ + [A]). The combined energies were subtracted from the zero-point energies of a clustered species ($[I + A]^-$) and the resulting differential in energy was taken as the binding energy of the species to iodine. The binding enthalpies for HPMTF, MISA, TPA and AlkOOH (The primary ROOH from Alkene oxidation) are -25.05, -20.04, -20.02, and -18.25 kcal/mol, respectively. The CIMS sensitivities are reported in **Table 1.1**. The absolute sensitivities of the Vocus to DMS and MeSH were determined through dynamic dilution of DMS

and MeSH standard supplied by compressed gas cylinder standards (5.08 ppm DMS in N_2, Praxair and 6.11 ppm MeSH in N_2, Airgas). The absolute sensitivities of the Vocus to CS_2, DMDS, DMSO, TME (98% 2,3-Dimethyl-2-butene, Sigma Aldrich), and DMS were calculated using the liquid calibration method described in Lavi et al (2018). The liquid calibration of DMS was within 3% of the gas cylinder calibration, validating the sensitivities calculated with the liquid calibration method. The Vocus sensitivities are reported in **Table 1.1**.

Limits of detection (LOD) of DMS, HPMTF, TPA, MTF, DMSO, MSIA, SO_2, and OCS were determined following the method of Bertram et al., (2011). The method assumes that random uncertainty in observed counts follows Poisson statistics and therefore the uncertainty in the signal and background count rate should be equivalent to the square root of the count rate, allowing signal-to-noise to be:

$$\frac{S}{N} = \frac{C_f[X]t}{\sqrt{C_f[X]t+2Bt}} \qquad \text{E1.1}$$

where C_f is the calibration factor, [X] is the analyte mixing ratio, t is the averaging time in seconds, and B is the background count rate. Background intensities were determined from chamber measurements taken before DMS, TME, and ozone were added. LODs at averaging time, t, are determined by solving for [X] at a S/N of 3. The LODs and their integration time are presented in **Table 1.1**. The optimal averaging time for the LOD calculation was determined by the calculation of the Allen variance.(Werle et al., 1993) The local minimum of the Allen variance plot for each instrument was used to calculate the optimal averaging time and the Allen variance was calculated over a 1-hour period when the chamber was at constant steady state concentration for all major species.

A custom-built laser-induced fluorescence (LIF) spectrometer (Rollins et al., 2016) and a Los Gatos Research Enhanced Performance (LGR) OCS analyzer (Berkelhammer et al., 2014) were used to detect sulfur dioxide (SO_2) and carbonyl sulfide (OCS), respectively. The sensitivity of the LIF-SO_2 measurement was consistently verified through an internal calibration procedure that was initiated hourly during the experiment. Basic details on the instrument were previously described in Rollins et al. (2016) and improved on in Rickly et al (2021). All OCS measurements were made using a Los Gatos Research, Enhanced Performance OCS analyzer (PN:914-0028). The analyzer was previously described by Berkelhammer (2014). It is a quantum cascade laser analyzer where OCS is detected at ~2050.40 cm^{-1}. Corrections are made for pressure broadening associated with water vapor and CO_2 but these are not relevant for the controlled experimental conditions of this study. Laboratory analysis shows that standard deviation of the OCS analyzer is as low as 4 pmol mol^{-1} (1-sigma) using an integration time of 300 s but the uncertainty under operational conditions was closer to 12 pmol mol^{-1} (Berkelhammer et al., 2016). A comparison between OCS measured from the analyzer against concentrations measured by GC-MS in nearby flask measurements associated with the NOAA GMD program (Montzka et al., 2007), suggest the accuracy of the instrument is better than 10 pmol mol^{-1} and the sensitivity across normal atmospheric ranges is better than 90% of the range detected from NOAA GMD GC-MS method (Berkelhammer et al., 2020). The LIF-SO_2 instrument sensitivity is reported as 26 counts per second ppt^{-1} with a 1 σ detection limit of 3.4 ppt over 1-second of integration.

1.3. Environmental Chamber Model Description

A 0-D box model that incorporates the Master Chemical Mechanism (MCM) v3.3.1 in the Framework for 0-D Atmospheric Modeling (F0AM)(Saunders et al., 2003; Wolfe et al., 2016) was used in this work. All chemical reactions and rate expressions added to the MCM are presented in

Table 1.2. The box model was run in two phases to mimic the dark OH chamber experiments performed: 1) a fill phase, where DMS and TME are added to the chamber, and 2) a reaction phase, where DMS, TME, and O_3 are added to the chamber. To account for the continuous flow regime, a fill term was added to the model to account for the consistent VOSC and TME concentration added to the chamber. In the fill phase, only three rates dictated the shape and concentration of the VOSC and TME, the fill term ($k_{fill} = 9.7 \times 10^{-5}$ s^{-1}) added to account for the continuous flow set up, a dilution term ($k_{dilution} = 9.7 \times 10^{-5}$ s^{-1}) to account for the instruments pulling on the chamber, and a wall loss term to account for reversable loss to the chamber walls. An experimentally derived wall loss term (k_{wall}) was determined by calculating the wall loss of known species (DMS, TME, SO_2, MeSH, DMDS, CS_2) during the filling of the chamber. The value used here is a simple first order loss rate that captures all potential loss processes within the chamber for TME and DMS. The wall loss term was calculated from the difference in VOSC (or TME) concentration exiting the chamber at steady state to that flowing directly into the chamber system. At steady state, the dilution and fill term of the continuous flow chamber should be at equilibrium and equal. The remaining deviation in VOSC concentration flowing into and out of the chamber must be due to secondary losses, in particular loss to the wall. The wall loss term for all other major stable VOSC and alkene RO_2 recombination species used in the model follows the recommendation of previous chamber experiments of similar size (J. E. Krechmer et al., 2016, 2020; Matsunaga & Ziemann, 2010), where the wall term is a portioning and equilibrium value. The wall loss term is expressed as two rate equations: 1) a gas phase species sticking to the wall ($k_{wall,\ multi}$) and 2) the condensed species off gassing to the wall ($k_{wall,\ multi} \times \frac{c^*}{c_w}$). $k_{wall,\ multi}$ is a value adopted from the recommendations of Krechmer et al, (2016), with the $k_{wall,\ multi}$ (3.6×10^{-3} s^{-1}) term being 3 orders of magnitude greater than the value of DMS to account for the faster equilibrium time with the

walls. This term was within a factor of 3 of the conditioning rate constants (1.6×10^{-3} s^{-1}) recommended by Krechmer et al, (2020). To account for the off gassing of the different species, a scaling factor was implemented based on the saturation vapor pressure (c^*, μg m^{-3}) and the equivalent organic mass concentration of the walls (c_w, μg m^{-3}). The c^* for HPMTF was calculated using the SIMPOL method (Pankow & Asher, 2008). The c^* for MTF, DMSO, MSIA, and MSA were calculated using literature values of their liquid vapor pressure, p_L^o (atm), at 298K. c_w was calculated using the recommendations of Krechmer et al, (2016), where the c_w is based upon the species c^* value. The c^* values for each of the major species were all within the same recommended c_w range and as such were all given the same set of rate equations describing their loss to the wall. The dry (< 0.5% RH) conditions of the chamber drastically reduce the magnitude of the wall loss term. The experimental and model chamber reached a constant concentration after approximately 20 hours of continuous flow. After that point the second phase of the model was initialized with the addition of ozone to the chamber supply flow. Ozone is introduced into to the chamber in the same way as DMS and TME, and the addition of ozone leads to the formation of OH through the ozonolysis of TME. OH is formed through the unimolecular decomposition of the zwitterionic carbonyl oxide, $(CH_3)_2COO$, generated by the bimolecular reaction of ozone and TME. The MCM uses a unit yield of ·OH from the decomposition of $(CH_3)_2COO$, while a more mechanistic formation of ·OH was used in the model to capture the concentration of the stabilized $(CH_3)_2COO$ species ($s(CH_3)_2COO$) which is known to react with SO_2 (Berndt et al., 2012; Huang et al., 2015). We used a OH-yield from Alam et al. (2013) of 0.83 for both the decomposition of the $(CH_3)_2COO$ and $s(CH_3)_2COO$ species as the dry chamber conditions and direct ·OH observations described in Alam et al. (2013) are more representative of the conditions studied here. Recommendations from the literature were used for the yield of $s(CH_3)_2COO$ from $(CH_3)_2COO$ decomposition,

unimolecular s$(CH_3)_2COO$ + M rate constant and the bimolecular s$(CH_3)_2COO$ + SO_2 rate constant(Berndt et al., 2012; Huang et al., 2015; Newland et al., 2015). Though the bimolecular reactions with water and sulfur dioxide were included, the dry (<0.5%) and low SO_2 concentrations of the chamber strongly favor the unimolecular decomposition pathway with a rate of ~300 s^{-1}.(Lester & Klippenstein, 2018) Ozone was added to the chamber and in the model in the same way as VOSC and TME with a fill term ($k_{fill} = 9.7 \times 10^{-5}$). The ozone concentration added to the supply line containing DMS and TME was constrained by the experiments at values of 30-80 ppbv, verified by a Thermo Scientific™ Model 49i Ozone Analyzer. The varying ozone concentrations were used to explore different OH and RO_2 oxidative conditions within the chamber. A wall loss term was applied to all major labile VOCs, while a dilution term was applied to all species within the chemical mechanism. A few modifications were made to the standard MCM to represent the conditions more accurately within the environmental chamber. The inclusion of peroxy radical (RO_2) + OH chemistry was added to capture all potential loss pathways for the RO_2 species within the chamber. Rate constants were taken from Fittschen (2019), while RO_2 species without an explicit rate constant were given values from species of similar structure. The MCM uses a unit yield of OH from the ozonolysis of TME. Here, we use the OH-yield from Alam et al. (2013) of 0.83 as the dry chamber conditions and direct OH observations described in Alam et al. (2013) are more representative of the conditions studied here. In addition, the decomposition can either generate OH or HO_2 and as such the OH yield term has a corresponding term for the generation of HO_2 that was added to the MCM.

1.3.1 Additions and modifications to HPMTF + OH mechanism

In a base version of the DMS oxidation model, a direct pathway to SO_2 from HPMTF oxidation does not exist. To account for the missing 30% of SO_2 presented in **Figure 2.2** of chapter

2, an additional mechanism can be made to the base multigenerational model presented in the main text. To sequester additional SO_2, in our current experimental conditions with high O_3 concentrations, we suggest implementing the reaction of the $HOOCH_2S•$ intermediate with O_3 by analogy to the $CH_3S• + O_3$ reaction, with k(298 K) = 4.9×10^{-12} cm^3 $molecule^{-1}$ s^{-1} and forming $HOOCH_2SO•$ radicals (Estep et al., 2020; Martínez et al., 2000). This radical could then analogously transform to SO_2 and provide a route to HPMTF + OH derived SO_2. In more pristine conditions, the $HOOCH_2SOO•$ intermediate may also isomerize to $HOOCH_2S•O_2$ and yield SO_2.(J. Chen et al., 2021) In total, we believe the following additions to the HPMTF + OH mechanism presented here can adequately reproduce the formation of OCS and an approximate closure of the sulfur budget within our chamber experiments:

a) The HPMTF+OH rate coefficient is optimized based on the experiments; the value remains well within the uncertainties of both theory and experiment
b) $CH_3S•$ and CH_2S are assumed to yield 100% SO_2; this is based on the latest experimental (this work), Chen et al. (2021) and theoretical data (J. Chen et al., 2021), but may disagree with some earlier theoretical work (Zhu & Bozzelli, 2006).
c) The reaction of $HOOCH_2S•$ with O_3 is implemented with a fitted rate coefficient and product yield.

A simplified mechanism for explaining HPMTF derived OCS production is presented below (**Figure 1.4**).

1.3.2 Additions and modifications to DMDS, CS_2 and MeSH mechanism

A detailed description of additions made to the MCM to fully the capture the oxidative mechanism of DMDS, MeSH and CS_2 is made in chapter 3, but a brief description will be made here. For MeSH, the OH-initiated loss was included based on the recommendations of

Butkovskaya & Setser, (2021), J. Chen et al., (2021), and Wine et al., (1984). To account for two main pathways of OH oxidation, an 87% yield to the hydrogen abstraction channel off a sulfur hydrogen forming the $CH_3S\cdot$ species, found in DMS oxidation, with the remaining 13% fractioning a hydrogen abstraction channel off a methyl hydrogen yielding $\bullet CH_2SH$. For DMDS, the OH-initiated loss was included based on the recommendations of (Berndt et al., 2020; Wine et al., 1981). Three major fates were included to the DMDS pathway: 1) the formation of the $CH_3S\cdot$ species from the initial OH-reaction with DMDS, 2) the inclusion of the formation and fate of the CH_3SOH species generated from the initial OH-reaction with DMDS, and 3) the formation of a recently discovered hydroperoxyl aldehyde, $HOOCH_2SSCHO$ (hydroperoxymethyl dithioformate, HPMDTF), formed from a minor hydrogen abstraction channel off a methyl hydrogen. Lastly, the OH-initiated loss for CS_2 was included based on the recommendations of (Hynes et al. (1988), McKee & Wine (2001), and Stickel et al. (1993). The CS_2 experiments were performed under zero air conditions at ambient pressure and for that reason the short-lived excited species (i.e OCS* and HOSO*) were not included and a flat yield to OCS and SO_2 was used.

1.4. Approximating the [RO_2] and [HO_2] within the chamber

The formation of HPMTF, generated by an isomerization mechanism of methyl sulfur peroxy radical (MTMP; $CH_3SCH_2O_2\bullet$), is dependent on the peroxy radical (RO_2), hydroperoxyl radical (HO_2) and NO_x ($NO + NO_2$) concentrations. These classes of species all partake in bimolecular reactions with MTMP that can compete with the HPMTF forming isomerization reaction. For this reason, the production rate of HPMTF within the model is dependent on the modeled concentration of RO_2, HO_2 and NO_x, and on the MTMP isomerization rate (k_{isom}) used in the model. Our chamber system is run under NO_x free conditions and low HO_2 conditions

($\tau_{MTMP+HO2}$ > 500s), which leaves the RO_2 concentration as the dominant competitor for MTMP. The low model HO_2 concentration is supported by the absence of H_2O_2 and other organic hydroperoxide species within the chamber. The HO_2 concentration is held at a low concentration as a result of fast bimolecular loss pathways with RO_2 species and the lack of a dominant production pathway. Experiments performed with H_2O_2 photolysis and high OH concentrations can facilitate higher concentrations of HO_2 through dominant reactions of OH with H_2O_2 or formaldehyde. Our chamber experiments do not facilitate either of these processes and as such low HO_2 concentrations are maintained. To validate the modeled RO_2 concentrations and ultimately the HPMTF production term, a series of model-measurement comparisons were conducted to verify [RO_2]. First, we compare the modeled and measured concentrations of the major sulfur and TME-derived RO_2 recombination species. In particular, we observed the time evolution of pinacol ($C_6H_{14}O_2$), a species that is formed by the reaction of general RO_2 with the primary TME-derived RO_2 species (Alk-O_2, C4ME2OHO2) formed from the OH oxidation and O_2 addition of TME. In addition to pinacol we observed MTF, a product of MTMP + RO_2 and a direct competitor of the HPMTF isomerization reaction. The model output demonstrates that the majority of the RO_2 are formed through the oxidation of TME, either by TME+O_3 or TME + OH reaction **(Figure 1.5a)**. Alk-O_2 is a dominant RO_2 species at the start of the chamber reactions as the OH rate constant with TME is near collision limit and sustained by the continuous flow setup providing additional TME to the chamber. Constrained by observations of TME throughout the chamber and the ozone concentration added to the chamber, our model predictions of pinacol match well with observations **(Figure 1.5b)**. Other species associated with TME RO_2 reactions (methylglyoxal, $C_3H_4O_2$ and C4ME2OHOOH, Alk-OOH) are observed with the Vocus and CIMS and compared to the model to further support the RO_2 concentrations within the chamber (**Figure 1.6b**). Lastly,

observations of MTF match well with the model output, indicating that the model and the new HPMTF reactions correctly match the experimental observations **(Figure 1.5b)**.

The absolute concentration of RO_2 within the chamber was calculated following the method developed by Crounse et al (2011), for calculating the hydroperoxyenal (HPALD) isomerization rate coefficient. In Crounse et al. (2011), the competition of the bimolecular reaction of the isoprene proxy radical and HO_2 and isomerization reaction is used to calculate the isomerization rate from the production rate over the first 2 hours of HPALD within an environmental chamber. Only the first two hours were used in the HPALD analysis and in our analysis as it is the period of time with linear change in products indicating a constant production. The absolute concentration of HO_2 is calculated by solving for $[HO_2]$ from the production rate of H_2O_2. Here, these equations were adapted to solve for the $[RO_2]$ from the production rate of pinacol and hydroxyacetone. Using the following set of equations, the $[RO_2]$ can be calculated as a function of the pinacol (or hydroxyacetone) production rate ($P_{pinacol}$), $k_{Alk\text{-}O2+RO2}$ (0.9×10^{-13} cm^3 $molecule^{-1}$ s^{-1}), the fraction of RO_2 that is Alk-O_2 (α_{AlkO_2}, 0.65), and the yield of pinacol from the Alk-O_2 + RO_2 reaction ($Y_{Pinacol}$, 0.3). All values are taken from the MCM.

$$P_{Pinacol} = Y_{Pinacol} k_{RO_2+Alk-O_2} [RO_2][AlkO_2] \quad \text{E1.2}$$

$$[AlkO_2] = \alpha_{AlkO_2} [RO_2] \quad \text{E1.3}$$

$$[RO_2] = \sqrt{\frac{P_{Pinacol}}{\alpha\, Y_{Pinacol}\, k_{RO_2+Alk-O_2}}} \quad \text{E1.4}$$

The primary assumption made in the calculation of the $[RO_2]$ in Eqn. 1.3 is the fraction of RO_2 that is $AlkO_2$ (α_{AlkO_2}). The α_{AlkO_2} value was determined to be 0.55, derived from the model. The α_{AlkO_2} value is independent of the DMS oxidation chemistry, as the only prominent sulfur

peroxy radical is MTMP at <1% of the total RO_2. Using the rate constants and product yields from the MCM, the average RO_2 concentration calculated within the first 1.5 hours of the chamber was 165 ± 50 pptv, with the uncertainty capturing the variability in the experiments. The average RO_2 concentration within the model was 165 ± 60 ppt, showing good agreement between the model results and values calculated from measured species. Both observations of RO_2 products over the entire chamber experiment and the first 1.5 hours, show good agreement between modelled and experimental results. The value presented here is the elevated concentration of RO_2 that arises at the beginning of the chamber experiment. After the first 2 hours of the chamber experiment, the direct determination of the RO_2 becomes more complicated. The higher RO_2 concentration and minimal contribution to loss processes allows for the determination of the isomerization reaction (k_{isom}), see **supplemental of Chapter 2**. Based upon good experiment and model agreement of RO_2 derived species, we can rely on the model to determine the steady state concentration of RO_2 within the chamber.

1.5. Assessment of potential background and artificial sources of OCS in the chamber

1.5.1 Background production from the oxidation of the chamber

To determine the background signal of molecules associated with the production of the oxidant (OH/NO3 production) or the oxidation of the chamber walls the second operational mode of the chamber was run. The chamber was run in the same continuous flow format, but the chamber was run by adding only ozone and TME or NO_2 to the chamber without a VOSC present. Two major species were of interest in the oxidation of the chamber without sulfur present, OCS and N_2O_5. The chamber was originally filled with only TME or NO2 until steady state was reached, then ozone was added to the system. As seen in **Figure 1.7a**, the chamber did not show any observable production of OCS when no DMS was present, compared to when DMS was present. This would

imply that any reactions between the oxidants and the walls of the chamber or along the tubing to the instrument produce OCS. The system was also run at the highest alkene concentration (~5ppb) and ozone (80 ppb) tested to put the largest possible strain on the system. For NO_3, the primary focus was to determine the contribution of nitrogen pentoxide (N_2O_5) at the 235 m/z mass associated with HPMTF detection. To determine the background of formation of N2O5 while sulfur oxidation was occurring, the chamber was also run using tri-deuterated dimethyl sulfide (d3-DMS). By utilizing d3-DMS, the mass of the deuterated HPMTF analogue, $H_2D_2C_2SO_3$ at mass 237m/z, would be shifted 2 masses units over from the peak at HPMTF and N_2O_5 at 235 m/Q. As seen in **Figure 1.7b**, the addition of O_3 at t = 0 induces the significant production at 237 m/Q rather than that of 235m/Q. From this observation, we can assume under similar oxidative conditions the production of N_2O_5 is insignificant compared to that of HPMTF within the chamber.

1.5.2 Carbonyl sulfide formation from OH-oxidation of carbon disulfide (CS_2)

Carbonyl sulfide (OCS) is known to be produced directly and indirectly from sulfur containing anthropogenic sources (Watts, 2000). To determine if OCS is being produced from either chamber or inlet off-gassing or a side reaction involving ozone and a surface within the experimental setup, the chamber was run with only TME and ozone present. By running the chamber in this way all surfaces throughout the experimental set up would experience OH and O_3 oxidation. No detectable signal of OCS was found during this experimentation. Only upon the addition of DMS was a detectable source of OCS found. To verify that a background of carbon disulfide (CS_2), another sulfur species known to generate OCS upon OH oxidation (Chin & Davis, 1993), within the DMS cylinder was not providing the source of OCS formation upon OH oxidation, a sensitivity test using the F0AM model was run to determine the amount of background CS_2 required to match the observed OCS concentrations. Model simulations found that the DMS

cylinder would need to have a CS_2 concentration at 10% of DMS within the DMS cylinder to match the OCS observations. In addition to the model test, CS_2 was calibrated for and measured throughout the chamber experiments. Using the same liquid calibration for TME and DMSO, the CS_2 sensitivity was calculated and used to determine the background concentration of CS_2 within the DMS cylinder and chamber. At most the cylinder could be containing a concentration 0.12% of the DMS cylinder concentration. This is under the assumption that all of the signal at 76.139 m/Q is a function of CS_2 and not from inadvertent DMS fragmentation within the PTR ionization region. In any case, the low contamination concentration within the chamber only provides a CS_2 concentration within the chamber of < 30ppt. At an overall OH rate constant of 1.2×10^{-12} cm^3 $molecule^{-1}$ s^{-1} (Hynes et al., 1988) and an OCS yield of 81% (Chin & Davis, 1993), the OCS yield would be <0.5 pptv. When the model was run under the discussed CS_2 conditions, no significant variability in the OCS yield from HPMTF was found. From the following experiments, we determined the OCS observed in our chamber is primarily a function of the OH oxidation of DMS.

1.5.3 Determine background production through 2 SLPM chamber design

In addition to OCS generated from the background, we ran the chamber experiment under a slower dilution rate 2 SLPM through the chamber ($k_{dil} = 4.4 \times 10^{-5}$ s^{-1}) to determine the effect on the OCS yield within the chamber. The bimolecular rate constant and subsequent lifetime of OCS to OH is 2×10^{-15} cm^3 $molec^{-1}$ s^{-1} and 16 years, respectively. Given the long lifetime and inert nature of OCS (implying an insignificant partitioning to the walls), the only OCS loss process was through chamber dilution. For this reason, the OCS concentration from DMS oxidation under a similar loss of DMS would be higher in the 2 SLPM experiments when compared to that of the 4 SLPM experiments. The 2 SLPM experiments observed an experimental yield ($\frac{\Delta OCS}{\Delta DMS}$) of 2.79 + 0.5 %, while the 4 SLPM experiments observed an experimental yield of 1.51 + 0.18%. Though

the OCS yields for the 4 and 2 SLPM experiments are different, the F0AM model implementing the HPMTF mechanism (with k_{isom} = 0.11, $k_{HPMTF+OH}$ = 1.4 ± 0.4 × 10^{-11} cm^3 $molecule^{-1}$ s^{-1}, and a ϕ_{OCS} = 13.3 ± 3.0 %) have good agreement within uncertainty between the experimental observation and model output of OCS (**Figure 1.1c**). The dependence on the dilution rate of the chamber implies that the production of OCS is dependent on the oxidation mechanism and not a constant yield from DMS oxidation.

1.6. Validation of sulfur oxidation products using gas chromatography

To verify the masses detected in the Vocus-PTR instrument are the sulfur species within the DMS oxidation scheme, HR fitting and gas chromatography separation were performed. The Vocus-PTR spectra contained a mass range of 10-504 m/Q and a resolution of ~5000 $m/\Delta m$, allowed for high resolution (chemical composition determination) fitting of the time of flight (TOF) peaks. The TOF peaks were integrated using the Igor Pro-implemented Tofware V3.3.2 software package (Aerodyne Research Inc. and Tofwerk AG). The sulfur species were also verified by checking the stable sulfur M+2 isotope (4.2% of total sulfur) within the mass spectra. A compact gas chromatography (GC) system (ARI Mod-GC; Aerodyne Research Inc.) used to separate sulfur species was coupled to the Vocus to create an ARI-GC-Vocus-PTR-MS system. The instrument is described in detail in Claflin, et al. 2020 but will be briefly described here(Claflin et al., 2021). The GC system uses a 30m Agilent DB-5 is nonpolar and low bleed column as the stationary phase and helium as the mobile phase. Air from the chamber is flown over a sample trap to preconcentrate the analytes in the flow before introducing to the GC column. The trap is flash heated to introduce the sample to the GC column, where the column is ramped in heat over 10 minutes to elute the species on the column. The analytes are measured with the Vocus-PTR instrument described previously. The GC system was used to isolate and identify potential species within the GC mass

spectrum from isomers and fragments. From the GC analysis (**Figure 1.8**), masses at $[C_2H_6S•H]^+$, $[CH_2S•H]^+$, $[C_2H_4OS•H]^+$, $[C_2H_6SO•H]^+$ and, $[C_2H_5S]^+$ were plotted and associated with DMS, thioformaldehyde, MTF, DMSO, and potentially hydroxymethyl methyl sulfide CH_3SCH_2OH, respectively. From the GC retention times, no peaks at the $[CH_2S•H]^+$ mass (**Figure 1.8b**) can be decoupled from fragments of larger masses (DMS at ~1.6 min and MTF at ~4.4 min). Based on this observation, we believe that the thioformaldehyde species associated with Barnes et al (1994) OCS mechanism is either not present in our system, in too low of concentration to be detected or is insensitive to the PTR instrument. The chromatogram of $[C_2H_4OS•H]^+$ associated with methyl thioformate (MTF) has no other sulfur species coelute at the 4.4 min retention time, leading us to believe that MTF is credibly in the system and detected by the Vocus instrument. The $[C_2H_5S]^+$ fragment observed in the Vocus instrument, has a strong correlation with DMS. From the GC chromatogram, we can see a peak at 3.4 min that is sperate from the major DMS peak at 1.6 min. The peak at 3.4 min does not coelute with any other species in the sulfur list of masses, and as such we have identified it as potentially hydroxymethyl methyl sulfide, CH_3SCH_2OH. This species, like MTF, is found within the MCM as a minor product (10% yield) of the MTMP + RO_2 reactions. Hydroxymethyl methyl sulfide in its protonated form would have the same mass as DMSO. As we can see from **Figure 1.8d and 1.8e**, DMSO ($[C_2H_6SO•H]^+$) has a unique retention time at 9.2 min, while hydroxymethyl methyl sulfide ($[C_2H_5S]^+$) has a unique retention time at 3.4 min. This leads us to believe that hydroxymethyl methyl sulfide is seen as the dehydrate fragment in the PTR separate from its DMSO isomer, seen as the protonated species. Unfortunately, the relatively large concentration of DMS, which fragments into $[C_2H_5S]^+$, made real time analysis of hydroxymethyl methyl sulfide throughout the experiment impossible.

1.7. Conclusion

The use of an environmental chamber for the analysis of the oxidation of VOCs under oxidative conditions representative of the marine environment has been presented here. By running the chamber under a continuous flow mode, a constant oxidative capacity can be maintained within the chamber allowing intermediates formed either as first or multi-generational products experience the same environment. A 0-D box model can be used in tandem with the environmental chamber to help explain the observations of the environmental chamber. An environmental chamber can be used to approximate the atmosphere, but the walls of the chamber bring additional loss pathways. Assessments of the dilution, wall loss and background oxidation pathways should be made, to isolate the process associated with the oxidation of the VOC and not the chamber. The work presented here was designed for the observations of sulfur oxidation but can be expanded to the oxidation of other VOCs, and organic aerosol formation.

References

Alam, M. S., Rickard, A. R., Camredon, M., Wyche, K. P., Carr, T., Hornsby, K. E., Monks, P. S., & Bloss, W. J. (2013). Radical product yields from the ozonolysis of short chain alkenes under atmospheric boundary layer conditions. *Journal of Physical Chemistry A*, *117*(47), 12468–12483. https://doi.org/10.1021/jp408745h

Berkelhammer, M., Alsip, B., Matamala, R., Cook, D., Whelan, M. E., Joo, E., Bernacchi, C., Miller, J., & Meyers, T. (2020). Seasonal Evolution of Canopy Stomatal Conductance for a Prairie and Maize Field in the Midwestern United States from Continuous Carbonyl Sulfide Fluxes. *Geophysical Research Letters*, *47*(6), e2019GL085652. https://doi.org/https://doi.org/10.1029/2019GL085652

Berkelhammer, M., Asaf, D., Still, C., Montzka, S., Noone, D., Gupta, M., Provencal, R., Chen, H., & Yakir, D. (2014). Constraining surface carbon fluxes using in situ measurements of carbonyl sulfide and carbon dioxide. *Global Biogeochemical Cycles*, *28*(2), 161–179. https://doi.org/10.1002/2013GB004644

Berkelhammer, M., Steen-Larsen, H. C., Cosgrove, A., Peters, A. J., Johnson, R., Hayden, M., & Montzka, S. A. (2016). Radiation and atmospheric circulation controls on carbonyl sulfide concentrations in themarine boundary layer. *Journal of Geophysical Research*, *121*(21), 13,113-13,128. https://doi.org/10.1002/2016JD025437

Berndt, T., Chen, J., Møller, K. H., Hyttinen, N., Prisle, N. L., Tilgner, A., Hoffmann, E. H., Herrmann, H., & Kjaergaard, H. G. (2020). SO2 formation and peroxy radical isomerization in the

atmospheric reaction of OH radicals with dimethyl disulfide. *Chemical Communications*, *56*(88), 13634–13637. https://doi.org/10.1039/D0CC05783E

Berndt, T., Jokinen, T., Mauldin III, R. L., Petaja, T., Herrmann, H., Junninen, H., Paasonen, P., Worsnop, D. R., & Sipila, M. (2012). Gas-phase ozonolysis of selected olefins: The yield of stabilized Criegee intermediate and the reactivity toward SO2. *The Journal of Physical Chemistry Letters*, *3*(19), 2892–2896.

Bertram, T. H., Kimmel, J. R., Crisp, T. A., Ryder, O. S., Yatavelli, R. L. N., Thornton, J. A., Cubison, M. J., Gonin, M., & Worsnop, D. R. (2011). A field-deployable, chemical ionization time-of-flight mass spectrometer. *Atmospheric Measurement Techniques*, *4*(7), 1471–1479. https://doi.org/10.5194/amt-4-1471-2011

Butkovskaya, N. I., & Setser, D. W. (2021). Reactions of OH and OD radicals with simple thiols and sulfides studied by infrared chemiluminescence of isotopic water products: Reaction OH + CH3SH revisited. *International Journal of Chemical Kinetics*, *53*(6), 702–715. https://doi.org/10.1002/kin.21475

Chen, J., Berndt, T., Møller, K. H., Lane, J. R., & Kjaergaard, H. G. (2021). Atmospheric Fate of the CH3SOO Radical from the CH3S + O2 Equilibrium. *The Journal of Physical Chemistry A*, *125*(40), 8933–8941. https://doi.org/10.1021/acs.jpca.1c06900

Chen, T., & Jang, M. (2012). Chamber simulation of photooxidation of dimethyl sulfide and isoprene in the presence of NO x. *Atmospheric Chemistry and Physics*, *12*(21), 10257–10269. https://doi.org/10.5194/acp-12-10257-2012

Chin, M., & Davis, D. D. (1993). Global sources and sinks of OCS and CS2 and their distributions. *Global Biogeochemical Cycles*, *7*(2), 321–337. https://doi.org/10.1029/93GB00568

Claflin, M. S., Pagonis, D., Finewax, Z., Handschy, A. V, Day, D. A., Brown, W. L., Jayne, J. T., Worsnop, D. R., Jimenez, J. L., Ziemann, P. J., de Gouw, J., & Lerner, B. M. (2021). An in situ gas chromatograph with automatic detector switching between PTR- and EI-TOF-MS: isomer-resolved measurements of indoor air. *Atmospheric Measurement Techniques*, *14*(1), 133–152. https://doi.org/10.5194/amt-14-133-2021

Estep, M. L., Moore III, K. B., & Schaefer III, H. F. (2020). Assessing the Viability of the Methylsulfinyl Radical-Ozone Reaction. *ChemPhysChem*, *21*(12), 1289–1294. https://doi.org/https://doi.org/10.1002/cphc.202000188

Huang, H.-L., Chao, W., & Lin, J. J.-M. (2015). Kinetics of a Criegee intermediate that would survive high humidity and may oxidize atmospheric SO2. *Proceedings of the National Academy of Sciences*, *112*(35), 10857–10862.

Hynes, A. J., Wine, P. H., & Nicovich, J. M. (1988). Kinetics and mechanism of the reaction of hydroxyl with carbon disulfide under atmospheric conditions. *The Journal of Physical Chemistry*, *92*(13), 3846–3852. https://doi.org/10.1021/j100324a034

Krechmer, J. E., Day, D. A., & Jimenez, J. L. (2020). Always Lost but Never Forgotten: Gas-Phase Wall Losses Are Important in All Teflon Environmental Chambers. *Environmental Science and Technology*, *54*(20), 12890–12897. https://doi.org/10.1021/acs.est.0c03381

Krechmer, J. E., Pagonis, D., Ziemann, P. J., & Jimenez, J. L. (2016). Quantification of Gas-Wall Partitioning in Teflon Environmental Chambers Using Rapid Bursts of Low-Volatility Oxidized Species Generated in Situ. *Environmental Science and Technology*, *50*(11), 5757–5765. https://doi.org/10.1021/acs.est.6b00606

Krechmer, J., Lopez-Hilfiker, F., Koss, A., Hutterli, M., Stoermer, C., Deming, B., Kimmel, J., Warneke, C., Holzinger, R., Jayne, J., Worsnop, D., Fuhrer, K., Gonin, M., & de Gouw, J. (2018). Evaluation of a New Reagent-Ion Source and Focusing Ion-Molecule Reactor for Use in Proton-

Transfer-Reaction Mass Spectrometry. *Analytical Chemistry*, *90*(20), 12011–12018. https://doi.org/10.1021/acs.analchem.8b02641

Lester, M. I., & Klippenstein, S. J. (2018). Unimolecular Decay of Criegee Intermediates to OH Radical Products: Prompt and Thermal Decay Processes. *Accounts of Chemical Research*, *51*(4), 978–985. https://doi.org/10.1021/acs.accounts.8b00077

Martínez, E., Albaladejo, J., Notario, A., & Jiménez, E. (2000). A study of the atmospheric reaction of CH3S with O3 as a function of temperature. *Atmospheric Environment*, *34*(29), 5295–5302. https://doi.org/https://doi.org/10.1016/S1352-2310(00)00348-4

Matsunaga, A., & Ziemann, P. J. (2010). Gas-wall partitioning of organic compounds in a teflon film chamber and potential effects on reaction product and aerosol yield measurements. *Aerosol Science and Technology*, *44*(10), 881–892. https://doi.org/10.1080/02786826.2010.501044

McKee, M. L., & Wine, P. H. (2001). Ab initio study of the atmospheric oxidation of CS2. *Journal of the American Chemical Society*, *123*(10), 2344–2353.

Montzka, S. A., Calvert, P., Hall, B. D., Elkins, J. W., Conway, T. J., Tans, P. P., & Sweeney, C. S. (2007). On the global distribution, seasonality, and budget of atmospheric carbonyl sulfide (COS) and some similarities to CO<inf>2</inf>. *Journal of Geophysical Research Atmospheres*, *112*(9), 1–15. https://doi.org/10.1029/2006JD007665

Newland, M. J., Rickard, A. R., Alam, M. S., Vereecken, L., Munoz, A., Ródenas, M., & Bloss, W. J. (2015). Kinetics of stabilised Criegee intermediates derived from alkene ozonolysis: reactions with SO 2, H 2 O and decomposition under boundary layer conditions. *Physical Chemistry Chemical Physics*, *17*(6), 4076–4088.

Novak, G., Vermeuel, M., & Bertram, T. (2019). Simultaneous Detection of Ozone and Nitrogen Dioxide by Oxygen Anion Chemical Ionization Mass Spectrometry: A Fast Time Response Sensor Suitable for Eddy Covariance Measurements. *Atmospheric Measurement Techniques Discussions*, *1*, 1–41. https://doi.org/10.5194/amt-2019-445

Pankow, J. F., & Asher, W. E. (2008). SIMPOL.1: A simple group contribution method for predicting vapor pressures and enthalpies of vaporization of multifunctional organic compounds. *Atmospheric Chemistry and Physics*, *8*(10), 2773–2796. https://doi.org/10.5194/acp-8-2773-2008

Rollins, A. W., Thornberry, T. D., Ciciora, S. J., McLaughlin, R. J., Watts, L. A., Hanisco, T. F., Baumann, E., Giorgetta, F. R., Bui, T. V., & Fahey, D. W. (2016). A laser-induced fluorescence instrument for aircraft measurements of sulfur dioxide in the upper troposphere and lower stratosphere. *Atmospheric Measurement Techniques*, *9*(9), 4601–4613. https://doi.org/10.5194/amt-9-4601-2016

Rosati, B., Christiansen, S., Wollesen de Jonge, R., Roldin, P., Jensen, M. M., Wang, K., Moosakutty, S. P., Thomsen, D., Salomonsen, C., Hyttinen, N., Elm, J., Feilberg, A., Glasius, M., & Bilde, M. (2021). New Particle Formation and Growth from Dimethyl Sulfide Oxidation by Hydroxyl Radicals. *ACS Earth and Space Chemistry*, *5*(4), 801–811. https://doi.org/10.1021/acsearthspacechem.0c00333

Saunders, S. M., Jenkin, M. E., Derwent, R. G., & Pilling, M. J. (2003). Protocol for the development of the Master Chemical Mechanism, MCM v3 (Part A): Tropospheric degradation of non-aromatic volatile organic compounds. *Atmospheric Chemistry and Physics*, *3*(1), 161–180. https://doi.org/10.5194/acp-3-161-2003

Stickel, R. E., Chin, M., Daykin, E. P., Hynes, A. J., Wine, P. H., & Wallington, T. J. (1993). Mechanistic studies of the hydroxyl-initiated oxidation of carbon disulfide in the presence of oxygen. *The Journal of Physical Chemistry*, *97*(51), 13653–13661.

Vermeuel, M. P., Novak, G. A., Alwe, H. D., Hughes, D. D., Kaleel, R., Dickens, A. F., Kenski, D., Czarnetzki, A. C., Stone, E. A., Stanier, C. O., Pierce, R. B., Millet, D. B., & Bertram, T. H. (2019). Sensitivity of Ozone Production to NOx and VOC Along the Lake Michigan Coastline. *Journal of Geophysical Research: Atmospheres*, *124*(20), 10989–11006. https://doi.org/https://doi.org/10.1029/2019JD030842

Vermeuel, M. P., Novak, G. A., Jernigan, C. M., & Bertram, T. H. (2020). Diel Profile of Hydroperoxymethyl Thioformate: Evidence for Surface Deposition and Multiphase Chemistry. *Environmental Science and Technology*, *54*(19), 12521–12529. https://doi.org/10.1021/acs.est.0c04323

Watts, S. F. (2000). The mass budgets of carbonyl sulfide, dimethyl sulfide, carbon disulfide and hydrogen sulfide. *Atmospheric Environment*, *34*(5), 761–779. https://doi.org/10.1016/S1352-2310(99)00342-8

Werle, P., Mücke, R., & Slemr, F. (1993). The limits of signal averaging in atmospheric trace-gas monitoring by tunable diode-laser absorption spectroscopy (TDLAS). *Applied Physics B Photophysics and Laser Chemistry*, *57*(2), 131–139. https://doi.org/10.1007/BF00425997

Wine, P. H., Kreutter, N. M., Gump, C. A., & Ravishankara, A. R. (1981). Kinetics of hydroxyl radical reactions with the atmospheric sulfur compounds hydrogen sulfide, methanethiol, ethanethiol, and dimethyl disulfide. *The Journal of Physical Chemistry*, *85*(18), 2660–2665. https://doi.org/10.1021/j150618a019

Wine, P. H., Thompson, R. J., & Semmes, D. H. (1984). Kinetics of OH reactions with aliphatic thiols. *International Journal of Chemical Kinetics*, *16*(12), 1623–1636. https://doi.org/10.1002/kin.550161215

Wolfe, G. M., Marvin, M. R., Roberts, S. J., Travis, K. R., & Liao, J. (2016). The framework for 0-D atmospheric modeling (F0AM) v3.1. *Geoscientific Model Development*, *9*(9), 3309–3319. https://doi.org/10.5194/gmd-9-3309-2016

Ye, Q., Goss, M. B., Isaacman-VanWertz, G., Zaytsev, A., Massoli, P., Lim, C., Croteau, P., Canagaratna, M., Knopf, D. A., Keutsch, F. N., Heald, C. L., & Kroll, J. H. (2021). Organic Sulfur Products and Peroxy Radical Isomerization in the OH Oxidation of Dimethyl Sulfide. *ACS Earth and Space Chemistry*. https://doi.org/10.1021/acsearthspacechem.1c00108

Zhu, L., & Bozzelli, J. W. (2006). Kinetics of the Multichannel Reaction of Methanethiyl Radical (CH3S•) with 3O2. *The Journal of Physical Chemistry A*, *110*(21), 6923–6937. https://doi.org/10.1021/jp056209m

Tables and Figures

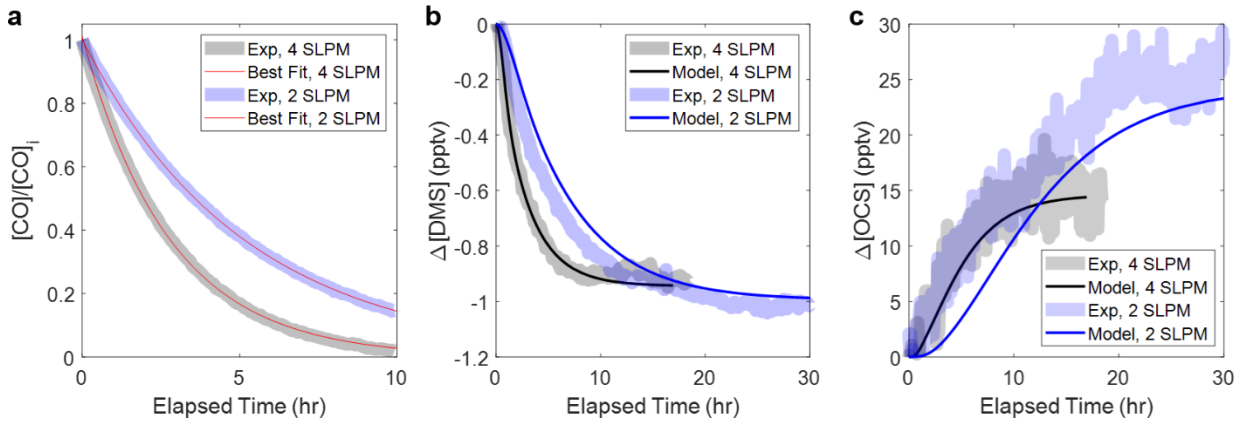

Figure 1.1: The environmental chamber was run at 2 different dilution rates to access the bias in the growth curves of the multiple sulfur species as a function of the dilution term. The dilution term for each of the experiments was determined by fitting the dilution of the background subtracted CO as the chamber was being filled with zero air after being purged with evaporated liquid nitrogen between experiments (a). Observation and model calculations of all the major sulfur species were made at both the 2 and 4 standard liter per minute flow rates (b, c).

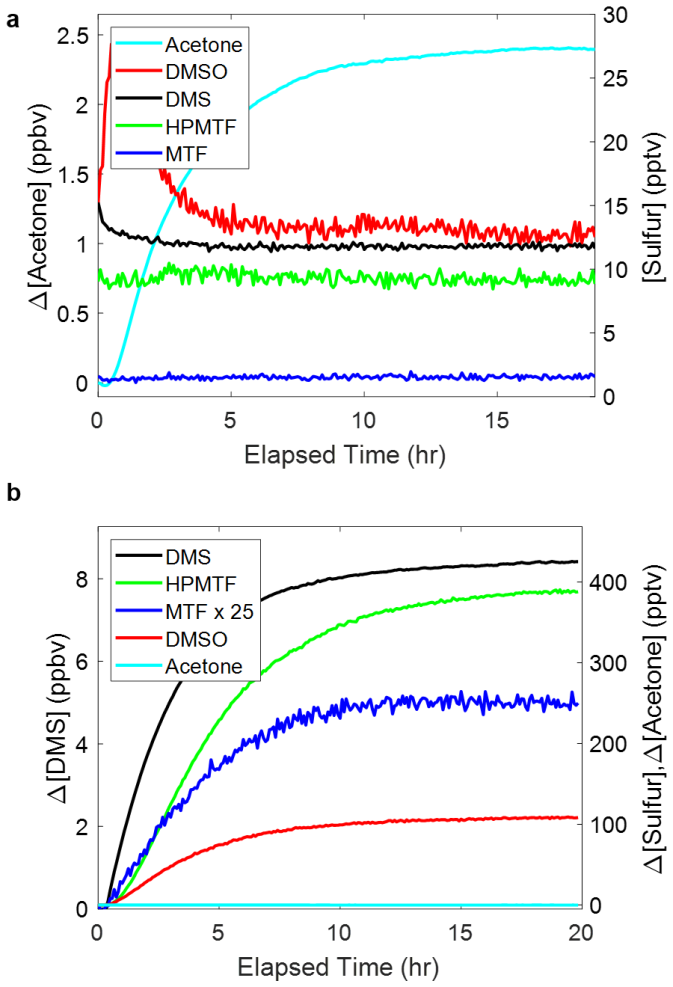

Figure 1.2: The masses in the environmental chamber were verified as originating from TME and DMS oxidation by running an add sulfur experiment. The chamber was originally run by adding ozone and TME to the chamber without DMS present (a). After the chamber reached steady state, DMS was added to the chamber and allowed to reach steady state (b). Species at masses corresponding to HPMTF, MTF and DMSO only moved off background while DMS was present (b), while acetone a known product from TME oxidation formed only when TME was oxidized (a).

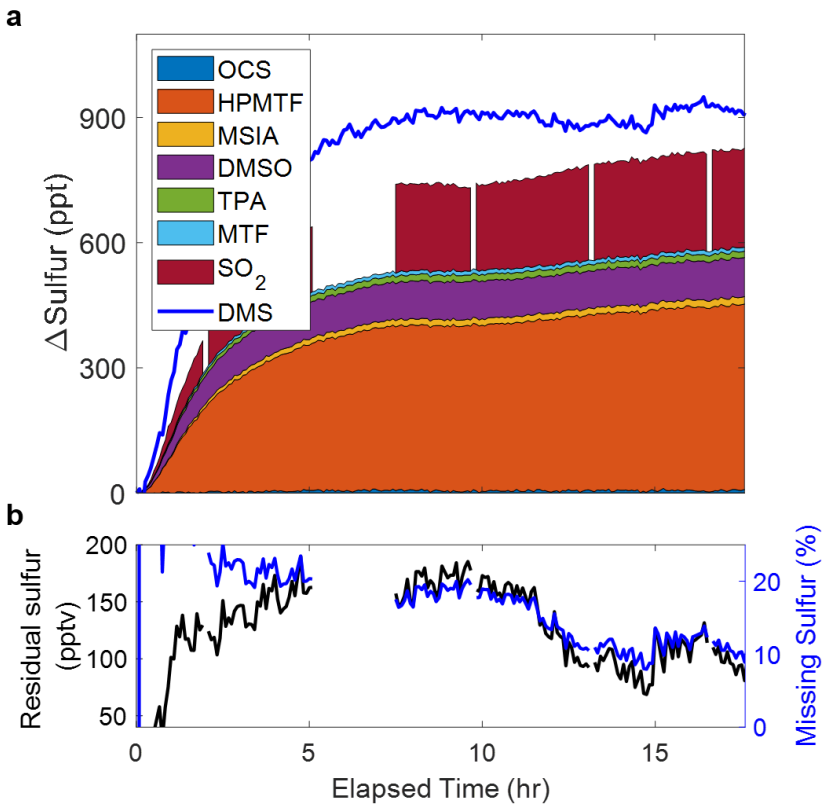

Figure 1.3: At t = 0 hr, ozone was added, initiating OH production, initiating the oxidation/loss of DMS. The amount of DMS lost to OH oxidation and the corresponding rise in sulfur oxidation products are presented HPMTF and MSIA measurements were made by the iodide CIMS instrument and DMSO and DMS measurements were made by the Vocus-PTR instrument. The adapted laser-induced fluorescence (LIF) spectrometer and a Los Gatos Research Enhanced Performance (LGR) OCS analyzer were used to detect sulfur dioxide (SO_2) and carbonyl sulfide (OCS), respectively.

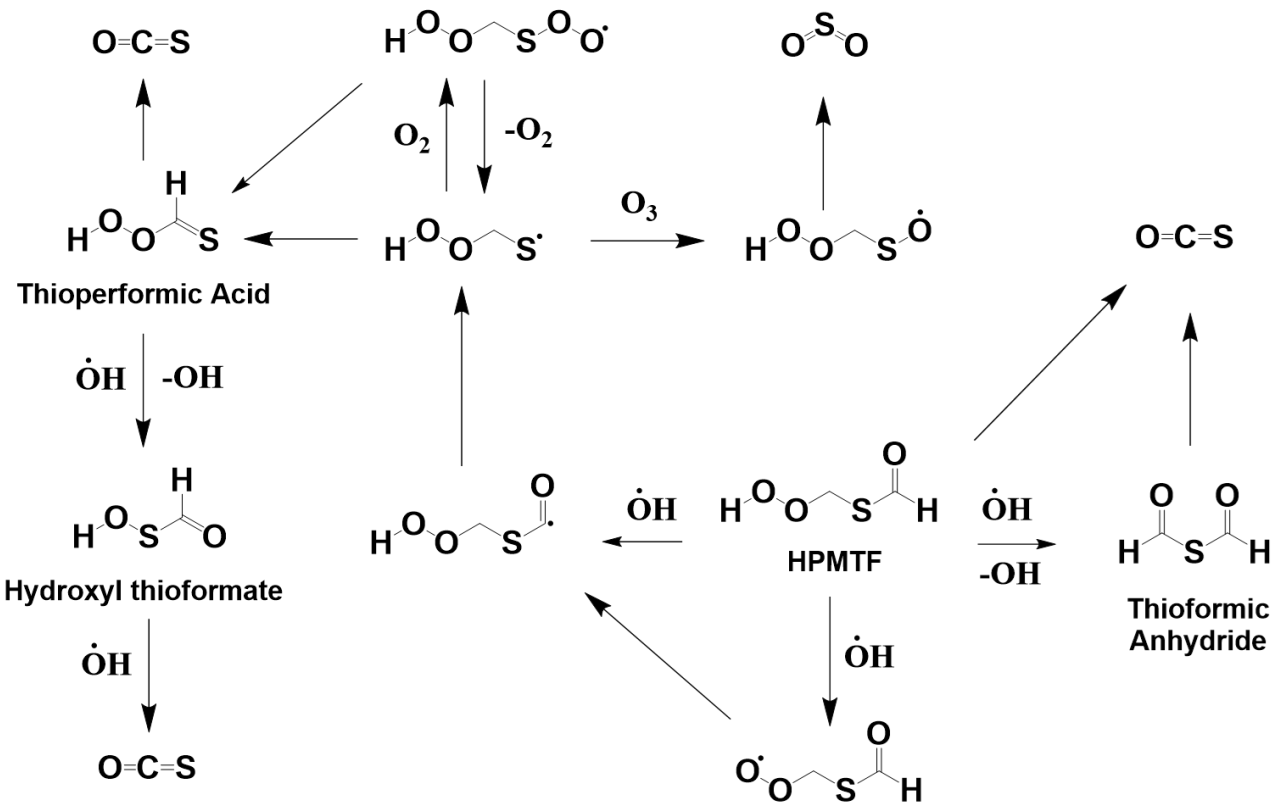

Figure 1.4: Oxidation mechanism of HPMTF with inclusion of the formation pathways for soluble intermediates: thioformic andydride, thioperformic acid, and hydroxyl thioformate.

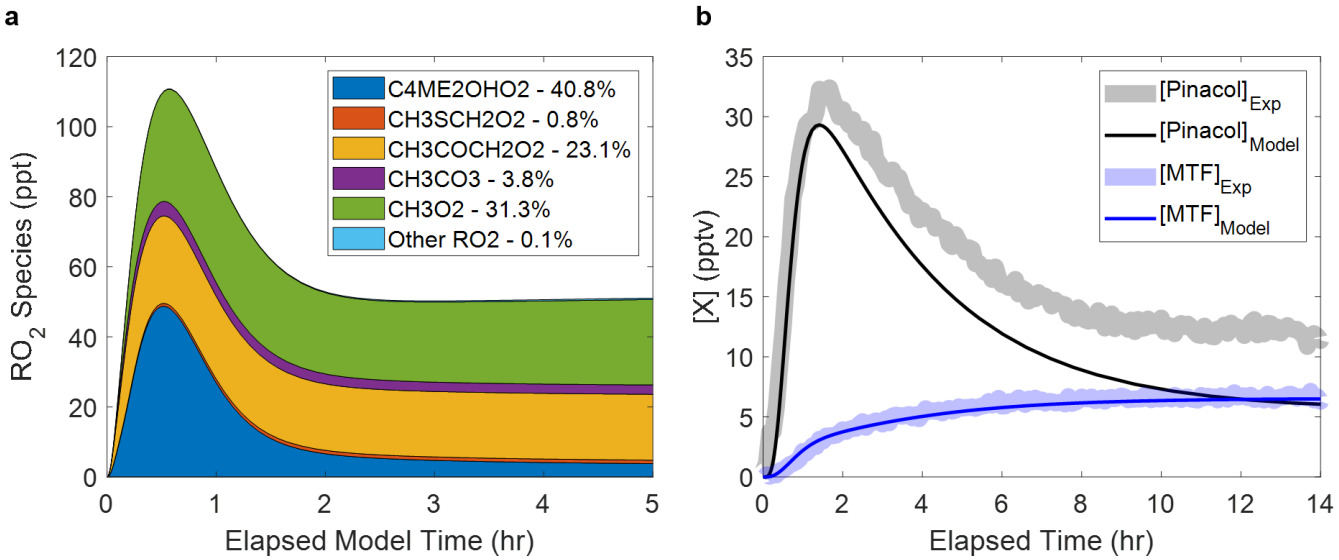

Figure 1.5: At t = 0 hr, ozone was added, initiating OH production, and the oxidation/loss of DMS. The product distribution for all the major species within the model are monitored to evaluate the steady state concentration of RO_2 within the chamber. $C4ME_2OHO_2$, $CH_3COCH_2O_2$ and CH_3CO_3, CH_3O_2 are all generated from the oxidation of TME (CH_3O_2 has minor contribution from DMS oxidation), while $CH_3SCH_2O_2$ (MTMP) is generated from OH + DMS (a). The experimental (translucent traces) and model (solid traces) observations for pinacol and methyl thioformate (MTF), products of RO_2 recombination chemistry from alkene and DMS oxidation, respectively (b). Pinacol and MTF are observed using the PTR-Vocus instrument with absolute sensitivities calculated by computational means.

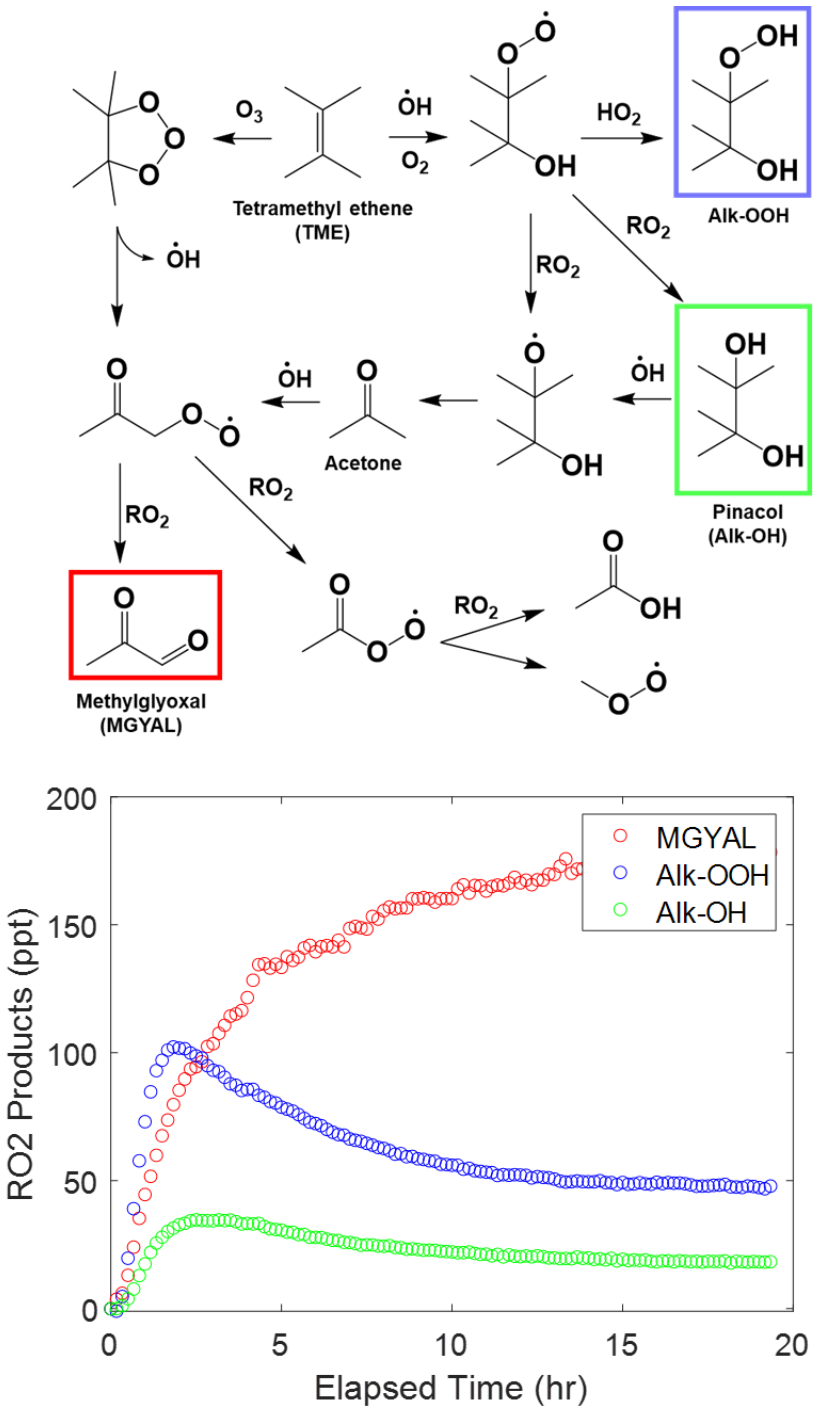

Figure 1.6: A simplified mechanism for the oxidation of TME with detectable species boxed is shown (top panel). At t = 0 hr, ozone was added, initiating OH production, and the oxidation/loss of TME (bottom panel). The product distribution for three major species within the chamber are monitored to evaluate the steady state concentration of RO_2 within the chamber.

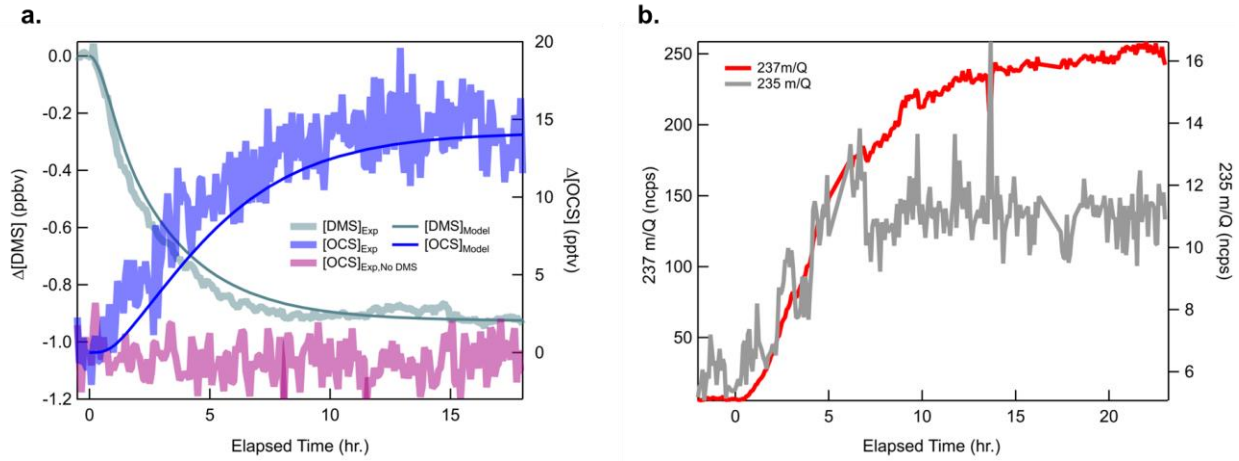

Figure 1.7: Measurements (translucent thick lines) and model calculations (solid thin lines) of S-containing reaction products of the OH-oxidation of DMS conducted in an environmental chamber under low NO_x oxidation conditions. Measurements of OCS performed under low NO_x oxidation conditions with (blue trace) and without (magenta trace) the presence of DMS conducted in the DORC. Measurements of mass 237 (red trace) and 235 (grey trace) by Iodine CIMS during the OH-oxidation of d3-DMS conducted in an environmental chamber under low NO_x oxidation conditions.

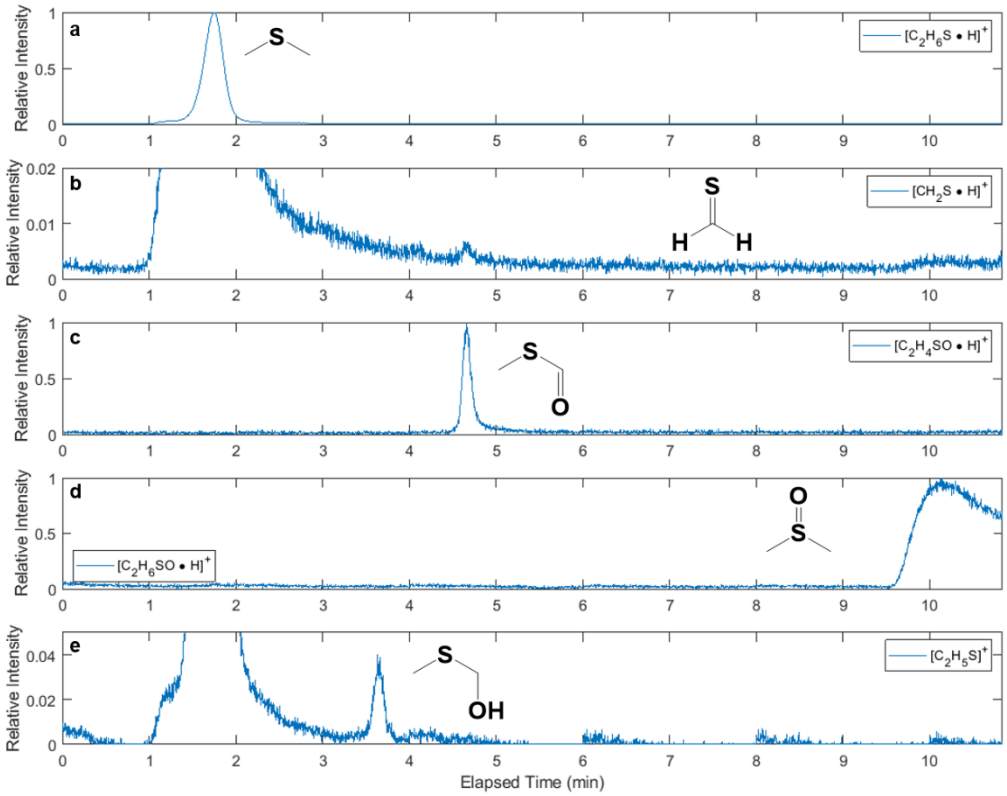

Figure 1.8: The chromatograms from the ARI-GC-Vocus-PTR-MS system of $[C_2H_6S•H]^+$ (a), $[CH_2S•H]^+$ (b), $[C_2H_4OS•H]^+$ (c), $[C_2H_6SO•H]^+$ (d) and, $[C_2H_5S]^+$ (e) associated with DMS, potentially thioformaldehyde, MTF, DMSO, and potentially hydroxymethyl methyl sulfide, CH_3SCH_2OH, respectively.

Table 1.1: Summary of instrument, sensitivity, background counts, and limits of detection (LOD) for HPMTF, MTF, DMSO, MSIA, SO_2, and OCS.

Species	**Instrument**	**Sensitivity**	**Integration Time (s)**	**Background (ncps, 1σ)**	**LOD (pptv)**
HPMTF	Iodine CIMS	5.00 ncps/ppt	25	8.30 ± 6.10	0.53
MSIA	Iodine CIMS	2.00 ncps/ppt	25	6.15 ± 5.30	2.29
TPA	Iodine CIMS	5.00 ncps/ppt	25	18.8 ± 8.6	0.78
DMS	Vocus PTR-MS	3.14 cps/ppt	25	56.00 ± 10.20	2.08
DMSO	Vocus PTR-MS	3.33 cps/ppt	25	23.78 ± 15.54	1.30
MTF	Vocus PTR-MS	1.98 cps/ppt	25	6.87 ± 5.52	1.22
Pinacol	Vocus PTR-MS	5.25 cps/ppt	25	57.18 ± 11.01	1.26
DMDS	Vocus PTR-MS	0.550 cps/ppt	25	11.34 ± 5.05	5.20
MeSH	Vocus PTR-MS	0.932 cps/ppt	25	4.98 ± 2.8	2.04
SO_2	LIF	26 cps/ppt	1	88.4	3.4
SO_2	Oxygen CIMS	1.089 ncps/ppt	25	435.82 ± 41.5	16.25
OCS	LGR	N/A	300	80.50 ± 34.37	2.21

Table 1.2: Summary of reaction equations and corresponding rate expressions and rate constants at 298K that were added to the MCM.

	Rate expression	k(298)‡
CH3SCH2O2 = HPMTF + OH (This study)	0.11	1.10E-01
CH3SCH2O2 = HPMTF + OH (Veres et al)	2.2433E11×exp(-9.8016E3/T) ×exp(1.0348E8/T^3)	5.80E-02
HPMTF + OH = OCS + Products	1.4E-11×ϕ_{OCS} (13%)	1.75E-12
HPMTF + OH = SO2 + CO	1.4E-11×ϕ_{SO_2} (87%)	1.22E-11
OCS + OH = SO2	1.1e-13×exp(-1200/T)	1.96E-15
DMS + Wall =	k_{wall}	3.58E-06
†A + Wall = A_{Wall}	$k_{wall,\ multi}$	3.58E-02
A_{Wall} = A	$k_{wall,\ multi} \times \frac{c^*}{c_w}$	1.79E-01
Flow in = DMS	k_{dil} ×$[DMS]_i^*$	2.55E+07
Flow in = O3	k_{dil}×$[O3]_i^*$	9.31E+07
Flow in = TME	k_{dil} ×$[TME]_i^*$	3.58E+06
CH3CCH3OOC = CH3COCH2O2 + OH	k_{dec} × ϕ_{OH} (83%) × ϕ_{CI} (35%)	2.91E+05
CH3CCH3OOC = CH3COCH2O2 + HO2	k_{dec} × ϕ_{HO_2} (17%) × ϕ_{CI} (35%)	5.95E+04
CH3CCH3OOC = sCH3CCH3OOC	k_{dec} × ϕ_{sCI} (65%)	6.50E+05
sCH3CCH3OOC + SO2 = CH3COCH3 + SO3	4.23E-13×exp(1760/T)	1.55E-10
sCH3CCH3OOC = CH3COCH2O2 + OH	400 × ϕ_{OH} (83%)	332
sCH3CCH3OOC = CH3COCH2O2 + HO2	400 × ϕ_{HO_2} (17%)	68
CH3O2 + OH = CH3O + HO2	1.6E-10×0.86	1.38E-10
CH3O2 + OH = CH3OH	1.6E-10×0.14	2.24E-11
C4ME2OHO2 + OH = C4ME2OHO + HO2	1.4E-10×0.5	7.00E-11
C4ME2OHO2 + OH = C4ME22OH	1.4E-10×0.5	7.00E-11
CH3COCH2O2 + OH = ACETOL	1.4E-10×0.5	7.00E-11
CH3COCH2O2 + OH = CH3COCH2O + HO2	1.4E-10×0.5	7.00E-11
TM124BPRO2 + OH = TM124BP2OH	1.4E-10×0.30	4.20E-11
TM124BPRO2 + RO2 = TM124BPRO	1.4E-10×0.70	9.80E-11

‡ The rate constants are in units of molecule cm^{-3} s^{-1}, s^{-1}, and cm^3 molecule $^{-1}$ s^{-1} referring to equations of "Flow in = ", "A = C" and "A + B = C" format, respectively

† A refers to HPMTF, MSIA, MSA, TPA, DMSO and MTF, all of which have a similar c* and c_w value resulting in a consistent wall term

* Refers to the concentration of DMS, TME, and Ozone that are spiked in the zero-air flow entering the chamber. This is a constant value attributed to a zeroth order reaction.

Chapter 2: Efficient production of carbonyl sulfide in the low-NO_x oxidation of dimethyl sulfide

Abstract

The oxidation of carbonyl sulfide (OCS) is the primary, continuous source of stratospheric sulfate aerosol particles, which can scatter shortwave radiation and catalyze heterogeneous reactions in the stratosphere. While it has been estimated that the oxidation of dimethyl sulfide (DMS), emitted from the surface ocean accounts for 8-20% of the global OCS source, there is no existing DMS oxidation mechanism relevant to the marine atmosphere that is consistent with an OCS source of this magnitude. We describe new laboratory measurements and theoretical analyses of DMS oxidation that provide a mechanistic description for OCS production from hydroperoxymethyl thioformate, a ubiquitous, soluble DMS oxidation product. We incorporate this chemical mechanism into a global chemical transport model, showing that OCS production from DMS is a factor of 3 smaller than current estimates, displays a maximum in the tropics consistent with field observations and is sensitive to multiphase cloud chemistry.

2.1 Introduction

Carbonyl sulfide (OCS) is the most abundant sulfur-containing gas in Earth's atmosphere with an estimated lifetime of greater than 2 years (Brühl et al., 2012; Chin & Davis, 1993a; Montzka et al., 2007). In the stratosphere, OCS is a principal precursor to sulfate aerosol which plays a critical role in Earth's radiation budget and can serve to catalyze heterogeneous reactions with importance to stratospheric ozone chemistry (Crutzen, 1976; Solomon et al., 1986). In the troposphere, OCS is readily consumed by the terrestrial biosphere, and has proven to be an effective tool for estimating gross primary production (GPP) (Asaf et al., 2013).

Despite the importance of OCS to stratospheric chemistry and its utility for estimating GPP, the magnitude and spatial distribution of OCS sources remain poorly constrained (Kremser et al., 2016; Ma et al., 2021). It has been shown that OCS is directly emitted to the atmosphere from oceans (Von Hobe et al., 2001), wetlands (Watts, 2000), and anoxic soils (Devai & DeLaune, 1995), is formed chemically in the atmosphere through the oxidation of dimethyl sulfide (DMS) (Barnes et al., 1994) and carbon disulfide (CS_2) (Chin & Davis, 1993b), and is released through a wide variety of anthropogenic activities (Zumkehr et al., 2018).

Recent isotopic and inverse modeling studies indicate that the marine environment is the dominant source region for OCS and that there is either an over-estimation of the terrestrial OCS sink or an unaccounted-for OCS source that seems to be centered in the tropical oceans based on atmospheric inversion studies (Berry et al., 2013; Davidson et al., 2021; Ma et al., 2021). In response to recent suggestions that the production of OCS from the OH-initiated oxidation of DMS may be a significant source of uncertainty in the OCS budget (Davidson et al., 2021; Ma et al., 2021) and new discoveries of the chemical mechanism of DMS oxidation (Berndt et al., 2019; Novak et al., 2021; Veres et al., 2020; Wu et al., 2015), we revisit here the chemical mechanism for OCS production in the oxidation of DMS.

Most existing global OCS emission inventories use a uniform yield (0.7%) to calculate OCS production (P_{OCS}) from DMS ocean emissions (E_{DMS}) (i.e. for E_{DMS} = 22 TgS yr^{-1}, P_{OCS} = 0.155 TgS yr^{-1}) (e.g. Kettle et al., 2002). The OCS yield from the OH-initiated oxidation of DMS originates from the early laboratory studies of Barnes et al. (1994) where the production of OCS was attributed to the photo-oxidation of thioformaldehyde (H_2CS), a product of peroxy radical ($RO_2\cdot$) bimolecular chemistry **(Figure 2.1).** Due to limitations in the analytical techniques available at the time, it was necessary to conduct these experiments at high precursor

concentrations which are not representative of typical marine conditions. The experimental conditions resulted in large $RO_2\cdot$ concentrations that over-emphasized bimolecular chemistry ($RO_2\cdot+RO_2\cdot$), thus shortening the lifetime of $RO_2\cdot$ ($\tau(RO_2\cdot)_{bimol} < 5$ s) at the expense of isomerization chemistry that is expected to dominate under pristine marine conditions. Recently, it has been shown that the methylthiomethyl peroxy radical radical (MTMP, $CH_3SCH_2O_2\cdot$), the primary peroxy radical formed following H-abstraction of DMS, efficiently isomerizes to a stable intermediate, hydroperoxymethyl thioformate (HPMTF, $HOOCH_2SCH{=}O$) which has been observed to be ubiquitous in marine environments (Berndt et al., 2019; Veres et al., 2020; Vermeuel et al., 2020; Wu et al., 2015; Ye et al., 2021). Given the key role of unimolecular isomerization and secondary chemistry in the oxidation of DMS, that was suppressed in previous experiments, it is essential to revisit the formation of OCS under conditions (i.e. $\tau(RO_2\cdot)_{bimol} > 100$ s) that accurately represent the marine environment.

Here, we present laboratory measurements of DMS oxidation conducted under dark, low RO_2 and NO_x-free conditions to determine the oxidation mechanism and reaction intermediates in the chemical trajectory that connects DMS emissions with OCS formation. Our experiments, supported by new quantum chemical and theoretical kinetic calculations on the extended HPMTF chemistry, show that OCS is formed in high yield in the OH oxidation of HPMTF. These results underscore that modeling global OCS formation from DMS oxidation as a single fixed yield is inconsistent with the current understanding of DMS oxidation chemistry that proceeds through several stable, soluble intermediates and their specific chemistry including removal *via* multiphase processes (Hoffmann et al., 2016; Novak et al., 2021; Veres et al., 2020). We incorporate a simplified version of the chemical mechanism developed here into a global chemical transport model to quantify P_{OCS} and its response to HPMTF cloud chemistry that sequesters HPMTF and

limits P_{OCS} in the cloudy marine boundary layer. We show that the multiphase and chemical mechanism-based approach results in a lower OCS global production rate with a spatial and temporal emission pattern different from the fixed-yield approach.

2.2 Methods

Detection and quantification of trace gases was conducted using two Chemical Ionization Mass Spectrometers (CIMS), an Aerodyne Compact Time of Flight CIMS (C-ToF) utilizing iodine ion chemistry (Bertram et al., 2011) and an Aerodyne/TOFWERK Vocus - Proton Transfer Reaction Time of Flight Mass Spectrometer (Vocus) (Krechmer et al., 2018). A custom-built laser-induced fluorescence (LIF) spectrometer (Rickly et al., 2021; Rollins et al., 2016) and a Los Gatos Research Enhanced Performance OCS analyzer (Berkelhammer et al., 2016) were used to detect sulfur dioxide (SO_2) and OCS, respectively. DMS and methane thiol (MeSH), used for instrument calibrations and the environmental chamber experiments, were supplied from compressed gas cylinders (Praxair, DMS at 5.08 ppm in N_2 and Airgas, MeSH at 6.11 ppm in N_2) diluted to the target concentration. The sensitivity of the C-ToF toward HPMTF was determined to be 5 ncps $pptv^{-1}$ using a flow reactor experiment previously described in the SI of Vermeuel et al. (2020) and was further verified by sulfur mass balance in the environmental chamber. For molecules identified in the Iodine CIMS mass spectrum, where commercially available standards were not available, absolute sensitivities were determined using the calculated binding enthalpy to iodine as described in Iyer et al (2016). Species identified in the Vocus - PTR mass spectrum, where commercially available standards were not available, were assigned absolute sensitivities by relating their literature proton affinity to those of species calibrated by liquid or cylinder methods (e.g. DMS, DMSO, acetone, and TME). Limits of detection (LOD) of HPMTF and OCS were determined to be 0.53 pptv and 2.21 pptv following the method of Bertram et al. (2011), at an integration time

of 25 and 300 seconds, respectively. Chamber experiments were run in a 0.6 m^3 5 mil (mil, 0.001 of an inch) PFA environmental chamber under ambient temperature (298 ± 1 K) and low relative humidity (<0.5% RH). The theoretical study is based on quantum chemical calculations at the CCSD(T)/aug-cc-pV(Q+d)Z//M06-2X-D3/aug-cc-pV(T+d)Z level of theory, combined with transition state theory and RRKM-master equation calculations incorporating all conformers. Detailed discussion of the experimental and theoretical methods can be found in the Chapter 1.

2.3 Production of OCS in the low-NO_x oxidation of DMS

To investigate the mechanism for OCS production from DMS under typical marine conditions, we conducted a series of dark, continuous flow environmental chamber experiments focused on the OH-initiated oxidation of DMS. Experiments were conducted at oxidant concentrations representative of the pristine marine environment ($[HO_x] \equiv [HO_2\cdot]+[\cdot OH]$ and $[NO_x] \equiv [NO]+[NO_2]$ <10 pptv, $[RO_2\cdot] < 150$ ppt and $\tau(CH_3SCH_2O_2\cdot)_{bimol} > 100$ s) (Creasey et al., 2003; Lee et al., 2009; Vaughan et al., 2012). Hydroxyl radicals (·OH) were generated by the ozonolysis of tetramethyl ethylene (TME). Dry synthetic air conditions (<0.5% RH, 80% N_2/ 20% O_2) were used to facilitate higher yields of ·OH from TME ozonolysis ($Y_{OH} > 0.8$) and to mitigate chamber wall losses (Alam et al., 2013; Donahue et al., 1998).

In our experiments, we observe consistent and reproducible (N=7) production of OCS in the OH-oxidation of DMS under oxidative conditions representative of the pristine marine atmosphere (**Figure 2.2a)**. As discussed below, OCS production in our experiment cannot be attributed solely to the photo-oxidation of H_2CS as previously suggested or experimental artifacts (**Figure 2.1**). We stress that the absolute fraction of OCS formed from DMS in this or any chamber study is specific to the experimental conditions of the environmental chamber (e.g., the fraction of

second generation products that are oxidized) and not directly applicable to all atmospheric conditions as P_{OCS} from DMS oxidation is a function of: 1) the temperature-dependent fraction of DMS that is oxidized to MTMP, 2) the fraction of MTMP that forms HPMTF, a function of the temperature-dependent MTMP isomerization rate, [NO], [HO_2·], and [RO_2·] and 3) the fraction of HPMTF that is lost to chemical reaction with OH, which we suggest to be the dominant pathway for the gas-phase production of OCS from DMS. It has also been suggested that photolysis of the peroxide group in HPMTF could lead to OCS formation (Khan et al., 2021). To generalize the experiments described here, we use a chemical box model constrained by experimental observations and theoretical kinetic calculations to examine the chemical mechanism that leads to OCS formation in the OH-oxidation of DMS and develop a simplified mechanistic model for OCS production that can be incorporated into global chemical transport models to more accurately describe DMS-derived OCS production.

2.4 Chemical Mechanism for OCS production in the OH-oxidation of DMS

We examined three possible gas-phase pathways for OCS formation from DMS in our experiments: 1) OH-oxidation of H_2CS, a product of MTMP bimolecular chemistry, 2) direct OCS formation from the OH-oxidation of HPMTF, a product of MTMP isomerization, and 3) OCS production from the oxidation of stable products of HPMTF OH-oxidation, such as thioformic anhydride (TFA) and thioperformic acid (TPA).

The production of OCS from the oxidation of H_2CS was originally suggested by Barnes et al. (1994), where H_2CS was proposed to be formed in the reaction of the methylthiyl (CH_3S·) radical and O_2, where CH_3S· is a prompt product of the reaction of MTMP with HO_2, RO_2, or NO (Barnes et al., 1996; Mardyukov & Schreiner, 2018; Yin et al., 1990). To evaluate the potential for the OH-oxidation of CH_3S· to produce OCS, we examined the OH-oxidation of methane thiol

(MeSH) as this reaction proceeds predominantly *via* H-abstraction leading to prompt and near unit yield of $CH_3S\cdot$, providing a clean test for the production of OCS from MTMP bimolecular chemistry. In the MeSH experiments, also conducted under low NO_x and $RO_2\cdot$ conditions, no OCS production was observed (**Figure 5.4a of chapter 3**) indicating that the OCS observed in the DMS experiment is not formed through MTMP bimolecular chemistry. This is supported by the work of Chen et al. (Chen et al., 2021), who also found that $CH_3S\cdot$ oxidizes to SO_2 in near unit yield and not H_2CS, a potential precursor to OCS.

The first-generation production of OCS from the OH-oxidation of HPMTF has only been studied theoretically, where the thermal OCS yield was previously calculated to be insignificant (<0.01%)(Wu et al., 2015). Here we revisit the production of OCS in the OH-oxidation of HPMTF using both experimental and theoretical tools. We first determine the rate constant for HPMTF+OH ($k_{HPMTF+OH}$), a key fundamental step that connects DMS and OCS, using a 0-D box model that incorporates the Master Chemical Mechanism (MCM) v3.3.1 in the Framework for 0-D Atmospheric Modeling (F0AM) (Jenkin et al., 1997; Saunders et al., 2003; Wolfe et al., 2016), constrained by chamber observations. In addition to the measurements of [HPMTF], we use measurements of dimethyl sulfoxide (DMSO) to constrain the fraction of DMS lost to the OH-addition channel (41%, consistent with known kinetics), methyl thioformate (MTF) to determine the $RO_2\cdot$ concentration and MTMP bimolecular reaction rates (see SI for more information), and OCS and SO_2 to constrain the terminal products of DMS oxidation within the model (**Figure 2.2b,c**). HPMTF production and loss rates were added to the existing MCM DMS oxidation mechanism and optimized to match observations, as discussed below. HPMTF production from MTMP involves a two-step isomerization mechanism that is rate-limited by the first H-shift (k_{isom}) that has been both calculated theoretically ($k_{isom,\ Veres}$ (293 K) = 0.041 s^{-1}, $k_{isom,\ Wu}$ (293 K) = 2.1 s^{-}

^{1}) (Veres et al., 2020; Wu et al., 2015) and experimentally determined ($k_{isom,\ Berndt}$ (295 K) = 0.23 ± 0.12 s^{-1}, $k_{isom,\ Ye}$ (293 K) = 0.09 (0.03 – 0.3) s^{-1}, $k_{isom,\ this\ study}$ (298 K) = 0.1 ± 0.05 s^{-1}) (Berndt et al., 2019; Ye et al., 2021). To determine $k_{HPMTF+OH}$ from the constrained box-model, we set k_{isom} = 0.1 s^{-1}. HPMTF loss is driven by: 1) gas-phase reaction with OH ($k_{HPMTF+OH}$,), 2) wall loss processes, and 3) chamber dilution intrinsic to a continuous flow regime. Using the box-model, constrained by the HPMTF growth curve and steady state concentration, and concentrations of other known sulfur species (DMS, DMSO, MTF, SO_2), $k_{HPMTF+OH}$ was determined to be 1.4 (0.27 – 2.4) × 10^{-11} cm^3 $molec^{-1}$ s^{-1}, where the range in $k_{HPMTF+OH}$ is based on propagation of all sources of systematic uncertainty in the experiment (**section 2.S1**). The experimentally determined rate ($k_{HPMTF+OH}$) is an order of magnitude faster than the theoretical rate originally proposed by Wu et al (2015), but within uncertainty of the experimentally-determined rate for the structurally similar molecule, methyl thioformate (k_{MTF+OH} = 1.11 ± 0.22 × 10^{-11} cm^3 $molec^{-1}s^{-1}$) and the theoretical rate determined in this study ($k_{HPMTF+OH}$ (298K) = 0.68 × 10^{-11} cm^3 $molec^{-1}$ s^{-1}). Additional chamber experiments performed to isolate the isomerization rate, HPMTF + OH loss rate, the sulfur product distribution, and model description are discussed in the SI.

In the OH-oxidation of HPMTF, we suggest that OCS can be formed as either a direct, first-generation product of HPMTF+OH, proceeding from the H-abstraction of the aldehydic hydrogen and the prompt decomposition of $HOOCH_2SC{\cdot}=O$ or as a multi-generational product following the OH-oxidation of the HPMTF reaction products thioformic anhydride (TFA, CHOSCHO) or thioperformic acid (TPA, HC(=S)OOH).

We first treat OCS formation empirically, using a simplified model where we determine the net OCS branching fraction from HPMTF+ ·OH ($\phi_{OCS} = 13\%$) required to sustain the measured OCS (**Figure 2.2a**). Uncertainty in the determination of ϕ_{OCS} ($8.5\% < \phi_{OCS} < 49\%$)

is dependent on the accuracy of the MTMP isomerization rate (k_{isom}) used to determine $k_{HPMTF+OH}$ (see SI). This analysis simplifies the chemical mechanism for inclusion in global models but does not permit correct accounting for multi-generational OCS production from TFA or TPA.

To further examine the multi-generational OH-oxidation of HPMTF, we also developed an extensive temperature dependent mechanistic framework for HPMTF oxidation to OCS based on theoretical kinetic calculations. Results from the multi-generational mechanistic model are also shown in **Figure 2.2**, where modeled steady-state [OCS] agrees to within a factor of two of the experimental measurement and a mechanistic pathway to describe the formation of TPA, observed in our study, is introduced. The pure theory-based multi-generation model does well to describe [OCS] and the existence of TPA, but additional chemistry or optimizations need to be introduced to fully capture the prompt formation of OCS and TPA, and the yield of SO_2 (**Figure 2.2b**). Remaining differences between the model prediction and the experiment could be due to reactions of the highly soluble intermediates occurring on the Teflon chamber walls, although these are expected to be suppressed due to the low relative humidity (< 0.5%) and the omission of gas-phase reactions of ozone with radical intermediates (e.g., $HOOCH_2S\cdot + O_3$) in the theoretical mechanism. It is important to note here that the gas-phase production of OCS from DMS proceeds through three very soluble species (HPMTF, TFA and TPA), the condensed phase chemistry of which is currently unknown, and likely significantly modulates the production of OCS from DMS in regions with high aerosol surface area or cloud cover. A more detailed discussion of model-measurement uncertainty, limitations in $k_{HPMTF+OH}$ and ϕ_{OCS} and the theoretical HPMTF mechanism can be found in the supplemental.

2.5 Global Estimates of OCS Production from DMS Oxidation

Global OCS production is modelled based on the simplified mechanism-based approach involving only first-generation HPMTF chemistry, i.e. $P_{OCS} = \phi_{OCS} \times k_{OH+HPMTF}[HPMTF][OH]$, where $k_{OH+HPMTF}$ is 1.4 × 10^{-11} cm^3 $molec^{-1}$ s^{-1} and $\phi_{OCS} = 13\%$. This approach is compared with the existing, fixed-yield model where $P_{OCS} = Y_{OCS} \times L_{DMS}$, Y_{OCS} = 0.7% and L_{DMS} is the loss rate of DMS to reaction with OH or $k_{DMS+OH}[OH][DMS]$. We used the GEOS-Chem global chemical transport model with an expanded DMS oxidation mechanism and model updates to halogen chemistry and cloud processing (Holmes et al., 2019; Novak et al., 2021; Veres et al., 2020; Wang et al., 2019, 2021) (version 12.9.2, www.geos-chem.org, see SI for more details). As shown in **Figure 2.3a**, the mechanism-based approach for calculating P_{OCS} (shown in red) results in a dramatic increase in the OCS source term from DMS oxidation (P_{OCS} = 680.1 GgS yr^{-1}) compared with the traditional, fixed-yield approach (green line, P_{OCS} = 106.1 GgS yr^{-1}). In the fixed-yield case P_{OCS} directly tracks DMS and OH concentrations, with enhancements in the Southern Ocean (Lana et al., 2011) (**Figure 2.4a,b**). In contrast, results from the mechanism-based scenario indicate strong OCS production in the tropics that is associated with warmer temperatures that favor HPMTF formation and thus OCS production.

As noted above, it is well established that soluble molecules such as HPMTF are efficiently removed from the atmosphere *via* uptake to clouds and aerosol particles and through surface deposition. Vermeuel et al. (2020) and Novak et al. (2021), showed that cloud-loss can be a dominant sink for HPMTF in the marine boundary layer. In the context of the OCS budget, efficient cloud-loss of HPMTF likely terminates OCS production, setting up a competition between OH driven gas-phase chemistry that yields OCS and multiphase chemistry that likely suppresses OCS production from HPMTF. Here, we assume that the condensed phase chemistry

of HPMTF, TFA, and TPA leads to sulfate (SO_4^{2-}) formation, although the condensed-phase chemistry of these intermediates is currently unknown and could lead to aqueous OCS production. To assess the impact of multiphase chemistry on OCS production from HPMTF, we utilize the entrainment-limited cloud loss parameterization developed by Holmes et al. (2019). As discussed in Novak et al. (2021), we find that multiphase chemistry has an irreversible and significant impact on [HPMTF] suppressing OCS production. The addition of HPMTF multiphase chemistry reduces P_{OCS} from 680.1 to 52.9 Gg S yr^{-1} with the largest differences found in regions of high cloud cover at high latitudes (Eastman et al., 2011; King et al., 2013) (**Figure 2.3a**). When compared to the fixed yield approach (**Figure 2.4a,b**), P_{OCS} derived from the HPMTF-based chemical mechanism (**Figure 2.4c,d**) is significantly lower in the Southern Ocean, where consistent cloud cover irreversibly sequesters HPMTF and limits OCS production. In all cases, the annual trend in P_{OCS} reflects seasonal differences in E_{DMS} and [·OH], where P_{OCS} peaks in January in the Southern Ocean, July in the North Atlantic, and nearly constant in the equatorial Pacific (**Figure 2.3b**). The meridional distribution of P_{OCS}, where P_{OCS} is largest in the tropics (**Figure 2.3b,** blue line), agrees qualitatively with the *a posteriori* marine OCS source found by Ma et al. (2021), which is markedly different than that derived from the fixed-yield approach (**Figure 2.3b**, green line).

Uncertainty in the marine OCS source has long hindered quantitative budget closure and obscured interpretation of historical trends in OCS (Campbell et al., 2017). Our study provides a critical constraint on the DMS-derived source of OCS, which previously was believed to account for over half of the marine OCS flux with CS_2 oxidation and direct emissions accounting for the residual marine sources. While this new work places a more concentrated source in the tropical oceans - consistent with the location of the expected missing OCS source (Berry et al., 2013) - the study suggests a smaller overall OCS flux from the ocean which is inconsistent with recent

suggestions that this source has generally been underestimated in global budgets (Launois et al., 2015; Ma et al., 2021). Consequently, the work raises important questions on whether the magnitude of the other marine sources such as CS_2 and direct emissions (Lennartz et al., 2021) are underestimated as suggested by Launois et al. (2015), or whether the land sink is overestimated. While the global analysis presented here significantly advances the representation OCS production from DMS, further refinement of the marine OCS source term will require detailed laboratory studies of HPMTF oxidation in the gas and condensed phase and assessment of multiphase cloud chemistry in global models.

Acknowledgements

This work was supported by the NSF Center for Aerosol Impacts on Chemistry of the Environment under Grant CHE 1801971. C.H.F. and C.D.H. acknowledge support by the Future Investigators in NASA Earth and Space Science and Technology program (80NSSC19K1368) and NASA New Investigator Program (NNX16AI57G).

Open research

Experimental and model outputs from chamber experiment and a list of differential equations used to generate the model outputs for the first and multi-generational mechanism are archived at http://digital.library.wisc.edu/1793/82416 on the MINDS@UW databasehttps://minds.wisconsin.edu/. The quantum chemical data is deposited under https://doi.org/10.26165/JUELICH-DATA/4JCZ9O. Version 12.9.2 of the GEOS-Chem global chemical transport model was used in this analysis and can be found at www.geos-chem.org.

2.S1 Uncertainty in the calculated $k_{HPMTF+OH}$ and ϕ_{OCS}

In this experiment, we calculate $k_{HPMTF+OH}$ and ϕ_{OCS} by minimizing the error between modeled and measured concentrations of HPMTF when the experiment has reached steady state. The accuracy of our calculation of $k_{HPMTF+OH}$ and ϕ_{OCS} is primarily sensitive to uncertainty in: 1) k_{wall} and k_{dil} as they compete with $k_{HPMTF+OH}$ × [OH] as the primary terms in $L_{HPMTF,}$ 2) the fraction of methylthiomethylperoxy radical (MTMP; $CH_3SCH_2O_2$•) that forms HPMTF, a function of [RO_2] and k_{isom} and 3) CIMS sensitivity to HPMTF as this determines $[HPMTF]_{meas}$. Uncertainty in the other terms in the MCM model do not contribute significantly to uncertainty in $k_{HPMTF+OH}$ and ϕ_{OCS}. In what follows we assess uncertainty in each of these terms.

2.S1.1 Uncertainty in k_{wall} and k_{dil}

In our experiment, the main HPMTF loss processes are wall loss (k_{wall} = $k_{wall,\ multi}$ × $\frac{c^*}{c_w}$ s^{-1}, see **Table 1.2**), dilution (k_{dil} = 9.7 ± 0.5 × 10^{-5} s^{-1}), and reaction with OH ($k_{OH+HPMTF}$ × [OH] = 3.0 × 10^{-5} s^{-1} for $k_{OH+HPMTF}$ = 2.1 × 10^{-11} cm^3 $molecule^{-1}$ s^{-1}). As a result, determination of $k_{OH+HPMTF}$ × [OH] relies on accurate assessment of k_{wall} and k_{dil}. The wall loss term, described in **Section 1.3 of Chapter 1**, is derived using the recommendations of Krechmer et al, (2016) and the c* value calculated using the SIMPOL technique described by Pankow and Asher 2007. Three terms drive the derived wall loss term: 1) $k_{wall,\ multi,}$ 2) saturation vapor pressure (c^*, μg m^{-3}) and 3) the equivalent organic mass concentration of the walls (c_w, μg m^{-3}). The model uses the $k_{wall,\ multi}$ to describe the rate of collisions with and off the wall. As this term is used to describe both the wall loss and the wall outgassing, the exact rate of the $k_{wall,\ multi}$ value does not make a significant difference. An order of magnitude in either direction of this value makes no change on the final value of HPMTF, nor a significant change in the rise curve. The second term c^* was derived from

a theoretically derived vapor pressure of HPMTF from the group contribution method SIMPOL(Pankow & Asher, 2008). As the exact vapor pressure or wall term could not be experimentally derived, this method was used to provide a best guess for the wall loss term. The SIMPOL method states a ±30% error for the 100 compounds it compared literature values to SIMPOL values. We used this general value to access the error associated with the c* value. The final term, c_w, was derived from the recommendation of Krechmer et al. (2016) and its relationship to c* is where most of the uncertainty in the wall loss term arises. Using the 30% error from the c* value and the lower extreme for the calculation of c_w within Krechmer et al. (2016), the lower extreme for the $\frac{c^*}{c_w}$ term is 5. The corresponding calculated $k_{HPMTF+OH}$ = 0.8 ± 0.3 × 10^{-11} cm^3 $molecule^{-1}$ s^{-1} and ϕ_{OCS} = 20.6 ± 5.0% (Compared to the recommended values of $k_{HPMTF+OH}$ = 1.4 ± 0.4 × 10^{-11} cm^3 $molecule^{-1}$ s^{-1} and ϕ_{OCS} = 13 ± 3%). The upper end of the $\frac{c^*}{c_w}$ term was 50, and as with values above 10, there were no significant changes in the HPMTF steady state value and calculated $k_{HPMTF+OH}$ and ϕ_{OCS}.

The dilution term was calculated from fitting the decay curve with a first-order exponential ($A = be^{-kt}$) of CO as it was diluted from the chamber. The uncertainty within the k_{dil} term was set by the range in values calculated across the 7 chamber experiments. The resulting uncertainty in the dilution term resulted in a deviation of the steady state HPMTF concentration of <10 ppt or an average deviation of 1% from the mean value. Given the low deviation in the HPMTF concentration, we presume the dilution term used to calculate the $k_{HPMTF+OH}$ and ϕ_{OCS} values are accurate and provide an insignificant source of uncertainty.

2.S1.2 Uncertainty in [RO_2] and k_{isom}

Based upon good experiment and model agreement of RO_2 derived species (Section 1.4 of Chapter 1), we can rely on the model to determine the steady state concentration of RO_2 within the chamber. Under the assumption that the model accurately predicts the RO_2 concentration, the uncertainty in the $k_{HPMTF+OH}$ and ϕ_{OCS} from RO_2 and k_{isom} can be evaluated. As shown, larger values of k_{isom} facilitate a larger production of HPMTF as the fraction of MTMP that partake in isomerization reactions increase relative to the bimolecular reaction with RO_2. The distinctive rise shape of the 10% error line on **Figure 1.3a-b** are indicative of the RO_2 concentration within the chamber and the corresponding fraction of MTMP that is forming HPMTF. At lower steady state concentrations of RO_2 within the chamber, the model and system become less sensitive to the isomerization rate constant as the unimolecular isomerization rate will always out compete the bimolecular RO_2 reaction. At higher RO_2 concentrations, the model and chamber become more sensitive to changes in the isomerization rate constant that is used. The concentration of RO_2 in the chamber at steady state is estimated to be 60 pptv (**Figure 1.5a**), resulting in reduced experimental sensitivity and mitigated variability in calculated $k_{HPMTF+OH}$ and ϕ_{OCS} to k_{isom} for values > 0.1 s^{-1} where isomerization reactions capturing >85% of the available MTMP and small changes in isomerization rates do not drastically impact P_{HPMTF}. This is made evident by the calculated $k_{HPMTF+OH}$ and ϕ_{OCS} for the $k_{isom,\ Veres}$ = 0.058 s^{-1}, $k_{isom,Ye}$ = 0.09 s^{-1}, and $k_{isom,Berndt}$ = 0.23 s^{-1} are 0.4 ± 0.3 × 10^{-11} cm^3 $molecule^{-1}$ s^{-1} and 36 ± 8%, 1.2 ± 0.3 × 10^{-11} cm^3 $molecule^{-1}$ s^{-1} and 15 ± 3.0%, and 2.1 ± 0.5 × 10^{-11} cm^3 $molecule^{-1}$ s^{-1} and 8.8 ± 2.0%, respectively. Current measurements and calculations of k_{isom} span 2 orders of magnitude ($k_{isom,\ Veres}$ = 0.058 s^{-1} - $k_{isom,\ Wu}$ = 2.1 s^{-1}) leading to orders of magnitude variations in the calculated $k_{HPMTF+OH}$ and ϕ_{OCS}. In our analysis, we derive $k_{HPMTF+OH}$ and ϕ_{OCS} for each k_{isom} value, and present $k_{HPMTF+OH}$ and ϕ_{OCS} using

k_{isom} measured in this study (see **section 2.S2**) as it is within uncertainty of the two current experimental values ($k_{isom,\ Berndt}$ (295 K) = 0.23 ± 0.12 s^{-1}, $k_{isom,\ Ye}$ (293 K) = 0.09 (0.03 – 0.3) s^{-1}) and the theoretical value of 0.1 s^{-1} calculated in this study (see **section 2.S2**).

2.S1.3 Uncertainty in CIMS HPMTF sensitivity (S_{HPMTF})

The primary component of the uncertainty in our calculated $k_{HPMTF+OH}$ and ϕ_{OCS}, for a given k_{isom}, stems from uncertainty in the HPMTF sensitivity used in calculating the concentration of HPMTF within the chamber. Based on mass balance, the HPMTF sensitivity is constrained to 4 – 6 ncps/pptv, as a sensitivity less than 4 ncps/pptv would lead to more oxidized sulfur than DMS lost and a sensitivity greater than 6 ncps/pptv would lead to >20% of the sulfur missing in the chamber. If the HPMTF measurement sensitivity (S_{HPMTF}) was the primary driver for uncertainty in the experiment, we can calculate $k_{HPMTF+OH}$ and ϕ_{OCS} as a function of S_{HPMTF} for a given k_{isom}. For S_{HPMTF} = 5 ncps/pptv and k_{isom} = 0.1 s^{-1}, as presented in the paper, $k_{HPMTF+OH}$ = 1.4 ± 0.4 × 10^{-11} cm^3 $molecule^{-1}$ s^{-1} and ϕ_{OCS} = 13 ± 3%. For S_{HPMTF} = 4 ncps/pptv, $k_{HPMTF+OH}$ = 2.4 ± 2.0 × 10^{-12} cm^3 $molecule^{-1}$ s^{-1} and ϕ_{OCS} = 49 ± 13%. For S_{HPMTF} = 6 ncps/pptv, $k_{HPMTF+OH}$ = 2.7 ± 0.5 × 10^{-11} cm^3 $molecule^{-1}$ s^{-1} and ϕ_{OCS} = 8.5 ± 1.9%. As a result, for k_{isom} = 0.1 s^{-1}, we conservatively estimate that $k_{HPMTF+OH}$ = 0.27 – 2.4 × 10^{-11} cm^3 $molecule^{-1}$ s^{-1} and ϕ_{OCS} = 8.5 - 49% based on uncertainty in S_{HPMTF}.

Taken collectively, uncertainty in the CIMS sensitivity is the largest contributor to uncertainty in $k_{HPMTF+OH}$ and ϕ_{OCS} for a given k_{isom}. In **Figure 2.S1**, we show the dependence of the calculated HPMTF + OH rate constant ($k_{HPMTF+OH}$) and OCS yield (ϕ_{OCS}) on the model HPMTF isomerization rate (k_{isom}). **Figure 2.S1a** presents a heat map of the percent difference in HPMTF model and measurement, defined as $\varepsilon_{HPMTF} = \left|\frac{[HPMTF]_{Model} - [HPMTF]_{Exp}}{[HPMTF]_{Exp}}\right| \times 100\%$, as a

function of the prescribed $k_{OH+HPMTF}$ and k_{isom}, where the dark black region represents the region of strongest model-measurement agreement. We show, in **Figure 2.S1b,** the range in ϕ_{OCS} values as a function of the prescribed $k_{OH+HPMTF}$ and k_{isom}. The dominant form of uncertainty within the model and experiment is the uncertainty attributed to the HPMTF sensitivity (S_{HPMTF}), accounting for ~20%. The probable range in ϕ_{OCS} at a given k_{isom} is constrained by the 20% error line from **Figure S4a,** with the 20% derived from S_{HPMTF}.

2.S2 Determination of the MTMP isomerization rate (k_{isom})

Using the modeled [RO_2] during the first 1.5 hours of the experiment, a MTMP isomerization rate was calculated using a modified version of the calculation described in Crounse et al (2011). Under the pristine conditions achieved within our environmental chamber, the HO_2 concentration is so low that the HO_2 bimolecular reaction is insignificant in determining the fate of MTMP ($\tau_{MTMP+HO2}$ > 500s). The dominant reaction pathways for MTMP loss are bimolecular reactions with RO_2 and the isomerization self-reaction. We use measurements of methyl thioformate as an indicator of the MTMP + RO_2 reaction and HPMTF formation as the indicator of the isomerization reaction. Using the following set of equations, the isomerization reaction can be calculated as a function of the HPMTF, MTF production rates (P_{HPMTF} and P_{MTF}), $k_{MTMP+RO2,}$ the yield of MTF from the MTMP + RO_2 reaction (Y_{MTF}), the fraction of MTF production that results from MTMP+RO_2 reactions (α_{RO_2}) and the [RO_2] calculated in the previous section.

$$P_{HPMTF} = k_{iso}\,[MSP] \quad \text{E4}$$

$$P_{MTF} = \alpha_{RO_2} Y_{MTF}\, k_{MSP+RO_2}\,[MSP][RO_2] \quad \text{E5}$$

$$k_{iso} = \frac{P_{HPMTF}\, Y_{MTF}\, k_{MSP+RO_2}}{\left\{\frac{k_{AlkO_2+RO_2}\, Y_{Pinacol}\, \alpha}{P_{Pinacol}}\right\}^{1/2} P_{MTF}} \quad \text{E6}$$

Using a Monte-Carlo like method to account for the uncertainty in sensitivities of the different species as well as the uncertainty in the rate constants a distribution in HPMTF isomerization reaction was calculated.(Ye et al., 2021) The values and uncertainties for S_{HPMTF}, S_{MTF}, $S_{Pinacol}$, α_{RO_2}, α_{AlkO_2} are 5 ± 1.5, 1.98 ± 0.5, 5.25 ± 1.5, 0.85 ± 0.15, and 0.55 ± 0.10, respectively. **Figure 2.S2a-c** show the linear fit of MTF, HPMTF and pinacol used to calculate the production rate of the three species. **Figure 2.S2d** shows the distribution in values with a median isomerization value of 0.1 ± 0.05 s^{-1} (1σ of geometric mean). The isomerization value falls within the uncertainty of the current literature values of HPMTF isomerization as listed above, and is in excellent agreement with the theoretical value in this work. The majority of the uncertainty in the calculated HPMTF isomerization rate constant is due to the HPMTF sensitivity and corresponding production rate value. The square root dependence of the RO_2 calculation also mitigates its role as a major driver of uncertainty within the isomerization calculation.

2.S3 Global model implementations of DMS oxidation in GEOS-Chem

The GEOS-Chem global chemical transport model (version 12.9.2, www.geos-chem.org) (The International GEOS-Chem User Community, 2020) is used to simulate the global production of OCS from DMS oxidation. The DMS simulation was previously described by Novak et al. (2021). Briefly, simulations for 2017 and 2018 are run at 4° × 5° horizonal resolution with 72 vertical levels and meteorology is from NASA MERRA-2 (Modern-Era Retrospective Reanalysis for Research and Applications, Version 2 (Gelaro et al., 2017)). Anthropogenic and biomass burning emissions are from CEDS-2020v1 (McDuffie et al., 2020) and GFED4.1s(RANDERSON et al., 2017), respectively. Ocean DMS fluxes depend on a climatology of concentrations in seawater (Lana et al., 2011) and meteorology-driven gas exchange velocities (Johnson, 2010; Nightingale et al., 2000). The chemical mechanism for DMS oxidation was described by Novak

et al. (2021) using a rate constant of 1.11 x 10^{-11} cm^3 $molecule^{-1}$ s^{-1} for OH abstraction from HPMTF.

In the main text, we show three scenarios for production of OCS from DMS. In the fixed-yield approach, OCS is produced from DMS+OH reactions (addition and abstraction) with a molar yield of 0.7 % (Barnes et al., 1994). In the other two scenarios, OCS is produced from OH+HPMTF reactions with a prompt 13 % yield. Those scenarios differ by one of them including multiphase loss of HPMTF in clouds and aerosols (Holmes et al., 2019), which account for over 90% of HPMTF loss (Novak et al., 2021), while the other does not.

References

Alam, M. S., Rickard, A. R., Camredon, M., Wyche, K. P., Carr, T., Hornsby, K. E., Monks, P. S., & Bloss, W. J. (2013). Radical product yields from the ozonolysis of short chain alkenes under atmospheric boundary layer conditions. *Journal of Physical Chemistry A*, *117*(47), 12468–12483. https://doi.org/10.1021/jp408745h

Asaf, D., Rotenberg, E., Tatarinov, F., Dicken, U., Montzka, S. A., & Yakir, D. (2013). Ecosystem photosynthesis inferred from measurements of carbonyl sulphide flux. *Nature Geoscience*, *6*(3), 186–190. https://doi.org/10.1038/ngeo1730

Barnes, I., Becker, K. H., & Patroescu, I. (1994). The tropospheric oxidation of dimethyl sulfide: A new source of carbonyl sulfide. *Geophysical Research Letters*, *21*(22), 2389–2392. https://doi.org/https://doi.org/10.1029/94GL02499

Barnes, I., Becker, K. H., & Patroescu, I. (1996). FTIR product study of the OH intiated oxidation of dimethyl sulphide: Observation of carbonyl sulphide and imethyl sulphoxide. *Atmospheric Environment*, *30*(10–11), 1805–1814. https://doi.org/10.1016/1352-2310(95)00389-4

Berkelhammer, M., Steen-Larsen, H. C., Cosgrove, A., Peters, A. J., Johnson, R., Hayden, M., & Montzka, S. A. (2016). Radiation and atmospheric circulation controls on carbonyl sulfide concentrations in themarine boundary layer. *Journal of Geophysical Research*, *121*(21), 13,113-13,128. https://doi.org/10.1002/2016JD025437

Berndt, T., Scholz, W., Mentler, B., Fischer, L., Hoffmann, E. H., Tilgner, A., Hyttinen, N., Prisle, N. L., Hansel, A., & Herrmann, H. (2019). Fast Peroxy Radical Isomerization and OH Recycling in the Reaction of OH Radicals with Dimethyl Sulfide. *Journal of Physical Chemistry Letters*, *10*(21), 6478–6483. https://doi.org/10.1021/acs.jpclett.9b02567

Berry, J., Wolf, A., Campbell, J. E., Baker, I., Blake, N., Blake, D., Denning, A. S., Kawa, S. R., Montzka, S. A., Seibt, U., Stimler, K., Yakir, D., & Zhu, Z. (2013). A coupled model of the global cycles of carbonyl sulfide and CO 2: A possible new window on the carbon cycle. *Journal of Geophysical Research: Biogeosciences*, *118*(2), 842–852. https://doi.org/10.1002/jgrg.20068

Bertram, T. H., Kimmel, J. R., Crisp, T. A., Ryder, O. S., Yatavelli, R. L. N., Thornton, J. A., Cubison, M. J., Gonin, M., & Worsnop, D. R. (2011). A field-deployable, chemical ionization time-of-flight

mass spectrometer. *Atmospheric Measurement Techniques*, *4*(7), 1471–1479. https://doi.org/10.5194/amt-4-1471-2011

Brühl, C., Lelieveld, J., Crutzen, P. J., & Tost, H. (2012). The role of carbonyl sulphide as a source of stratospheric sulphate aerosol and its impact on climate. *Atmospheric Chemistry and Physics*, *12*(3), 1239–1253. https://doi.org/10.5194/acp-12-1239-2012

Campbell, J. E., Berry, J. A., Seibt, U., Smith, S. J., Montzka, S. A., Launois, T., Belviso, S., Bopp, L., & Laine, M. (2017). Large historical growth in global terrestrial gross primary production. *Nature*, *544*(7648), 84–87. https://doi.org/10.1038/nature22030

Chen, J., Berndt, T., Møller, K. H., Lane, J. R., & Kjaergaard, H. G. (2021). Atmospheric Fate of the CH3SOO Radical from the CH3S + O2 Equilibrium. *The Journal of Physical Chemistry A*, *125*(40), 8933–8941. https://doi.org/10.1021/acs.jpca.1c06900

Chin, M., & Davis, D. D. (1993a). Global sources and sinks of OCS and CS2 and their distributions. *Global Biogeochemical Cycles*, *7*(2), 321–337. https://doi.org/10.1029/93GB00568

Chin, M., & Davis, D. D. (1993b). Global sources and sinks of OCS and CS2 and their distributions. *Global Biogeochemical Cycles*, *7*(2), 321–337. https://doi.org/10.1029/93GB00568

Creasey, D. J., Evans, G. E., Heard, D. E., & Lee, J. D. (2003). Measurements of OH and HO2 concentrations in the Southern Ocean marine boundary layer. *Journal of Geophysical Research D: Atmospheres*, *108*(15), 1–12. https://doi.org/10.1029/2002jd003206

Crutzen, P. J. (1976). The possible importance of CSO for the sulfate layer of the stratosphere. *Geophysical Research Letters*, *3*(2), 73–76. https://doi.org/https://doi.org/10.1029/GL003i002p00073

Davidson, C., Amrani, A., & Angert, A. (2021). Tropospheric carbonyl sulfide mass balance based on direct measurements of sulfur isotopes. *Proceedings of the National Academy of Sciences of the United States of America*, *118*(6), 1–6. https://doi.org/10.1073/pnas.2020060118

Devai, I., & DeLaune, R. D. (1995). Formation of volatile sulfur compounds in salt marsh sediment as influenced by soil redox condition. *Organic Geochemistry*, *23*(4), 283–287. https://doi.org/10.1016/0146-6380(95)00024-9

Donahue, N. M., Kroll, J. H., Anderson, J. G., & Demerjian, K. L. (1998). Direct observation of OH production from the ozonolysis of olefins. *Geophysical Research Letters*, *25*(1), 59–62. https://doi.org/10.1029/97GL53560

Eastman, R., Warren, S. G., & Hahn, C. J. (2011). Variations in cloud cover and cloud types over the Ocean from surface observations, 1954-2008. *Journal of Climate*, *24*(22), 5914–5934. https://doi.org/10.1175/2011JCLI3972.1

Gelaro, R., McCarty, W., Su?rez, M. J., Todling, R., Molod, A., Takacs, L., Randles, C. A., Darmenov, A., Bosilovich, M. G., Reichle, R., Wargan, K., Coy, L., Cullather, R., Draper, C., Akella, S., Buchard, V., Conaty, A., da Silva, A. M., Gu, W., … Zhao, B. (2017). The Modern-Era Retrospective Analysis for Research and Applications, Version 2 (MERRA-2). *Journal of Climate*, *30*(14), 5419–5454. https://doi.org/10.1175/JCLI-D-16-0758.1

Hoffmann, E. H., Tilgner, A., Schrödner, R., Bräuer, P., Wolke, R., & Herrmann, H. (2016). An advanced modeling study on the impacts and atmospheric implications of multiphase dimethyl sulfide chemistry. *Proceedings of the National Academy of Sciences of the United States of America*, *113*(42), 11776–11781. https://doi.org/10.1073/pnas.1606320113

Holmes, C. D., Bertram, T. H., Confer, K. L., Graham, K. A., Ronan, A. C., Wirks, C. K., & Shah, V. (2019). The Role of Clouds in the Tropospheric NOx Cycle: A New Modeling Approach for Cloud Chemistry and Its Global Implications. *Geophysical Research Letters*, *46*(9), 4980–4990. https://doi.org/10.1029/2019GL081990

Iyer, S., Lopez-Hilfiker, F., Lee, B. H., Thornton, J. A., & Kurtén, T. (2016). Modeling the Detection of Organic and Inorganic Compounds Using Iodide-Based Chemical Ionization. *Journal of Physical Chemistry A*, *120*(4), 576–587. https://doi.org/10.1021/acs.jpca.5b09837

Jenkin, M. E., Saunders, S. M., & Pilling, M. J. (1997). The tropospheric degradation of volatile organic compounds: A protocol for mechanism development. *Atmospheric Environment*, *31*(1), 81–104. https://doi.org/10.1016/S1352-2310(96)00105-7

Johnson, M. T. (2010). A numerical scheme to calculate temperature and salinity dependent air-water transfer velocities for any gas. *Ocean Science*, *6*(4), 913–932. https://doi.org/10.5194/os-6-913-2010

Kettle, A. J., Kuhn, U., Von Hobe, M., Kesselmeier, J., & Andreae, M. O. (2002). Global budget of atmospheric carbonyl sulfide: Temporal and spatial variations of the dominant sources and sinks. *Journal of Geophysical Research Atmospheres*, *107*(22), 1–16. https://doi.org/10.1029/2002JD002187

Khan, M. A. H., Bannan, T. J., Holland, R., Shallcross, D. E., Archibald, A. T., Matthews, E., Back, A., Allan, J., Coe, H., Artaxo, P., & Percival, C. J. (2021). Impacts of Hydroperoxymethyl Thioformate on the Global Marine Sulfur Budget. *ACS Earth and Space Chemistry*, *5*(10), 2577–2586. https://doi.org/10.1021/acsearthspacechem.1c00218

King, M. D., Platnick, S., Menzel, W. P., Ackerman, S. A., & Hubanks, P. A. (2013). Spatial and temporal distribution of clouds observed by MODIS onboard the terra and aqua satellites. *IEEE Transactions on Geoscience and Remote Sensing*, *51*(7), 3826–3852. https://doi.org/10.1109/TGRS.2012.2227333

Krechmer, J., Lopez-Hilfiker, F., Koss, A., Hutterli, M., Stoermer, C., Deming, B., Kimmel, J., Warneke, C., Holzinger, R., Jayne, J., Worsnop, D., Fuhrer, K., Gonin, M., & De Gouw, J. (2018). Evaluation of a New Reagent-Ion Source and Focusing Ion-Molecule Reactor for Use in Proton-Transfer-Reaction Mass Spectrometry. *Analytical Chemistry*, *90*(20), 12011–12018. https://doi.org/10.1021/acs.analchem.8b02641

Kremser, S., Thomason, L. W., von Hobe, M., Hermann, M., Deshler, T., Timmreck, C., Toohey, M., Stenke, A., Schwarz, J. P., Weigel, R., Fueglistaler, S., Prata, F. J., Vernier, J.-P., Schlager, H., Barnes, J. E., Antuña-Marrero, J.-C., Fairlie, D., Palm, M., Mahieu, E., … Meland, B. (2016). Stratospheric aerosol—Observations, processes, and impact on climate. *Reviews of Geophysics*, *54*(2), 278–335. https://doi.org/https://doi.org/10.1002/2015RG000511

Lana, A., Bell, T. G., Simó, R., Vallina, S. M., Ballabrera-Poy, J., Kettle, A. J., Dachs, J., Bopp, L., Saltzman, E. S., Stefels, J., Johnson, J. E., & Liss, P. S. (2011). An updated climatology of surface dimethlysulfide concentrations and emission fluxes in the global ocean. *Global Biogeochemical Cycles*, *25*(1), 1–17. https://doi.org/10.1029/2010GB003850

Launois, T., Belviso, S., Bopp, L., Fichot, C. G., & Peylin, P. (2015). A new model for the global biogeochemical cycle of carbonyl sulfide – Part 1: Assessment of direct marine emissions with an oceanic general circulation and biogeochemistry model. *Atmos. Chem. Phys.*, *15*(5), 2295–2312. https://doi.org/10.5194/acp-15-2295-2015

Lee, J. D., Moller, S. J., Read, K. A., Lewis, A. C., Mendes, L., & Carpenter, L. J. (2009). Year-round measurements of nitrogen oxides and ozone in the tropical North Atlantic marine boundary layer. *Journal of Geophysical Research: Atmospheres*, *114*(D21). https://doi.org/https://doi.org/10.1029/2009JD011878

Lennartz, S. T., Gauss, M., von Hobe, M., & Marandino, C. A. (2021). Monthly resolved modelled oceanic emissions of carbonyl sulphide and carbon disulphide for the period 2000–2019. *Earth Syst. Sci. Data*, *13*(5), 2095–2110. https://doi.org/10.5194/essd-13-2095-2021

Ma, J., Kooijmans, L. M. J., Cho, A., Montzka, S. A., Glatthor, N., Worden, J. R., Kuai, L., Atlas, E. L., & Krol, M. C. (2021). Inverse modelling of carbonyl sulfide: Implementation, evaluation and implications for the global budget. *Atmospheric Chemistry and Physics*, *21*(5), 3507–3529. https://doi.org/10.5194/acp-21-3507-2021

Mardyukov, A., & Schreiner, P. R. (2018). Atmospherically Relevant Radicals Derived from the Oxidation of Dimethyl Sulfide. *Accounts of Chemical Research*, *51*(2), 475–483. https://doi.org/10.1021/acs.accounts.7b00536

McDuffie, E. E., Smith, S. J., O'Rourke, P., Tibrewal, K., Venkataraman, C., Marais, E. A., Zheng, B., Crippa, M., Brauer, M., & Martin, R. V. (2020). A global anthropogenic emission inventory of atmospheric pollutants from sector- and fuel-specific sources (1970--2017): an application of the Community Emissions Data System (CEDS). *Earth System Science Data*, *12*(4), 3413–3442. https://doi.org/10.5194/essd-12-3413-2020

Montzka, S. A., Calvert, P., Hall, B. D., Elkins, J. W., Conway, T. J., Tans, P. P., & Sweeney, C. S. (2007). On the global distribution, seasonality, and budget of atmospheric carbonyl sulfide (COS) and some similarities to CO<inf>2</inf>. *Journal of Geophysical Research Atmospheres*, *112*(9), 1–15. https://doi.org/10.1029/2006JD007665

Nightingale, P. D., Malin, G., Law, C. S., Watson, A. J., Liss, P. S., Liddicoat, M. I., Boutin, J., & Upstill-Goddard, R. C. (2000). In situ evaluation of air-sea gas exchange parameterizations using novel conservative and volatile tracers. *Global Biogeochemical Cycles*, *14*(1), 373–387. https://doi.org/https://doi.org/10.1029/1999GB900091

Novak, G. A., Fite, C. H., Holmes, C. D., Veres, P. R., Neuman, J. A., Faloona, I., Thornton, J. A., Wolfe, G. M., Vermeuel, M. P., Jernigan, C. M., Peischl, J., Ryerson, T. B., Thompson, C. R., Bourgeois, I., Warneke, C., Gkatzelis, G. I., Coggon, M. M., Sekimoto, K., Bui, T. P., … Bertram, T. H. (2021). Rapid cloud removal of dimethyl sulfide oxidation products limits SO 2 and cloud condensation nuclei production in the marine atmosphere. *Proceedings of the National Academy of Sciences*, *118*(42), e2110472118. https://doi.org/10.1073/pnas.2110472118

Pankow, J. F., & Asher, W. E. (2008). SIMPOL.1: A simple group contribution method for predicting vapor pressures and enthalpies of vaporization of multifunctional organic compounds. *Atmospheric Chemistry and Physics*, *8*(10), 2773–2796. https://doi.org/10.5194/acp-8-2773-2008

RANDERSON, J. T., VAN DER WERF, G. R., GIGLIO, L., COLLATZ, G. J., & KASIBHATLA, P. S. (2017). *Global Fire Emissions Database, Version 4.1 (GFEDv4)*. ORNL Distributed Active Archive Center. https://doi.org/10.3334/ORNLDAAC/1293

Rickly, P. S., Xu, L., Crounse, J. D., Wennberg, P. O., & Rollins, A. W. (2021). Improvements to a laser-induced fluorescence instrument for measuring SO2 - Impact on accuracy and precision. *Atmospheric Measurement Techniques*, *14*(3), 2429–2439. https://doi.org/10.5194/amt-14-2429-2021

Rollins, A. W., Thornberry, T. D., Ciciora, S. J., McLaughlin, R. J., Watts, L. A., Hanisco, T. F., Baumann, E., Giorgetta, F. R., Bui, T. V., & Fahey, D. W. (2016). A laser-induced fluorescence instrument for aircraft measurements of sulfur dioxide in the upper troposphere and lower stratosphere. *Atmospheric Measurement Techniques*, *9*(9), 4601–4613. https://doi.org/10.5194/amt-9-4601-2016

Saunders, S. M., Jenkin, M. E., Derwent, R. G., & Pilling, M. J. (2003). Protocol for the development of the Master Chemical Mechanism, MCM v3 (Part A): Tropospheric degradation of non-aromatic volatile organic compounds. *Atmospheric Chemistry and Physics*, *3*(1), 161–180. https://doi.org/10.5194/acp-3-161-2003

Solomon, S., Garcia, R. R., Rowland, F. S., & Wuebbles, D. J. (1986). On the depletion of Antarctic ozone. *Nature*, *321*(6072), 755–758. https://doi.org/10.1038/321755a0

Vaughan, S., Ingham, T., Whalley, L. K., Stone, D., Evans, M. J., Read, K. A., Lee, J. D., Moller, S. J., Carpenter, L. J., Lewis, A. C., Fleming, Z. L., & Heard, D. E. (2012). Seasonal observations of OH and HO2in the remote tropical marine boundary layer. *Atmospheric Chemistry and Physics*, *12*(4), 2149–2172. https://doi.org/10.5194/acp-12-2149-2012

Veres, P. R., Andrew Neuman, J., Bertram, T. H., Assaf, E., Wolfe, G. M., Williamson, C. J., Weinzierl, B., Tilmes, S., Thompson, C. R., Thames, A. B., Schroder, J. C., Saiz-Lopez, A., Rollins, A. W., Roberts, J. M., Price, D., Peischl, J., Nault, B. A., Møller, K. H., Miller, D. O., … Ryerson, T. B. (2020). Global airborne sampling reveals a previously unobserved dimethyl sulfide oxidation mechanism in the marine atmosphere. *Proceedings of the National Academy of Sciences of the United States of America*, *117*(9), 4505–4510. https://doi.org/10.1073/pnas.1919344117

Vermeuel, M. P., Novak, G. A., Jernigan, C. M., & Bertram, T. H. (2020). Diel Profile of Hydroperoxymethyl Thioformate: Evidence for Surface Deposition and Multiphase Chemistry. *Environmental Science and Technology*, *54*(19), 12521–12529. https://doi.org/10.1021/acs.est.0c04323

Von Hobe, M., Cutter, G. A., Kettle, A. J., & Andreae, M. O. (2001). Dark production: A significant source of oceanic COS. *Journal of Geophysical Research: Oceans*, *106*(C12), 31217–31226. https://doi.org/10.1029/2000jc000567

Wang, X., Jacob, D. J., Downs, W., Zhai, S., Zhu, L., Shah, V., Holmes, C. D., Sherwen, T., Alexander, B., Evans, M. J., Eastham, S. D., Neuman, J. A., Veres, P. R., Koenig, T. K., Volkamer, R., Huey, L. G., Bannan, T. J., Percival, C. J., Lee, B. H., & Thornton, J. A. (2021). Global tropospheric halogen (Cl, Br, I) chemistry and its impact on oxidants. *Atmos. Chem. Phys.*, *21*(18), 13973–13996. https://doi.org/10.5194/acp-21-13973-2021

Wang, X., Jacob, D. J., Eastham, S. D., Sulprizio, M. P., Zhu, L., Chen, Q., Alexander, B., Sherwen, T., Evans, M. J., Lee, B. H., Haskins, J. D., Lopez-Hilfiker, F. D., Thornton, J. A., Huey, G. L., & Liao, H. (2019). The role of chlorine in global tropospheric chemistry. *Atmospheric Chemistry and Physics*, *19*(6), 3981–4003. https://doi.org/10.5194/acp-19-3981-2019

Watts, S. F. (2000). The mass budgets of carbonyl sulfide, dimethyl sulfide, carbon disulfide and hydrogen sulfide. *Atmospheric Environment*, *34*(5), 761–779. https://doi.org/10.1016/S1352-2310(99)00342-8

Wolfe, G. M., Marvin, M. R., Roberts, S. J., Travis, K. R., & Liao, J. (2016). The framework for 0-D atmospheric modeling (F0AM) v3.1. *Geoscientific Model Development*, *9*(9), 3309–3319. https://doi.org/10.5194/gmd-9-3309-2016

Wu, R., Wang, S., & Wang, L. (2015). New mechanism for the atmospheric oxidation of dimethyl sulfide. The importance of intramolecular hydrogen shift in a CH3SCH2OO radical. *Journal of Physical Chemistry A*, *119*(1), 112–117. https://doi.org/10.1021/jp511616j

Ye, Q., Goss, M. B., Isaacman-VanWertz, G., Zaytsev, A., Massoli, P., Lim, C., Croteau, P., Canagaratna, M., Knopf, D. A., Keutsch, F. N., Heald, C. L., & Kroll, J. H. (2021). Organic Sulfur Products and Peroxy Radical Isomerization in the OH Oxidation of Dimethyl Sulfide. *ACS Earth and Space Chemistry*. https://doi.org/10.1021/acsearthspacechem.1c00108

Yin, F., Grosjean, D., Flagan, R. C., & Seinfeld, J. H. (1990). Photooxidation of dimethyl sulfide and dimethyl disulfide. II: Mechanism evaluation. *Journal of Atmospheric Chemistry*, *11*(4), 365–399. https://doi.org/10.1007/BF00053781

Zumkehr, A., Hilton, T. W., Whelan, M., Smith, S., Kuai, L., Worden, J., & Campbell, J. E. (2018). Global gridded anthropogenic emissions inventory of carbonyl sulfide. *Atmospheric Environment*, *183*(March), 11–19. https://doi.org/10.1016/j.atmosenv.2018.03.063

Figures and Tables

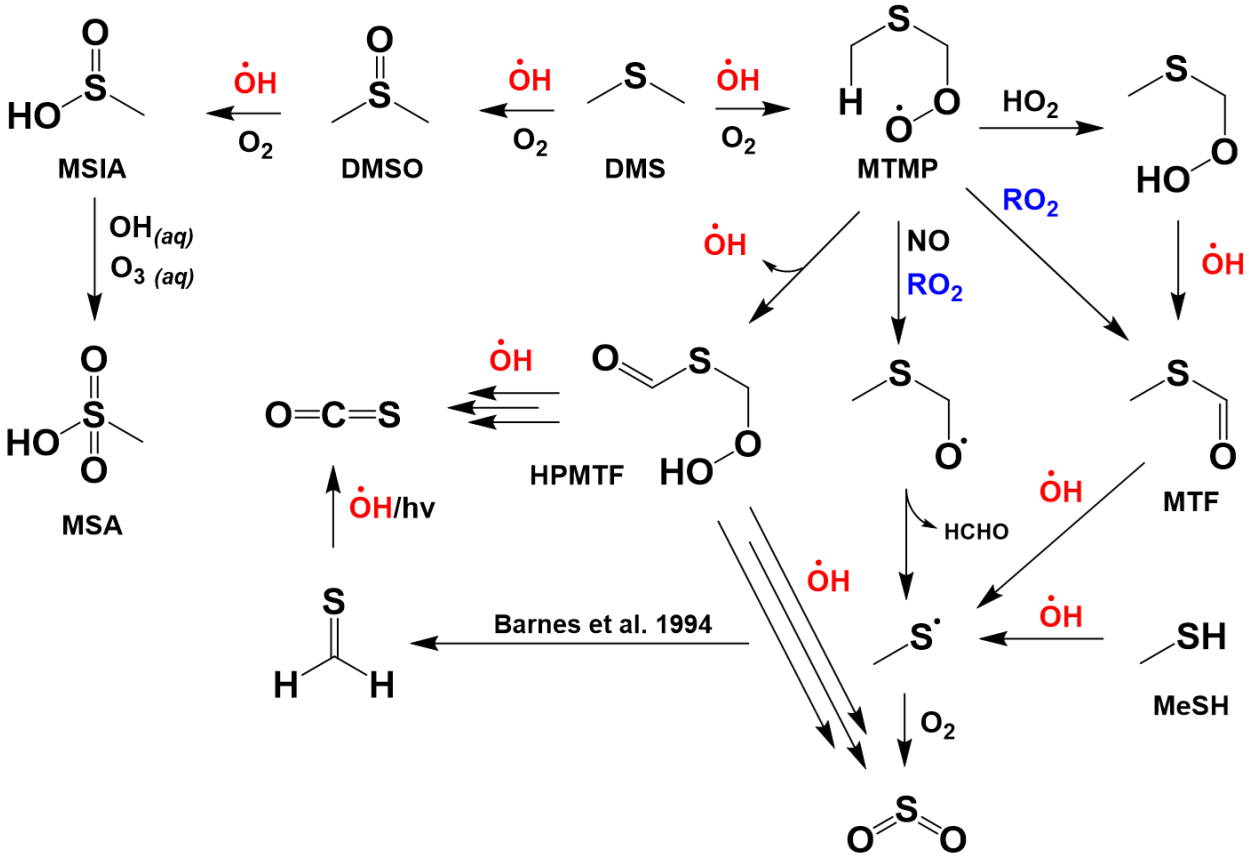

Figure 2.1: Chemical mechanism for the gas-phase OH-oxidation of dimethyl sulfide. Simplified chemical mechanism for the production of carbonyl sulfide (OCS) in the gas-phase OH-oxidation of dimethyl sulfide (DMS) and methanethiol (MeSH). The mechanism shown here combines the work of Barnes et al. (1994) and the HPMTF-derived OCS production pathway proposed here. The triplicate arrows pointing away from HPMTF denote multi-step mechanisms.

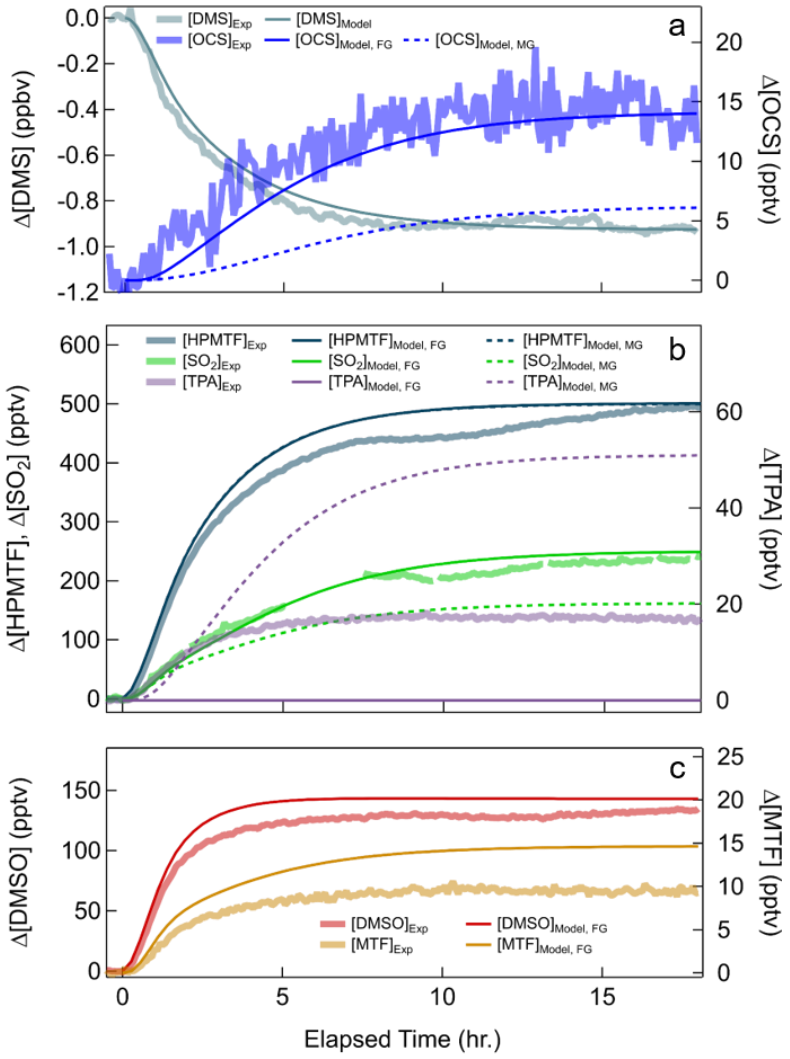

Figure 2.2: Laboratory measurements of OCS production from the OH-oxidation of DMS. Measurements (translucent thick lines) and first generational (FG, solid thin lines) and multi-generational (MG, dashed thin lines) model calculations of S-containing reaction products of the OH-oxidation of DMS. Measurements were conducted in an environmental chamber under low NO_x oxidation conditions. Reaction products include: carbonyl sulfide (OCS), hydroperoxymethyl thioformate (HPMTF), sulfur dioxide (SO_2), thioperformic acid (TPA), methyl thioformate (MTF), and dimethyl sulfoxide (DMSO).

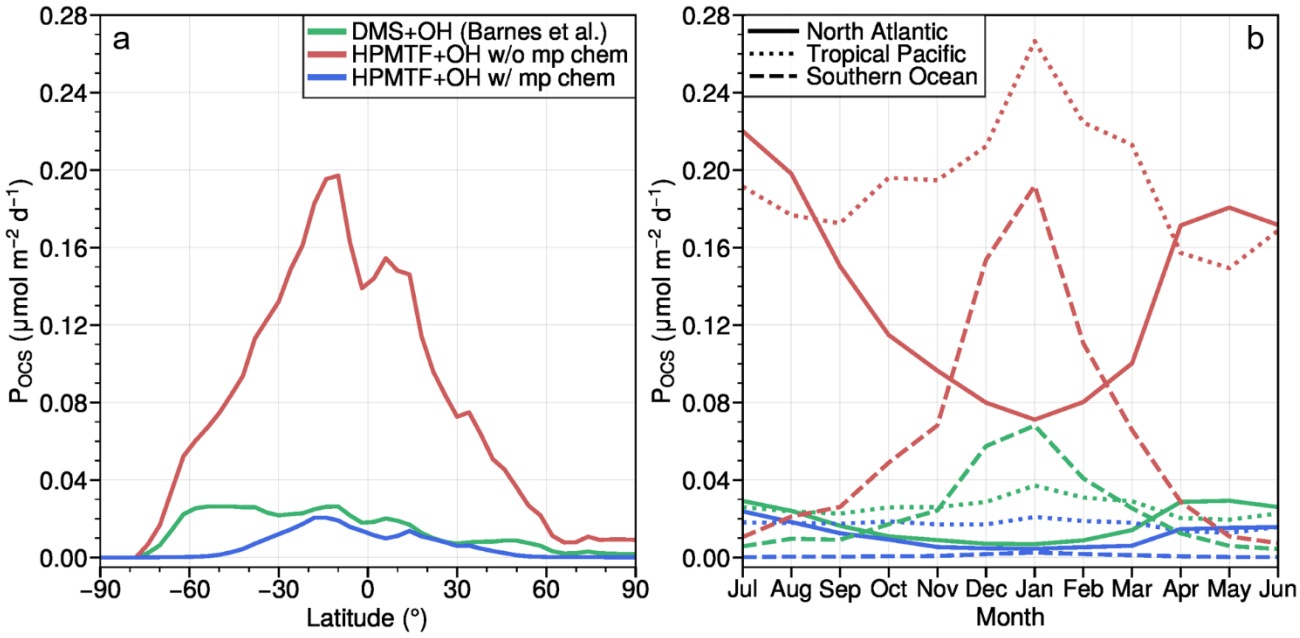

Figure 2.3: Modeled meridional and annual distribution of column OCS production from the oxidation of DMS. a, Modeled meridional distribution of OCS production (P_{OCS}). The green trace depicts P_{OCS} calculated as a fixed yield (0.7%) of total DMS emission, the red and blue traces incorporate the HPMTF-based OCS production mechanism for an OCS branching fraction ($\phi_{OCS} = 13\%$) in the HPMTF+ ·OH reaction with (blue) and without (red) multiphase chemistry. **b**, Modeled annual distribution of P_{OCS} for three marine regions for each of the three model representations of P_{OCS} shown in panel a. A map defining the three marine regions is shown in the **Figure 2.S3**.

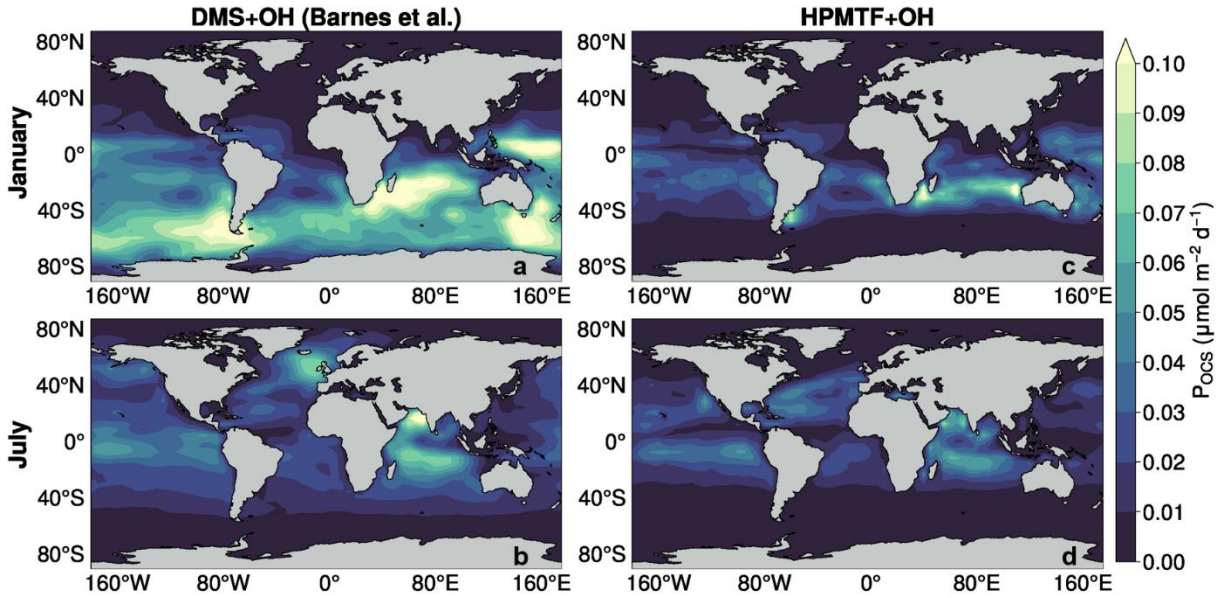

Figure 2.4: Global distribution of column OCS production from the oxidation of DMS. Modeled global distribution of OCS production (P_{OCS}) calculated as a fixed yield (0.7%) of total DMS emission (**a,b**) and the HPMTF-based P_{OCS} mechanism at a ϕ_{OCS} of 13% with multiphase chemistry (**c,d**) during the month of January (**b,d**) and July (**a,c**).

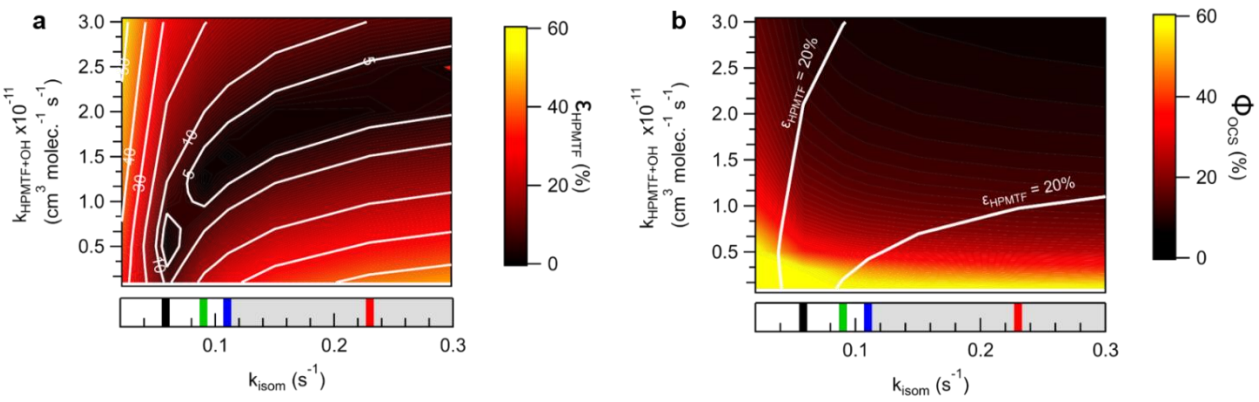

Figure 2.S1: Measurement constraints on the HPMTF + OH rate constant ($k_{OH+HPMTF}$) and the OCS yield from HPMTF + OH (ϕ_{OCS}). Panel a shows the error, defined as $\varepsilon_{HPMTF} = \left|\frac{[HPMTF]_{Model} - [HPMTF]_{Exp}}{[HPMTF]_{Exp}}\right| \times 100\%$, as a function of the prescribed $k_{OH+HPMTF}$ and k_{isom}, where the dark black region represents the region of highest certainty. As shown, $k_{OH+HPMTF}$ and ϕ_{OCS} depend strongly on k_{isom}, for which there have been five prior determinations: Veres et al. (2020)(0.04 s^{-1}, black bar), Ye et al (2021) (0.09 s^{-1}, green bar), this study (0.1 s^{-1}, blue bar), Berndt et al. (2019)(0.23 s^{-1}, red bar), and Wu et al. (2015)(2 s^{-1}, not shown). The gray shaded region represents the reported uncertainty of Berndt et al experimental value (a). The 20% error contour edges from panel a are shown in panel b, where the colorscale is the resulting OCS yield ($\phi_{OCS} = \frac{P(OCS)}{L_{chem}(HPMTF)}$) as a function of the prescribed model $k_{OH+HPMTF}$ and k_{isom} (b).

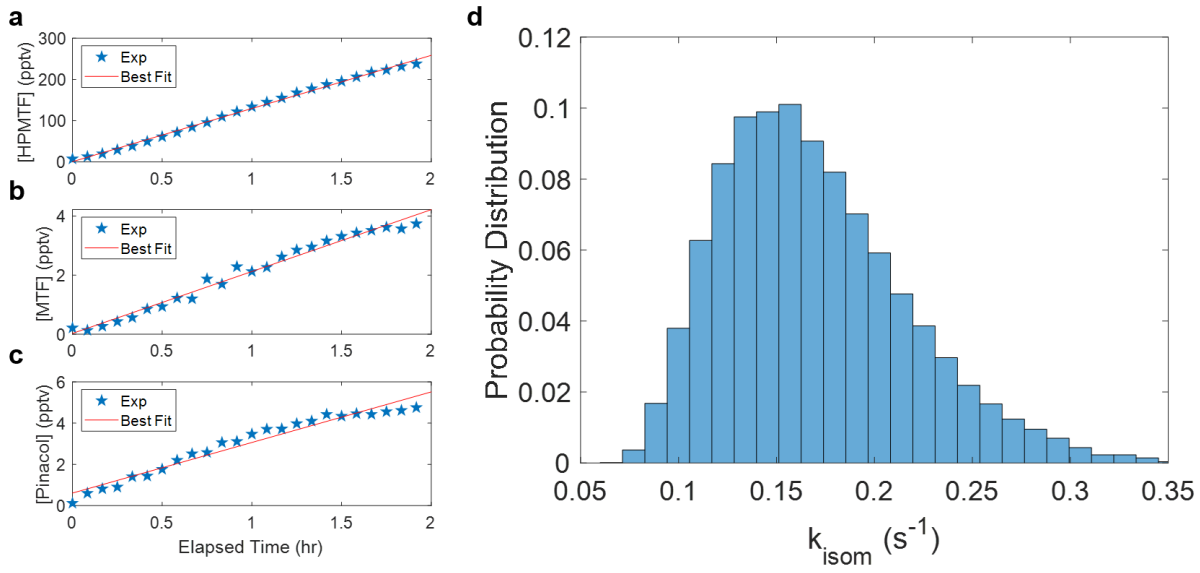

Figure 2.S2: The calculation of the HPMTF isomerization rate is adapted from the procedure used by Crounse et al (2011). Observations of HPMTF (a), MTF (b), and Pinacol (c) species during oxidation of dimethyl sulfide (DMS). Results from only one experiment are shown, but all experiments are used for the calculation of the isomerization rate. Lines represent the best fit parameters from linear ordinary least-squares regression. The probability distribution of the isomerization rate constants is shown (d). The mean value for probability distribution fitted to a normal gaussian product distribution is 0.1 ± 0.05 s^{-1} (1σ of mean).

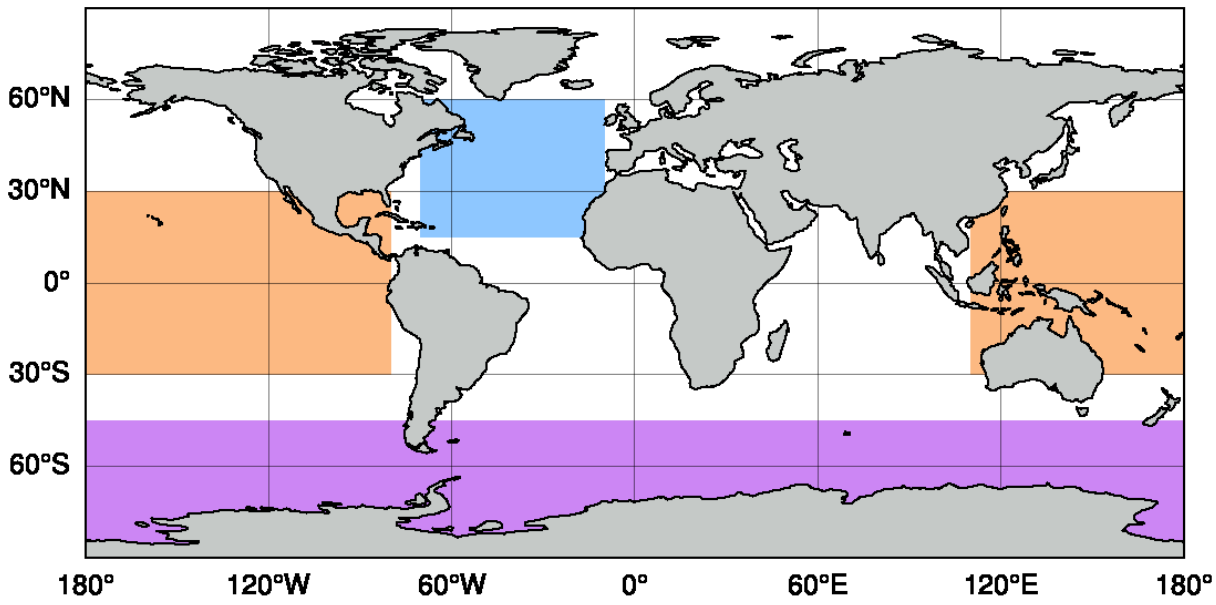

Figure 2.S3: The blue, orange and purple marine regions refer to the North Atlantic, Tropic Pacific and Southern Ocean traces of **Figure 2.3** panel b, respectively.

Chapter 3: Carbonyl sulfide and sulfur dioxide yields from the low NOx oxidation of marine sulfur species

Abstract

The oxidation of atmospheric sulfur compounds has been the subject of investigation over the past decades due to the importance sulfur has on Earth's climate and radiation budget. Dimethyl sulfide (DMS), emitted from the surface ocean, is known to contribute to aerosol particle formation and growth in the pristine marine atmosphere. Though emitted in lower concentrations than DMS, other sulfur-containing trace gases such as dimethyl disulfide (DMDS), methanethiol (MeSH) and carbon disulfide (CS_2) are released from the ocean and contribute to sulfate aerosol formation. Recent laboratory investigations have shown that the OH-oxidation of DMS, under conditions relevant to the pristine marine environment, is an efficient source of carbonyl sulfide (OCS). The emergence of new autoxidation mechanisms, previously undetected intermediates, and experiment dependent product distributions lead us to reexamine the OH-oxidation and OCS production from relevant marine sulfur containing compounds. We find an experimental OCS yield (i.e., $\Delta OCS/\Delta Sulfur$) of 106 ± 16%, 199 ± 40%, and 123 ± 5%for methanethiol and carbon disulfide, respectively. While OCS significance may vary between the species, methanethiol and carbon disulfide have a significant experimental SO_2 yield (i.e., $\Delta SO_2/\Delta Sulfur$) of 0%, 0.3 ± 0.2%, and 77 ± 5%, respectively. Absolute and experimental yields for DMS and DMDS should not be directly used as the formation of SO_2 and OCS can be mechanism specific (e.g., fraction of isomerization vs bimolecular reaction). By modeling the chamber outputs, we find DMS and DMDS both present routes to OCS in low yield (<1% in both species), assumed through their hydroperoxyl aldehyde intermediates.

3.1 Background

Sulfur is an essential component of Earth's biogeochemical system with particular importance to global climate. Depending on the source, sulfur can enter the atmosphere in a variety of reduced and oxidized forms. A key species within the sulfur cycle is sulfur dioxide (SO_2). SO_2 can be emitted directly to the atmosphere through anthropogenic (e.g., coal combustion) or natural (e.g., passive and eruptive volcanic emissions) processes and it can be produced through the oxidation of reduced sulfur compounds. SO_2 plays an important role in air quality as it contributes to acid rain and haze events known to be detrimental to aquatic systems, forests and human health, as well as climate regulation, through oxidation to sulfate aerosols, by scattering incoming solar radiation directly or indirectly by increasing cloud condensation nuclei (CCN) (T.-M. Chen et al., 2007; Galí et al., 2018). SO_2 can be emitted directly to the atmosphere through anthropogenic (e.g. coal combustion, ship emissions) or natural (e.g. volcanic eruptions, biomass burning) processes and it can be produced through the oxidation of reduced and oxidized sulfur compounds (Barnes et al., 2006; Bates et al., 1992; Faloona, 2009; Rodhe, 1999; Wine, Kreutter, et al., 1981). Global anthropogenic emissions of SO_2 have been dropping over the past decades as regional emission standards have taken hold (Shukla et al., 2019). The global burden of SO_2 is primarily driven by the combustion of sulfur containing fuels, mineral ore processing and global shipping with an estimated emission of c.a. 70 TgS yr^{-1} (Faloona, 2009; Liu et al., 2000; Rodhe, 1999). Additional direct SO_2 emissions can come through the passive and explosive emission of SO_2 from volcanoes, an efficient source of direct emissions to the stratosphere, and through biomass burning thought to supply c.a. 9 and 1 TgS yr^{-1} to the atmosphere, respectively (Bates et al., 1992; Langner & Rodhe, 1991; Pinto et al., 1989). Lastly, SO_2 can be added to the atmosphere through the oxidation of emitted reduced sulfur species either from terrestrial (e.g. forests, marshes, and fresh water) or

marine origins (Bates et al., 1992). A significant source of reduced sulfur to the atmosphere is the ocean, with origins primarily driven by biological activity. The primary sulfur molecule emitted is dimethyl sulfide (DMS), with minor contributions of 4.7, 0.213 and 0.243 TgS yr^{-1} from methanethiol (MeSH), dimethyl disulfide (DMDS), and carbon disulfide (CS_2), respectively (Lee & Brimblecombe, 2016). The oxidation mechanism and resulting concentrations and volatility of the oxidation products determines the formation and growth rates of aerosol particles to cloud condensation nuclei (CCN) sizes in marine environments, with consequent effects on Earth's radiative budget (Galí et al., 2018; Korhonen et al., 2008; Vallina et al., 2006). In addition, the oxidation of marine sulfur species leads to the production of carbonyl sulfide (OCS). Accurate estimates of marine carbonyl sulfide (OCS) sources are critical for both modeling stratospheric aerosol concentrations, as OCS is an important precursor to stratospheric sulfate aerosol particles, and for estimating gross primary production, as OCS is readily consumed by the terrestrial biosphere. Despite the importance of OCS to both stratospheric aerosol chemistry and as an effective proxy for CO_2 plant uptake, considerable uncertainty remains in the sources and sinks of OCS. A large source of this uncertainty arises in the marine sources, stemming in part from an incomplete understanding of the oxidation of marine sulfur gases. Recent isotopic and inverse modeling studies of global OCS indicate that the marine environment is the dominant source region for OCS and that there is an unaccounted-for OCS source over the tropical oceans. It is not yet clear what fraction of marine-derived OCS is directly emitted from the ocean compared with that formed in the oxidation of biogenic and marine reduced sulfur species (e.g. DMS, MeSH, DMDS, and CS_2). In response to recent suggestions that the production of OCS from the OH-initiated oxidation of other marine sulfur species may be a significant source of uncertainty in the OCS budget, we have revisited the chemical mechanism for OCS production in the oxidation of

known sulfur compounds emitted to the marine atmosphere (DMS, DMDS, MeSH and CS_2). In addition to the contribution to OCS production, we reexamine the production of SO_2 from reduced sulfur oxidation under oxidative conditions indicative of the remote marine environment.

3.1.1 DMS emission and atmospheric fate

Dimethyl sulfide (DMS) is biogenically produced molecule emitted from the ocean that contributes to the greatest magnitude of the examined sulfur species (c.a. 28 TgS yr^{-1}) (Bates et al., 1992; Lana et al., 2011). Once emitted from the ocean, DMS is primarily oxidized by the hydroxy radical (OH) via one of two initial steps: OH addition or hydrogen abstraction, as seen in **Figure 5.1** (Barnes et al., 2006; Barone et al., 1996; Yin et al., 1990). It has been demonstrated that the peroxy radical species (RO_2) formed by the OH addition pathway will primarily transform into highly soluble species (e.g**.** dimethyl sulfoxide and methanesulfinic acid) which contribute to aerosol growth (Hoffmann et al., 2016; Kreidenweis & Seinfeld, 1988). Until recently, it was thought that the peroxy radical formed following hydrogen abstraction can react with various radical species including nitric oxide (NO), the hydroperoxyl radical (HO_2), or other RO_2 species leading to the production of SO_2 (R3 in Fig. 1). Recent computational, laboratory, and field-studies have shown that the textbook representation of DMS oxidation by OH radicals is incomplete (Jernigan, Fite, et al., 2022; G. A. Novak et al., 2021; Veres et al., 2020; Vermeuel et al., 2020). Specifically, it is now known that the primary peroxy radical, methylthiomethyl peroxy radical (MTMP, $CH_3SCH_2OO\cdot$), formed from the OH-initiated oxidation of DMS, rapidly isomerizes *via* a unimolecular 2-step hydrogen shift reaction to form the stable product hydroperoxymethyl thioformate (HPMTF; $HOOCH_2SCHO$). HPMTF is ubiquitous in the marine environment (Veres et al., 2020) and it is estimated that >45% of emitted DMS goes on to form HPMTF (Fung et al., 2021; G. A. Novak et al., 2021; Vermeuel et al., 2020). Recent laboratory measurements have

found that the gas phase reaction of HPMTF with OH is relatively slow ($k_{HPMTF+\ OH}$ = 1.4 × 10^{-11} cm^3 $molec^{-1}s^{-1}$) and that SO_2 and OCS are the primary stable reaction products (Jernigan, Fite, et al., 2022). Novak et al (2021) and Vermeuel et al. (2020) showed that multiphase loss processes (i.e. dry deposition, reactive uptake to aerosol particles, and cloud loss) can be the primary loss mechanism for HPMTF. As such, SO_2 and OCS production from DMS depends on the production and fate of the soluble intermediates (such as HPMTF) resulting in a mechanism dependent SO_2 and OCS product yield.

3.1.2 MeSH emission and atmospheric fate

Methanethiol (MeSH) is a reduced sulfur species emitted from the ocean, with similar biological origins to dimethyl sulfide (Kiene, 1996; Kiene & Linn, 2000). While MeSH is produced in higher yields than DMS in sea water, it is also consumed more rapidly by marine microorganisms (Kiene, 1996). The spatial and temporal distribution of DMS emissions are well constrained by decades of ship-based measurements (Galí et al., 2018; Lana et al., 2011). In comparison, significantly less is known about the emission rate of MeSH and the contribution of MeSH to SO_2 production. Recent, simultaneous measurements of DMS and MeSH sea-to-air emissions suggest that the emission rates of DMS and MeSH may be closely related, permitting one to scale MeSH emissions (E_{MeSH}) to DMS emissions (E_{DMS}) (Lawson et al., 2020; Lee & Brimblecombe, 2016; G. A. Novak et al., 2022). Using ambient measurements, Novak et al. (2022) and Lawson et al. (2020), determined $\frac{E_{MeSH}}{E_{DMS}+E_{MeSH}}$ to be between 0.14-0.25. Scaling global DMS emissions (28 TgS yr^{-1}) by this emission ratio, leads to a global MeSH emission rate of 5 TgS yr^{-1}. Once emitted to the atmosphere, MeSH is primarily oxidized by the hydroxyl radical with an atmospheric lifetime of 8 hours at [OH] = 1 × 10^6 molecule cm^{-3} (Butkovskaya & Setser, 2021; Lawson et al., 2020; Wine et al., 1984), which is approximately a factor of 4.7 shorter than the

atmospheric lifetime of DMS (1.64 days). The OH-initiated oxidation of MeSH proceeds predominantly *via* OH-addition leading to prompt and near unit yield of $CH_3S\cdot$ (**Figure 5.3**). This thioradical ($CH_3S\cdot$) is expected to react primarily with ozone (O_3) or O_2 to form SO_2 in near unit yield. Recent laboratory measurements, performed under low NO_x conditions, report a yield of 0.98 consistent with these expectations (J. Chen et al., 2021). While we expect a high SO_2 yield from the OH-oxidation of MeSH, there are no reported measurements of the OCS yield from the OH-oxidation of MeSH. Given the large, expected emission rate of MeSH, even a minor product yield of OCS would be an important contribution to the global OCS budget.

3.1.3 DMDS emission and atmospheric fate

Dimethyl disulfide (DMDS) is reduced dimethyl polysulfide species with both marine and terrestrial origins. Few measurements have been made of DMDS, due to the expected low concentrations of DMDS and the relatively short lifetime of DMDS in the atmosphere (<2 hour) (Berndt et al., 2020; Wine, Kreutter, et al., 1981). Along with MeSH and DMS, the emission of DMDS is tied to biological activity (Kettle et al., 2001). Only a few studies have observed marine DMDS, with most concluding that DMDS emissions are more significant in coastal regions when compared to the open ocean. Coastal and marshland regions have elevated seawater MeSH concentrations that through oxidation can lead to the formation of DMDS (Cooper et al., 1987; de Mello et al., 1987; Richards et al., 1991; Turner et al., 1995). Using the recommendations of Lee and Brimblecombe (2016), a global emission of DMDS is estimated to be on the order of 0.2 TgS yr^{-1}. The magnitude of this value is approximated by scaling DMDS emissions to DMS using the observations from Tanzer & Heumann (1992). In the terrestrial regions, DMDS can be generated in higher concentrations than DMS during biomass burning events (Lee & Brimblecombe, 2016; Perraud et al., 2016). Once emitted, DMDS is primarily removed from the atmosphere by reactions

with hydroxyl radicals (OH), with a lifetime of 1.3 hours at [OH] = 1×10^6 molecule cm^{-3} (Wine, Kreutter, et al., 1981) **(Figure 5.5)**. In addition, DMDS is rapidly photolyzed, with a lifetime 3.7 hours at 40°N at noon (Hearn et al., 1990) and can be oxidized by the nitrate radical (NO_3) at a rate constant of $7.4 \pm 1.5 \times 10^{-13}$ cm^3 $molec^{-1}$ s^{-1} (Dlugokencky & Howard, 1988; Wallington et al., 1986). Like DMS, it was originally thought that DMDS would be efficiently converted to SO_2 through $CH_3S\cdot$ chemistry similar to that found in the OH-oxidation of DMS and MeSH (**Figure 5.1 and 5.3**). Recent work performed by Berndt et al. (2020) and Van Rooy et al. (2021), found additional channels for DMDS oxidation via a hydrogen shift mechanism similar to that of MTMP within the DMS oxidation mechanism. Recently discovered pathways within the DMDS oxidation mechanism makes it a prime target for the reinvestigation of its SO_2 and OCS yield under marine oxidative conditions.

3.1.4 CS_2 emission and atmospheric fate

Carbon disulfide (CS_2) is a reduced sulfur compound with marine sources driven by biological and photochemical processes (Watts, 2000). Previous measurements of CS_2 and OCS indicate that both species are present in higher concentrations in coastal (Chin & Davis, 1993; Kim & Andreae, 1987; Lennartz et al., 2021; T Lennartz et al., 2020; Watts, 2000). The natural sources of CS_2 in these environments are the anerobic processing of rotting organic matter (Khalil & Rasmussen, 1984), biological activity of phytoplankton (Xie et al., 1999), the photolysis of sulfur containing amino acids (Q. Du et al., 2017), and activity of volcanoes (Chin & Davis, 1993). CS_2 has an anthropogenic source derived primarily from leakage during its use as a solvent and reagent within the industrial manufacturing of regenerated cellulose rayon and cellophane (Chin & Davis, 1993). Most of the measurements of CS_2 were made more than 40 years ago leading to a lack of global spatial and temporal concentration and emission patterns as well as large sources of

uncertainty in the emission term (T Lennartz et al., 2020; Whelan et al., 2018). Once emitted to the atmosphere, CS_2 is efficiently oxidized by OH (τ_{OH} = 5 days) to form OCS and SO_2 at a branching of 0.81 and 1.21, respectively (Chin & Davis, 1993; Hynes et al., 1988; Stickel et al., 1993) (**Figure 5.7**). CS_2 can also be lost through the photo-oxidation of an electronically excited state leading to a lifetime on the order of >1 day (4.5×10^{-5} s^{-1} at 0 km, with low quant yield) (Wine, Chameides, et al., 1981). The high yield of OCS from the OH-oxidation of CS_2 makes it a prominent source of OCS in the atmosphere with global models estimating 0.084 TgS yr^{-1} of OCS is produced indirectly from marine CS_2 oxidation (Kettle et al., 2002; Ma et al., 2021).

3.2 Methods

3.2.1 Measurements of Reduced and Oxidized Sulfur Species

The detection and quantification of a wide array of sulfur containing trace gases was conducted with two Chemical Ionization Mass Spectrometers (CIMS): a Compact Time of Flight CIMS (C-ToF) utilizing iodine anion or oxygen anion chemistry (Bertram et al., 2011; G. Novak et al., 2019; Vermeuel et al., 2019) and an Aerodyne/TOFWERK Vocus - Proton Transfer Reaction Time of Flight Mass Spectrometer (Vocus) (J. Krechmer et al., 2018). Sulfur dioxide (SO_2) measurements were made by the oxygen anion CIMS instrument at a mass of 64 m/Q and 112 m/z corresponding to $[SO_2]^-$ and $[SO_5]^-$. A Los Gatos Research Enhanced Performance (LGR) OCS analyzer was used to detect carbonyl sulfide (OCS) (Berkelhammer et al., 2016). The sensitivities and signal intensity for all species recorded by the iodine and oxygen anion CIMS C-ToF instrument are presented as normalized counts per second (ncps), where the intensity is normalized to one million (10^6) counts per second, calculated as the sum of -m/*Q* 127 ($[I]^-$) and 145 ($[I \cdot H_2O]^-$) and of -m/*Q* 32 ($[O_2]^-$) and 50 ($[O_2 \cdot H_2O]^-$), respectively. The absolute sensitivities

of the Vocus to DMS and MeSH and the oxygen anion CIMS to SO_2 and O_3 were determined through dynamic dilution of a standard supplied by compressed gas cylinder standards (5.08 ppm DMS in N_2, Praxair, 6.11 ppm MeSH in N_2, Airgas, and 4.93 ppm SO_2 in N_2, Scott Marrin). The absolute sensitivities of the Vocus to TME (98% 2,3-Dimethyl-2-butene, Sigma Aldrich), CS_2 (≥99% Carbon disulfide, Sigma Aldrich), DMDS (≥99.0% Dimethyl disulfide, Sigma Aldrich), and DMS (≥99.0% Dimethyl sulfide, Sigma Aldrich) were calculated using the liquid calibration method described in Lavi et al (2018). DMS, DMDS, and MeSH were all detected as at the MH^+ mass driven by a proton transfer from a protonated water cluster, while CS_2 was observed at the M^+. The relatively small proton affinity of CS_2 (682 kJ/mol) compared to that of DMS (831 kJ/mol) makes the detection of CS_2 at MH^+ mass (typical of PTR detection) more difficult, as such minor complications arose as the ionization route for CS_2 (detected as M^+) is different from the other masses in PTR [(Blake et al., 2006). The PTR system works by the reagent ion (H_3O^+) ionizing the analytes through a proton transfer reaction. CS_2 is detected as a charge transfer product, meaning any residual O_2^+ and NO^+ generated within the ionization source or in the PTR drift region could be ionizing CS_2^+. A normalization to any one potential species in the mass spectra could be used to recover the drop in sulfur signal indicative of oxidation as seen in the MeSH, DMS and DMDS experiments. Oxidation was still assumed to occur within the CS_2 experiments as Acetone (product of TME oxidation), OCS and SO_2 were all produced upon addition of ozone. A compact gas chromatography (GC) system (ARI Mod-GC; Aerodyne Research Inc.) was coupled to the Vocus to create an ARI-GC-Vocus-PTR-MS system. The instrument is described in detail in Claflin et al. (2021), but will be briefly described here. The GC system uses a 30m Agilent DB-5 is nonpolar and low bleed column as the stationary phase and helium as the mobile phase. Air from the chamber, the gas cylinders and the permeation sources were flown over a sample trap to

preconcentrate the analytes in the flow before introducing to the GC column. The trap is flash heated to introduce the sample to the GC column, where the column is ramped in heat over 10 minutes to elute the species on the column. All OCS measurements were made using a Los Gatos Research, Enhanced Performance OCS analyzer (PN:914-0028). The analyzer was previously described by Berkelhammer et al. (2014).

3.2.2 Environmental Chamber

In typical experiments, O_3, TME, and the sulfur precursor (e.g. DMS, MeSH, DMDS, or CS_2) were mixed in an environmental chamber run under a continuous flow regime. Details of the experimental set up has been reported previously (Jernigan, Fite, et al., 2022). The experiments were run in a rectangular 0.6 m^3, 5 mil (mil, 0.001 of an inch) PFA environmental chamber under ambient temperature (~298K), dark, dry (<0.5% RH), and "NO_x free" conditions. The dry and NO_x free conditions were verified throughout the experiment by observations of the absolute concentration of water vapor, observed by the LGR OCS analyzer, and NO_2 was monitored using oxygen anion CIMS at m/Q 61 (NO_2^-) (G. Novak et al., 2019). The chamber was run under a continuous flow regime in 2 distinct stages: 1) we first fill the chamber with the targeted sulfur precursor gas and TME, and 2) once the chamber has reached steady-state, we add O_3 to initialize oxidation. The chamber was operated by flowing *ca.* 4 standard liters per minute (SLPM) of zero air with a sulfur precursor, TME and ozone into the chamber and pulling from the chamber with the three instruments used for monitoring the trace gases and a small diaphragm pump. The chamber was flushed with dry nitrogen to remove all volatile organic compounds (VOC) within the chamber between each experiment. The various VOCs were introduced to the chamber by a mass flow controller backed by cylinder (5.08 ppm mixture of DMS or 6.11 ppm mixture of MeSH in nitrogen) or by flowing nitrogen over an in-house built permeation tube (TME, 98% 2,3-

dimethyl-2-butene, Sigma Aldrich; DMDS, ≥99% dimethyl disulfide, Sigma Aldrich; CS_2, ≥99% carbon disulfide, Sigma Aldrich) sheltered in a temperature-controlled heat block. Ozone, used for initializing the formation of OH through the ozonolysis of TME, was supplied to the chamber by a custom-built ozone generator with the output ozone concentrations of 40 – 60 ppb. Dry synthetic air conditions (<0.5% RH, 80% N_2/ 20% O_2) were used to facilitate higher yields of hydroxyl radicals (·OH) from TME ozonolysis (Y_{OH} > 0.8) and to mitigate chamber wall losses (Alam et al., 2013; Donahue et al., 1998).

CS_2 is used as a solvent and organic synthesis reagent. The industrial applications and sulfur composition makes it the source of a potential artifact within the pure sulfur samples used throughout the chamber experimentations. CS_2 was found in minor concentrations within the each of the liquid samples. The amount of CS_2 was constrained during the real-time oxidation of each of the species (measured at 76.139 in the Vocus PTR) as well as offline using a GC attached to the Vocus instrument. The contribution to the OCS signal attributed to the CS_2 contamination was accounted for in the analysis of each of the sulfur compounds. In all cases, the contribution to the OCS production as a function of CS_2 oxidation was minor compared to that of the sulfur species ($P_{OCS,CS2}$<1 pptv).

3.2.3 Environmental Chamber Model Description

A 0-D box model that incorporates the Master Chemical Mechanism (MCM) v3.3.1 in the Framework for 0-D Atmospheric Modeling (F0AM) (Saunders et al., 2003; Wolfe et al., 2016) was used in this work. Details of the model framework has been reported previously (Jernigan, Fite, et al., 2022). To capture all potential production and loss pathways within the chamber, a fill and dilution term ($k_{dilution}$) and experimentally and theoretical derived wall loss terms (k_{wall}) were added to the model. An experimentally derived wall loss term (k_{wall}) was determined by calculating

the wall loss of known species (DMS, DMDS, MeSH, CS_2, SO_2 and TME) during the filling of the chamber, while a theoretical value for k_{wall} based on a partioning and equilibrium value was used for major oxidation products (e.g. DMSO, MSIA, CH_3SOH, HPMDTF) (J. E. Krechmer et al., 2016, 2020; Matsunaga & Ziemann, 2010). The current online version of the MCM (v3.3.1) does not include the recent isomerization chemistry as described in recent publications(Berndt et al., 2019, 2020; Veres et al., 2020; Wu et al., 2015). For DMS oxidation, the formation and OH-initiated loss of HPMTF was added based on recommendations of Jernigan et al. (2022) and Ye et al. (2021). For MeSH, the OH-initiated loss was included based on the recommendations of Butkovskaya & Setser, (2021), J. Chen et al. (2021), and Wine et al. (1984). The primary product of MeSH OH-oxidation is the formation of $CH_3S\cdot$ species found in DMS oxidation. An additional OH-oxidation pathway, recently observed Butkovskaya & Setser (2021), driven by a hydrogen abstraction off a methyl hydrogen, was included in the model. The new channel facilitates the formation of additional radicals (e.g. $\cdot OOCH_2SH$) in the initial step of MeSH OH oxidation, where the textbook oxidation lead to unit yield of $CH_3S\cdot$. For DMDS, the OH-initiated loss was included based on the recommendations of Berndt et al., (2020) and Wine, Kreutter, et al. (1981). Two chemical pathways were included to the DMDS pathway: 1) an OH addition channel forming the $CH_3S\cdot$ species and CH_3SOH (methanesulfenic acid) generated from the initial OH-reaction with DMDS, and 2) a hydrogen abstraction channel forming the $CH_3SSCH_2\cdot$ alkyl radical. $CH_3SSCH_2\cdot$ can recombine with ambient oxygen and undergo two hydrogen shift mechanisms to form a recently discovered hydroperoxyl aldehyde, $HOOCH_2SSCHO$ (hydroperoxymethyl dithioformate, HPMDTF). Given the similarity of CH_3SOH species to methyl hydroperoxide (CH_3OOH), MCM values for CH_3OOH were used. Lastly, the OH-initiated loss for CS_2 was included based on the recommendations of Hynes et al. (1988), McKee & Wine (2001), and Stickel et al. (1993). The

CS_2 experiments were performed under zero air conditions at ambient pressure and for that reason the short-lived excited species (i.e OCS* and HOSO*) were not included and a flat yield to OCS and SO_2 was used. A few modifications were made to the standard MCM to represent the oxidative conditions more accurately within the environmental chamber. The inclusion of peroxy radical (RO_2·) + ·OH chemistry was added to capture all potential loss pathways for the RO_2· species within the chamber. Rate constants were taken from Fittschen (2019), while RO_2· species without an explicit rate constant were given values from species of similar structure. ·OH is formed through the unimolecular decomposition of the zwitterionic carbonyl oxide, $(CH_3)_2COO$, generated by the bimolecular reaction of ozone and TME. The MCM uses a unit yield of ·OH from the decomposition of $(CH_3)_2COO$, while a more mechanistic formation of ·OH was used in the model to capture the concentration of the stabilized $(CH_3)_2COO$ species ($s(CH_3)_2COO$) which is known to react with SO_2 (Berndt et al., 2012). We used a OH-yield from Alam et al. (2013) of 0.83 for both the decomposition of the $(CH_3)_2COO$ and $s(CH_3)_2COO$ species as the dry chamber conditions and direct ·OH observations described in Alam et al. (2013) are more representative of the conditions studied here. Recommendations from Cox et al., (2020) and Newland et al., (2020) were used for the yield of $s(CH_3)_2COO$ from $(CH_3)_2COO$ decomposition, unimolecular $s(CH_3)_2COO$ + M rate constant and the bimolecular $s(CH_3)_2COO$ + SO_2 rate constant.

Branching fractions and approximated rate constants not found in the literature were approximated and derived using the 0-D box model. The experimental value and uncertainty were determined by iterating the box model until a lower limit of error was found across the major detectable sulfur species within the chamber. The error for each of the major sulfur species was determined using the following equation:

$$\varepsilon_{Sulfur} = \left|\frac{[Sulfur]_{Model} - [Sulfur]_{Exp}}{[Sulfur]_{Exp}}\right| \times 100\% \qquad \text{E5.1}$$

3.3 Results and Discussion

3.3.1 Dimethyl sulfide oxidation

The results of the DMS OH-oxidation experiments are discussed in detail in Chapter 2, and were published in (Jernigan, Fite, et al., 2022). We briefly review these results here for comparison with the experiments with MeSH, DMDS, and CS_2. In the DMS OH-oxidation experiments, we observe OCS and SO_2 production under oxidative conditions representative of the pristine marine atmosphere (**Figure 5.2**). The production of OCS was attributed to the OH-oxidation of HPMTF either as a direct, first-generation product of HPMTF+OH or as a multi-generational product following the OH-oxidation of the HPMTF reaction products thioformic anhydride (TFA, CHOSCHO) or thioperformic acid (TPA, HC(=S)OOH). The production of OCS was attributed to HPMTF oxidation as we were able to eliminate the potential contributions of: i) the photo-oxidation of H_2CS (discussed in the section on MeSH) and ii) production of OCS from CS_2 contamination (discussed in the section on CS_2) (**Figure 5.1**). We observe a substantial OCS yield compared to previous work, however we stress that the absolute fractions of OCS and SO_2 formed from DMS in this or any chamber study are specific to the experimental conditions and should not be used in global climate models. Rather, a precise DMS oxidation mechanism should be included with accurate OCS production yields for each elementary step of the reaction mechanism. The absolute yields (i.e., $\Delta OCS/\Delta DMS$) are not directly applicable to all atmospheric conditions as the fraction of OCS and SO_2 produced will be a function of: 1) the competing temperature-dependent reaction pathways of DMS + OH (i.e. OH addition vs H-abstraction) 2) the temperature-dependence of isomerization chemistry that competes with bimolecular chemistry involving [NO], [HO_2·], and [RO_2·] and 3) the fraction of intermediates that are lost via chemical reaction with OH compared with those irreversible lost to multiphase processes. We used an observationally

constrained 0-D atmospheric model to constrain both the rate constant for OH reaction with HPMTF (1.4×10^{-11} cm^3 $molec^{-1}$ s^{-1}) and the product yield of OCS and SO_2 (0.13 and 0.87, respectively). This mechanism was implemented in the GEOS-Chem global chemical transport model to assess the global importance of DMS as a precursor to OCS. Work performed by Jernigan et al found that taking the extended DMS mechanism into account lead to a global production of 0.053 TgS yr^{-1} for OCS.

3.3.2 Methanethiol oxidation

In the MeSH experiments, conducted under the same low NO_x and RO_2 conditions, no production of OCS above the instrument detection limit was observed (**Figure 5.4a**). The lack of OCS production lends an insight into the mechanistic formation of OCS within the DMS, DMDS and MeSH OH-oxidation mechanism. Barnes et al. (1994) suggested that the production of OCS originated from the oxidation of thioformaldehye (H_2CS), where H_2CS was proposed to be formed in the reaction of the methylthiyl ($CH_3S\cdot$) radical and O_2. $CH_3S\cdot$ is an important radical species that forms promptly from reactions of MTMP with HO_2, RO_2, or NO in DMS oxidation, and forms in near unit yield as a first-generation product in the OH oxidation of MeSH and DMDS (Barnes et al., 1996; Mardyukov & Schreiner, 2018; Wine, Kreutter, et al., 1981; Yin et al., 1990). In the MeSH experiments, also conducted under dark, low NO_x and $RO_2\cdot$ conditions, no OCS production was observed (**Figure X**) indicating that any OCS observed in the DMS, DMDS, or MeSH experiments is not formed through $CH_3S\cdot$ and subsequently MTMP bimolecular chemistry. This is supported by the work of Chen et al. (2021), who also found that $CH_3S\cdot$ oxidizes to SO_2 in near unit yield and not H_2CS, a potential precursor to OCS. In support of previous work, we observe sulfur dioxide (SO_2), produced at a yield of 106 ± 16% (**Figure 5.4b**). An experimental yield greater than 100% for the OH oxidation of MeSH can be explained by experimental uncertainty

within the calibration factors of MeSH and SO_2 and in the minor presence of Dimethyl disulfide (DMDS) within the MeSH cylinder. The presence of DMDS within the cylinder was verified in real-time by the presence of the ion $C_2H_7S_2H^+$ identified in the chamber experimentation performed on pure DMDS. Additionally, the relative contribution of the $C_2H_7S_2H^+$ ion compared to CH_4SH^+, used to identify MeSH within the Vocus, was found to increase slowly over the course of months. This steady rise in the contribution would imply the slow oxidation of MeSH to DMDS within the gas cylinder. Lastly, a gas chromatography analysis was performed on the MeSH cylinder found the presence of DMDS at a retention time consistent to that found of GCs taken on a pure DMDS sample. The contribution of DMDS oxidation to the production of SO2 within the MeSH experimentation was made by constraining the loss of DMDS as a function of the presence of OH. DMDS was further verified as minor component of the MeSH cylinder through the decay in the DMDS signal. DMDS has an OH rate constant of 2.3×10^{-10} cm^3 $molec.^{-1}$ s^{-1}, almost and order of magnitude faster than MeSH. The distinguishable difference in the drops of the CH_4SH^+ ion and $C_2H_7S_2H^+$ would imply two separate species both oxidizing within the environmental chamber. Using the SO_2 yield observed within the DMDS oxidation experiments (199%), the contribution to SO_2 from DMDS oxidation (<0.5 ppbv) was accounted.

We also observe an unknown sulfur containing ion ($[CH_2SO•H]^+$) that might be related to the formation of $•CH_2SH$, whose yield from MeSH OH-oxidation via a hydrogen abstraction channel has been shown to be 13% (**Figure 5.4b**) (Butkovskaya & Setser, 2021). Though the unidentified ion presents new insight into a new oxidation pathway of MeSH, the end goal of MeSH oxidation stays consistent. The observed unit yield of SO_2 from MeSH oxidation and the fast rise time of the $[CH_2SO•H]^+$ ion species would imply that an intermediate within the MeSH oxidation mechanism is short-lived and efficiently converts to sulfur dioxide. Assuming a global

production of MeSH as a function of the global DMS emission term, we would assume that the global production of SO_2 from MeSH oxidation would be on the order of 4.7 to 7 TgS yr^{-1}.

3.3.3 Dimethyl disulfide oxidation

In the OH initiated oxidation of DMDS, we observe an experimental SO_2 yield of 199 ± 40%, consistent with the findings of previous researcher performed under varying oxidative conditions (**Figure 5.6a**) (Berndt et al., 2020; Wine, Kreutter, et al., 1981). While SO_2 is the primary product observed within the oxidation of DMDS, minor concentrations of carbonyl sulfide (OCS), methane sulfinic acid (MSIA), methane sulfenic acid (CH_3SOH), and a recently discovered isomerization product $HOOCH_2SSCHO$ (hydroperoxymethyl dithioformate, HPMDTF) were observed (Berndt et al., 2020). We observe an absolute OCS yield (i.e., ΔOCS/ΔDMDS) of 0.3 ± 0.2% throughout our chamber experiments. The origin of OCS within the DMDS oxidation mechanism is thought to come about from a mechanism like that of DMS oxidation through HPMTF. The high yield of SO2 consistent with previous work would imply that the main route of DMDS oxidation is through the OH addition channel leading to the formation of the $CH_3S\cdot$ and CH_3SOH. As in MeSH OH-oxidation, $CH_3S\cdot$ is thought to efficiently convert to SO_2 through reactions with ozone or oxygen. The significant loss in DMDS (>5 ppb) would imply a significant fraction of sulfur is transported through $CH_3S\cdot$. Given the lack of OCS production in MeSH oxidation and the relatively low yield of OCS from DMDS oxidation, we postulate that the formation of OCS from the oxidation of marine sulfur emerges through the further processing of sulfur containing hydroperoxyl aldehyde intermediates (i.e., HPMTF and HPMDTF). The fast stabilization of HPMDTF within the chamber would imply a fast loss rate. While an absolute rate constant for HPMDTF with OH is unknown, the value is assumed to be the dominant form of loss within the chamber and on the order of magnitude as DMDS + OH, $k_{DMDS+OH} = 2.3 \times 10^{-10}$ cm^3

molec^{-1} s^{-1}. Using a sensitivity similar to HPMTF, we estimate the concentration of HPMDTF withing the chamber to be approximately 20 ppt and can be explained by a minor production channel. We assumed a low yield for the H-abstraction channel (2%, postulated by Berndt et al 2021). In tandem with HPMDTF, observations were made of CH_3SOH (detected at m/z 191) and MSIA (detected at 207 m/z in Iodine and 79 m/z in Oxygen anion CIMS), intermediates formed by the dominant OH-addition channel of DMDS oxidation. While absolute sensitivities of these molecules were not experimentally determined, approximate sensitivities were calculated by relating the binding energy of other detected molecules within the chamber (Iyer et al., 2016; Jernigan, Fite, et al., 2022; Lopez-Hilfiker et al., 2016). Evaluating the significance of the CH_3SOH species is complicated by the presence of sulfur dioxide. SO_2 can be detected as a cluster ($[I \bullet SO_2]^-$) at 191 m/z in iodine CIMS under dry conditions contributing to the intensity at 191 m/z with CH_3SOH. Under the assumption that all intensity at 191 m/z is attributed to SO_2, the SO_2 yield from DMDS would be 350% (**Figure 5.6b**). The excessive yield compared to the other experiments leads us to believe that another species contributes to the observed signal at 191 m/z mass. The contribution to 191 m/z associated to CH_3SOH was calculated by utilizing the SO_2 yield from DMDS oxidation calculated here (199%) and converting that assumed SO_2 concentration into a signal intensity using an experimentally measured SO_2 sensitivity. Given the significant fraction of SO_2 generated in the chamber, most of the signal at 191 m/z is assigned to SO_2 with a detectable fraction assigned to CH_3SOH. While both species show significant rises off the baseline, the overall high yield of SO_2 within the chamber would imply that both CH_3SOH and MSIA are not major sulfur reservoirs within DMDS oxidation, but rather transient intermediates. MSIA, constrained and detected in the DMS oxidation experiments, has a OH rate constant of 9 x 10^{-11} cm^3 molec^{-1} s^{-1}with unit yield to SO_2. As there is no known OH rate constant for CH_3SOH, the

value for a structurally similar species methyl hydroperoxide, CH_3OOH, was assumed (k_{MHP+OH} = 9.5 x 10^{-12} cm^3 $molec^{-1}$ s^{-1}). Using the stated values for MSIA and CH_3SOH oxidation, a high yield of SO_2 from the OH oxidation of DMDS can be understood.

We find that good agreement between the model and the experiments requires the inclusion of the reaction of the zwitterionic carbonyl oxide, $(CH_3)_2COO$ with SO_2 and the reaction of CH_3SOH with O_3, as recommend by Berndt et al. (2020). Our results suggest that only 3-5% of the SO_2 loss is driven by the reactions with $(CH_3)_2COO$, while the majority is driven by dilution, inherent to the continuous flow design. Though the effect on SO_2 is minor there is an additional effect on the OH concentration within the chamber. Secondly, the addition of the CH_3SOH reaction with ozone was needed to capture the SO_2 production within the chamber. Without the reaction and a significant loss pathway, CH_3SOH accumulates and starts to act as a significant reservoir (>50% of sulfur) within the DMDS oxidation mechanism. To recover the SO_2 observed within the chamber, the reaction with O_3 needs to be added or the lifetime of the CH_3SOH needs to be greatly reduced. The rate constant recommended by Berndt et al (2020) at 2×10^{-11} cm^3 $molec^{-1}$ s^{-1} is much faster than most other O_3 reactions and even greater than know reactions with ROOH or sulfur containing species (1×10^{-19} cm^3 $molec^{-1}$ s^{-1} for DMS) (L. Du et al., 2007). It is likely that the species is decomposing or tautomerizing in the gas phase to eventually decompose into a transient species that can readily form SO_2.

Assuming a global production of DMDS of 0.21 TgS yr^{-1}, we would assume an upper limit of the global production of SO_2 and OCS from oceanic DMDS oxidation would be on the order of 6×10^{-4} and 0.21 TgS yr^{-1}, respectively. The production of OCS and a minor component of SO_2 from DMDS would be environment dependent as it is assumed to form through HPMDTF oxidation, similar to that of HPMTF. We assume an upper limit for OCS here as the conditions

presented in the chamber represent that of the remote marine environment, where NO and RO_2 concentrations are low, favoring isomerization reactions. As DMDS is more significant in coastal regions, the potential for urban and terrestrial influence would be greater than that of the marine environments; higher NO_x and RO_2 concentrations could reduce the fraction of HPMDTF formed and subsequently OCS production. The near unit yield of SO_2 and short OH lifetime of DMDS would imply that any DMDS emitted to the atmosphere will quickly form SO_2. We also present the SO_2 yield as an upper limit as HPMDTF could be lost to multiphase pathways, similar to HPMTF, sequestering production of SO_2 and OCS.

3.3.4 Carbon disulfide oxidation

In the OH initiated oxidation of CS_2, we observe a consistent OCS yield (i.e., $\Delta OCS/\Delta CS_2$) of 77 ± 5%, consistent with the findings of previous research conducted under higher oxidant conditions, shorter time scales, lower pressures and more photolytic influence (**Figure 5.8**) (Barnes et al., 1983; Hynes et al., 1988; Jones et al., 1983; Stickel et al., 1993). Due to complications in our ability to measure CS_2 loss during the addition of ozone and subsequent formation of OH, the relative yield of SO_2 and OCS were derived by relating the rise of the two species. Based on the assumption and lack of observations of other stable intermediates within CS_2 oxidation, the ratio of OCS to SO_2 was used to determine the yield from the oxidation of OCS. Across multiple chamber experiments, a OCS to SO_2 ratio of 0.62 ± .02 was found and translated to a OCS and SO_2 yield of 77 ± 5% and 123 ± 5%, respectively. Though the loss of CS_2 was not constrained within the experiment, the OH concentration and steady state concentration within the chamber before oxidation was constrained for every experimentation. Using the natural log decay of trimethyl benzene, a minor artifact within the TME permeation source, an approximate concentration of OH was calculated within the chamber. Constrained by the initial conditions, the

production of OCS and SO_2, and the OH concentration, the 0D box model was able to verify the experimental yields determined using the ratio of OCS to SO_2 method.

Assuming a global production of CS_2 of 0.08 – 0.30 TgS yr^{-1}, we would assume that the global production of SO_2 and OCS from oceanic CS_2 oxidation would be on the order of 0.050 – 0.19 and 0.03 – 0.11 TgS yr^{-1}, respectively. The global production of OCS from the OH-oxidation of CS_2 calculated here falls within the uncertainty of value typically derived in global climate models (i.e. 0.084 TgS yr^{-1}) (Kettle et al., 2002; Ma et al., 2021).

3.4 Conclusions

In this study, we find an OCS yield (i.e., ΔOCS/ΔSulfur) of 0%, 0.3 ± 0.2%, and 77 ± 5% for methanthiol, dimethyl disulfide and carbon disulfide respectively. While OCS significance may vary between the species, methanthiol, dimethyl disulfide and carbon disulfide have a significant SO_2 yield (i.e., $\Delta SO_2/\Delta$Sulfur) of 106 ± 16%, 199 ± 40%, and 123 ± 5%, respectively. While a direct yield of OCS and SO_2 should not be used from DMS oxidation, due to the strong dependence on environmental parameters on the oxidative mechanism (Fung et al., 2021; Jernigan, Fite, et al., 2022; G. A. Novak et al., 2021), experimental yields for MeSH, DMDS and CS_2 can be used within global climate models. MeSH, DMDS, and CS_2 oxidized under oxidative conditions representative of the marine atmosphere, lead to prompt formation of SO_2 in high yield. Previous work looking into the oxidation of these sulfur species have investigated the yield under short time scales and under high oxidative conditions. Yield found here and previously both point to high SO_2 yields, which implies that the various intermediates observed within the oxidative mechanism, don't act as significant sulfur reservoirs. While all sulfur species facilitate significant yields for SO_2, only CS_2 has a comparable OCS yield. DMS and DMDS both present routes to OCS in low yield, assumed through their hydroperoxyl aldehyde intermediates (HPMTF and HPMDTF). The

assumed and measured heterogeneous loss of hydroperoxyl aldehyde intermediates lends to the importance of multiphase loss processes include dry deposition, reactive uptake to aerosol particles, and cloud loss (Fung et al., 2021; Jernigan, Cappa, et al., 2022; Jernigan, Fite, et al., 2022; G. A. Novak et al., 2021; Vermeuel et al., 2020). When multiphase loss processes are included, global model simulations predict a 35% decrease in global SO_2 production and a 92% decrease in global OCS production from DMS oxidation. While reactive surface area, temperature, and oxidative conditions has a significant effect on the global production of SO_2 and OCS, the lack of stable sulfur reservoir and product distribution temperature dependences makes the yield of SO_2 and OCS from MeSH, DMDS and CS_2 more direct. For MeSH, a global emission of 4.7 – 7.0 TgS per year would result in a unit conversion to SO_2 with its significance enhanced in colder regions where co-emitted DMS is shuttled down the OH-addition channel away from SO_2 production (G. A. Novak et al., 2022). MeSH did not show any production of OCS from OH oxidation, indicating that the MeSH term is unlikely to help elucidate the missing marine OCS production. For DMDS, a global emission term of ~0.2 TgS yr^{-1} and a SO_2 yield of 199% would imply a global burden of 0.2 TgS yr^{-1} of SO_2 and a value of $0 – 6 \times 10^{-4}$ TgS yr^{-1} of OCS. The small emission term and low observed yield of OCS from the chamber experiments makes DMDS's contribution to the marine OCS source likely insignificant on the global scale. A global emission of CS_2 of 0.08 – 0.30 TgS yr^{-1} would imply a global burden of 0.049 – 0.18 TgS yr^{-1} of SO_2 and 0.07 – 0.28 TgS yr^{-1} of OCS. The spread in the OCS production from CS_2 is primarily limited by measurements of CS_2 emissions on broad spatial and temporal scales (T Lennartz et al., 2020; Whelan et al., 2018). To improve the understanding of the marine OCS term, additional temporal and special measurements of CS_2 across the marine environment could greatly increases the uncertainty in the indirect OCS production from CS_2.

Figures and Tables

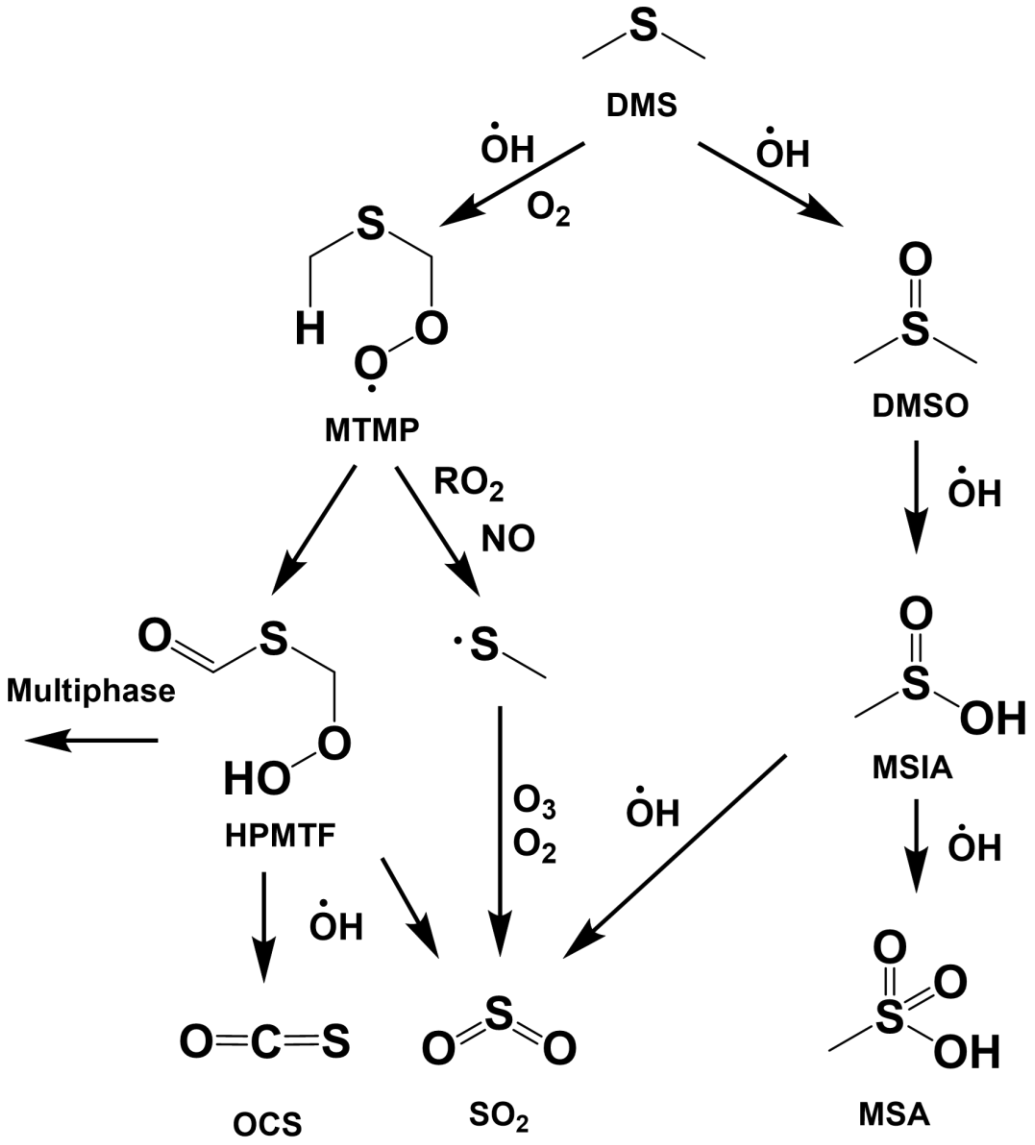

Figure 5.1: Simplified oxidation mechanism of dimethyl sulfide (DMS) with inclusion of HPMTF multiphase loss.

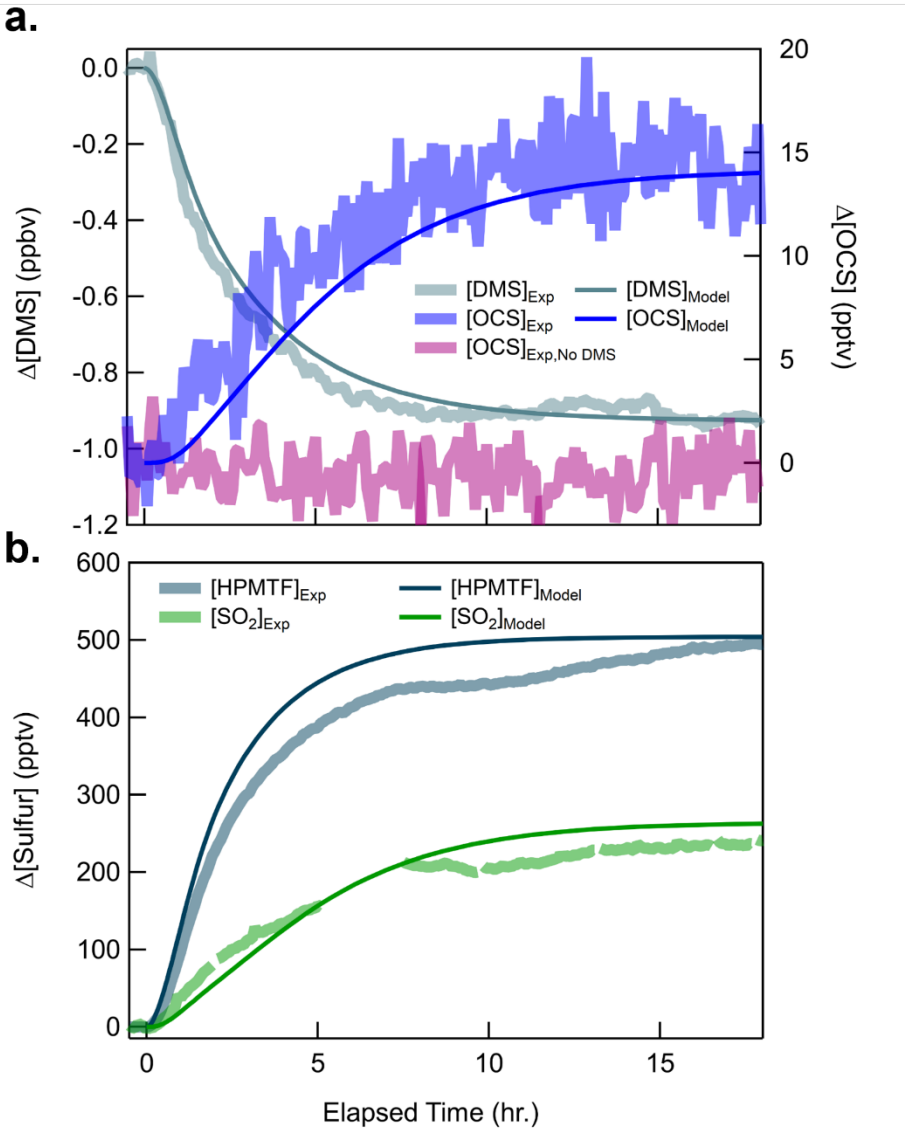

Figure 5.2: Laboratory measurements of OCS, SO_2 and HPMTF production from the OH-oxidation of DMS**.** Measurements (translucent thick lines) and model output (solid thin lines) of the reaction products of the OH-oxidation of DMS.

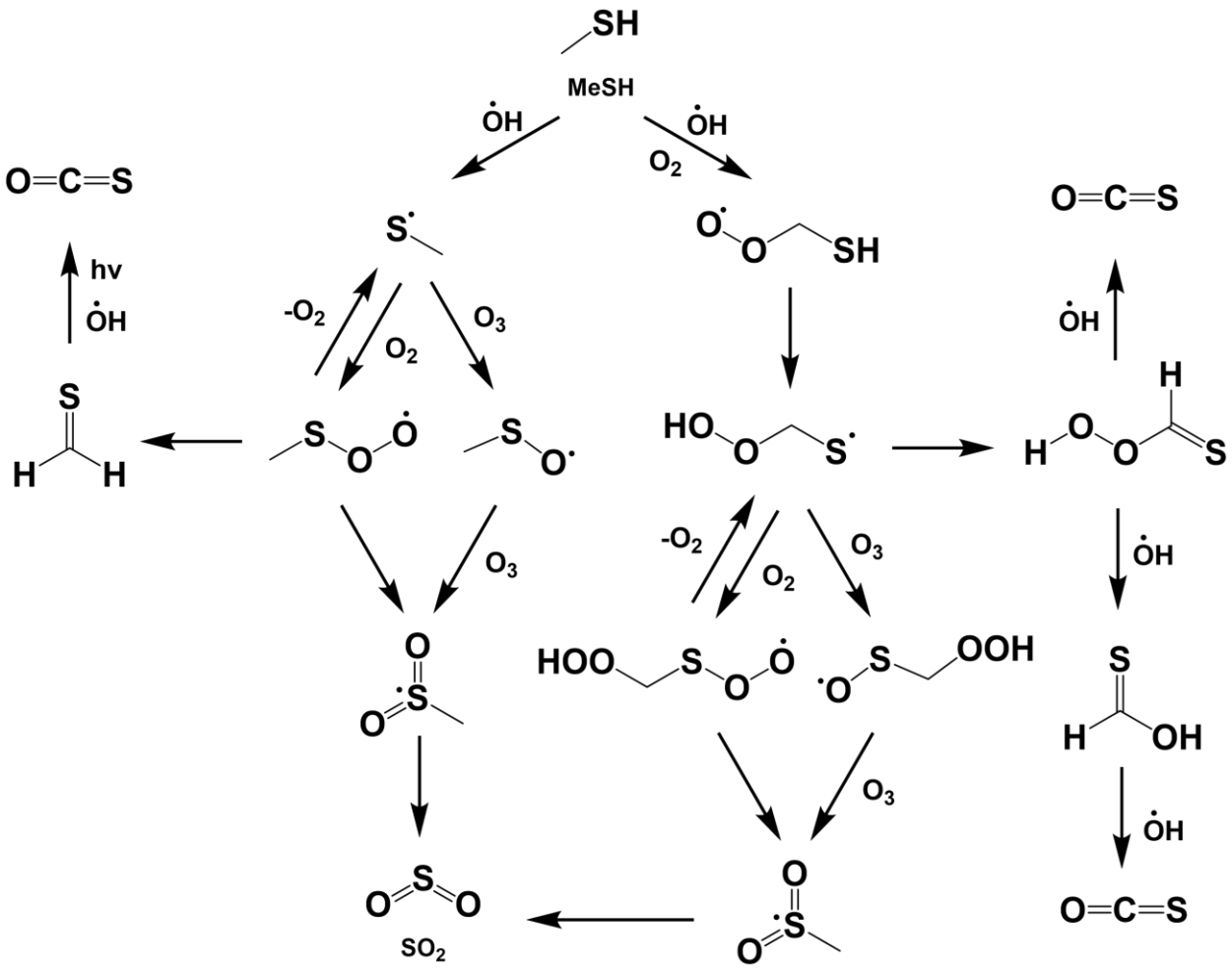

Figure 5.3: Oxidation mechanism of methanethiol (MeSH) with inclusion of the methyl hydrogen abstraction pathway.

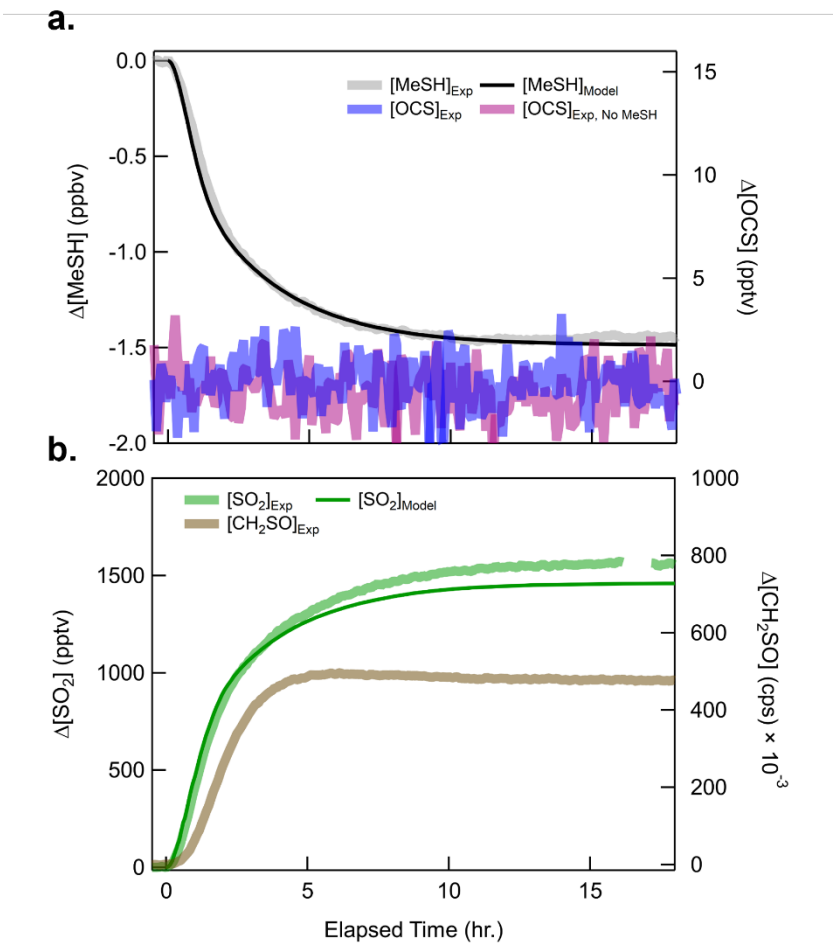

Figure 5.4: Laboratory measurements of OCS, SO_2 and CH_2SO production from the OH-oxidation of MeSH**.** Measurements (translucent thick lines) and model output (solid thin lines) of the reaction products of the OH-oxidation of MeSH.

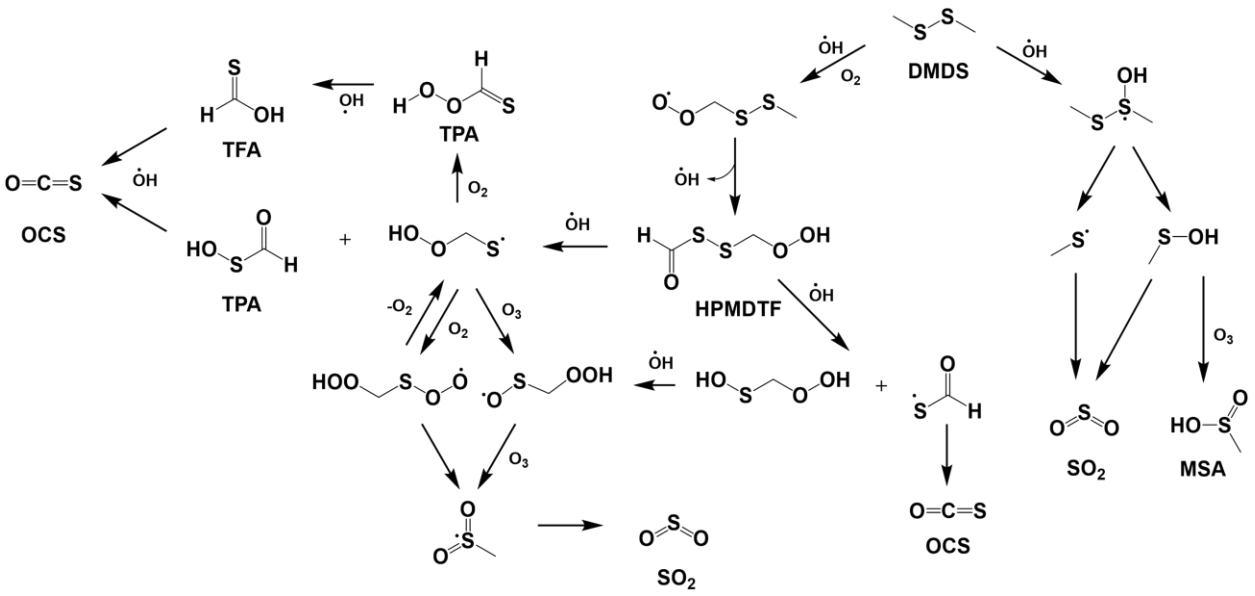

Figure 5.5: Oxidation mechanism of dimethyl disulfide (DMDS) with inclusion of the formation of HPMDTF.

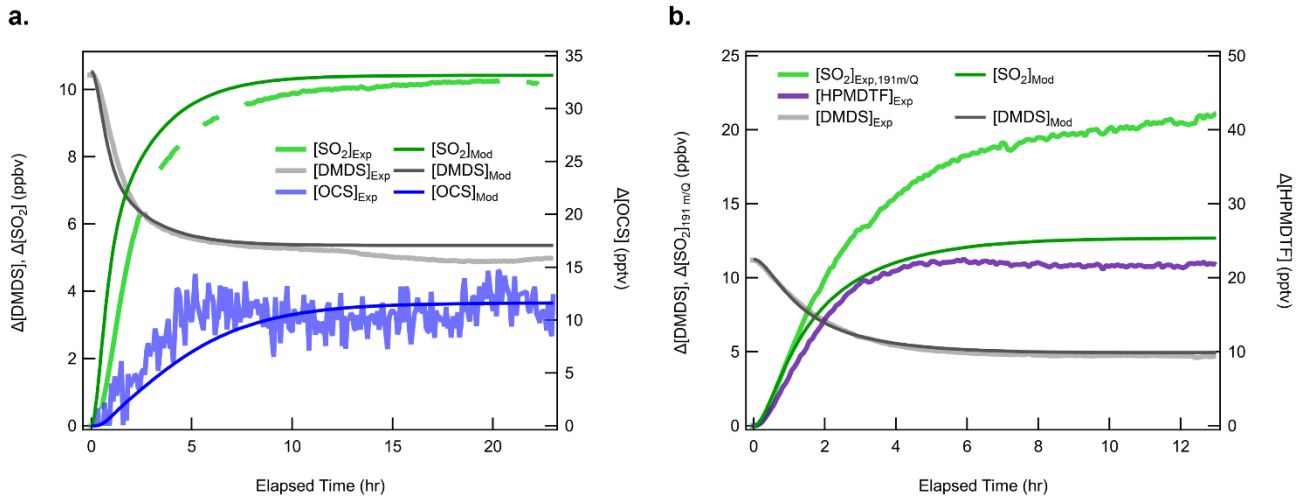

Figure 5.6: Laboratory measurements of OCS, SO_2 and HPMDTF production from the OH-oxidation of DMDS**.** Measurements (translucent thick lines) and model output (solid thin lines) of the reaction products of the OH-oxidation of DMDS.

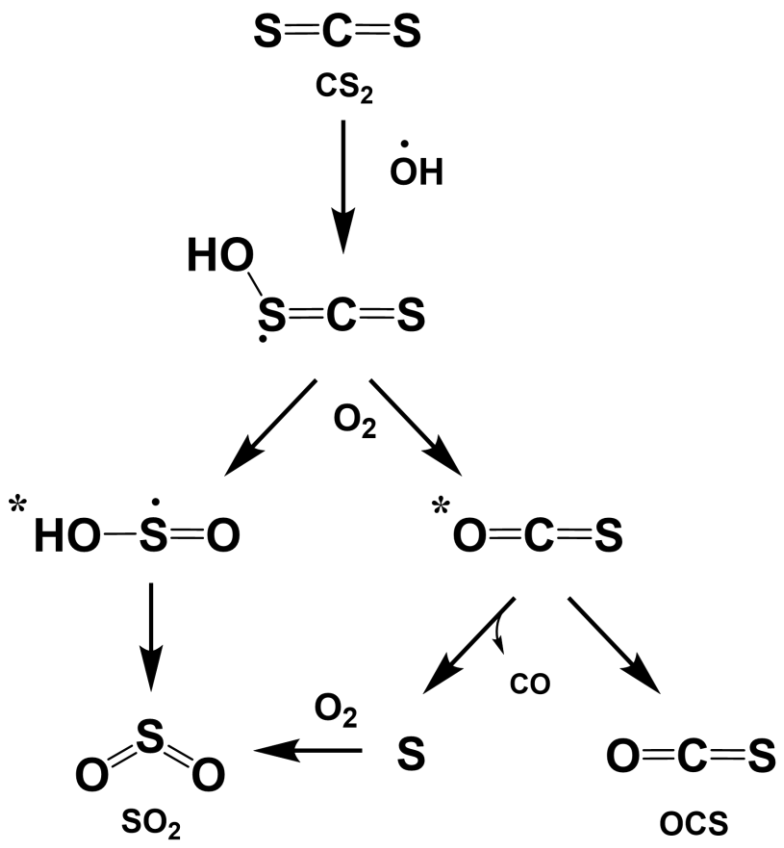

Figure 5.7: Oxidation mechanism of carbon disulfide (CS_2).

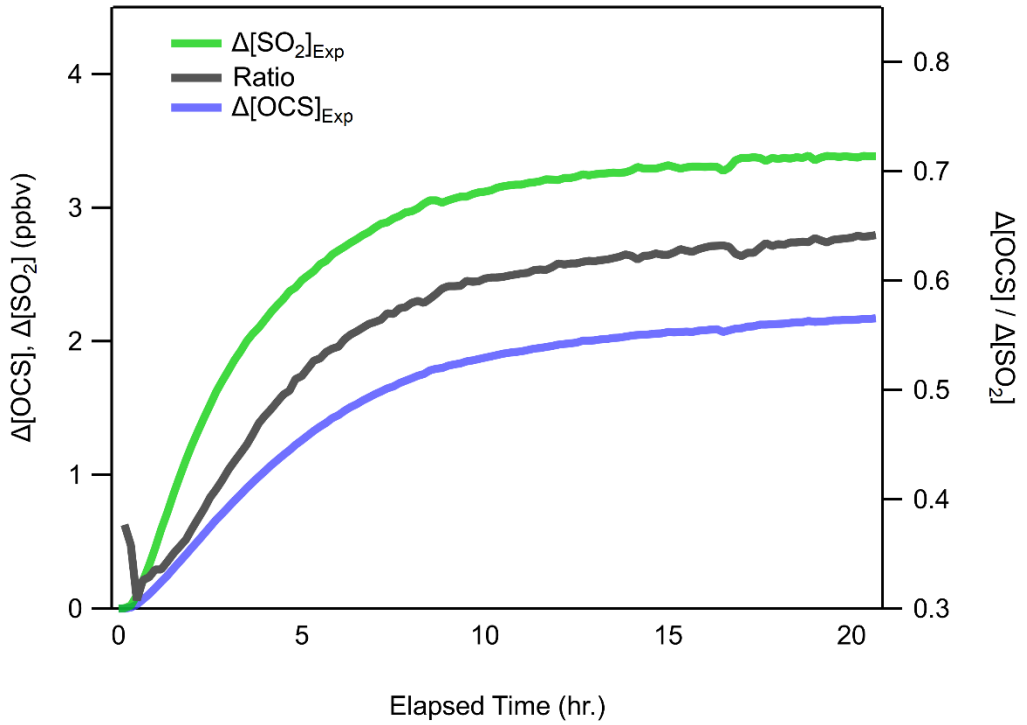

Figure 5.8: Laboratory measurements of OCS (blue line) production, SO_2 (green line) production and the ratio of OCS to SO_2 (black line) from the OH-oxidation of CS_2.

Table 5.1: Oceanic emission (TgS yr^{-1}), molar yield (%) and approximated global production (TgS yr^{-1}) of carbonyl sulfide (OCS) and sulfur dioxide (SO_2) from the OH-oxidation of dimethyl sulfide (DMS), methane thiol (MeSH), dimethyl disulfide (DMDS) and carbon disulfide (CS_2).

VOSC	Ocean emission (TgS yr^{-1})	OCS Molar Yield (%)	OCS production (TgS yr^{-1})	SO_2 Molar Yield (%)	SO_2 production (TgS yr^{-1})
DMS	28.5	‡Multi	0.056 – 0.68	‡Multi	†Add'l model
CS_2	0.08 – 0.30	38	0.03 – 0.11	62	0.050 – 0.19
MeSH	4.7 – 7.0	0	0	0	4.7 – 7.0
DMDS	0 – 0.21	<0.3	$0 – 6 \times 10^{-4}$	99.5	0 – 0.21

‡ The molar yield is not a single value, but dependent on the environmental parameters present during the oxidation of DMS with a particular dependence on the fate of HPMTF.

† Additional global climate modeling is required to determine the range in SO_2 production from the OH-oxidation of DMS

Chapter 4: Reactive uptake of hydroperoxymethyl thioformate to sodium chloride and sodium iodide aerosol particles

Abstract

The oxidation products of dimethyl sulfide (DMS) contribute to the production and growth of cloud condensation nuclei (CCN) in the marine boundary layer. Recent work demonstrates DMS is oxidized by OH radicals to the stable intermediate hydroperoxymethyl thioformate (HPMTF), which is both globally ubiquitous and efficiently lost to multiphase processes in the marine atmosphere. At present, there are no experimental measurements of the reactive uptake of HPMTF to aerosol particles, limiting model implementation of multiphase HPMTF chemistry. Using an entrained aerosol flow reactor combined with chemical ionization mass spectrometry (CIMS), we measured the reactive uptake coefficient (γ) of HPMTF to dry sodium chloride (NaCl), wet NaCl, and wet sodium iodide (NaI) particles to be $1.9 \pm 1.3 \times 10^{-4}$, $1.6 \pm 0.6 \times 10^{-3}$, and $9.2 \pm 2.3 \times 10^{-1}$, respectively. While we did not directly measure the condensed-phase products of HPMTF reactive uptake in this experiment, the ionization products observed in the CIMS instrument provide mechanistic insight on the reaction mechanism of HPMTF with halides.

4.1 Introduction

Dimethyl sulfide (DMS) is a biogenically produced molecule emitted primarily from the ocean and is a significant source of reduced sulfur to the atmosphere.(Bates et al., 1992; Lana et al., 2011) Once emitted, DMS is primarily oxidized by OH and BrO radicals leading ultimately to the formation of both low volatility, water soluble oxidation products (e.g., sulfuric acid and methane sulfonic acid) and long-lived sulfur reservoir species (e.g., carbonyl sulfide). Until recently, it was thought that DMS was mainly oxidized to sulfur dioxide (SO_2) and methane

sulfonic acid (MSA) at high yield, where SO_2 can be further oxidized to sulfuric acid (H_2SO_4) leading to new particle formation while MSA condenses to existing particle resulting in particle growth. As a result, the mechanism by which DMS is oxidized determines the formation and growth rates of aerosol particles to cloud condensation nuclei (CCN) sizes in marine environments, with consequent effects on Earth's radiative budget.(Galí et al., 2018; Korhonen et al., 2008; Vallina et al., 2006) The aerosol radiative forcing by natural aerosols, such as DMS-derived aerosol particles, accounts for the largest uncertainty in radiative forcing in climate models.(Carslaw et al., 2013)

Recent computational, laboratory, and field-studies have shown that the textbook representation of DMS oxidation by OH radicals is incomplete.(Jernigan et al., 2022; Novak et al., 2021; Veres et al., 2020a; Vermeuel et al., 2020a) Specifically, it is now understood that the primary peroxy radical formed from the OH-initiated oxidation of DMS, methylthiomethyl peroxy radical (MTMP, $CH_3SCH_2OO\cdot$), can rapidly isomerize *via* a unimolecular 2-step hydrogen shift reaction to form the stable product hydroperoxymethyl thioformate (HPMTF; $HOOCH_2SCHO$). Isomerization competes with reaction of MTMP with other species, such as NO, but in the marine environment it is estimated that >45% of emitted DMS goes on to form HPMTF(Fung et al., 2021; Khan et al., 2021; Novak et al., 2021; Vermeuel et al., 2020a), resulting in HPMTF being globally ubiquitous.(Veres et al., 2020a) Recent laboratory measurements have found that the gas phase loss of HPMTF to OH is relatively slow ($k_{HPMTF+\ OH} = 1.4 \times 10^{-11}$ cm^3 $molec^{-1}s^{-1}$) allowing multiphase pathways to contribute substantially to the loss of HPMTF the marine atmosphere.(Fung et al., 2021; Jernigan et al., 2022; Novak et al., 2021) Multiphase loss processes include dry deposition, reactive uptake to aerosol particles, and cloud loss. When multiphase loss processes are included, global model simulations predict a 35% decrease in global SO_2 production

and a 92% decrease in global OCS production from DMS oxidation.(Fung et al., 2021; Jernigan et al., 2022; Novak et al., 2021) However, the condensed phase chemistry included in these models is largely unconstrained owing to a lack of direct laboratory measurements of HPMTF uptake coefficients.

In the absence of laboratory measurements of HPMTF multiphase chemistry, global models have used a range of reasonable reactive uptake coefficients for HPMTF ($0.001 < \gamma(\text{HPMTF}) < 0.03$) derived from structurally similar molecules.(Khan et al., 2021; Novak et al., 2021; Vermeuel et al., 2020b) Here, we present laboratory measurements of the reactive uptake of HPMTF to sodium chloride (NaCl) and sodium iodide (NaI) using an entrained aerosol flow reactor combined with chemical ionization mass spectrometry (CIMS). Observations of HPTMF fragmentation within the CIMS instrument under controlled collisional energies are used to make inferences about the condensed phase oxidation mechanism of HPMTF on sea salt aerosol.

4.2 Methods

4.2.1 Generation and detection of aerosol particles and HPMTF

Aerosol particles were generated with a constant output atomizer (TSI Inc., Model 3076) from dilute solutions (ca. 0.5 wt %) of sodium chloride (Sigma-Aldrich, >99.0% purity) and sodium iodine (Sigma-Aldrich, >99.0% purity). The wet aerosol stream was passed through one or more diffusion dryers to condition the aerosol flow to a known relative humidity (RH). As discussed below, γ(HPMTF) was calculated from the dependence of the HPMTF loss rate to the aerosol surface area concentration ($0 - 2 \times 10^5$ μm^2 cm^{-3}). The number concentration of aerosol particles within the flow reactor was modulated by directing a variable fraction of the aerosol flow through either a high-efficiency particulate air filter (PALL, PN 12144) or an unfiltered bypass

line.(Bertram et al., 2009) HPMTF was quantified using a Compact Time of Flight (C-ToF) Chemical Ionization Mass Spectrometer utilizing iodine ion chemistry.(Veres et al., 2020b) Particle size distributions and total surface area concentrations (S_a) of the aerosol particles were measured with a Scanning Electrical Mobility Sizer (SEMS, Model 2002 BMI) and the total aerosol number concentration was verified by comparison with a water-based Condensation Particle Counter (CPC, TSI Model 3787). To account for the difference in relative humidity and subsequent aerosol size distribution of the particles in the flow reactor (30-50% RH) and the SEMS (~10% RH), a particle growth factor was applied to the total aerosol size distribution using the assumption of spherical dry particles. Growth factors for NaCl and NaI particles were taken from Laskina et al.(Laskina et al., 2015) and Minambres et al.(Miñambres et al., 2014), respectively.

4.2.2 Calculation of the HPMTF Reactive Uptake Coefficient

The reactive uptake of HPMTF to aerosol particles was measured at ambient temperature (298 K) and ~1 atm of synthetic zero air (80% N_2, 20% O_2) in a 79 cm cylindrical glass bulk flow reactor (7.6 cm ID) coated in halocarbon wax (Halocarbon, Halocarbon wax series 600) with an average reaction time of 50.5 ± 7.7 seconds. The reaction time of the flow reactor is determined by the inlet flow rate of the instruments and an additional diaphragm pump used to set the total flow through the reactor (4.15 standard liters per minute, SLPM). The relative humidity of the aerosol + HPMTF stream was measured by an RH probe (Vaisala, Model HMP110) at the end of the flow reactor. At present, there is no reported organic synthesis of HPMTF, thus a pure source of HPMTF is not commercially available for experimentation. A steady source of HPMTF in air ([HPMTF] = 450 – 550 ppt) was generated from the OH-initiated oxidation of DMS within a 0.6 m^3 PTFE environmental chamber run under a continuous flow mode at ambient temperature and 1 atm of synthetic, dry zero air, as described in Jernigan et al.(Jernigan et al., 2022) The relative

humidity of the flow reactor was set by the ratio of a humified aerosol flow (RH>80%) and the dry flow of the HPMTF source flow (RH<1%). Fine tuning of the reactor RH was done by supplementing humified zero air to the inlet of the flow reactor, keeping the total flow at 4.15 SLPM. By varying the number of diffusion dryers, the age of the dryers, and the volumetric flow of the supplemental humidified air, a range of flow reactor RH was achieved (30-50% RH).

The following expressions was used to derive the pseudo-first-order rate coefficient for reactant gas loss to particles (k_{het})(Bertram et al., 2009) (E4.3):

$$\ln([\mathrm{HPMTF}]_i) = \ln\left([HPMTF]_f^{w/\ NaX}\right) + (k_{wall} + k_{het}) \cdot \Delta t \quad \text{(E4.1)}$$

$$\ln([\mathrm{HPMTF}]_i) = \ln\left([\mathrm{HPMTF}]_f^{w/o\ NaX}\right) + (k_{wall}) \cdot \Delta t \quad \text{(E4.2)}$$

$$k_{het} = \left(\frac{1}{\Delta t}\right) \ln\left(\frac{[\mathrm{HPMTF}]_f^{w/o\ NaX}}{[\mathrm{HPMTF}]_f^{w/\ NaX}}\right) \quad \text{(E4.3)}$$

where $[\mathrm{HPMTF}]_i$, $[\mathrm{HPMTF}]_f^{w/o\ NaX}$, and $[\mathrm{HPMTF}]_f^{w/\ NaX}$, are the concentrations of a HPMTF entering the flow reactor, exiting the flow reactor without NaX (X = Cl^-, I^-) particles present, and exiting the flow reactor with NaX particles present, respectively. k_{wall}, k_{het}, and Δt refer to the unimolecular loss rate constant with the wall (units of s^{-1}), the pseudo-first-order rate coefficient for reactant gas loss to particles (units of s^{-1}), and the average reaction time within the flow reactor (units of s), respectively.

The observed first-order rate coefficient for reactant gas loss to particles can also be written as a function of the particle surface area and dependent on the reactive uptake of the gas to a surface (E4):

$$k_{het}(S_a) = \frac{\omega \cdot \gamma}{4} \times S_a \quad \text{(E4.4)}$$

where S_a is the total surface area of the aerosol stream per unit volume ($0 – 2 \times 10^{-3}$, units of cm^{-1}), ω is the mean molecular speed of HPMTF (2.6×10^4, units of cm s^{-1}) and γ is the measured uptake coefficient (unitless). A linear regression of k_{het} and aerosol surface area yields a slope of ($\frac{\omega \cdot \gamma}{4}$). The absolute sensitivity of the HPMTF is not required for the calculation of the reactive uptake as the equation relies on the ratio of the HPMTF concentrations with and without aerosol. In terms of I^- CIMS sensitivity, previous studies have found the $I{:}I{\cdot}H_2O$ ratio, that is the relationship between the intensity of the iodide ion (127 m/Q) to that of the iodide water cluster (145 m/Q), has a strong effect on the absolute sensitivity of the species of interest.(Vermeuel et al., 2020b) Over the course of multiple experiments, the $I{:}I{\cdot}H_2O$ ratio was consistent (<2% change) for experiments of a target RH. The CIMS sensitivity to HPMTF was assumed to be constant over a given experiment as long as the $I{:}I{\cdot}H_2O$ ratio remained constant.

4.3 Results and Discussion

4.3.1 Reactive Uptake of HPMTF

The response of HPMTF to changes in particle surface area for a representative experiment is shown in **Figure 4.1**. Results from the HPMTF uptake experiments are shown in **Figure 4.2**, where individual k_{het} is plotted against the measured S_a at the end of the flow reactor. Each k_{het} data point was calculated using E4.3, where $[\mathrm{HPMTF}]_f^{w/o\ NaX}$ and $[\mathrm{HPMTF}]_f^{w/\ NaX}$ are determined for each S_a concentration. The average residence time (Δt) within the flow reactor, used in E3, was 50.5 ± 7.7 s as discussed above. This was determined using the delay time between the removal or addition of the aerosols within the flow reactor and the detection of a change in the signal of HPMTF and I_2, a product of O_3 and NaI aerosol. The experimental derived Δt was used to approximate the uncertainty in the average residence time HPMTF. As seen in E4.4, the slope of

the regression of k_{het} on S_a is a direct observation of the reactive uptake of HPMTF (γ_{HPMTF}) onto NaCl and NaI aerosols (**Figure 4.2**). Experimental points were removed from the regression when large differences in the residence time (due to inlet clogging) and RH (>5% RH), were observed between the particle on and particle off states. Significant changes in the residence time and RH within a step could result in deviations in Δt and k_{wall}, that are required to be constant in E4.1 and E4.2.

4.3.1.1 HPMTF uptake to NaCl aerosol particles

For the NaCl uptake experiments, two RH values, indicative of an RH above and below the efflorescence point of NaCl (43% RH)(Biskos et al., 2006; Pinterich et al., 2017; Weis & Ewing, 1999), were explored to determine the role of particle liquid water (**Figure 4.2**). The hygroscopic growth factor for NaCl ranges from about 1.4 at 43% RH (the ERH) to 1.6 at 60% RH. These correspond to increases in surface area of factors of 1.96 to 2.56 over the dry particles (measured at 10% RH).(Biskos et al., 2006; Pinterich et al., 2017; Weis & Ewing, 1999) At a relative humidity >43%, k_{het} was strongly correlated with S_a ($R^2 = 0.94$), resulting in a calculated reactive uptake coefficient (γ) of $1.6 \pm 0.6 \times 10^{-3}$. In contrast, observations at RH <43% yielded a reactive uptake coefficient of $1.9 \pm 1.3 \times 10^{-4}$. The enhanced γ on effloresced compared to dry NaCl aerosols implies that HPMTF's solubility and hydrolysis reactions play a role in the uptake of HPMTF. No detectable gas-phase products of the HPMTF reaction were detected with the I^- CIMS.

4.3.1.2 HPMTF uptake to NaI aerosol particles

The NaI uptake experiments were only performed at a single relative humidity, as pure NaI particles remain hydrated at all relative humidity values considered here.(Miñambres et al., 2011)

A reactive uptake coefficient of $9.2 \pm 2.3 \times 10^{-1}$ was determined from the linear regression. The observed increase in HPMTF uptake, relative to NaCl, implies an increased chemical reactivity of HPMTF with NaI. As HPMTF's solubility and hydrolysis would be similar under similar RH values and aerosol phase state, chemical reactions involving iodine are likely driving the increased loss compared to uptake on NaCl. When reactions at the aerosol surface are fast, gas-phase diffusion can be the rate limiting factor in the observed loss.(Fuchs & Sutugin, 1971; Hanson & Kosciuch, 2003) To account for the impact of diffusion limitations on our measured uptake coefficient (γ_{exp}), we corrected γ for the NaI experiments using the approach outlined by Hanson and Kosciuch (2003).(Hanson & Kosciuch, 2003) Using our observed average log-normal particle size distribution with a radius (r_p) of 32 nm and width (ln σ) of 0.61, we calculate and apply a gas-diffusion correction coefficient ($\lambda(\overline{r_s})$) of 0.3 to determine the actual value of γ (E5).

$$\frac{1}{\gamma} = \frac{1}{\gamma_{exp}} - \lambda(\overline{r_s}) \quad \text{(E5)}$$

The only gas-phase product observed was I_2 (detected as $[I_3]^-$ at 381 m/Q) following the addition of NaI particles to the flow reactor. While previous work has found reactions of iodide with ROOH species can liberate I_2 (Cadle & Huff, 1950), isolation of this path is difficult given the efficient production of I_2 from the reaction of ozone with I^-.(Garland & Curtis, 1981) Based on the concentration of I_2, we expect that most (if not all) of the I_2 production arises from the reaction of ozone (present within the HPMTF flow at concentrations of 50 – 80 ppb) with iodide anions either on the reactor wall or in the suspended particles.(Rouvière et al., 2010)

4.3.2 Insight into HPMTF condensed phase reactions

The dependence of γ(HPMTF) on halide speciation suggests that HPMTF reacts preferentially with I^- compared with Cl^-, and HPMTF uptake is not driven solely by solubility and

hydrolysis reactions. The differing halide reactivity towards peroxide oxidation or nucleophilic substitution at the carbonyl functional groups of HPMTF could explain the difference in reactive uptake.(Cadle & Huff, 1950; Lowry & Richardson, 1987) While we did not directly measure the products of HPMTF multiphase chemistry, we can consider the product ion distribution in the CIMS to discern the dominant reaction pathways for HPMTF in small halide-water clusters. The CIMS can be operated either using I^- (the default operating condition) or Cl^- as the reagent ion, and these are predominately observed as $X^-(H_2O)_n$ clusters with HPMTF detected as $X^-(HPMTF)(H_2O)_n$.(Staudt, 2019) The reactivity of HPMTF in these small halide-water clusters provides insight into how HPMTF might react with hydrated NaI and NaCl particles. Experimentally, by changing the collisional energy imparted on the $X^-(HPMTF)(H_2O)_n$ cluster in the CIMS to induce dissociation of the cluster, we can identify whether a reaction has occurred in the cluster within the CIMS. It is important to note that the added collisional energy is not large enough to induce a chemical reaction, just to break apart the ion-neutral cluster. This is accomplished in the CIMS by scanning the electric field at the entrance to one of the focusing quadrupoles.(Brophy & Farmer, 2016; Lopez-Hilfiker et al., 2016) In the absence of a reaction, the $X^-(HPMTF)(H_2O)_n$ cluster will dissociate to X^-, H_2O, and neutral HPMTF and no new product ion will be observed. If a reaction has occurred in the $X^-(HPMTF)(H_2O)_n$ cluster, we would observe a commensurate increase in a product ion signal with the decrease in $X^-(HPMTF)$ signal. When scans were run using either ionization modes, a dominant peak at 235 m/z and 143 m/z was identified and attributed to a HPMTF cluster with iodine and chloride, respectively. Under both ionization modes, we observe an increase in the intensity of $CHOS^-$ (61 m/z) as the declustering voltage was increased within the CIMS instrument and that corresponds to a decrease in the HPMTF cluster signal (**Figure 4.3**). The change in the measured CIMS ion intensity was not

conserved in the experiment, were we measure a 2 ncps decrease in I^-(HPMTF) compared to a to 1 ncps increase in $CHOS^-$ for the iodine CIMS. A similar result was found for the Cl^- CIMS experiment. This discrepancy could be due to differences in the transmission of the two ions, dissociation of HPMTF into minor fragments, or declustering of I^-(HPMTF) into a neutral HPMTF + I^-. Nonetheless, for both I^- and Cl^- these results provide evidence that HPMTF reacts with halide ions, at least in these small clusters, to produce some new product (here, detected as $CHOS^-$).

While we did not directly probe the condensed phase reaction of HPMTF, the CIMS product ion distribution provides insight into the outcome of a reaction between HPMTF and a halide ion in a small cluster. To explain the formation of the $CHOS^-$ ion, we suggest a substitution like reaction between the reagent ion and HPMTF:

$$[X]^- + HOOCH_2SCHO \rightarrow [X \cdot HOOCH_2SCHO]^- \rightarrow HOOCH_2X + [SCHO]^- \quad X = I, C$$

If HPMTF reacts in a similar way with a hydrated ion either at the surface or in the bulk of an aqueous aerosol, this analysis suggests that HPMTF may form $CHOS^-$ as the first-generation product. It is not yet clear what the condensed-phase fate of the $CHOS^-$ ion is. Given that thioformic acid (TFA, CH(=O)SH) and its conjugate base ($CHOS^-$) are structurally similar to formic acid (HCOOH) and its conjugate base formate ($HCOO^-$), we may be able to use the condensed phase reactions of formate as an indicator of what the condensed phase fate of $CHOS^-$ is. By analogy to HCOOH:$HCOO^-$ chemistry, we propose two potential fates of thioformic acid; OH oxidation and evaporation.(Chameides & Davis, 1983) The asymmetric nature to TFA:$CHOS^-$ would allow for two competing product distributions, H_2S:HS^- + CO_2 and H_2O:HO^- + OCS,(Anbar

& Neta, 1967; Jacob, 1986) with the eventual fate of aqueous hydrogen sulfide (H_2S) ending as sulfate (SO_4^{2-}) through ·OH and ozone reactions.(Hoigné et al., 1985; Zhang & Millero, 1993) The evaporation of thioformic acid could lead to a similar product distribution though OH oxidation in the gas phase rather than aqueous (Wine et al., 1985).

4.4 Conclusions and Atmospheric implications

We report measurements of γ(HPMTF) to dry sodium chloride (NaCl), wet NaCl, and wet sodium iodide (NaI) particles, with values of $1.9 \pm 1.3 \times 10^{-4}$, $1.6 \pm 0.6 \times 10^{-3}$, and $9.2 \pm 2.3 \times 10^{-1}$, respectively. We find that HPMTF uptake is enhanced on deliquesced aerosol surfaces and increased nucleophilicity of the species within the aerosol. Insights from the product ion distribution within the I^- CIMS suggest that the aqueous phase chemistry of HPMTF lead to the formation of H_2S, OCS and sulfate through a thioformic intermediate, however focused investigations are needed to explore this chemistry.

Recent work evaluating the fate and atmospheric implications of HPMTF used an uptake value of 0.01 for HPMTF to marine aerosols, whose composition is primarily composed of sea salt ions (e.g. Na^+, Cl^-, and SO_4^{2-}),(O'Dowd & de Leeuw, 2007; Xiao et al., 2018) and cloud droplets in a global chemical transport model.(Novak et al., 2021) A tenfold reduction in γ(HPMTF), as presented here, would lead to an overall decrease in the fraction of HPMTF that is lost to aerosol particles. Due to large cloud drop surface area and long in-cloud residence times, we do not expect the reduction in γ(HPMTF) reported here to impact modeled HPMTF loss to clouds. This is consistent with the direct measurements of rapid HPMTF cloud loss reported in Novak et al.(Novak et al., 2021)

The reactive uptake to and subsequent oxidation of HPMTF in marine aerosol may be different than that reported here for NaCl, due to variations in particle acidity and chemical composition.(Angle et al., 2021; Bertram et al., 2018) Previous studies on uptake of carbonyl compounds(Kroll et al., 2005; Liggio et al., 2005; Liggio & Li, 2006; Wu et al., 2015) and a structurally similar molecule to HPMF (hydroperoxmethyl formate)(Thamm et al., 1996) have shown that the reaction kinetics depend on both acidity and ionic strength. For this reason, we recommend additional laboratory work on the magnitude of uptake value and the product distribution of HPMTF to organic enriched, acidic, and chemically complex surfaces. In both Jernigan et al.(Jernigan et al., 2022) and Novak et al.(Novak et al., 2021) it was assumed that HPMTF multiphase chemistry led to sulfate formation, arresting OCS formation in the OH-oxidation of HPMTF. Future work should explore the potential for production of OCS in the condensed-phase oxidation of HPMTF.

Acknowledgements

This work was supported by the NSF Center for Aerosol Impacts on Chemistry of the Environment under Grant CHE 1801971.

References

Anbar, M., & Neta, P. (1967). A compilation of specific bimolecular rate constants for the reactions of hydrated electrons, hydrogen atoms and hydroxyl radicals with inorganic and organic compounds in aqueous solution. *The International Journal of Applied Radiation and Isotopes*, *18*(7), 493–523. https://doi.org/https://doi.org/10.1016/0020-708X(67)90115-9

Angle, K. J., Crocker, D. R., Simpson, R. M. C., Mayer, K. J., Garofalo, L. A., Moore, A. N., Mora Garcia, S. L., Or, V. W., Srinivasan, S., Farhan, M., Sauer, J. S., Lee, C., Pothier, M. A., Farmer, D. K., Martz, T. R., Bertram, T. H., Cappa, C. D., Prather, K. A., & Grassian, V. H. (2021). Acidity across the interface from the ocean surface to sea spray aerosol. *Proceedings of the National Academy of Sciences*, *118*(2), e2018397118. https://doi.org/10.1073/pnas.2018397118

Bates, T. S., Lamb, B. K., Guenther, A., Dignon, J., & Stoiber, R. E. (1992). Sulfur emissions to the atmosphere from natural sourees. *Journal of Atmospheric Chemistry*, *14*(1), 315–337. https://doi.org/10.1007/BF00115242

Bertram, T. H., Cochran, R. E., Grassian, V. H., & Stone, E. A. (2018). Sea spray aerosol chemical composition: elemental and molecular mimics for laboratory studies of heterogeneous and multiphase reactions. *Chemical Society Reviews*, *47*(7), 2374–2400. https://doi.org/10.1039/C7CS00008A

Bertram, T. H., Thornton, J. A., & Riedel, T. P. (2009). An experimental technique for the direct measurement of N_2O_5 reactivity on ambient particles. *Atmospheric Measurement Techniques Discussions*, *2*(2), 689–723. https://doi.org/10.5194/amtd-2-689-2009

Biskos, G., Malinowski, A., Russell, L. M., Buseck, P. R., & Martin, S. T. (2006). Nanosize Effect on the Deliquescence and the Efflorescence of Sodium Chloride Particles. *Aerosol Science and Technology*, *40*(2), 97–106. https://doi.org/10.1080/02786820500484396

Brophy, P., & Farmer, D. K. (2016). Clustering, methodology, and mechanistic insights into acetate chemical ionization using high-resolution time-of-flight mass spectrometry. *Atmospheric Measurement Techniques*, *9*(8), 3969–3986. https://doi.org/10.5194/amt-9-3969-2016

Cadle, R. D., & Huff, H. (1950). The The Oxidation of Iodide to Iodine by Dilute Solutions of Organic Peroxides. *The Journal of Physical Chemistry*, *54*(8), 1191–1195.

Carslaw, K. S., Lee, L. A., Reddington, C. L., Pringle, K. J., Rap, A., Forster, P. M., Mann, G. W., Spracklen, D. v., Woodhouse, M. T., Regayre, L. A., & Pierce, J. R. (2013). Large contribution of natural aerosols to uncertainty in indirect forcing. *Nature*, *503*(7474), 67–71. https://doi.org/10.1038/nature12674

Chameides, W. L., & Davis, D. D. (1983). Aqueous-phase source of formic acid in clouds. *Nature*, *304*(5925), 427–429. https://doi.org/10.1038/304427a0

Fuchs, N. A., & Sutugin, A. G. (1971). High-dispersed aerosols. In *Topics in current aerosol research* (p. 1). Elsevier.

Fung, K. M., Heald, C., Kroll, J., Wang, S., Jo, D., Gettelman, A., Lu, Z., Liu, X., Zaveri, R., Apel, E., Blake, D., Jimenez, J.-L., Campuzano-Jost, P., Veres, P., Bates, T., Shilling, J., & Zawadowicz, M. (2021). Exploring DMS oxidation and implications for global aerosol radiative forcing. *Atmospheric Chemistry and Physics*, *2021*, 1–58. https://doi.org/10.5194/acp-2021-782

Galí, M., Levasseur, M., Devred, E., Simó, R., & Babin, M. (2018). Sea-surface dimethylsulfide (DMS) concentration from satellite data at global and regional scales. *Biogeosciences*, *15*(11), 3497–3519. https://doi.org/10.5194/bg-15-3497-2018

Garland, J. A., & Curtis, H. (1981). Emission of iodine from the sea surface in the presence of ozone. *Journal of Geophysical Research: Oceans*, *86*(C4), 3183–3186. https://doi.org/https://doi.org/10.1029/JC086iC04p03183

Hanson, D., & Kosciuch, E. (2003). The NH3 Mass Accommodation Coefficient for Uptake onto Sulfuric Acid Solutions. *The Journal of Physical Chemistry A*, *107*(13), 2199–2208. https://doi.org/10.1021/jp021570j

Hoigné, J., Bader, H., Haag, W. R., & Staehelin, J. (1985). Rate constants of reactions of ozone with organic and inorganic compounds in water—III. Inorganic compounds and radicals. *Water Research*, *19*(8), 993–1004. https://doi.org/https://doi.org/10.1016/0043-1354(85)90368-9

Jacob, D. J. (1986). Chemistry of OH in remote clouds and its role in the production of formic acid and peroxymonosulfate. *Journal of Geophysical Research: Atmospheres*, *91*(D9), 9807–9826. https://doi.org/https://doi.org/10.1029/JD091iD09p09807

Jernigan, C. M., Fite, C. H., Vereecken, L., Berkelhammer, M. B., Rollins, A. W., Rickly, P. S., Novelli, A., Taraborrelli, D., Holmes, C. D., & Bertram, T. H. (2022). Efficient Production of Carbonyl Sulfide in the Low-NO x Oxidation of Dimethyl Sulfide . *Geophysical Research Letters*, *49*(3), e2021GL096838. https://doi.org/10.1029/2021gl096838

Khan, M. A. H., Bannan, T. J., Holland, R., Shallcross, D. E., Archibald, A. T., Matthews, E., Back, A., Allan, J., Coe, H., Artaxo, P., & Percival, C. J. (2021). Impacts of Hydroperoxymethyl Thioformate on the Global Marine Sulfur Budget. *ACS Earth and Space Chemistry*, *5*(10), 2577–2586. https://doi.org/10.1021/acsearthspacechem.1c00218

Korhonen, H., Carslaw, K. S., Spracklen, D. v., Mann, G. W., & Woodhouse, M. T. (2008). Influence of oceanic dimethyl sulfide emissions on cloud condensation nuclei concentrations and seasonality over the remote Southern Hemisphere oceans: A global model study. *Journal of Geophysical Research Atmospheres*, *113*(15), 1–16. https://doi.org/10.1029/2007JD009718

Kroll, J. H., Ng, N. L., Murphy, S. M., Varutbangkul, V., Flagan, R. C., & Seinfeld, J. H. (2005). Chamber studies of secondary organic aerosol growth by reactive uptake of simple carbonyl compounds. *Journal of Geophysical Research Atmospheres*, *110*(23), 1–10. https://doi.org/10.1029/2005JD006004

Lana, A., Bell, T. G., Simó, R., Vallina, S. M., Ballabrera-Poy, J., Kettle, A. J., Dachs, J., Bopp, L., Saltzman, E. S., Stefels, J., Johnson, J. E., & Liss, P. S. (2011). An updated climatology of surface dimethlysulfide concentrations and emission fluxes in the global ocean. *Global Biogeochemical Cycles*, *25*(1), 1–17. https://doi.org/10.1029/2010GB003850

Laskina, O., Morris, H. S., Grandquist, J. R., Qin, Z., Stone, E. A., Tivanski, A. v, & Grassian, V. H. (2015). Size Matters in the Water Uptake and Hygroscopic Growth of Atmospherically Relevant Multicomponent Aerosol Particles. *The Journal of Physical Chemistry A*, *119*(19), 4489–4497. https://doi.org/10.1021/jp510268p

Liggio, J., & Li, S. M. (2006). Reactive uptake of pinonaldehyde on acidic aerosols. *Journal of Geophysical Research Atmospheres*, *111*(24), 1–12. https://doi.org/10.1029/2005JD006978

Liggio, J., Li, S. M., & McLaren, R. (2005). Reactive uptake of glyoxal by particulate matter. *Journal of Geophysical Research D: Atmospheres*, *110*(10), 1–13. https://doi.org/10.1029/2004JD005113

Lopez-Hilfiker, F. D., Iyer, S., Mohr, C., Lee, B. H., D'Ambro, E. L., Kurtén, T., & Thornton, J. A. (2016). Constraining the sensitivity of iodide adduct chemical ionization mass spectrometry to multifunctional organic molecules using the collision limit and thermodynamic stability of iodide ion adducts. *Atmospheric Measurement Techniques*, *9*(4), 1505–1512.

Lowry, T. H., & Richardson, K. S. (1987). *Mechanism and theory in organic chemistry* (Vol. 294). Harper & Row New York.

Miñambres, L., Méndez, E., Sánchez, M. N., Castaño, F., & Basterretxea, F. J. (2011). Water uptake properties of internally mixed sodium halide and succinic acid particles. *Atmospheric Environment*, *45*(32), 5896–5902. https://doi.org/10.1016/j.atmosenv.2011.06.062

Miñambres, L., Méndez, E., Sánchez, M. N., Castaño, F., & Basterretxea, F. J. (2014). The effect of low solubility organic acids on the hygroscopicity of sodium halide aerosols. *Atmospheric Chemistry and Physics*, *14*(20), 11409–11425. https://doi.org/10.5194/acp-14-11409-2014

Novak, G. A., Fite, C. H., Holmes, C. D., Veres, P. R., Neuman, J. A., Faloona, I., Thornton, J. A., Wolfe, G. M., Vermeuel, M. P., Jernigan, C. M., Peischl, J., Ryerson, T. B., Thompson, C. R., Bourgeois, I., Warneke, C., Gkatzelis, G. I., Coggon, M. M., Sekimoto, K., Bui, T. P., … Bertram, T. H. (2021). Rapid cloud removal of dimethyl sulfide oxidation products limits SO 2 and cloud condensation nuclei production in the marine atmosphere. *Proceedings of the National Academy of Sciences*, *118*(42), e2110472118. https://doi.org/10.1073/pnas.2110472118

O'Dowd, C. D., & de Leeuw, G. (2007). Marine aerosol production: a review of the current knowledge. *Philosophical Transactions of the Royal Society A: Mathematical, Physical and Engineering Sciences*, *365*(1856), 1753–1774. https://doi.org/10.1098/rsta.2007.2043

Pinterich, T., Spielman, S. R., Wang, Y., Hering, S. v, & Wang, J. (2017). A humidity-controlled fast integrated mobility spectrometer (HFIMS) for rapid measurements of particle hygroscopic growth. *Atmos. Meas. Tech.*, *10*(12), 4915–4925. https://doi.org/10.5194/amt-10-4915-2017

Rouvière, A., Sosedova, Y., & Ammann, M. (2010). Uptake of Ozone to Deliquesced KI and Mixed KI/NaCl Aerosol Particles. *The Journal of Physical Chemistry A*, *114*(26), 7085–7093. https://doi.org/10.1021/jp103257d

Staudt, S. (2019). Heterogeneous Reactions of Nocturnal Nitrogen Oxides at Atmospherically Relevant Aqueous Interfaces. In *ProQuest Dissertations and Theses*. https://ezproxy.library.wisc.edu/login?url=https://www.proquest.com/dissertations-theses/heterogeneous-reactions-nocturnal-nitrogen-oxides/docview/2306547863/se-2?accountid=465

Thamm, J., Wolff, S., Turner, W. v, Gäb, S., Thomas, W., Zabel, F., Fink, E. H., & Becker, K. H. (1996). Proof of the formation of hydroperoxymethyl formate in the ozonolysis of ethene: synthesis and FT-IR spectra of the authentic compound. *Chemical Physics Letters*, *258*(1), 155–158. https://doi.org/https://doi.org/10.1016/0009-2614(96)00625-2

Vallina, S. M., Simó, R., & Gassó, S. (2006). What controls CCN seasonality in the Southern Ocean? A statistical analysis based on satellite-derived chlorophyll and CCN and model-estimated OH radical and rainfall. *Global Biogeochemical Cycles*, *20*(1), 1–13. https://doi.org/10.1029/2005GB002597

Veres, P. R., Andrew Neuman, J., Bertram, T. H., Assaf, E., Wolfe, G. M., Williamson, C. J., Weinzierl, B., Tilmes, S., Thompson, C. R., Thames, A. B., Schroder, J. C., Saiz-Lopez, A., Rollins, A. W., Roberts, J. M., Price, D., Peischl, J., Nault, B. A., Møller, K. H., Miller, D. O., … Ryerson, T. B. (2020a). Global airborne sampling reveals a previously unobserved dimethyl sulfide oxidation mechanism in the marine atmosphere. *Proceedings of the National Academy of Sciences of the United States of America*, *117*(9), 4505–4510. https://doi.org/10.1073/pnas.1919344117

Veres, P. R., Andrew Neuman, J., Bertram, T. H., Assaf, E., Wolfe, G. M., Williamson, C. J., Weinzierl, B., Tilmes, S., Thompson, C. R., Thames, A. B., Schroder, J. C., Saiz-Lopez, A., Rollins, A. W., Roberts, J. M., Price, D., Peischl, J., Nault, B. A., Møller, K. H., Miller, D. O., … Ryerson, T. B. (2020b). Global airborne sampling reveals a previously unobserved dimethyl sulfide oxidation mechanism in the marine atmosphere. *Proceedings of the National Academy of Sciences of the United States of America*, *117*(9), 4505–4510. https://doi.org/10.1073/pnas.1919344117

Vermeuel, M. P., Novak, G. A., Jernigan, C. M., & Bertram, T. H. (2020a). Diel Profile of Hydroperoxymethyl Thioformate: Evidence for Surface Deposition and Multiphase Chemistry. *Environmental Science & Technology*. https://doi.org/10.1021/acs.est.0c04323

Vermeuel, M. P., Novak, G. A., Jernigan, C. M., & Bertram, T. H. (2020b). Diel Profile of Hydroperoxymethyl Thioformate: Evidence for Surface Deposition and Multiphase Chemistry. *Environmental Science and Technology*, *54*(19), 12521–12529. https://doi.org/10.1021/acs.est.0c04323

Weis, D. D., & Ewing, G. E. (1999). Water content and morphology of sodium chloride aerosol particles. *Journal of Geophysical Research: Atmospheres*, *104*(D17), 21275–21285. https://doi.org/https://doi.org/10.1029/1999JD900286

Wine, P. H., Astalos, R. J., & Mauldin III, R. L. (1985). Kinetic and mechanistic study of the hydroxyl+ formic acid reaction. *The Journal of Physical Chemistry*, *89*(12), 2620–2624.

Wu, Q. Q., Huang, L. B., Liang, H., Zhao, Y., Huang, D., & Chen, Z. M. (2015). Heterogeneous reaction of peroxyacetic acid and hydrogen peroxide on ambient aerosol particles under dry and humid conditions: Kinetics, mechanism and implications. *Atmospheric Chemistry and Physics*, *15*(12), 6851–6866. https://doi.org/10.5194/acp-15-6851-2015

Xiao, H.-W., Xiao, H.-Y., Shen, C.-Y., Zhang, Z.-Y., & Long, A.-M. (2018). Chemical Composition and Sources of Marine Aerosol over the Western North Pacific Ocean in Winter. In *Atmosphere* (Vol. 9, Issue 8). https://doi.org/10.3390/atmos9080298

Zhang, J.-Z., & Millero, F. J. (1993). The products from the oxidation of H2S in seawater. *Geochimica et Cosmochimica Acta*, *57*(8), 1705–1718. https://doi.org/https://doi.org/10.1016/0016-7037(93)90108-9

Figures

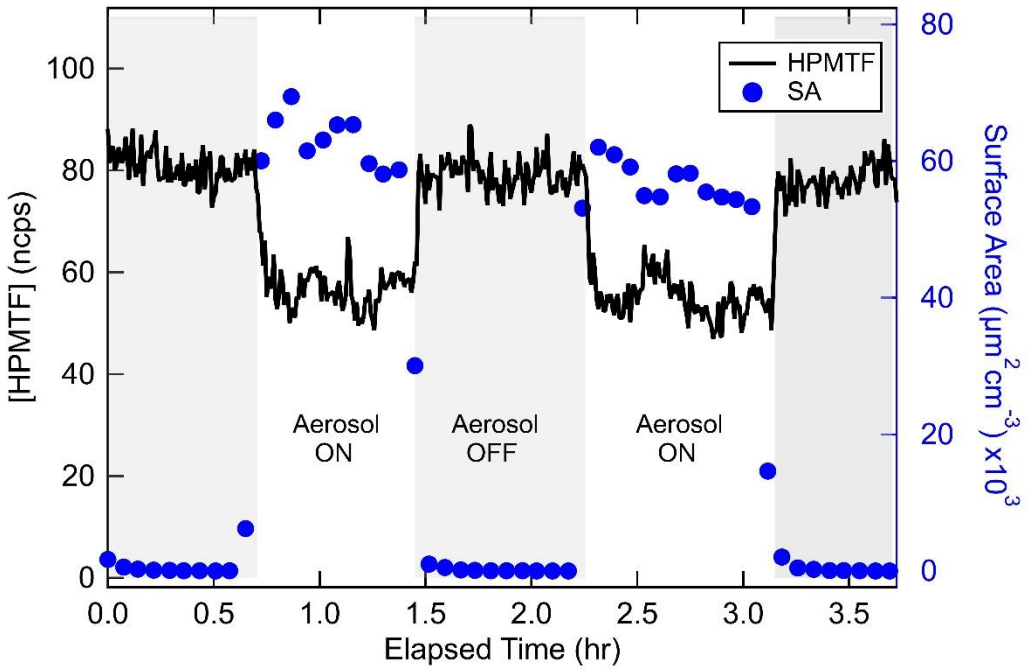

Figure 4.1: HPMTF (black trace) and total aerosol surface area (blue circles) measured at the base of the flow reactor during a representative experiment at 50.5% RH where particles are modulated on (white section) and off (grey section) using a high-efficiency particulate air filter.

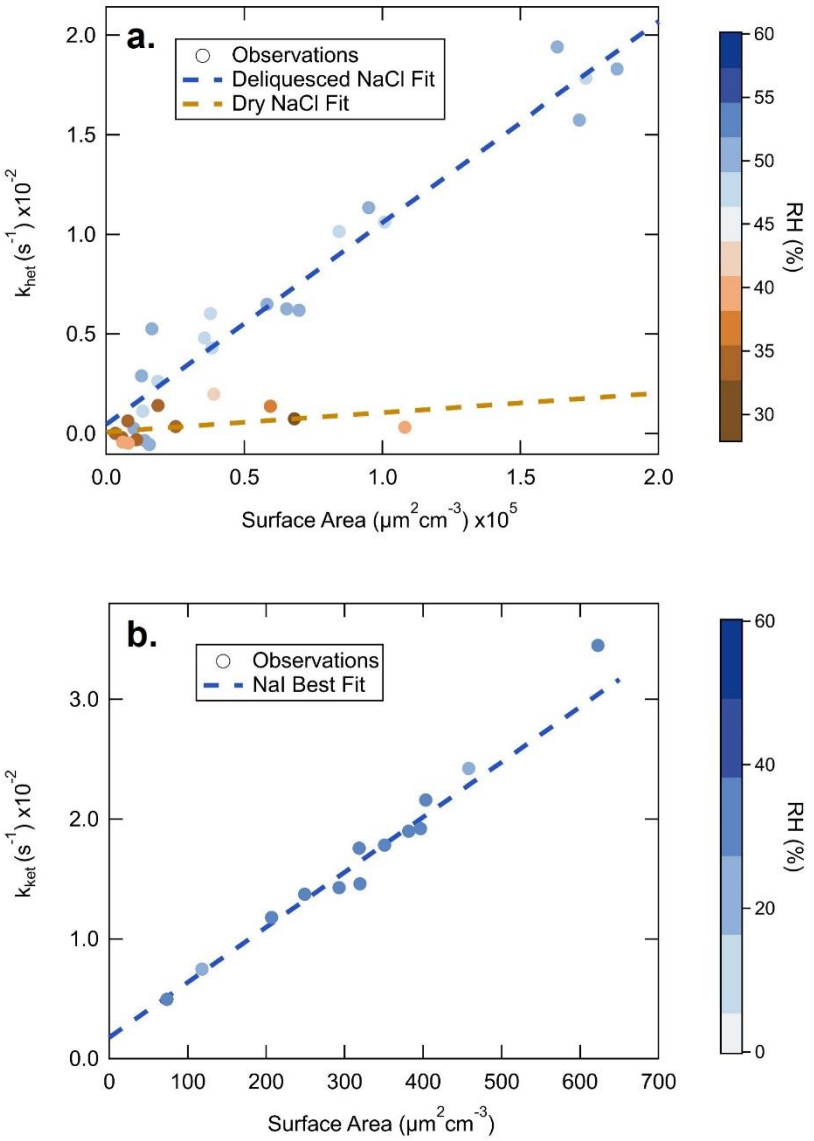

Figure 4.2: Measured pseudo first-order rate coefficients (k_{het}) for the loss of HPMTF to dry sodium chloride (NaCl) (a, <43%RH), wet NaCl (a, >43%RH), and wet sodium iodide (b, NaI >0%RH) (b) particles as a function of particle surface area concentration. The color bar indicates the measured relative humidity within the flow reactor with the white section denoting the efflorescence relative humidity for NaCl (a) and NaI (b). The dashed lines represent least squares fits of the observed data points.

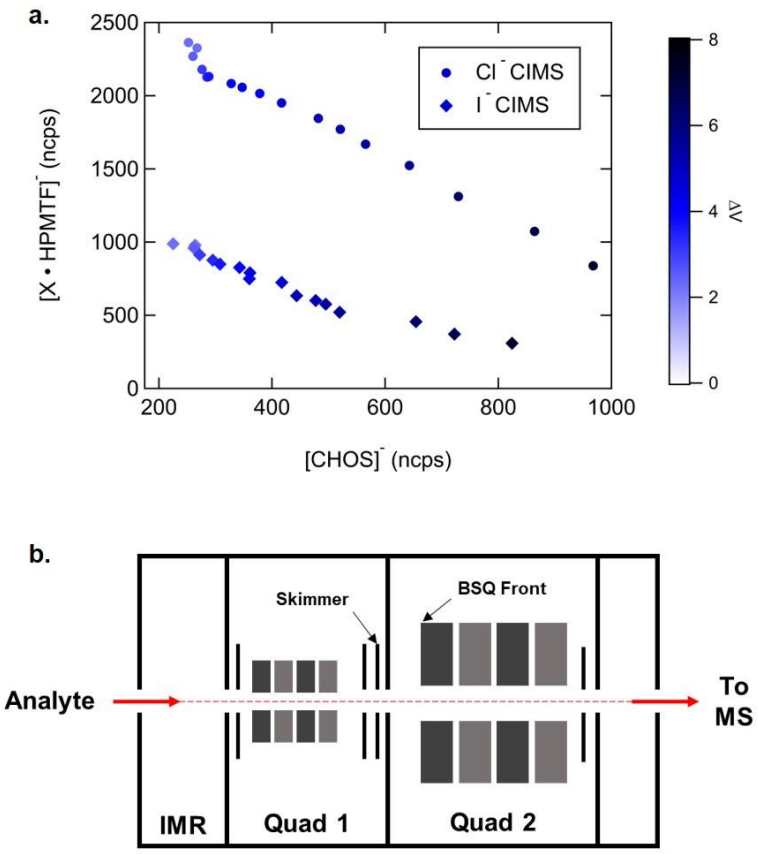

Figure 4.3: Relationship between the intensity of the reagent ion (Iodide in diamonds and Chloride in circles) clustered with HPMTF $[X{\cdot}HPMTF]^-$ (at 235 and 143 m/z, respectively) and the ion $[CHSO]^-$ (at 61 m/z) as a function of the magnitude of the declustering voltage represented by the colorbar (**top panel**). A schematic of the C-ToF instrument with the skimmer and big segmented quadrupole (BSQ) front voltages labeled to represent the declustering region (**bottom panel**). Halide clusters are formed in the ion molecule region (IMR) and guided to the mass analyzer (MS) through two focusing quadrupole regions (Quad 1 and 2).

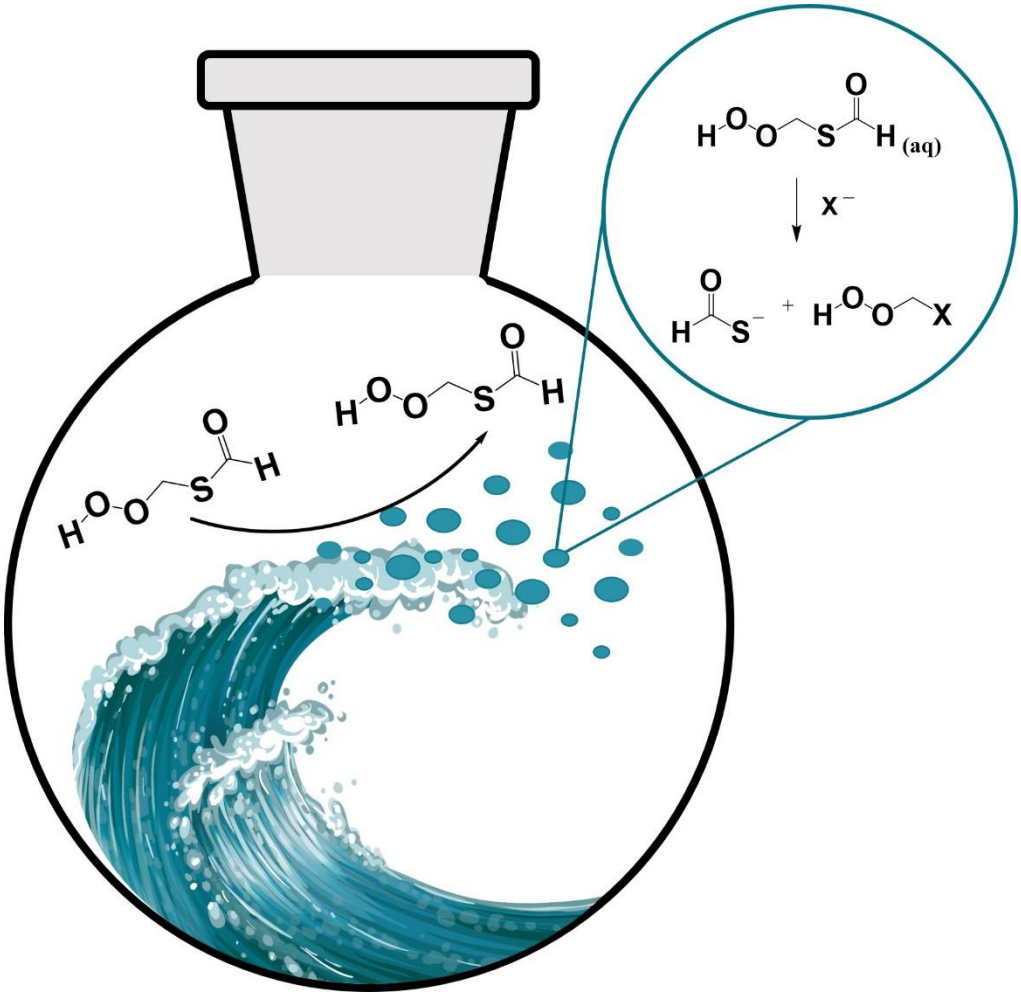

Table of Contents Art

Chapter 5: Sulfate and carbonyl sulfide production from aqueous processing of dimethyl sulfide oxidation products

Abstract

The oxidation products of dimethyl sulfide (DMS) contribute to the production and growth of cloud condensation nuclei (CCN) in the marine boundary layer. Laboratory and field measurements have demonstrated that DMS is oxidized by OH radicals to the stable intermediate hydroperoxymethyl thioformate (HPMTF), which is both globally ubiquitous and efficiently lost to multiphase processes in the marine atmosphere. Currently, the condensed phase chemistry included in chemical transport models relies on the assumption that HPMTF is irreversibly lost to atmospheric surfaces arresting carbonyl sulfide (OCS) production and forming sulfate at unit yield. At present, there are no experimental measurements of the sulfate and carbonyl sulfide yield from the aqueous processing of HPMTF. Using a custom-built bubbler apparatus combined with chemical ionization mass spectrometry (CIMS), a OCS analyzer and ion chromatography, we measured the yield of OCS and sulfate within MilliQ water to be <1% and >100%, respectively. While we did not directly observe the condensed-phase mechanisms of HPMTF in this experiment, the relative yields of OCS and sulfate provide mechanistic insight on the hydrolysis mechanism of HPMTF.

5.1 Introduction

Dimethyl sulfide (DMS) is a reduced sulfur compound that is produced and emitted from the ocean leading to a significant source of reduced sulfur to the atmosphere (Bates et al., 1992; Lana et al., 2011). Once emitted, DMS is oxidized by either the hydroxyl radical (OH) or halogen radicals (e.g. BrO, Cl) resulting in low volatility oxidation products that can nucleate new or grow

existing aerosol particles to cloud condensation nuclei (CCN) sizes and subsequently impact Earth's radiative budget(Galí et al., 2018; Korhonen et al., 2008; Vallina et al., 2006). The majority of the DMS oxidation products are low volatility and water soluble (e.g., sulfuric acid and methane sulfonic acid) or long-lived sulfur reservoir species (e.g., carbonyl sulfide, OCS). Until recently, the textbook definition of DMS oxidation resulted in sulfur dioxide (SO_2) and methane sulfonic acid (MSA) production at high yield, where SO_2 oxidation would go on to encourage new particle formation through sulfuric acid (H_2SO_4), while MSA contributes to particle growth through condensation. Recent computational, laboratory, and field work has uncovered a new sulfur reservoir, hydroperoxymethyl thioformate (HPMTF; $HOOCH_2SCHO$), upending the conventional DMS oxidation mechanism (Berndt et al., 2019; Jernigan, Fite, et al., 2022; Veres et al., 2020; Vermeuel et al., 2020) Recent laboratory measurements have found that the gas phase loss of HPMTF to OH is relatively slow ($k_{HPMTF+\ OH} = 1.4 \times 10^{-11}$ $cm^3\,molec^{-1}s^{-1}$) and the reactive uptake to marine aerosols is phase and compositionally dependent, allowing multiphase pathways to contribute substantially to the loss of HPMTF the marine atmosphere (Fung et al., 2021; Jernigan, Fite, et al., 2022; G. A. Novak et al., 2021). The current understanding is the loss of HPMTF to aerosol and cloud surfaces is irreversible, leading to a decrease in the global SO_2 and OCS product formed through the OH-oxidation of HPMTF (Fung et al., 2021; G. A. Novak et al., 2021). However, the condensed phase chemistry included in these models relied on the assumption that HPMTF is irreversibly lost to atmospheric surfaces arresting OCS production and ubiquitously forming sulfate.

At this point there are no laboratory measurements of the aqueous processing of HPMTF and its tie to sulfate and OCS formation. Here, we present laboratory measurements of the OCS and sulfate yield from HPMTF in MilliQ water using a custom-built bubbler combined with gas

and aqueous phase sulfur measurements. Observations of the sulfate and OCS yield under neutral pH and the absence of sea salt ions are used to make inferences about hydrolysis reactions that are likely to dominate in reactions occurring in dilute cloud droplets.

5.2 Methods

5.2.1 Generation and detection of gaseous sulfur species for condensed phase analysis

The gas-phase concentrations of HPMTF, nitric acid (HNO_3), nitrogen dioxide (NO_2), and SO_2 were quantified using a Compact Time of Flight (C-ToF) Chemical Ionization Mass Spectrometer utilizing iodine and oxygen anion chemistry, respectively (Bertram et al., 2011; Huey, 2007; Jernigan, Fite, et al., 2022; G. Novak et al., 2019). All OCS, CO and H_2O measurements were made using a Los Gatos Research, Enhanced Performance OCS analyzer (PN:914-0028), previously described by Berkelhammer (Berkelhammer et al., 2014). In the absence of a pure source of HPMTF available for experimentation, HPMTF ([HPMTF] = 800-1200 ppt) was generated from the NO_3-initiated oxidation of DMS within a 0.6 m^3 PTFE environmental chamber run under a continuous flow mode at ambient temperature and 1 atm of synthetic, dry zero air, as described in Jernigan et al. (2022). Previous experimentation on HPMTF used the ozonolysis of tetramethyl ethene (TME) to generate the hydroxyl radical (OH) to initialize the oxidation of DMS and formation of HPMTF. This work used the ozonolysis of NO_2 to generate the nitrate radical (NO_3) to initiate oxidation of DMS and subsequently HPMTF. The presence of NO_2 and ozone can lead to the production of nitrogen pentoxide (N_2O_5) detected at the 235 m/Q mass associated also associated with HPMTF detection in the C-ToF. To determine the background of formation of N_2O_5 (at 235 m/Q) during sulfur oxidation, the chamber was also run using dimethyl-1,1,1-d_3 sulfide (DMS-D_3). By utilizing DMS-D_3, the mass of the deuterated

HPMTF analogue, $H_2D_2C_2SO_3$ at mass 237 m/z, is shifted 2 masses units over from the peak at HPMTF and N_2O_5 at 235 m/Q. All aqueous HPMTF experiments were performed with DMS as the sulfur source. A mass flow controller backed by a gas cylinder containing a 5.08 ppm mixture of DMS and 1.188 ppm of NO_2 in nitrogen was used to supply known concentrations to the chamber. Ozone, used for initializing the formation of NO_3 was supplied to the chamber by a custom-built ozone generator. The chamber was allowed to react for >20 hours before the condensed phase experiments were started to allow all species within the chamber to reach a constant concentration.

5.2.2 Carbonyl sulfide And Sulfate Production from Loss of Aquatically Sequestered HPMTF (CASPLASH)

The carbonyl sulfide and sulfate yield from HPMTF hydrolysis was determined using a custom-built fritted bubbler system (**Figure 5.1**). The fritted bubblier system was made up of a coarse grain glass fritted set within a glass receptacle set atop by a solenoid three-way valve to direct flow either through the bubblier or a bypass line. Each experiment was run by passing 680 standard cubic centimeters per minute (sccm) of chamber air through the glass receptacle containing 20 ml of ultrapure MilliQ water (Milli-Q® Reference). The chamber air flow was supplied to the bubblier system using a micro diaphragm gas pump (UNMP 830 Series). For each experiment, the chamber air was pulled from the chamber through the gas pump to the glass fritted system or bypassed the fritted system to the detection instruments. The 680 sccm flow used for analysis of the production yield was measured out of the bubblier system between experiments using an inline flow meter (TSI Model 4043). All experiments were run by overflowing the instruments to eliminate the potential of sampling ambient air.

For the OCS analysis, the production of OCS from HPMTF hydrolysis was determined by comparing the drop in HPMTF signal to that of the OCS production. The HPMTF concentrations entering the bubblier system was varied by diluting chamber air flow with UHP N_2. There is a known dependence of the measured OCS concentration on the gas-phase water concentration as measured by the OCS analyzer. In this experiment, there is a significant change in water content between air sampled directly from the environmental ($[H_2O] < 8 \times 10^1$ ppm) and air coming from the bubbler ($[H_2O] = 2 \times 10^4$ ppm). To account for the water dependence in the OCS measurement, the background concentrations at high and low water content were determine by running the bubblier set up under the same oxidative conditions without DMS (a sulfur source) present.

For the sulfate analysis, the concentration of sulfate within the bubbled MilliQ water was determined using ion chromatography. For each experiment, the same concentration of chamber air was supplied to the diaphragm pump and subsequently to the bubbler system. To evaluate the sulfate production at different chamber air exposures, the amount of time the chamber air flowed through the system was varied. The relative exposure was determined by relating the concentration of gas phase molecules (e.g. HPMTF), the flow rate and the bubbling time. After each bubbling experiment 2 ml of water was removed from the fritted system to a 2.5 ml plastic IC vial. The remaining volume was measured and a new 20 ml of MilliQ water was added to the fritted system. 20 ml of MilliQ water was used for each experiment to ensure the bubblier system was completely submerged even after extended bubbling and water volume loss. The sulfate concentration was measured by ion chromatography (IC), conducted on Thermo Electron Dionex chromatography system. An AS-18 250 mm analytical and 50 mm guard columns were used, both 2 mm in diameter, with a 23 nM solution of KOH used as the eluent. The system was run under a constant current and flow rate at 15 A and 0.250 ml/min for 15 min, respectively. A sulfate yield associated

with the aqueous processing of HPMTF was determined by correcting for sulfate formed from reactions of SO_2 and O_3 also present within the chamber flow. A mixture of SO_2 and ozone, held at concentrations similar to that of the chamber flow (0.86 and 75 ppb, respectively), were run through the diaphragm and bubblier system to isolate the contribution of sulfate formation from SO_2 multiphase processing.

5.3 Results and Discussion

5.3.1 Validation of HPMTF formation from the NO_3 oxidation of DMS

The evaluation of the HPMTF formation from the NO_3 oxidation of DMS will be addressed in detail in future studies. Here, we briefly describe the chemistry of HPMTF production from the reaction of DMS with NO_3. As seen in **Figure 1.7** and discussed in section 5.1 of chapter 1, the addition of O_3 at t = 0 to a chamber containing a steady state concentration of dimethyl-1,1,1-d_3 sulfide (DMS-D_3) and NO_2 induces the significant production at 237 m/Q rather than that of 235 m/Q. From this observation, we can assume under similar oxidative conditions the production of N_2O_5 is insignificant compared to that of HPMTF within the chamber. Additionally, the chamber is run in excess of ozone (60-80 ppb) over NO_2 (2-5 ppb), promoting the formation of NO_3 ($O_3 + NO_2 \rightarrow NO_3$) rather than that of N_2O_5 ($NO_3 + NO_2 \rightarrow N_2O_5$). The sustained ozone concentration and dark chamber conditions allows for the efficient consumption and conversion of nitric oxide (NO) to NO_2 within the camber ($NO + O_3 \rightarrow NO_2 + O_2$), as well as the mitigation of any photolytic reactions leading to the regeneration of NO from NO_2 ($NO_2 + h\nu \rightarrow NO + O(3P)$). The result of the environmental oxidative conditions is a sustained near zero concentration of NO important within the chamber experiments as it rapidly reacts with organic peroxy radicals ($RO_2\cdot$), arresting HPMTF formation. NO_3 has the potential to react with MTMP, but the low concentrations

of NO_3, relatively high concentrations of DMS, and assumed slow reaction of NO_3 with MTMP and HPMTF allows HPMTF to accumulate in high yields. The decision to use NO_3 oxidation over that of TME + O_3 was to reduce the yield of OH-addition products within the DMS oxidation mechanism. The products of the OH-addition channel include dimethyl sulfoxide (DMSO), methane sulfnic acid (MSIA) and methane sulfonic acid (MSA), of which all are known to be efficiently lost be multiphase processes. HPMTF is the only detectable prominent sulfur molecule other than DMS and SO_2 within the NO_3 oxidation experiment. The contribution to sulfate from the oxidation of aqueous DMS is taken to be minimal due to the slow rate constants of DMS and its aqueous oxidation products (e.g. DMSO) with the only prominent aqueous oxidant, ozone. From these observations, we assume that all production of OCS or sulfate will arise from the aqueous processing of HPMTF, unless stated otherwise. Minor amounts of DMSO, MSIA and MSA are observed within the NO_3 + DMS chamber experiments, assumed to form through the OH oxidation of DMS. The major route in the chamber of OH generation is through the isomerization of MTMP forming HPMTF, as determined by experimental modeling. While these species are detectable in the chamber, they are subsequently lost in the transportation through the diaphragm pump. A significant loss of HPMTF (c.a. 30%) was lost through the pump system, leading to the assumption that other low volatility or multiphase prone species would be similarly lost.

5.3.2 Aqueous production of carbonyl sulfide from DMS oxidation

The loss of HPMTF as a function of pushing chamber air containing a steady state concentration of DMS + NO_3 species through and bypassing the bubbler system is shown in **Figure 5.2**. HPMTF is efficiently and irreversibly lost upon suppling the chamber air flow through the bubblier to the CIMS and OCS instruments. The HPMTF signal during the bubbling region does

not grow above zero over extended scales (>8 hour) indicating that HPMTF is not accumulating and eventually off gassing from the aqueous medium. We propose that the loss of HPMTF to the aqueous medium is both efficient and irreversible, following the findings of others on aerosols, cloud droplets and the ocean surface (Jernigan, Cappa, et al., 2022; G. A. Novak et al., 2021; Vermeuel et al., 2020). Additionally, a significant recovery time is observed between the switching from the bubbling phase to sampling air directly from the environmental chamber. The extended rise time is assumed to be associated with the drying of the walls of the tubing within the CIMS instrument. We assume that all HPMTF is lost to the water in the bubbler and not that of the subsequent tubing and hence we calculate the absolute concentration of HPMTF lost from the steady state concentration of HPMTF calculated during the bubbler bypass phase. Other sulfur and nitrogen containing species are present within the chamber flow and are subsequently pushed through the diaphragm pump into the aqueous system.

The bubbling of HPMTF generated a significant change in the water content between the dry chamber air and the bubbled chamber flow. This resulted in a 30-60 pptv change in the measured OCS background between the wet and dry flow with dry flow having the higher concentration. To account for the background change in the OCS measurement, an empirical humidity correction was applied to the OCS measurements. To determine the humidity dependence, a consistent flow of liquid evaporated nitrogen was run through a bubblier and a bypass flow at varying ratios. To determine the experimental background concentration of OCS under the dry and wet conditions, the same experimental set up was run utilizing a chamber run under the same oxidative conditions without DMS present. The average baselines of OCS under the dry and wet conditions were used to background subtract the OCS experiments. Lastly, natural fluctuations associated with instrument drift overtime were normalized to remove variations in the

OCS concentrations not associated with HPTMF bubbling. As seen in **Figure 5.3,** there is no detectable rise in the OCS signal as a function of the HPMTF lost to the aqueous system. At a 300s averaging for the OCS, a limit of detection of 7 ppt above the baseline and utilizing the largest drop in HPMTF observed (800 pptv) we can assume the OCS yield from aqueous HPMTF in MilliQ water within our uncertainty is less than 1%.

5.3.3 Aqueous production of sulfate (SO_4^{2-}) from DMS oxidation

The sulfate yield was determined by relating the mass of HPMTF added to the aqueous system to the mass of the non-SO_2 sulfate measured by the IC system. To account for sulfate generated through background processes and chamber SO_2 oxidation, chamber air containing the oxidants without DMS present and with SO_2 and O_3 at concentrations comparable to that observed in the experiment, were run through the bubblier system. The sulfate concentrations, normalized to 20 ml of solution, from the three set of experiments are presented in **Figure 5.4a**. The concentrations were normalized to 20 ml of volume to account for the 0.8 ml per hour of volume loss associated with the vigorous bubbling of the system. The vigorous bubbling allowed for small bubbles and high surface area exposure of the chamber air, as well as increase agitation and bubbling bursting promoting gas emission. The sulfate concentration is constrained by the "chamber exposure" which is determined by multiplying the flow rate through the bubblier (units of cm^3/min) and the time of exposure (units of minutes) to give a volume of air that has passed through the aqueous system (units of cm^3). An exposure volume was used to account for the complex mixture of air that is passing through the bubblier system in particular the mix of HPMTF and SO_2 both of which capable of forming sulfate in solution. The oxidized chamber air without DMS present, showed little to no production of sulfate lending to a lack of sulfate production from

the apparatus and sample preparation. A significant fraction of sulfate (30 – 60%) was produced when the SO_2 and ozone concentrations from the chamber were matched. The contribution to sulfate from SO_2 was considered by background subtracting the sulfate yield from the best fit of the $SO_2 + O_3$ analysis at each chamber exposure. The remaining sulfate production is then assumed to be a function of HPMTF oxidation or enhanced sulfate yield due to the presence of HPMTF. To relate the amount of HPMTF that entered the aqueous medium to the amount of sulfate formed within the bubblier, the concentrations of HPMTF and sulfate were converted to units of nanograms of sulfur. Both were normalized to the 20 ml of water in the bubblier. The mass of HPMTF within the water was calculated by multiplying the concentration of HPMTF within the chamber air (2.1×10^{10} molec. cm^{-3} or 820 pptv at 298K and 760 torr) by the bubbler exposure. The background SO_2 subtracted sulfate and the HPMTF masses were converted to units of nanograms of sulfur to provide a direct comparison in the yield from HPMTF to sulfate (**Figure 5.4b**). A range in yields of HPMTF are shown on **Figure 5.4b** with the best fit indicating a yield of 133%.

While a sulfate yield of > 100% from HPMTF is likely within the total uncertainty of the analysis, it could also be due an enhancement related to known hydroperoxide chemistry. One possible route for increased sulfate production is through hydroperoxides (ROOH) functional group of HPMTF with dissolved S(IV) to form sulfate (Dovrou et al., 2019; Lind et al., 1987). The added presence of ROOH functional group could enhance the formation of sulfate by increasing the routes of oxidation of available S(IV). Once consequence of generating HMPTF through NO_3+DMS chemistry is the reduction in additional ROOH that are formed in the traditional generation of HPMTF from the ozonolysis of TME. The environmental chamber is set up to promote RO_2 chemistry and isomerization reaction, but a minor production of HO_2 still exists

validated by the observation of a ROOH species originating from an TME RO_2 species. A second route for enhanced sulfate formation within the MilliQ system is through oxidation of S(IV) by NO_2 (Martin et al., 1981). The output of the chamber showed no detectable concentration of NO_2 detected as $[NO_2]^-$ in the oxygen anion CIMS instrument. This is due to the higher concentration of ozone and dark conditions in the chamber which titrate and regenerate NO_2, respectively.

5.4 Conclusions and Atmospheric Implications

We report measurements of product yields of OCS and sulfate from HPMTF. We determined that the OCS yield from HPMTF is < 1% and that the sulfate yield from HPMTF hydrolysis is >100%.. The observations made here validate the work performed by others that assumed irreversible loss of HPTMF, prompt sulfate formation, and limited OCS formation following aqueous phase chemistry of HPMTF.

While a reaction mechanism for HPMTF was not directly observed, general trends can be assumed based on the structure of the molecule. The current aqueous chemical loss pathway for HPMTF is suspected to be one similar of other carbonyl species, a hydrogenation of the carbonyl group. Previous studies have seen that this pathway, typically catalyzed by the presence of an acidic aerosol, is the dominant pathway for carbonyl loss (Kroll et al., 2005; Liggio et al., 2005; Liggio & Li, 2006; Wu et al., 2015). Support for potential HPMTF reactions in the aqueous medium exist within the oxygen equivalent form of HPMTF, hydroperoxmethyl formate (HPMF), formed in combustion engines from DME oxidation and the combination of formic acid and the simplest stabilized carbonyl oxide (CH_2OO) (Moshammer et al., 2015, 2016; Neeb et al., 1995; Thamm et al., 1996). For example, Thamm et al (1996) found HPMF to have an aqueous lifetime of 7 and 140 min at pH of 3.5 and 1.0, respectively. HPMF was found to be stable when dissolved

in chloroform and lost rapidly in aqueous condition unless the solution was held under highly acidic conditions.

An alternative reaction mechanism for HPMTF in water is a 1,5 cyclization and decomposition of HPMTF. We discuss this in Appendix A of this thesis. In short, the mechanism postulated and investigated computationally presents a pathway forming a cyclic hydroperoxyl aldehyde that would later decompose into a set of sulfur containing organic acids. If HPMTF is lost through a carbonyl loss pathway or through the cyclization/decomposition, the products of either of these reactions can result in the production of more water-soluble species, organic acids. The high yield of sulfate and lack of OCS observed from the bubbling experimentation would imply that the acids formed here are preferentially going on to form sulfate rather than dehydrate to from OCS (Jernigan, Cappa, et al., 2022). The work performed here can be applied to the global system, but additional work should be performed to investigate other routes and mechanisms of aqueous HPMTF processing. In particular, a focus on the role of ionic strength and acidity should be taken into account as they are critical components of atmospheric surfaces.

References

Bates, T. S., Lamb, B. K., Guenther, A., Dignon, J., & Stoiber, R. E. (1992). Sulfur emissions to the atmosphere from natural sourees. *Journal of Atmospheric Chemistry*, *14*(1), 315–337. https://doi.org/10.1007/BF00115242

Berkelhammer, M., Asaf, D., Still, C., Montzka, S., Noone, D., Gupta, M., Provencal, R., Chen, H., & Yakir, D. (2014). Constraining surface carbon fluxes using in situ measurements of carbonyl sulfide and carbon dioxide. *Global Biogeochemical Cycles*, *28*(2), 161–179. https://doi.org/10.1002/2013GB004644

Berndt, T., Scholz, W., Mentler, B., Fischer, L., Hoffmann, E. H., Tilgner, A., Hyttinen, N., Prisle, N. L., Hansel, A., & Herrmann, H. (2019). Fast Peroxy Radical Isomerization and OH Recycling in the Reaction of OH Radicals with Dimethyl Sulfide. *Journal of Physical Chemistry Letters*, *10*(21), 6478–6483. https://doi.org/10.1021/acs.jpclett.9b02567

Bertram, T. H., Kimmel, J. R., Crisp, T. A., Ryder, O. S., Yatavelli, R. L. N., Thornton, J. A., Cubison, M. J., Gonin, M., & Worsnop, D. R. (2011). A field-deployable, chemical ionization time-of-flight mass spectrometer. *Atmospheric Measurement Techniques*, *4*(7), 1471–1479. https://doi.org/10.5194/amt-4-1471-2011

Dovrou, E., Rivera-Rios, J. C., Bates, K. H., & Keutsch, F. N. (2019). Sulfate Formation via Cloud Processing from Isoprene Hydroxyl Hydroperoxides (ISOPOOH). *Environmental Science & Technology*, *53*(21), 12476–12484. https://doi.org/10.1021/acs.est.9b04645

Fung, K. M., Heald, C., Kroll, J., Wang, S., Jo, D., Gettelman, A., Lu, Z., Liu, X., Zaveri, R., Apel, E., Blake, D., Jimenez, J.-L., Campuzano-Jost, P., Veres, P., Bates, T., Shilling, J., & Zawadowicz, M. (2021). Exploring DMS oxidation and implications for global aerosol radiative forcing. *Atmospheric Chemistry and Physics*, *2021*, 1–58. https://doi.org/10.5194/acp-2021-782

Galí, M., Levasseur, M., Devred, E., Simó, R., & Babin, M. (2018). Sea-surface dimethylsulfide (DMS) concentration from satellite data at global and regional scales. *Biogeosciences*, *15*(11), 3497–3519. https://doi.org/10.5194/bg-15-3497-2018

Huey, L. G. (2007). Measurement of trace atmospheric species by chemical ionization mass spectrometry: Speciation of reactive nitrogen and future directions. *Mass Spectrometry Reviews*, *26*(2), 166–184.

Jernigan, C. M., Cappa, C. D., & Bertram, T. H. (2022). Reactive Uptake of Hydroperoxymethyl Thioformate to Sodium Chloride and Sodium Iodide Aerosol Particles. *The Journal of Physical Chemistry A*. https://doi.org/10.1021/acs.jpca.2c03222

Jernigan, C. M., Fite, C. H., Vereecken, L., Berkelhammer, M. B., Rollins, A. W., Rickly, P. S., Novelli, A., Taraborrelli, D., Holmes, C. D., & Bertram, T. H. (2022). Efficient Production of Carbonyl Sulfide in the Low-NO x Oxidation of Dimethyl Sulfide . *Geophysical Research Letters*, *49*(3), e2021GL096838. https://doi.org/10.1029/2021gl096838

Korhonen, H., Carslaw, K. S., Spracklen, D. v., Mann, G. W., & Woodhouse, M. T. (2008). Influence of oceanic dimethyl sulfide emissions on cloud condensation nuclei concentrations and seasonality over the remote Southern Hemisphere oceans: A global model study. *Journal of Geophysical Research Atmospheres*, *113*(15), 1–16. https://doi.org/10.1029/2007JD009718

Kroll, J. H., Ng, N. L., Murphy, S. M., Varutbangkul, V., Flagan, R. C., & Seinfeld, J. H. (2005). Chamber studies of secondary organic aerosol growth by reactive uptake of simple carbonyl compounds. *Journal of Geophysical Research Atmospheres*, *110*(23), 1–10. https://doi.org/10.1029/2005JD006004

Lana, A., Bell, T. G., Simó, R., Vallina, S. M., Ballabrera-Poy, J., Kettle, A. J., Dachs, J., Bopp, L., Saltzman, E. S., Stefels, J., Johnson, J. E., & Liss, P. S. (2011). An updated climatology of surface dimethlysulfide concentrations and emission fluxes in the global ocean. *Global Biogeochemical Cycles*, *25*(1), 1–17. https://doi.org/10.1029/2010GB003850

Liggio, J., & Li, S. M. (2006). Reactive uptake of pinonaldehyde on acidic aerosols. *Journal of Geophysical Research Atmospheres*, *111*(24), 1–12. https://doi.org/10.1029/2005JD006978

Liggio, J., Li, S. M., & McLaren, R. (2005). Reactive uptake of glyoxal by particulate matter. *Journal of Geophysical Research D: Atmospheres*, *110*(10), 1–13. https://doi.org/10.1029/2004JD005113

Lind, J. A., Lazrus, A. L., & Kok, G. L. (1987). Aqueous phase oxidation of sulfur (IV) by hydrogen peroxide, methylhydroperoxide, and peroxyacetic acid. *Journal of Geophysical Research: Atmospheres*, *92*(D4), 4171–4177.

Martin, L. R., Damschen, D. E., & Judeikis, H. S. (1981). The reactions of nitrogen oxides with SO2 in aqueous aerosols. *Atmospheric Environment (1967)*, *15*(2), 191–195.

Moshammer, K., Jasper, A. W., Popolan-Vaida, D. M., Lucassen, A., Diévart, P., Selim, H., Eskola, A. J., Taatjes, C. A., Leone, S. R., Sarathy, S. M., Ju, Y., Dagaut, P., Kohse-Höinghaus, K., & Hansen, N. (2015). Detection and Identification of the Keto-Hydroperoxide (HOOCH2OCHO) and Other Intermediates during Low-Temperature Oxidation of Dimethyl Ether. *Journal of Physical Chemistry A*, *119*(28), 7361–7374. https://doi.org/10.1021/acs.jpca.5b00101

Moshammer, K., Jasper, A. W., Popolan-Vaida, D. M., Wang, Z., Bhavani Shankar, V. S., Ruwe, L., Taatjes, C. A., Dagaut, P., & Hansen, N. (2016). Quantification of the Keto-Hydroperoxide (HOOCH2OCHO) and Other Elusive Intermediates during Low-Temperature Oxidation of Dimethyl Ether. *Journal of Physical Chemistry A*, *120*(40), 7890–7901. https://doi.org/10.1021/acs.jpca.6b06634

Neeb, P., Horie, O., & Moortgat, G. K. (1995). The nature of the transitory product in the gas-phase ozonolysis of ethene. *Chemical Physics Letters*, *246*(1), 150–156. https://doi.org/https://doi.org/10.1016/0009-2614(95)01073-I

Novak, G. A., Fite, C. H., Holmes, C. D., Veres, P. R., Neuman, J. A., Faloona, I., Thornton, J. A., Wolfe, G. M., Vermeuel, M. P., Jernigan, C. M., Peischl, J., Ryerson, T. B., Thompson, C. R., Bourgeois, I., Warneke, C., Gkatzelis, G. I., Coggon, M. M., Sekimoto, K., Bui, T. P., … Bertram, T. H. (2021). Rapid cloud removal of dimethyl sulfide oxidation products limits SO 2 and cloud condensation nuclei production in the marine atmosphere. *Proceedings of the National Academy of Sciences*, *118*(42), e2110472118. https://doi.org/10.1073/pnas.2110472118

Novak, G., Vermeuel, M., & Bertram, T. (2019). Simultaneous Detection of Ozone and Nitrogen Dioxide by Oxygen Anion Chemical Ionization Mass Spectrometry: A Fast Time Response Sensor Suitable for Eddy Covariance Measurements. *Atmospheric Measurement Techniques Discussions*, *1*, 1–41. https://doi.org/10.5194/amt-2019-445

Thamm, J., Wolff, S., Turner, W. v, Gäb, S., Thomas, W., Zabel, F., Fink, E. H., & Becker, K. H. (1996). Proof of the formation of hydroperoxymethyl formate in the ozonolysis of ethene: synthesis and FT-IR spectra of the authentic compound. *Chemical Physics Letters*, *258*(1), 155–158. https://doi.org/https://doi.org/10.1016/0009-2614(96)00625-2

Vallina, S. M., Simó, R., & Gassó, S. (2006). What controls CCN seasonality in the Southern Ocean? A statistical analysis based on satellite-derived chlorophyll and CCN and model-estimated OH radical and rainfall. *Global Biogeochemical Cycles*, *20*(1), 1–13. https://doi.org/10.1029/2005GB002597

Veres, P. R., Andrew Neuman, J., Bertram, T. H., Assaf, E., Wolfe, G. M., Williamson, C. J., Weinzierl, B., Tilmes, S., Thompson, C. R., Thames, A. B., Schroder, J. C., Saiz-Lopez, A., Rollins, A. W.,

Roberts, J. M., Price, D., Peischl, J., Nault, B. A., Møller, K. H., Miller, D. O., … Ryerson, T. B. (2020). Global airborne sampling reveals a previously unobserved dimethyl sulfide oxidation mechanism in the marine atmosphere. *Proceedings of the National Academy of Sciences of the United States of America*, *117*(9), 4505–4510. https://doi.org/10.1073/pnas.1919344117

Vermeuel, M. P., Novak, G. A., Jernigan, C. M., & Bertram, T. H. (2020). Diel Profile of Hydroperoxymethyl Thioformate: Evidence for Surface Deposition and Multiphase Chemistry. *Environmental Science and Technology*, *54*(19), 12521–12529. https://doi.org/10.1021/acs.est.0c04323

Wu, Q. Q., Huang, L. B., Liang, H., Zhao, Y., Huang, D., & Chen, Z. M. (2015). Heterogeneous reaction of peroxyacetic acid and hydrogen peroxide on ambient aerosol particles under dry and humid conditions: Kinetics, mechanism and implications. *Atmospheric Chemistry and Physics*, *15*(12), 6851–6866. https://doi.org/10.5194/acp-15-6851-2015

Figures

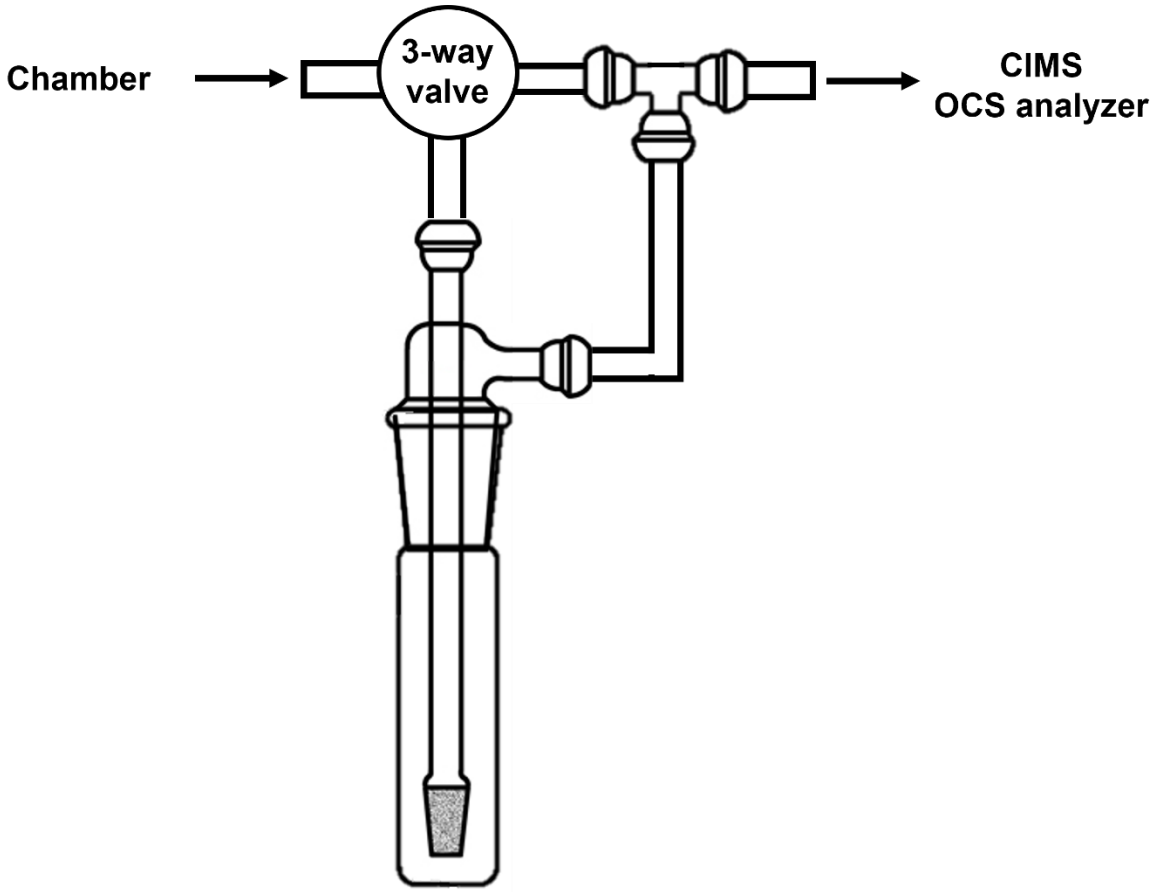

Figure 5.1: Schematic of HPMTF bubblier system.

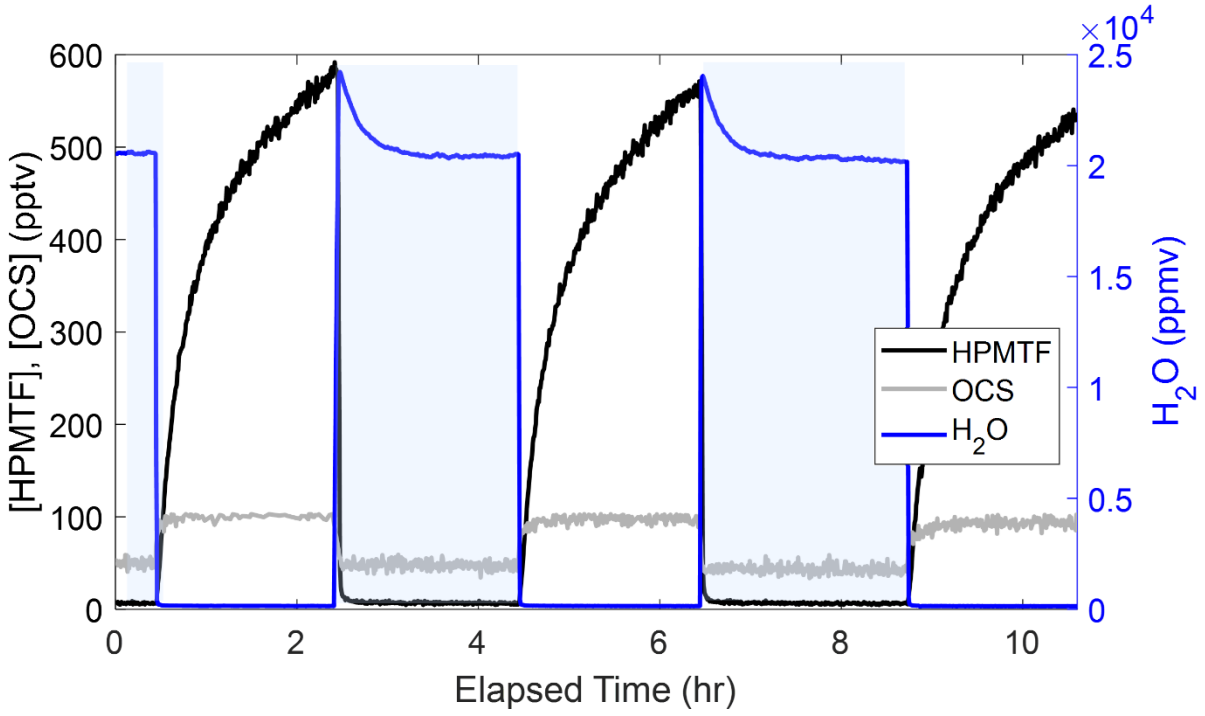

Figure 5.2: HPMTF (black trace), OCS (grey trace) and water (blue trace) measured at the end of the bubblier system during a representative experiment where chamber air is modulated through (blue section) and bypassing (white section) the bubblier system.

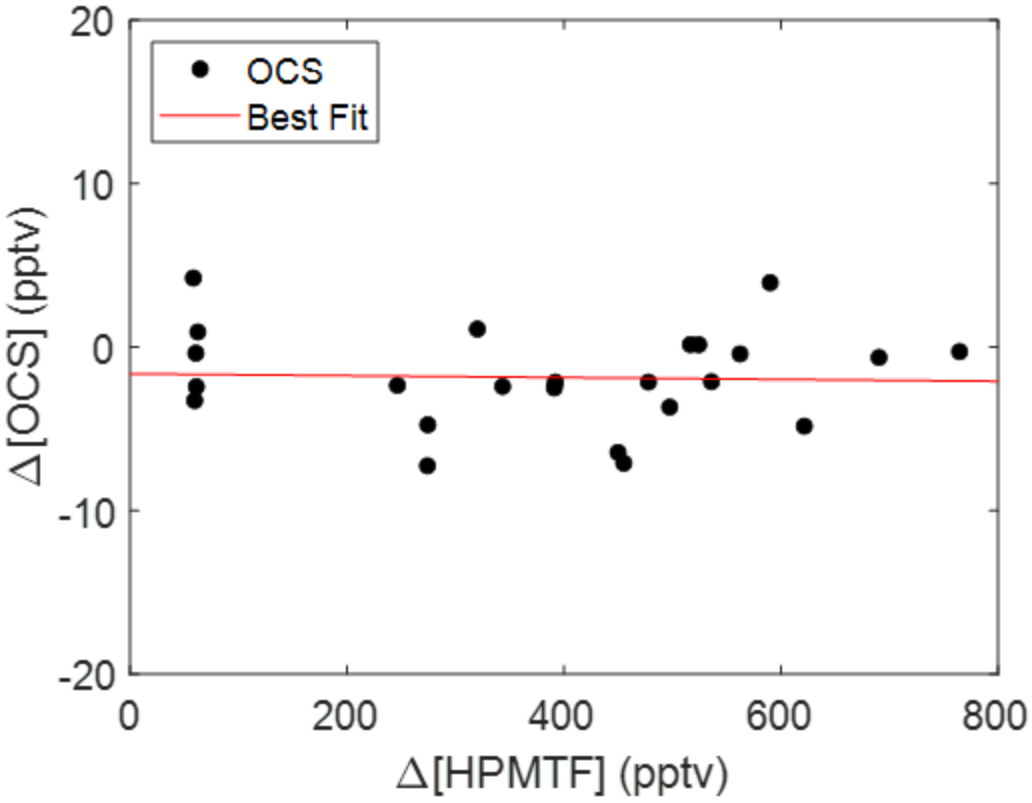

Figure 5.3: The concentration of carbonyl sulfide (black dots) as a function of HPTMF lost to the bubble apparatus. The best fit through the experimental observations is presented as the red trace with a slope <0.001.

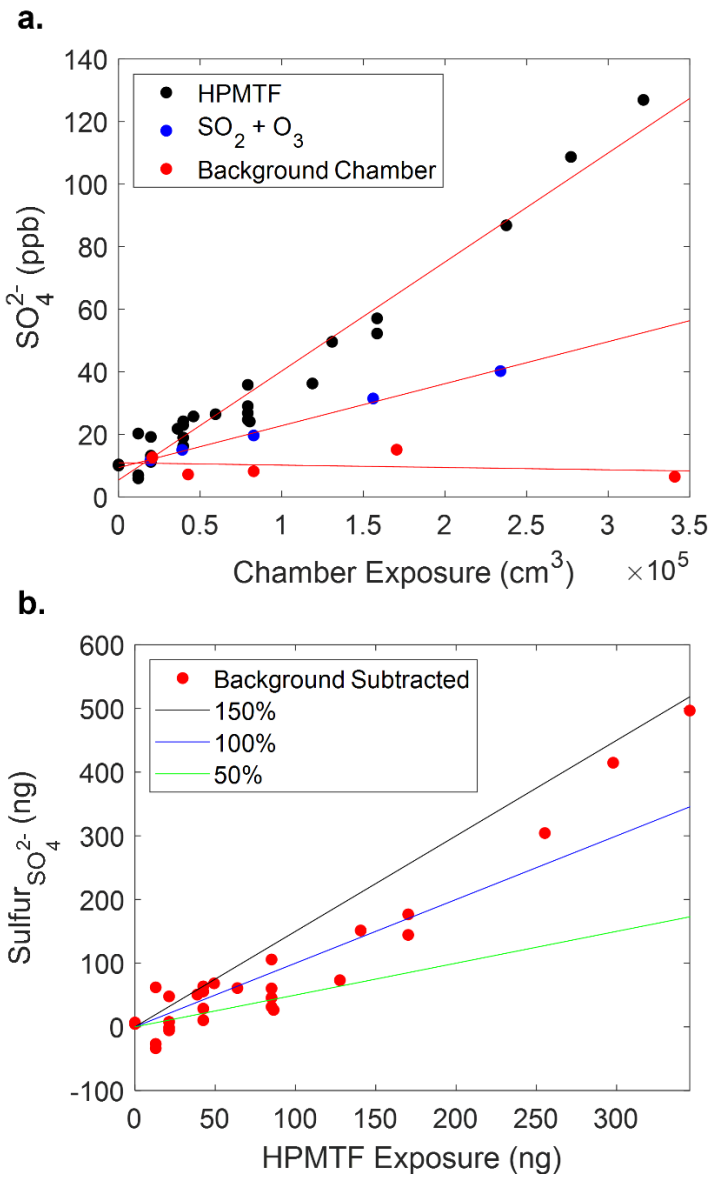

Figure 5.4: (a) The concentration of sulfate (SO_4^{2-}) calculated by IC that was found by bubbling a set volume of chamber air through a custom bubbler apparatus. Air containing the reactants and products of a DMS + NO_3 chamber with DMS present (black dots), without DMS present (red dots), and air containing ozone (O_3) and sulfur dioxide (SO_2) at the similar concentrations of the DMS + NO_3 chamber with DMS present experiment (blue dots) is shown. A linear fit is drawn through each of the three experiments to indicate the relative slope of each. (**b**) The mass of sulfur in the form of sulfate taken from the difference in sulfate mass from the DMS + NO_3 chamber with DMS present experiments between that of an exposure weighted sulfate mass if only SO_2 and ozone were present regressed against the mass of sulfur in the form of HPMTF that was taken up by the bubbler solution is shown (red dots). A percent yield of 50 (green trace), 100 (red trace), and 150 (black track) from the HPMTF to form sulfate is shown.

Appendix A: Cyclization and Korcek decomposition of HPMTF

A.1 Introduction

The utilization of computational chemistry and free energy calculations have been used previously to determine the rate of reactions, distribution of products, understanding of chemical spectra and the instrument sensitivity to difficult to calibrate compounds. Gaussian 09 is an electronic structure package that allows for the prediction of chemical properties of atoms, molecules and reactive systems (Frisch, 2009). Utilizing the thermodynamic properties calculated by the Gaussian 09 program, the free energy, vibrational frequency and transition states of various intermediates and reaction pathways within the sulfur oxidation method could be investigated.

The hydroperoxyenals (HPALDs) are a class of highly functional hydrocarbons produced during the oxidation of various volatile organic carbon species (Crounse et al., 2011; Jalan et al., 2013; Novak et al., 2021; Thamm et al., 1996). HPALD formation can dominate in completely different oxidative environments, with dimethyl sulfide and isoprene forming HPALDs under remote low oxidative ambient conditions and propane and dimethyl ether forming HPALDs within the high temperatures of combustion engines. In either case, the primarily formation pathway of the HPALD species is through an isomerization reaction either driven by increased temperature or by the lack of bimolecular reactants (**Figure A1a**). Once formed, the HPALDs are primarily thought to be further oxidized through photo-oxidation or thermal decomposition pathways. Previous work has found an additional loss pathway for the HPALDs species driven by an isomerization reaction. The original work investigating HPALD cyclization was performed within oxidized lipid species(Jensen et al., 1979, 1981). Researchers found the intramolecular reaction of the hydroperoxyl group attacking the carbonyl carbon forming a stable ring structure to be fast.

They later found that the cyclic hydroperoxyl aldehydes (c-HPAL) will decompose into organic acids, later referred to as a Korcek decomposition (**Figure A1b**). While the cyclization of other hydroperoxyl aldehydes, particularly within the oxidation of dimethyl ether (DME) and propane, have been experimentally and theoretically investigated, they were performed under conditions atypical of the ambient environment, within combustion engines at T>500K (Moshammer et al., 2015, 2016). We examine the potential for hydroperoxymethyl thioformate (HPMTF), the sulfur analogue to DME and propane, to cyclize in the gas phase to a cyclic hydroperoxyl aldehydes (c-HPALS) as well as the subsequent decomposition of the c-HPALs into organic acids. The mechanistic pathways investigated here can be expanded to potential reactions founds in isoprene, propane and dimethyl ether oxidation under atmospheric conditions.

A.2 Methods

A.2.1 Calculation of the free point energy of species

The free energy and vibrational frequency of each of the reactants, products, and transition state species were carried out are carried out at the M062X/6-311+G(2d,p) level of theory. The highly-parameterized hybrid meta exchange-correlation functionals, M062X, is used due to its strong performance in unimolecular and association barrier height calculations (Zhao & Truhlar, 2008). A 6-311+G(2d,p) basis was used within the DFT calculations due to its ability to accurately determine the chemical properties, while reducing the computational time of the experiment.

To approximate an ensemble of geometries within the reactants and products, a weighted average of the energies was made for each species. This was done by calculating the zero-point energy of each of the species at a variety of different molecular orientations. For example, HPMTF can exist in an open and closed form corresponding to the aldehyde and hydroperoxyl group either

pointing away or toward each other, respectively. The difference in the orientation results in a difference of 2 kcal/mol. For this reason, the orientation of acidic hydrogens, sulfur atoms and carbonyl groups were varied to determine an approximation for the ensemble of orientations. The average ensemble was used to determine the free energy differences between the reactant, products and transition states throughout the process. A transition state optimization and frequency were calculated and determined using the same level of theory as the reactants and products. Each of the transition states were verified by confirming the presence of an imaginary transition frequency and the observation of the desired reaction within the imaginary frequency. An intrinsic reaction coordinate calculation was performed on each of the transition state species to determine the potential product distribution (Fukui, 1981). A zero-point energy optimization was made on each of the reactants and products identified from the IRC. The following process was calculated for the cyclization and korcek decomposition of the propane, dimethyl ether and dimethyl sulfide equivalent hydroperoxyl aldehyde.

A.2.1 Calculation of the free energy and theoretical rate constant of reactions

The free energy of a reaction was calculated as the enthalpy of the ensemble of the products minus the energy of the ensemble of the reactants for each of the investigated reactions. The theoretical rate coefficients for the cyclization and decomposition reactions were determined using the Arrhenius equation (**EA1**), where A, Ea, and RT correspond to the pre-exponential factor, the activation energy of the reaction, and average kinetic energy in the system at temperature (T):

$$k = A \cdot \mathrm{e}^{\frac{-E_a}{RT}} \qquad \text{(EA1)}$$

The pre-exponential factor can also be referred to as the attempt frequency and is taken to be the number of times per second that the system vibrates along the reaction pathway. The imaginary frequency calculated from the transition state optimization was transformed into units of (s^{-1}) to calculate the attempt frequency of the reaction. The activation energy of the reaction was calculated was calculated as the enthalpy of the ensemble of the products minus the energy of the optimized transition state species.

A.3 Results and Discussion

A.3.1 Free energy differences within reaction mechanism

The overview of the reaction coordinate for the cyclization of HPMTF to the cyclic hydroperoxyl aldehyde (1,2-Oxa-3-hydroxyl-4-thiacyclopentane, c-HPMTF) and the subsequent decomposition of that species into two organic sulfur containing acids is shown in **Figure A2.** The free energy difference in the cyclization reaction of HPMTF → c-HPMTF was found to be -4 kcal/mol with an activation energy of 43 kcal/mol. With an imaginary frequency of -1708 cm^{-1}, a rate coefficient of 2.8×10^{-17} s^{-1} was determined for the cyclization of HPMTF under vacuum at 300K (**Figure A3a**). HPMTF was found to have two main structures an open form and a closed form, named by the position of the carbonyl group within the overall structure. The closed form refers to the carbonyl oxygen pointing inward towards the hydroperoxyl hydrogen, while the open form has the two groups pointing away from each other. The closed form was found to have a zero-point energy 2.5 kcal/mol lower than the open form. The closed form closely resembles the optimized transition state structure of the cyclization product. This could imply the lower energy state HPMTF preferentially exists in a state ready to undergo the cyclization reaction. The decomposition of the c-HPMTF can proceed down one of two pathways forming either a

thiocarbonic acid species (HOC(O)SH) and formaldehyde or a thioformic acid species (HC(O)SH) and formic acid (**Figure A3b**). In both reactions, the peroxide bond within the c-HPMTF breaks along with one of the two carbon-sulfur bonds. The asymmetric nature of c-HPMTF allows for two product distributions to form. Reaction 1 of **Figure A2** refers to the decomposition of c-HPMTF to formaldehyde and thiocarbonic acid driven by the dissociation of the peroxide and methylene carbon sulfur bond. The free energy of korcek decomposition 1 (KD1) was found to be -63 kcal/mol with an activation energy of 33.2 kcal/mol. The calculated imaginary frequency of -852 cm^{-1} would translate to a first order loss rate of 1.57×10^{-11} s^{-1} at 300K. Korcek decomposition 1 (KD2) refers to the decomposition of c-HPMTF to formic acid and thioformic acid driven by the dissociation of the peroxide bond and the hydroxyl carbon sulfur bond. Similarly, KD2 was found to have a free energy of the reaction of -69.43 kcal/mol with an activation energy of 30.4 kcal/mol. Using a calculated imaginary frequency of -793 cm^{-1}, the first order loss rate was determined to be 1.61×10^{-11} s^{-1} at 300K. All free energy differences, transition state frequencies, and rate constants can be found in **Table A1**.

A.3.1 Validation of computational methodology

In addition to DMS, the cyclization and decomposition processes were examined for propane. For the cyclization of the propane hydroperoxyl aldehyde (keto hydroperoxide, KHP), an activation energy of the reaction of 28 kcal/mol and an imaginary frequency of -1559.56 cm^{-1} was calculated. The cyclized KHP can also decompose through 2 separate pathways forming formic acid and acetaldehyde or acetic acid and formaldehyde. A free energy of the reaction of -66.23 kcal/mol and -61.53 were calculated for reaction 1 and 2, respectively. An activation energy of the reaction of 32.47 kcal/mol and 34.16 kcal/mol with an imaginary frequency of -834.08 and -819.29 cm^{-1} was calculated for reaction 1 and 2, respectively. The free energy and activation energy values

calculated for propane were found to agree with the values calculated by Jalan et al 2013(Jalan et al., 2013) within 5% and 20%, respectively. The comparable values and trends in the values calculated here against previously published values implies the methodology tested here holds with previous literature on a similar system.

A.4 Conclusion and atmospheric implications

The rate coefficient observed here is orders of magnitude slower than the gas-phase and heterogeneous loss pathways known to HPMTF (Jernigan, Cappa, et al., 2022; Jernigan, Fite, et al., 2022). Using a lifetime to cyclization calculated here of millennia would imply that the loss of gas-phase HPMTF via cyclization is insignificant under ambient conditions. While the decomposition rate for KD2 is 2 orders of magnitude faster than KD1 both are sufficiently slow on the atmospheric scale. If the c-HPMTF were to from under atmospheric conditions, it would most likely be lost via photolytic means, driven by the labile peroxide bond, or by heterogeneous loss pathways (Magi et al., 1997; Matthews et al., 2005; Qin et al., 2018). In all cases, the activation energy barrier required for the reaction is too great for the reaction to proceed under ambient conditions. In order to overcome this barrier at atmospheric temperatures, a catalyst or stabilizing environment for the transition state would have to be present. Jalan et al 2013 found the addition of formic acid can stabilize and catalyze the cyclization of the keto hydroperoxide species (2013). While the observed reactions are unlikely to proceed in the gas-phase, we propose that the reactions could occur under aqueous conditions. The current aqueous chemical loss pathway for HPMTF is suspected to be one similar of other carbonyl species, a hydrogenation of the carbonyl group. Previous studies have seen that this pathway, typically catalyzed by the presence of an acidic aerosol, is the dominant pathway for carbonyl loss (Kroll et al., 2005; Liggio et al., 2005; Liggio & Li, 2006; Wu et al., 2015). We suspect this to be true for HPMTF, but also propose a secondary

loss pathway via the 1,5 cyclization and decomposition explored here. We suppose that this reaction that occurs under high temperatures in the gas phase could also occur in the aqueous phase stabilize by water molecules and catalyzed by an acidic environment. Support for potential HPMTF cyclization in the aqueous medium exist within the oxygen equivalent form of HPMTF, hydroperoxmethyl formate (HPMF), formed in combustion engines from DME oxidation and the combination of formic acid and the simplest stabilized carbonyl oxide (CH_2OO) (Moshammer et al., 2015, 2016; Neeb et al., 1995; Thamm et al., 1996). Work performed by Thamm et al 1996, found HPMF to have an aqueous lifetime of 7 and 140 min at pH of 3.5 and 1.0, respectively. HPMF was found to be stable when dissolved in chloroform and lost rapidly in aqueous condition unless the solution was held under highly acidic conditions. Following the trends identified for HPMF, we suspect HPMTF could decompose rapidly in cloud droplets. If HPMTF is lost through a carbonyl lost pathway or through the korcek decomposition, the products of either of these reactions can result in the production of more water-soluble species, organic acids. Following the product distribution investigate here or the products identified in Chapter 2 utilizing the declustering HPMTF within the CIMS, two sulfur containing organic acids can form, thioformic acid (TFA, CH(=O)SH) and carbonothioic O,S-acid (TCA, HOC(=O)SH). Given that TFA and TCA are structurally similar to formic acid (HCOOH) and carbonic acid (H_2CO_3), respectively, we can use the condensed phase reactions of HCOOH and H_2CO_3 as an indicator of what the condensed phase fate of HPMTF might be. By analogy to HCOOH:HCOO- chemistry, we propose two potential aqueous fates of thioformic acid; OH oxidation and evaporation. The asymmetric nature to TFA would allow for two competing product distributions, H_2S:HS- + CO_2 and H_2O:HO + OCS. By analogy to H_2CO_3 chemistry, we propose the primary fate of thiocarbonyl acid is the dehydration (e.g. $H_2CO_3 \rightarrow H_2O + CO_2$). The asymmetric nature to thiocarbonic acid would allow

for two competing product distributions, $H_2S + CO_2$ and $H_2O + OCS$ (Belviso et al., 1967; Elliott et al., 1989). In both cases, we propose the eventual production of two sulfur containing intermediates, hydrogen sulfide (H_2S) and carbonyl sulfide (OCS). The eventual fate of aqueous hydrogen sulfide (H_2S) is an efficient conversion to sulfate (SO_4^{2-}) through ·OH and ozone reactions. In contrast, OCS is a highly stable and insoluble species that would likely off-gas from the aqueous solution. The implication of this aqueous OCS production would lead to the re-examination of the marine OCS production term. Work performed in Chapter 2 of this thesis assumed the irreversible loss of HPMTF to cloud droplets arrested OCS formation by diverting sulfur away from HPMTF + OH to OCS. Additional work should be done on HPMTF's phase within the particle given the potential large fraction of HPMTF being lost to cloud droplets and atmospheric aerosols, the implications for hygroscopicity could be significant.

References

Belviso, S., Mihalopoulos, N., & Ba Cuong Nguyen. (1967). The supersaturation of carbonyl sulfide (OCS) in rain waters. *Atmospheric Environment (1967)*, *21*(6), 1363–1367. https://doi.org/10.1016/0004-6981(67)90083-2

Crounse, J. D., Paulot, F., Kjaergaard, H. G., & Wennberg, P. O. (2011). Peroxy radical isomerization in the oxidation of isoprene. *Physical Chemistry Chemical Physics*, *13*(30), 13607–13613. https://doi.org/10.1039/c1cp21330j

Elliott, S., Lu, E., & Rowland, F. S. (1989). Rates and Mechanisms for the Hydrolysis of Carbonyl Sulfide in Natural Waters. *Environmental Science and Technology*, *23*(4), 458–461. https://doi.org/10.1021/es00181a011

Frisch, A. (2009). gaussian 09W Reference. *Wallingford, USA, 25p*, *470*.

Fukui, K. (1981). The path of chemical reactions-the IRC approach. *Accounts of Chemical Research*, *14*(12), 363–368.

Jalan, A., Alecu, I. M., Meana-Pañeda, R., Aguilera-Iparraguirre, J., Yang, K. R., Merchant, S. S., Truhlar, D. G., & Green, W. H. (2013). New pathways for formation of acids and carbonyl products in low-temperature oxidation: The Korcek decomposition of γ- ketohydroperoxides. *Journal of the American Chemical Society*, *135*(30), 11100–11114. https://doi.org/10.1021/ja4034439

Jensen, R. K., Korcek, S., Mahoney, L. R., & Zinbo, M. (1979). Liquid-phase autoxidation of organic compounds at elevated temperatures. 1. The stirred flow reactor technique and analysis of primary products from n-hexadecane autoxidation at 120-180. degree. C. *Journal of the American Chemical Society*, *101*(25), 7574–7584.

Jensen, R. K., Korcek, S., Mahoney, L. R., & Zinbo, M. (1981). Liquid-phase autoxidation of organic compounds at elevated temperatures. 2. Kinetics and mechanisms of the formation of cleavage products in n-hexadecane autoxidation. *Journal of the American Chemical Society*, *103*(7), 1742–1749.

Jernigan, C. M., Cappa, C. D., & Bertram, T. H. (2022). Reactive Uptake of Hydroperoxymethyl Thioformate to Sodium Chloride and Sodium Iodide Aerosol Particles. *The Journal of Physical Chemistry A*. https://doi.org/10.1021/acs.jpca.2c03222

Jernigan, C. M., Fite, C. H., Vereecken, L., Berkelhammer, M. B., Rollins, A. W., Rickly, P. S., Novelli, A., Taraborrelli, D., Holmes, C. D., & Bertram, T. H. (2022). Efficient Production of Carbonyl Sulfide in the Low-NO x Oxidation of Dimethyl Sulfide . *Geophysical Research Letters*, *49*(3), e2021GL096838. https://doi.org/10.1029/2021gl096838

Kroll, J. H., Ng, N. L., Murphy, S. M., Varutbangkul, V., Flagan, R. C., & Seinfeld, J. H. (2005). Chamber studies of secondary organic aerosol growth by reactive uptake of simple carbonyl compounds. *Journal of Geophysical Research Atmospheres*, *110*(23), 1–10. https://doi.org/10.1029/2005JD006004

Liggio, J., & Li, S. M. (2006). Reactive uptake of pinonaldehyde on acidic aerosols. *Journal of Geophysical Research Atmospheres*, *111*(24), 1–12. https://doi.org/10.1029/2005JD006978

Liggio, J., Li, S. M., & McLaren, R. (2005). Reactive uptake of glyoxal by particulate matter. *Journal of Geophysical Research D: Atmospheres*, *110*(10), 1–13. https://doi.org/10.1029/2004JD005113

Magi, L., Schweitzer, F., Pallares, C., Cherif, S., Mirabel, P., & George, C. (1997). Investigation of the Uptake Rate of Ozone and Methyl Hydroperoxide by Water Surfaces. *The Journal of Physical Chemistry A*, *101*(27), 4943–4949. https://doi.org/10.1021/jp970646m

Matthews, J., Sinha, A., & Francisco, J. S. (2005). The importance of weak absorption features in promoting tropospheric radical production. *Proceedings of the National Academy of Sciences*, *102*(21), 7449–7452.

Moshammer, K., Jasper, A. W., Popolan-Vaida, D. M., Lucassen, A., Diévart, P., Selim, H., Eskola, A. J., Taatjes, C. A., Leone, S. R., Sarathy, S. M., Ju, Y., Dagaut, P., Kohse-Höinghaus, K., & Hansen, N. (2015). Detection and Identification of the Keto-Hydroperoxide (HOOCH2OCHO) and Other Intermediates during Low-Temperature Oxidation of Dimethyl Ether. *Journal of Physical Chemistry A*, *119*(28), 7361–7374. https://doi.org/10.1021/acs.jpca.5b00101

Moshammer, K., Jasper, A. W., Popolan-Vaida, D. M., Wang, Z., Bhavani Shankar, V. S., Ruwe, L., Taatjes, C. A., Dagaut, P., & Hansen, N. (2016). Quantification of the Keto-Hydroperoxide (HOOCH2OCHO) and Other Elusive Intermediates during Low-Temperature Oxidation of Dimethyl Ether. *Journal of Physical Chemistry A*, *120*(40), 7890–7901. https://doi.org/10.1021/acs.jpca.6b06634

Neeb, P., Horie, O., & Moortgat, G. K. (1995). The nature of the transitory product in the gas-phase ozonolysis of ethene. *Chemical Physics Letters*, *246*(1), 150–156. https://doi.org/https://doi.org/10.1016/0009-2614(95)01073-I

Novak, G. A., Fite, C. H., Holmes, C. D., Veres, P. R., Neuman, J. A., Faloona, I., Thornton, J. A., Wolfe, G. M., Vermeuel, M. P., Jernigan, C. M., Peischl, J., Ryerson, T. B., Thompson, C. R., Bourgeois, I., Warneke, C., Gkatzelis, G. I., Coggon, M. M., Sekimoto, K., Bui, T. P., … Bertram, T. H. (2021). Rapid cloud removal of dimethyl sulfide oxidation products limits SO 2 and cloud condensation nuclei production in the marine atmosphere. *Proceedings of the National Academy of Sciences*, *118*(42), e2110472118. https://doi.org/10.1073/pnas.2110472118

Qin, M., Chen, Z., Shen, H., Li, H., Wu, H., & Wang, Y. (2018). Impacts of heterogeneous reactions to atmospheric peroxides: Observations and budget analysis study. *Atmospheric Environment*, *183*, 144–153.

Thamm, J., Wolff, S., Turner, W. v, Gäb, S., Thomas, W., Zabel, F., Fink, E. H., & Becker, K. H. (1996). Proof of the formation of hydroperoxymethyl formate in the ozonolysis of ethene: synthesis and FT-IR spectra of the authentic compound. *Chemical Physics Letters*, *258*(1), 155–158. https://doi.org/https://doi.org/10.1016/0009-2614(96)00625-2

Wu, Q. Q., Huang, L. B., Liang, H., Zhao, Y., Huang, D., & Chen, Z. M. (2015). Heterogeneous reaction of peroxyacetic acid and hydrogen peroxide on ambient aerosol particles under dry and humid conditions: Kinetics, mechanism and implications. *Atmospheric Chemistry and Physics*, *15*(12), 6851–6866. https://doi.org/10.5194/acp-15-6851-2015

Zhao, Y., & Truhlar, D. G. (2008). The M06 suite of density functionals for main group thermochemistry, thermochemical kinetics, noncovalent interactions, excited states, and transition elements: two new functionals and systematic testing of four M06-class functionals and 12 other function. *Theoretical Chemistry Accounts*, *120*(1), 215–241. https://doi.org/10.1007/s00214-007-0310-x

Figures and Tables

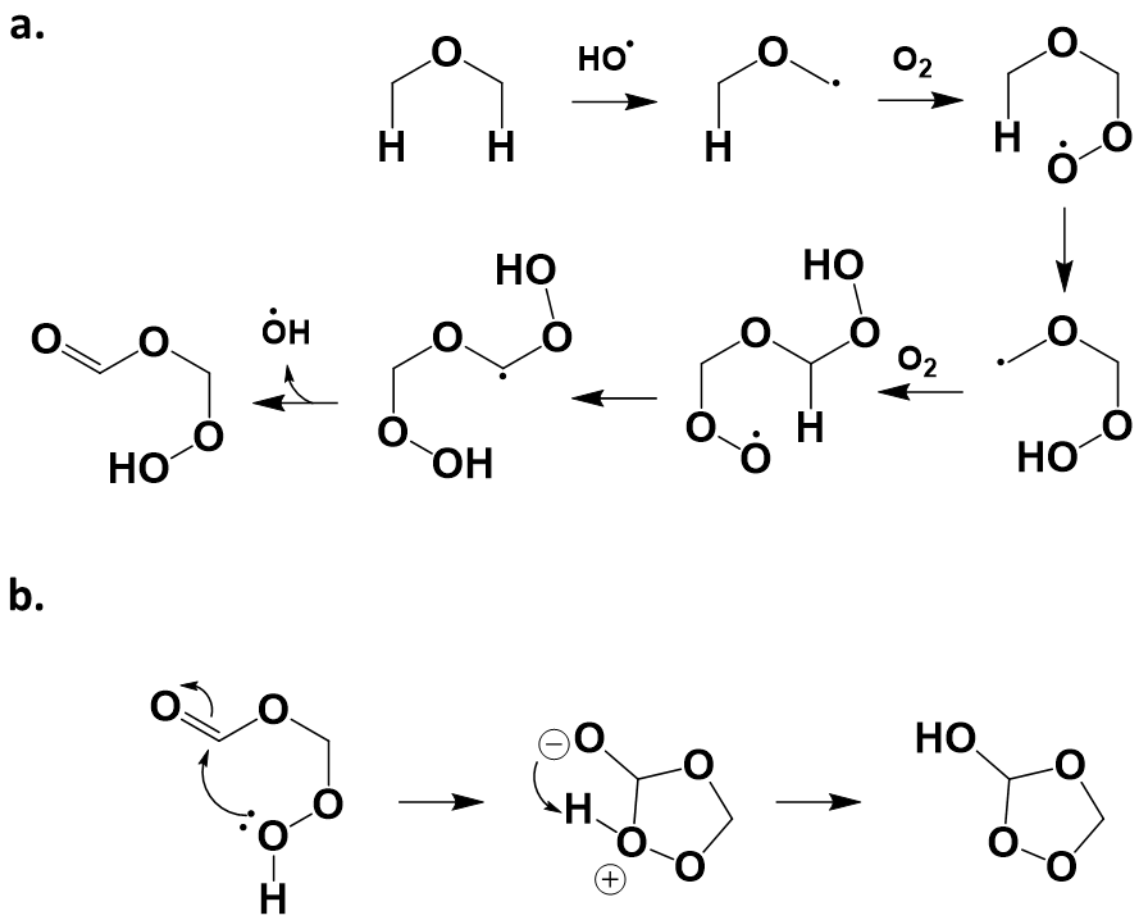

Figure A1. Isomerization reaction initiated by the OH oxidation of dimethyl ether forming the hydroperoxyl aldehyde, hydroperoxymethyl formate, HPMF (a). Cyclization of HPMF forming the cyclic HPMF.

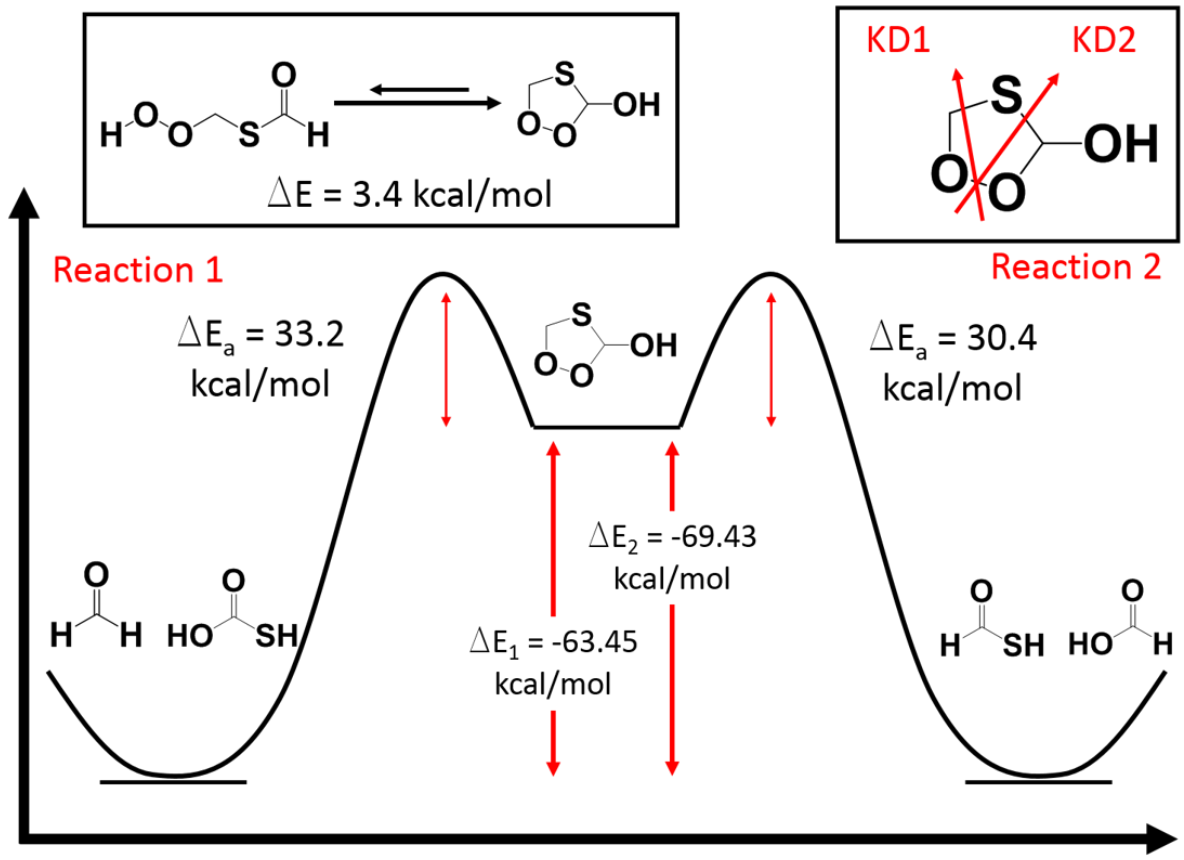

Figure A2. Overview of the energy diagram for the cyclization of hydroperoxymethyl thioformate (HPMTF) and korcek decomposition of cyclic HPMTF.

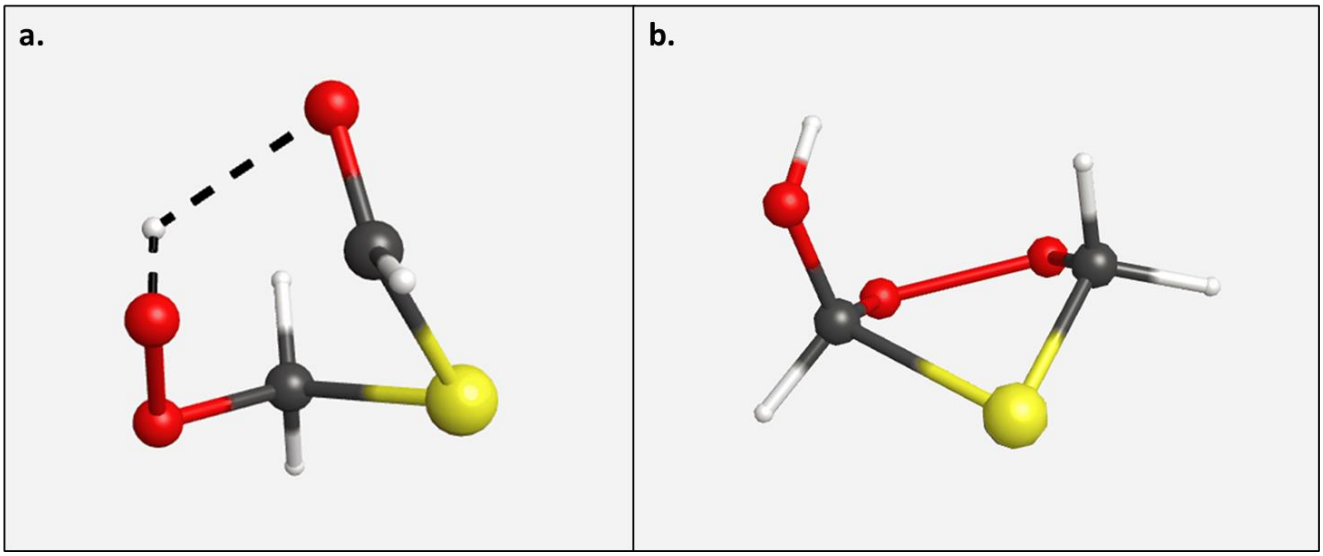

Figure A3. Transition state optimization the cyclization of HPMTF (a) and korcek decomposition of cyclic HPMTF (b).

Reaction	$\tilde{\nu}$ (cm^{-1})	A (s^{-1})	E_a(kcal/mol)	k @300K
HPMTF ⇌ c-HPMTF	**-1708.86**	**5.13E+13**	**41.49**	**2.83E-17**
c-HPMTF ⇌ KD1	**-852.4504**	**2.56E+13**	**33.2**	**1.57E-11**
c-HPMTF ⇌ KD2	**-793.2571**	**2.38E+13**	**30.4**	**1.61E-09**

Reaction	$\tilde{\nu}$ (cm^{-1})	A (s^{-1})	E_a(kcal/mol)	k @300K
HPMF ⇌ c-HPMF	**-1559.56**	**2.10E+08**	**28**	**7.98E-13**
c-HPMF ⇌ Rxn 1	**-834.08**	**3.40E+13**	**34.4**	**2.78E-12**
c-HPMF ⇌ Rxn 2	**-819.29**	**3.70E+13**	**36.8**	**5.37E-14**

Table A1. Imaginary frequency, attempt frequency, activation energy and first-order rate constant at 300K for the reactions of HPMF and HPMTF.

Appendix B: Dimethyl sulfide and DMS-Cl oxidation under photolytic initiation

B.1. Methods

B.1.1 Instrumentation

The experimentation and detection of DMS oxidation products were performed with a Chemical Ionization Time of Flight Mass spectrometer (CI-ToF) with a resolving power (m/Δm) of 1000 and a "low pressure" IMR (75 torr) (Bertram et al., 2011), as well as a long time-of-flight chemical ionization mass spectrometer (L-ToF-CIMS) with a resolving power of 6000-8000 and atmospheric pressure IMR (ATM-IMR) (Zhao et al.,2018). The use of the ATM-IMR over the low pressure IMR used throughout the thesis is the increased the detection of labile RO_2 species and reduced residual wall sampling from sticky sulfur molecules. To predict the selectivity of the reagent ion, computational chemistry was used to simulate an analyte's Chemical Ionization sensitivity. A study by Iyer et al., has shown a linear trend between the measured sensitivity (counts/parts per trillion) of a given acid molecule and its computed binding energy with iodine (2016). A technique similar to this was used to determine the ability to detect various DMS oxidation products by iodine benzene cluster cation CIMS, or $C_6H_6(C_6H_6)_n^+$ CIMS, (B-CIMS).

B-CIMS has been shown to have good sensitivity for several reduced sulfur molecules and volatile organic carbon (VOC) species, such as DMS, dimethyl disulfide (DDMS), and alpha pinene (Kim et al., 2016; Lavi et al., 2018). Where PTR-, I-, and CF_3O^--CIMS can probe for specific functional groups, such as aldehydes, alcohols, and hydroperoxides (Huey et al., 2007), the specificity for sulfur containing compounds opens the potential for B-CIMS to detect and quantify the short-lived sulfur containing RO_2 species. As currently understood, B-CIMS proceeds either via an adduct formation between a sulfur lone pair and a benzene cation, or a charge transfer

from a benzene cation cluster to the analyte for analytes with an ionization energy lower than the benzene dimer (Lavi et al., 2018). To avoid overlap between the reagent ion, benzene, and dimethyl sulfoxide (detected as the charge transfer at 78 m/Q), deuterated benzene (C_6D_6) was used as the reagent ion.

B.1.2 Isolating MTMP formation via monochlorodimethyl sulfide oxidation

Recently, it has been shown that the methylthiomethyl peroxy radical radical (MTMP, $CH_3SCH_2O_2\cdot$), the primary peroxy radical formed following H-abstraction of DMS (Reaction 2 (R2) of Figure B1), efficiently isomerizes to a stable intermediate, hydroperoxymethyl thioformate (HPMTF, $HOOCH_2SCH{=}O$) which has been observed to be ubiquitous in marine environments(Berndt et al., 2019b; Veres et al., 2020; Vermeuel et al., 2020; Wu et al., 2015; Ye et al., 2021). Up to this point the determination of the isomerization rate has been performed utilizing OH-initiated oxidation(Berndt et al., 2019a; Jernigan et al., 2022; Veres et al., 2020; Ye et al., 2021). Given the two pathways of OH-oxidation, a significant fraction, at ambient temperatures, is lost the OH addition complicating direct measurements of the isomerization reaction. To preferentially direct the hydrogen abstraction channel and autoxidation pathway, monochlorodimethyl sulfide (DMS-Cl) in tandem with a home-built ultraviolet (UV) light flow reactor, DMS Autoxidation Flow Tube (DAFT) was used, as seen in **Figure B2**. In the presence of 254 nm UV light, a homolytic cleavage of the chloride-carbon bond and formation of the MTMP was proposed (**see R5 Figure B1**). The fate of MTMP could then be studied in a calibrated flow reactor as a function of residence time and oxidant loadings, before sampling in the CI-ToFMS. Utilizing the same experimental set up as the DMS-Cl experimentation, the OH-initiated oxidation experiments were run utilizing the photolysis of hydrogen peroxide (H_2O_2) with 254 nm light in the DAFT. The 254 nm light photolyzes the H_2O_2 into two OH molecules that subsequently react

with DMS or remaining H_2O_2. The OH can abstract hydrogen from H_2O_2 to produce HO_2, which is a competitive reactant with MTMP. Using the known photolysis rate constant, approximate UV flux and H_2O_2 concentration, the concentrations of OH and HO_2 were calculated with a 0-D box model utilizing MCM 3.2.1 chemistry (Saunders et al., 2003; Wolfe et al., 2016). To determine the appearance of photolysis dependent species, a "lamp on/lamp off" experimentation was used. The existence and growth of different MS peaks were compared when the lamp was on and off, and High Resolution (HR) fitting along with chemical intuition was used to determine the identity of lamp dependent peaks.

The photolysis of DMS-Cl or the trace gas mixture containing DMS and H_2O_2 occurred in the only DAFT where it would then be introduced into a calibrated flow reactor for kinetic analysis. At the time of experimentation an autoxidation rate had not yet been calculated and, as such, a wide range of time scales was tested. Long time-scales experiments were done on the Thornton lab flow tube at UW-Seattle which has been well characterized and described elsewhere (Zhao et al., 2018). Short time-scales were done on a shortened version of the Thornton flow reactor. The 1 meter long, 7.6 internal diameter (ID) Thornton flow tube is capable of investigating reaction time scales on the order of minutes, while the 20 cm long, 2.54 cm ID shortened reactor probed time scales on the order of 1 to 10 seconds.

B.2. Results and Discussion

B.2.1 Binding efficiency and detection of sulfur species by CIMS

To validate the potential for B-CIMS and I-CIMS to detect molecules from the chamber, the binding efficiency for molecules both within the DMS oxidation and tetramethyl ethene (TME) mechanism are presented in **Table B1 and Table B2**, respectively. The binding energy for benzene

with the sulfur compounds was found to be heavily dependent on the delocalization and withdrawing groups around the sulfur lone pairs. This can be seen by the significant drop in the binding energy when carbonyl groups are substituted on the DMS framework. Based upon the theoretical values, electron withdrawing groups, such as -OOH, -OH and -Cl, demonstrated a reduction in the binding energy and ionization energy with benzene clusters. For this reason, B-CIMS is proposed to have a weaker sensitivity to some of the important oxidized sulfur intermediated (e.g. HPMTF, methyl thioformate). Iodine CIMS shows strong binding enthalpies for a variety of oxidize sulfur species within the DMS oxidation mechanism. In particular, the binding of a handful key intermediates are close to that of formic acid and nitric acid, known to be detectable by I CIMS (Huey, 2007).

B.2.2 Photooxidation of DMS-Cl

The photo-oxidation of DMS-Cl showed promise as a route to exploring and preferentially observing the hydrogen abstraction pathway. When the UV was turned on, a prompt loss of DMS-Cl was observed with a corresponding rise in signal attributed to MTMP in the B-CIMS **(Figure B3)**. While the DMS-Cl experiments did show the presence of oxidation as a function of UV lights, the spectra were dominated by unwanted side reactions that complicated potential observations of MTMP isomerization. Primary complications within the DMS-Cl experiments included the formation of dimers and chlorine containing compounds radicals driven by the cleavage and recombination of the sulfur carbon bond, and by Cl radical oxidation. The DMS-Cl experimentation showed a photolysis dependent increase in signal at 108 and 192 m/Q within the B-CIMS experimentation, whose mass correspond to the mass where a charge transfer and benzene adduct of HPMTF would be detected. The signal was not attributed to HPMTF as the two masses presented an isotopic pattern indicative of a chlorine or disulfide bond, not present in HPMTF.

Both chlorine and sulfur have isotopes at M+2, but sulfur's 4% abundance compared to chlorine's 30% abundance allows for the distinction and elemental characterization of peak clusters. The unwanted peaks are proposed to be products of DMS-Cl photolysis and recombination or by unknown ion chemistry within the IMR. No observations above baseline for ROOH or HPMTF were made by I-CIMS in the DMS-Cl experimentation. Though MTMP is assumed to be detected in the B-CIMS experimentation, the lack observations of further oxidation products within the I-CIMS would imply either the mischaracterization of the MTMP peak or the inability to detect the products forming within the DMS-Cl experiment. Based upon the significant increase in MTMP intensity, the oxidative reaction would favor that of a high RO_2 oxidative space, promoting the formation of methyl thioformate and sulfur dioxide through MTMP recombination reactions. Given the critical feature of directing the hydrogen abstraction pathway, future experiments with DMS-Cl are still under consideration, such as reducing light intensity and using white (non-UV) light.

B.2.3 Photooxidation of DMS by H_2O_2

The photo-oxidation of DMS by H_2O_2 presented a cleaner and textbox observation of DMS oxidation when compared to DMS-Cl. Throughout the experiments, performed within the flow reactor under the longer timescales, observations were made of HPMTF, methylthiomethyl hydroperoxide (MTMHP), H_2O_2 and HO_2 at mass 235, 221, 161 160, respectively. Prompt and strong intensities were observed at the masses corresponding to H_2O_2, HO_2, and ROOH, indicating high concentrations of HO_2 within the flow reactor. To generate OH at concentrations significant enough to promote detectable changes within the CIMS, excess concentrations of H_2O_2 (~1ppm) were added to the reaction. The subsequent reaction of OH and H_2O_2 created an excess of HO_2 in the flow reactor (approx. 100 ppb) resulting in a dominating competitive reaction with MTMP. At

high HO_2, the autoxidation reaction could not compete with the HO_2 reaction shuttling a majority of the MTMP into the MTMHP species, as seen in **R3 of Figure B1**. Observations of HPMTF with the ROOH species were made when additional efforts were made to reduce the concentration of H_2O_2. In the low H_2O_2 experimentation, lamp-dependent peaks at 221, 252 and 235 m/z were detected, pointing to the formation of the MTMHP, OOROOH and HPMTF species, respectively. The OOROOH species is a proposed intermediate in the autoxidation pathway that may have a short lifetime due to its theoretical rate constant of 75 s-1 at 298K (Wu et al., 2015). While the autoxidation product has been detected in the previous experiments, kinetic information could not credibly be determined from the available dataset due to availability of only theoretical sensitivities and low signal intensities. Given that some experimentations showed loss in DMS signal without the addition of H_2O_2, potential unwanted photolysis could be occurring within the DAFT. The side reactions may include photolysis of O_2 and H_2O by the small amount of 185nm light emitted by the low-pressure Hg Lamp. Some preliminary modeling of the DAFT system shows that some O(1D) and OH generation could result from oxygen and water photolysis, respectively. Future considerations and alterations to the experimental set up will be made to reduce the complication associated with HO_2 production and unwanted photolysis reactions.

References

Berndt, T., Scholz, W., Mentler, B., Fischer, L., Hoffmann, E. H., Tilgner, A., Hyttinen, N., Prisle, N. L., Hansel, A., & Herrmann, H. (2019a). Fast Peroxy Radical Isomerization and OH Recycling in the Reaction of OH Radicals with Dimethyl Sulfide. *Journal of Physical Chemistry Letters*, *10*(21), 6478–6483. https://doi.org/10.1021/acs.jpclett.9b02567

Berndt, T., Scholz, W., Mentler, B., Fischer, L., Hoffmann, E. H., Tilgner, A., Hyttinen, N., Prisle, N. L., Hansel, A., & Herrmann, H. (2019b). Fast Peroxy Radical Isomerization and OH Recycling in the Reaction of OH Radicals with Dimethyl Sulfide. *Journal of Physical Chemistry Letters*, *10*(21), 6478–6483. https://doi.org/10.1021/acs.jpclett.9b02567

Bertram, T. H., Kimmel, J. R., Crisp, T. A., Ryder, O. S., Yatavelli, R. L. N., Thornton, J. A., Cubison, M. J., Gonin, M., & Worsnop, D. R. (2011). A field-deployable, chemical ionization time-of-flight mass spectrometer. *Atmospheric Measurement Techniques*, *4*(7), 1471–1479. https://doi.org/10.5194/amt-4-1471-2011

Huey, L. G. (2007). Measurement of trace atmospheric species by chemical ionization mass spectrometry: Speciation of reactive nitrogen and future directions. *Mass Spectrometry Reviews*, *26*(2), 166–184.

Jernigan, C. M., Fite, C. H., Vereecken, L., Berkelhammer, M. B., Rollins, A. W., Rickly, P. S., Novelli, A., Taraborrelli, D., Holmes, C. D., & Bertram, T. H. (2022). Efficient Production of Carbonyl Sulfide in the Low-NO x Oxidation of Dimethyl Sulfide . *Geophysical Research Letters*, *49*(3), e2021GL096838. https://doi.org/10.1029/2021gl096838

Saunders, S. M., Jenkin, M. E., Derwent, R. G., & Pilling, M. J. (2003). Protocol for the development of the Master Chemical Mechanism, MCM v3 (Part A): Tropospheric degradation of non-aromatic volatile organic compounds. *Atmospheric Chemistry and Physics*, *3*(1), 161–180. https://doi.org/10.5194/acp-3-161-2003

Veres, P. R., Andrew Neuman, J., Bertram, T. H., Assaf, E., Wolfe, G. M., Williamson, C. J., Weinzierl, B., Tilmes, S., Thompson, C. R., Thames, A. B., Schroder, J. C., Saiz-Lopez, A., Rollins, A. W., Roberts, J. M., Price, D., Peischl, J., Nault, B. A., Møller, K. H., Miller, D. O., … Ryerson, T. B. (2020). Global airborne sampling reveals a previously unobserved dimethyl sulfide oxidation mechanism in the marine atmosphere. *Proceedings of the National Academy of Sciences of the United States of America*, *117*(9), 4505–4510. https://doi.org/10.1073/pnas.1919344117

Vermeuel, M. P., Novak, G. A., Jernigan, C. M., & Bertram, T. H. (2020). Diel Profile of Hydroperoxymethyl Thioformate: Evidence for Surface Deposition and Multiphase Chemistry. *Environmental Science and Technology*, *54*(19), 12521–12529. https://doi.org/10.1021/acs.est.0c04323

Wolfe, G. M., Marvin, M. R., Roberts, S. J., Travis, K. R., & Liao, J. (2016). The framework for 0-D atmospheric modeling (F0AM) v3.1. *Geoscientific Model Development*, *9*(9), 3309–3319. https://doi.org/10.5194/gmd-9-3309-2016

Wu, R., Wang, S., & Wang, L. (2015). New mechanism for the atmospheric oxidation of dimethyl sulfide. The importance of intramolecular hydrogen shift in a CH3SCH2OO radical. *Journal of Physical Chemistry A*, *119*(1), 112–117. https://doi.org/10.1021/jp511616j

Ye, Q., Goss, M. B., Isaacman-VanWertz, G., Zaytsev, A., Massoli, P., Lim, C., Croteau, P., Canagaratna, M., Knopf, D. A., Keutsch, F. N., Heald, C. L., & Kroll, J. H. (2021). Organic Sulfur Products and Peroxy Radical Isomerization in the OH Oxidation of Dimethyl Sulfide. *ACS Earth and Space Chemistry*. https://doi.org/10.1021/acsearthspacechem.1c00108

Figures and Tables

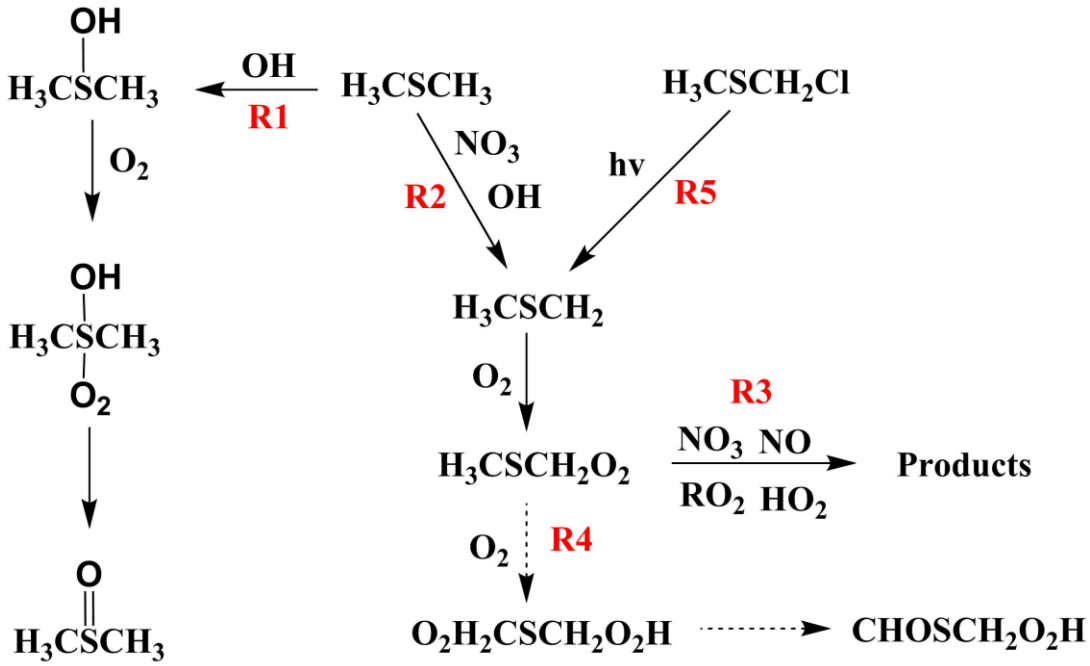

Figure B1: The theoretical and experimental oxidation pathways of DMS and DMS-Cl.

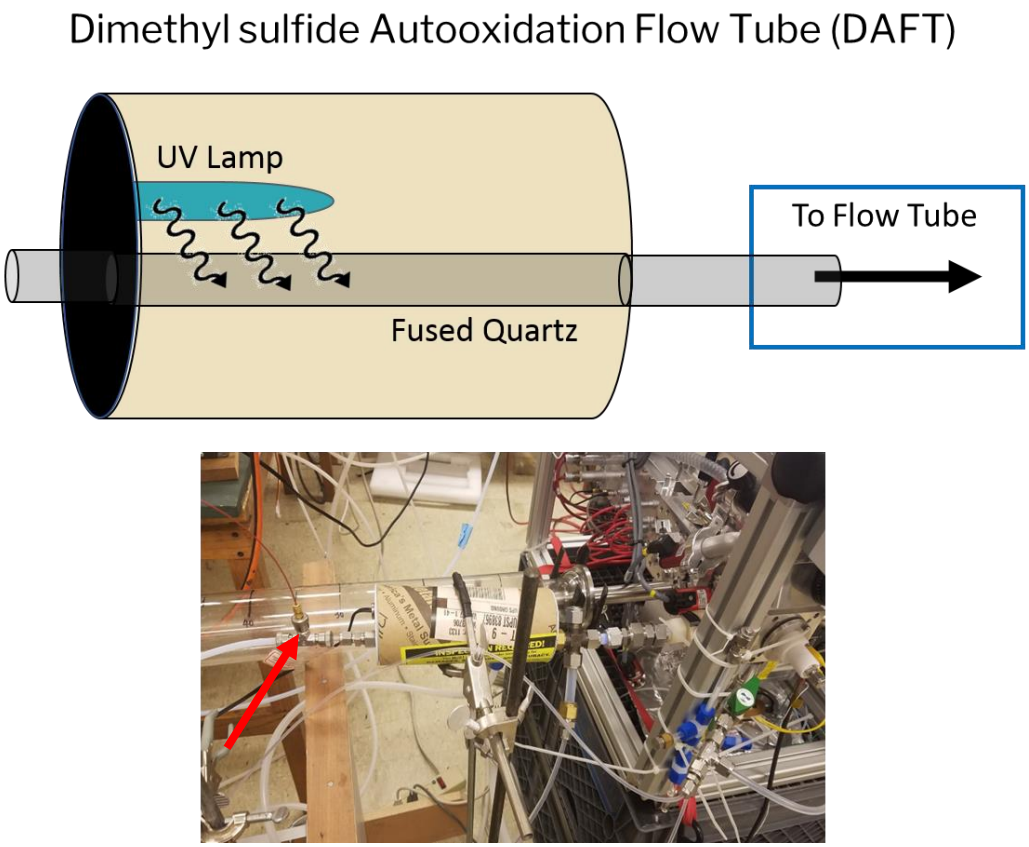

Figure B2: Cartoon schematic and image of the Dimethyl sulfide Autoxidation Flow Tube (DAFT)

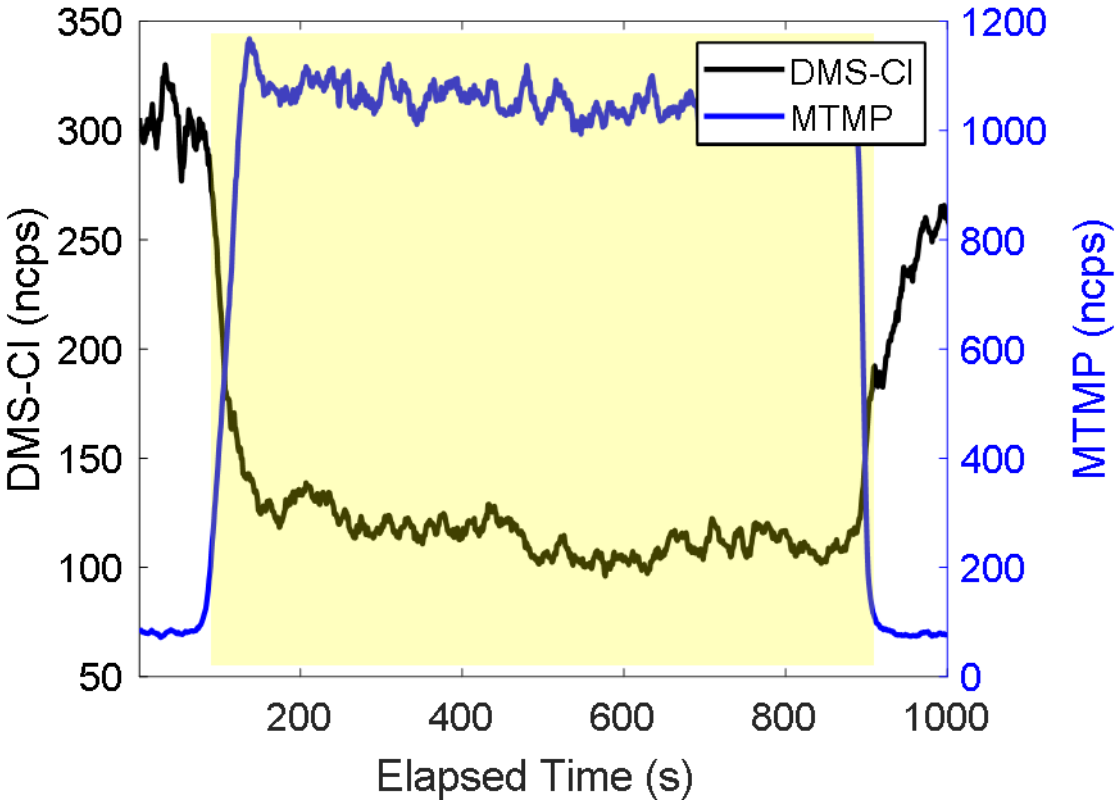

Figure B3: Detection of monochlorodimethyl sulfide (DMS-Cl) and methylthiomethyl peroxy radical (MTMP) during the DMS-Cl photolysis experiments utilizing B-CIMS. The yellow region indicates the time of the experiment while the UV light was turned on.

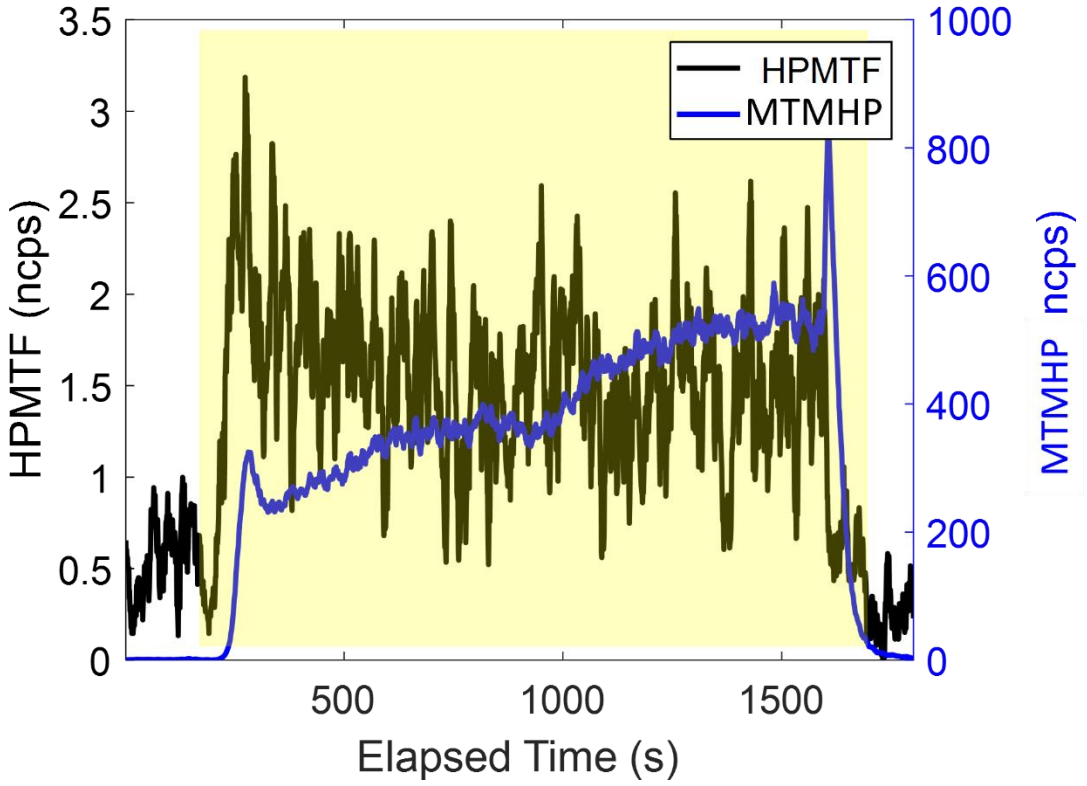

Figure B4: Detection of hydroperoxyl methyl thioformate (HPMTF) and hydroperoxy methyl sulfide (ROOH) during the OH oxidation of DMS utilizing H_2O_2 photolysis experiments with observations made by I-CIMS. The yellow region indicates the time of the experiment while the UV light was turned on.

Table B1. Binding Energies for Benzene CIMS utilizing M06/ 6-311+G(2d,p) level of theory

Cluster	Molecular E (hartree)	Cluster E (hartree)	ΔE (hartree)	ΔE (kcal/mol)
DMS-BenzCation	-709.5688971	-709.6215546	-0.0527	-33.0431
CH3SCH2OOH - BenzCat	-860.0706053	-860.1194527	-0.0488	-30.6522
HPMTF - BenzCation	-934.0836789	-934.1137026	-0.0300	-18.8402
CH3SCH2OO - BenzCat	-859.4263906	-859.4690193	-0.0426	-26.7499
COHSCH2OO - BenzCation	-933.4355334	-933.4647156	-0.0292	-18.3121
DMSO - BenzCation	-784.9245091	-784.9663295	-0.0418	-26.2426
Methanthiol - BenzCation	-670.4508277	-670.4919021	-0.0411	-25.7745
VinylSulfate - BezCat	-934.1333893	-934.1569601	-0.0236	-14.7909
MTF - BenzCat	-783.758285	-783.7899333	-0.0316	-19.8596
OCS - BenzCat	-743.2960586	-743.3105083	-0.0144	-9.0673
MTMP - BenzCat	-859.964102	-859.9950845	-0.0310	-19.4418
DimethDisulfide - BenzCat	-1107.763268	-1107.824735	-0.0615	-38.5711
Acetonitrile - BenzCat	-364.3364888	-364.3611959	-0.0247	-15.5039
DCM - BenzCat	-1191.323848	-1191.339923	-0.0161	-10.0874
Diethyl Ether - BenzCat	-465.1122346	-465.1416629	-0.0294	-18.4665
ChloroDMS - BenzCat	-1169.165877	-1169.21306	-0.0472	-29.6073
CCl4 - BenzCat	-2110.510831	-2110.525744	-0.0149	-9.3578
CHOSCHO - BenzCat	-857.6243582	-857.6407684	-0.0164	-10.2975
CH3SCH2 - BenzCat	-708.9132286	-708.9605832	-0.0474	-29.7155
C2H5SO2 - H2O - Benz	-935.6550321	-935.7050061	-0.0500	-31.3591
H2O2 - Benzcat	-383.184749	-383.20372	-0.0190	-11.9045
HO2 - BenzCat - Triplet	-382.5530068	-382.5732507	-0.0202	-12.7033
CH3SCHO - BenzCat	-783.6002746	-783.630897	-0.0306	-19.2158
CH3SOH - BenzCat	-745.49203	-745.5480429	-0.0560	-35.1486
CH3SSOH - BenzCat	-1143.669672	-1143.747115	-0.0774	-48.5960
CH2S - BenzCat	-669.0935883	-669.1346792	-0.0411	-25.7849
CH3SCH2OH - BenzCat	-784.7732238	-784.820746	-0.0475	-29.8206
Tetramethyl Ethylene - BenzCat	-467.2412469	-467.3068163	-0.0656	-41.1454
Trimethyl Ethylene-BenzCat	-427.9781483	-428.0321926	-0.0540	-33.9133

Table B2. Binding Energies for Iodine CIMS utilizing M06/ 6-311+G(2d,p) level of theory

Cluster	Molecular E (hartree)	Cluster E (hartree)	ΔE (hartree)	ΔE (kcal/mol)
CH3SOOH - Iodine	-7508.283664	-7508.313433	-0.02977	-18.680
CH3S(O)2OOH - Iodine	-7658.69984	-7658.7293	-0.02946	-18.486
CH3S(O)OOH - Iodine	-7583.485665	-7583.508649	-0.02298	-14.423
CH3SCH2OOH - Iodine	-7547.560147	-7547.586397	-0.02625	-16.472
HO2 - Iodine	-7070.223751	-7070.253943	-0.03019	-18.946
H2O2 - Iodine	-7070.855493	-7070.872259	-0.01677	-10.521
HOOCH2SCH2OO - I	-7697.246565	-7697.280575	-0.03401	-21.341
HOOCH2SCH2OOH - I	-7697.878449	-7697.912064	-0.03361	-21.093
cHPMTF - Iodine	-7621.579108	-7621.611756	-0.03265	-20.487
CH2OS - I	-7432.010653	-7432.027928	-0.01728	-10.841
CH2O2S - I(OH)	-7507.244639	-7507.282544	-0.03791	-23.786
CH2OS - I	-7432.009249	-7432.038504	-0.02925	-18.358
CH2O2S Inward - I	-7507.241347	-7507.288903	-0.04756	-29.842
CH2O2S Invert - I(SH)	-7507.250389	-7507.270714	-0.02032	-12.754
Keto-Carboxylic Sulfide - I	-7620.535427	-7620.574846	-0.03942	-24.736
Nitric - I	-7200.17963	-7200.21508	-0.03545	-22.245
Formic - I	-7109.047842	-7109.086039	-0.03820	-23.969
Formamide - I	-7089.164266	-7089.190248	-0.02598	-16.304
N2O5 - I	-7404.589724	-7404.628811	-0.03909	-24.528
Nitric - I	-7200.17963	-7200.215077	-0.03545	-22.243
Acetic Acid - I	-7148.330873	-7148.35129	-0.02042	-12.812
Glyoxal - I	-7222.331447	-7222.364331	-0.03288	-20.635
Tert-Butyl Hydroperoxide - I	-7227.919102	-7227.941884	-0.02278	-14.295
ThioDiAldehyde - I	-7545.295102	-7545.326025	-0.03092	-19.404
OCHOCHO - I	-7222.333743	-7222.368212	-0.03447	-21.630
Trans-Glyoxal - I	-7147.087219	-7147.117601	-0.03038	-19.065
Cis-Glyoxal - I	-7147.080329	-7147.114803	-0.03447	-21.633
MSIA - I	-7508.374531	-7508.406468	-0.03194	-20.040
MSA - I	-7583.591318	-7583.621525	-0.03021	-18.955
HPMTF - Closed - I	-7621.591166	-7621.617616	-0.02645	-16.598
HPMTF - Open - I	-7621.587222	-7621.627141	-0.03992	-25.050
ClNO2 - I	-7584.573182	-7584.592448	-0.01927	-12.090
AlkOOH - I	-7381.65622	-7381.683697	-0.02748	-17.242
AlkOOH-cis - I	-7381.66072	-7381.6898	-0.02908	-18.248
C2H4O3S - Acid - I	-7621.712252	-7621.756012	-0.04376	-27.460
HPMTF(S=O) Closed - I	-7696.74806	-7696.779341	-0.03128	-19.629
HPMTF - Open - S=O - I	-7696.740146	-7696.789276	-0.04913	-30.829
Thioperformic acid - I	-7507.107442	-7507.139351	-0.03191	-20.023

CH3SOH - I	-7433.168009	-7433.19272	-0.02471	-15.506
SO2 - I	-7467.943731	-7467.974756	-0.03103	-19.469
HPMDTF - I	-8019.788418	-8019.809677	-0.02126	-13.340
DMSO - I	-7472.41993	-7472.44389	-0.02396	-15.035